Characterization of T2L2 (Time Transfer by Laser Link) on the Jason 2 ocean altimetry satellite and Micrometric laser ranging

Patrick Vrancken

Université de Nice - Sophia Antipolis, UFR Sciences
Ecole Doctorale Sciences Fondamentales et Appliquées

THESE
pour obtenir le titre de
Docteur en Sciences
de l'Université de Nice - Sophia Antipolis
Discipline: Sciences de l'Univers

présentée et soutenue par
Patrick VRANCKEN

Characterization of T2L2 (Time Transfer by Laser Link) on the Jason 2 ocean altimetry satellite and Micrometric laser ranging

Thèse dirigée par Etienne SAMAIN et Pierre EXERTIER
soutenue le 23 Septembre 2008 à Calern

Membres du jury:

M. François VERNOTTE	Observatoire de Besançon	*Président*
M. Noël DIMARCQ	Observatoire de Paris	*Rapporteur*
M. Ulrich SCHREIBER	Technische Universität München	*Rapporteur*
M. Eduard IGENBERGS	Technische Universität München	*Examinateur*
M. Pierre EXERTIER	Observatoire de la Côte d'Azur	*Directeur*
M. Etienne SAMAIN	Observatoire de la Côte d'Azur	*Co-Directeur*
M. François GUERIN	THALES Alenia Space	*Invité*
M. Philippe GUILLEMOT	Centre National des Etudes Spatiales	*Invité*

Meinem Großvater Helmut Kasperczyk.

Abstract

Many aspects of our modern life rely on global networks of highly synchronized elements, such as the internet and navigation systems. Today, new generations of atomic clocks, such as atomic fountains and optical clocks drive the requirements on the devices that permit the establishment of these precisely synchronized networks or time scales.

The T2L2 (Time Transfer by Laser Link) scheme, based on the technology of satellite laser ranging (SLR), is a radically new means for tomorrow's clock synchronization. The T2L2 experiment was accepted in 2005 by CNES to fly as a passenger instrument on the ocean altimetry satellite Jason 2, in order to prove the concept and the aimed performance of optical time transfer. After a short development phase, the instrument was delivered by the industrial partners beginning 2007.

The main part of this work treats the thorough characterization of the T2L2 flight instrument.
For this purpose, a highly complex test bed has been developed by the Observatoire de la Côte d'Azur (OCA), including all important elements of the T2L2 operation scheme, such as laser and other luminous irradiation, clocks and geometry simulation. By this means, the operation of the T2L2 instrument aboard the satellite could be reproduced in a laboratory environment.

This allowed the detailed characterization in two respects: First, we obtained substantial data for the calibration of the instrument which are essential for the proper operation and exploitation of T2L2. Thus, they permit on the one hand an optimum configuration of instrumental settings depending on the prevailing conditions. On the other hand, we are able to establish high fidelity correction tables or algorithms for the processing of the raw data.

The second aspect is the evaluation of the performance of the T2L2 flight instrument in terms of time / frequency metrology: The performed test campaigns allowed to prove that the instrument meets the imposed requirements in all important aspects of the envisaged time transfer.

Further, a detailed analysis of the whole scheme, including the performance of the space instrument as well as of the ground segment (i.e. a satellite laser ranging station) has been performed. By means of this "error budget" we could demonstrate the final performance of the whole laser-based time transfer: With a time stability of some picoseconds when integrating measurements over a satellite pass of some hundred seconds, T2L2 will be able to compare today's most advanced clocks such as atomic fountains. The absolute accuracy has been determined to be less than 50 ps in common view configuration.

Hence T2L2 will permit, starting few weeks after its launch on June 20 of this year, to perform time transfer on a precision and accuracy level never reached before, what will allow, in its turn, remarkable scientific and technological applications.

The second part of the present document is oriented to the extension of the technology used for SLR and T2L2 to another field of application, the high-resolution measurement

of absolute distances in space. Two complementary teams of the Observatoire de la Côte d'Azur started in 2005 a collaboration, named ILIADE, in order to unify their respective competences in interferometry and time of flight measurement. This goal shall be reached by the use of frequency combs that have recently gained much public attention due to the award of the Nobel Prize to its inventors in 2005. The frequency comb promises to perform time-of-flight measurements on the modulated optical carrier wave (the pulses) and simultaneously interferometry on the comb frequency lines.

An important step towards the feasibility of this approach is to reach the threshold of the wavelength by event timing and phase measurement at very high rates. My work comprises the characterization of some ultra-high bandwidth opto-electronic and timing equipment to be employed at that purpose. We could show that this level of performance in distance measurement is effectively coming into the reach of today's technology.

The ILIADE scheme would allow to perform distance measurements on the same level of performance as the clock connected to the used frequency comb, that is to say on the order of at least 10^{-15}, meaning for instance a micrometer over one million kilometers, and this in an absolute manner (i.e. giving a number with 15 significant digits).

Such an advanced performance in terms of ranging will enable the search of anomalous gravity in space, new types of Earth and planetary geodesy and high-fidelity metrology of future space telescopes.

Keywords Time transfer, metrology, satellite laser ranging, space instrument, distance measurement, time of flight, interferometry, frequency comb.

Résumé

Maintes aspects de notre vie moderne reposent sur des réseaux d'échelle mondiale et composés d'éléments synchronisés, comme internet et les systèmes de navigation. Aujourd'hui, des nouvelles générations d'horloges atomiques, comme des fontaines atomiques et des horloges optiques, déterminent les exigences envers les dispositifs qui permettent l'établissement de ces réseaux synchronisés, ou échelles de temps.

Le schéma de T2L2 (Transfert de Temps par Lien Laser), basé sur la technologie de la télémétrie laser sur satellite (SLR), représente un moyen radicalement nouveau pour la synchronisation des horloges de demain. L'expérience T2L2 fut acceptée par le CNES en 2005 en tant qu'instrument passager sur le satellite d'altimétrie des mers Jason 2, afin de prouver la viabilité d'un transfert de temps optique par satellite. Après une phase de développement courte, l'instrument spatial a été livré par les partenaires industriels début 2007.

La partie majeure de ce travail de thèse traite la caractérisation intégrale de l'instrument spatial T2L2.
A cette fin, un banc de test de haute complexité fut développé à l'Observatoire de la Côte d'Azur (OCA); il inclut tous les éléments importants du schéma opérationnel de T2L2, comme l'irradiation par laser et par d'autres sources, des horloges et la simulation de la géométrie. Ce banc a reproduit en laboratoire l'utilisation de l'instrument spatial T2L2 sur le satellite.

Ceci a permis la caractérisation de l'instrument spatial à deux égards: Premièrement, on a obtenu des données substantielles pour la calibration de l'instrument; elles sont essentielles pour l'utilisation et l'exploitation sans faille de T2L2 car elles permettent une configuration optimale des paramètres de l'instrument dépendant sur les conditions dominantes. D'autre part, ce travail fournit des données pour l'établissement des tableaux ou algorithmes de correction pour le traitement des données brutes venant du satellite.

Le deuxième volet est l'évaluation de la performance en métrologie temps / fréquence de l'instrument de vol T2L2: Les campagnes d'essai ont permis de prouver que l'instrument respecte les exigences dans tous les aspects importants du transfert de temps envisagé.

Par ailleurs, une analyse approfondie de tout le schéma a été menée, incluant la performance de l'instrument spatial ainsi que celle du segment sol (c'est-à-dire, une station de télémétrie laser). A l'aide de ce « bilan d'erreurs », on a démontré la performance finale de tout le transfert de temps. Avec une stabilité de quelques picosecondes, en intégrant des mesures sur un passage du satellite de quelques centaines de secondes, T2L2 permettra de comparer les horloges les plus avancées d'aujourd'hui, incluant les fontaines atomiques. L'exactitude absolue d'un transfert de temps a été déterminée à moins que 50 ps en configuration de vue commune.

Par conséquent, T2L2 permettra, quelques semaines après son lancement au 20 juin de cette année, d'effectuer des transferts de temps d'un niveau de précision et d'exactitude jamais atteint. Ceci, en revanche, contribuera à des applications scientifiques et technologiques de haut niveau.

La deuxième partie du travail de thèse est orientée autour de l'extension de la technologie de télémétrie laser et de T2L2 à un autre domaine d'application, la mesure absolue et de très haute résolution de distances dans l'espace. Deux équipes complémentaires de l'Observatoire de la Côte d'Azur avaient démarré une collaboration en 2005, nommé ILIADE, afin de réunir leurs compétences respectives en interférométrie et mesure de temps de vol. Cet objectif devra être atteint en utilisant un laser de peigne de fréquences qui avait retenu l'attention du public à cause de la remise du prix Nobel à ses inventeurs en 2005. Le peigne de fréquences devra permettre d'effectuer des mesures de temps de vol sur la porteuse optique modulée (les impulsions laser) en parallèle avec une mesure interférométrique sur les raies de fréquence.

Un pas important vers la faisabilité de cette approche est d'atteindre le seuil de la longueur d'onde par chronometrie et par la mesure de phase à haute cadence. Mon travail porte sur la caractérisation de l'équipement de détection et de datation à haute bande passante. On a démontré que ce niveau de performance en mesure de distance est effectivement à la portée de la technologie d'aujourd'hui.

Le schéma d'ILIADE permettra d'effectuer des mesures de distance au même niveau de performance que l'horloge connectée sur le peigne de fréquence, c'est-à-dire de l'ordre de 10^{-15}, ainsi permettant des précisions d'un micron sur un million de kilomètres et ceci d'une façon exacte.

Une telle performance en télémétrie permettra la recherche d'anomalies gravitationelles dans l'espace; elle ouvrira de nouveaux horizons pour la géodésie terrestre et planétaire et procurera une métrologie hyperfine pour des futurs télescopes spatiaux.

Mots-clés Transfert de temps, métrologie, télémétrie laser sur satellite, instrument spatial, mesure de distance, temps de vol, interférométrie, peigne laser.

Remerciements

Ce travail fut réalisé du janvier 2005 au septembre 2008 au sein du groupe Recherche et Développement en Métrologie du département GEMINI[1] de l'Observatoire de la Côte d'Azur. Une thèse doctorale, surtout avec un sujet instrumental, est un acheminement de travaux qui ne sont jamais à résoudre par une seule personne. De ce fait j'ai à remercier beaucoup de personnes qui m'ont aidé tout au long de cette aventure pour enfin aboutir au résultat final et la synthèse ci-présente.

Premièrement je voudrais exprimer mes plus grands remerciements à Etienne Samain, mon directeur de thèse, pour son soutien inégale, pour ses qualités d'instruction et sa disposition ouverte pour discuter des questions simples ou complexes une n-ième fois. Je le remercie également pour son enthousiasme contagieux dans le travail de recherche et sa fraternité aimable que ce soit pendant des opérations instrumentales ou simplement autour de la tasse café obligatoire.
Je remercie aussi Pierre Exertier, également directeur de thèse, pour son accueil au laboratoire, son soutien, les discussions et sa prédisposition de placer nos activités dans un contexte scientifique plus grand.
Je tiens également à remercier le jury de thèse : Noël Dimarcq de l'Observatoire de Paris-SYRTE, rapporteur de thèse, pour les commentaires précieux sur le manuscrit et les discussions tout au long de ma thèse. Ich danke ebenso Ulrich Schreiber von der Fundamentalstation Wettzell, ebenso Berichterstatter, für die hilfreichen Kommentare und die Gespräche während meiner ganzen Zeit am Observatoire. Je remercie Francois Vernotte de l'Observatoire de Besançon pour la présidence lors de la soutenance et Eduard Igenbergs de la Technische Universität München pour son soutien et les conversations illuminantes que l'on a pu menées depuis mes études en astronautique. Je suis très reconnaissant à François Guerin de Thales Alenia Space pour le suivie régulier et constructif et ses commentaires sur le manuscrit et à Philippe Guillemot du CNES pour son amitié, les manips ensemble et les maintes discussions utiles.

Je voudrais aussi exprimer mes remerciements à Thales Alenia Space et le Centre National des Etudes Spatiales (CNES) pour le financement de la bourse de thèse.

Ensuite, je voudrais remercier toute l'équipe qui m'a accueilli et intégré avec tant d'amabilité. Dans le désordre, je remercie : Grégoire Martinot-Lagarde pour son sens d'enseignement, son humour et ses argumentations (des fois insolites), le lointain Robert Dalla pour sa fraternité, Hervé Viot pour son caractère et nos plans de faire, un jour, une sortie de ski rando ensemble, Jocelyn Paris pour les innombrables larmouilles de café de commerce équitable, ses réflexions sur la langue française (qu'elle soit écrite ou de l'argot) et son humour persévérant, Jonathan Weick pour son amitié et les heures de conduite Roq - Calern dans le silence, Jean-Francois Mangin pour son enseignement et ses contes, Françoise Baumont pour

[1] Enfin fusionné dans l'équipe AstroGéo dans le département Géosciences Azur.

sa gentillesse, Aurélien Dréan pour son engagement et sa patience lors d'un n-ième re-design de la mécanique, Olivier Dupont pour son amitié et son aide précieuse, Dominique Albanese pour sa fraternité, pour l'astronomie, pour son amour de la musique, les films, l'art et pour en finir les chemin de fer miniature, Jean-Marie Torre pour son amitié, son savoir-vivre et pour parfois être une mauvaise tête adorable, Jean-Louis Oneto pour son amabilité et pour être Jean-Louis Oneto en original, et enfin Franck Para, mon collègue de bureau au Schmidt, pour son amitié, son amour pour un certain groupe de musique allemand (que l'on ne mentionnera pas ici) et pour être le farceur qu'il est.

Je remercie également les laseristes de la station mobile, Maurice Furia, Maurice Laplanche, Emmanuel Queven, Etienne Cuot et Monique et Francis Pierron pour l'aide, l'enseignement et les discussions précieuses.

Plus généralement je tiens à remercier les gens de Calern pour leur accueil cordial et leur aide précieuse dans tous les aspects, que ce soit pour le travail scientifique, administratif ou autre : Ainsi, un grand merci à Bernadette Nascimben pour toute l'aide et pour être un peu l'âme de Calern, à Serge Roata et Didier Doudon, à Marie-Thérèse Hoogstoel, Vincent di Gioia et Nicolas Marais pour la cuisine excellente, à Frédéric Morand pour l'accueil au Schmidt et les conversations, à Christian Delmas, Alain Blazit, Jean-Louis Chevassut et Guy Merlin, à Christian Pollas pour son amitié, le GMA et les Polasseries, et finalement un grand merci aux gens sans lesquels rien, mais absolument rien ne marcherait au plateau, au service technique, nommément Alain Gomez, Charly Parvillé, Philippe Bruneau et Jaques Depeyre pour leur aide, que ce soit avec des tables optiques ou des cables électriques; un autre grand merci à l'équipe de l'atelier, à Richard Brunet, Christian Munier et Xavier Martin pour leur aide et les plus belles pièces de mécanique qui soient.

Ainsi je pourrais poursuivre pour les gens de Roquevignon, mais malheureusement il irait bien au-delà du cadre de vous nommer tous mais sachez que j'ai beaucoup d'amour et respect pour vous.

De plus, je tiens à remercier et saluer mes collègues-doctorants, à commencer par Christophe Buisset pour son amitié, la Corse et les apéros, mais aussi Stéphane Sacuto, Fabien Patru, Nayyer Fazel, Samer Kanaan, Clément Courde, Jordi Fontdecaba et Olivier Minazzoli. Aussi un grand merci à mon collègue de bureau pendant la phase de rédaction, Marcello Borges.

Je remercie également, pour les discussions et idées inspirantes autour ILIADE, les gens du département ARTEMIS à Nice, en particulier Nary Man, Alain Brillet, Michel Lintz, Francois Bondu et Christophe Bourcier.
Je remercie aussi toute autre personne que j'aurais pu oublier par négligence.

Ich danke ebenso meinen Eltern und Großeltern für ihre stete Unterstützung, ohne sie wäre all dies nicht möglich gewesen.

Ici en dernier, mais en première place dans mon cœur, je voudrais remercier mon épouse Sandra pour son amour et son soutien.

Contents

Introduction

Time and space have always been of great interest for mankind. The measurement of time has been important since the earliest days of human culture, for the calculation of the right date of sowing and harvest, the knowledge of low and high tide and not at least for the determination of holy days.

The precise determination of space, or distance in multiple dimensions dates also back in the earliest days of human history: land had to be delimited and estimated, edifices to be erected and ships to be navigated.

The last point already refers to a strong connection of space and time and their measurement: Today, the unit of distance, the meter, is defined by the second (in turn defined by quantum physics) and the light speed which is a fundamental constant. Today's navigation (by GNSS systems) relies on the retrieval of time and position information of satellites. Finally, distances to remote satellites (in Earth orbit or somewhere else in the solar system) are determined with a time-of-flight measurement.

Since their discovery by Maxwell in 1865 and their physical demonstration by Hertz in 1888, electromagnetic radiation has been the tool of choice for various technological and scientific applications, including the measurement of space and time: The constancy of light speed provides a type of caliper for the units of space and time.

In the 1960s a new version of source of electromagnetic radiation was invented: The laser, providing monochromatic, directive and coherent radiation in the visible spectrum. The said aspects provide new capabilities, in particular for the measurement of time and space.

It is at this pivot of time and distance measurement and optical techniques that is situated the present thesis. It comprises two major topics: The Time Transfer by Laser Link (T2L2) experiment with the characterization of the flight instrument build for the Jason 2 satellite mission. The second topic is situated in the context of a revolutionary evolution of two different disciplines of optical distance measurement: Interferometry and time-of-flight measurement.

The first part starts with an introduction to the measurement and in particular to the comparison of remote time scales (or clocks), what is called time transfer in the following. The principle of optical time transfer is introduced.

The second chapter describes in detail the optical time transfer instrument T2L2, relying on satellite laser ranging (SLR) technology. The T2L2 instrument, designed for the Jason 2 satellite, will allow to perform comparisons of today's most advanced clocks over continental and even inter-continental distances.

The third chapter represents one of the main parts of the present thesis, the meticulous characterization of the T2L2 instrument in laboratory environment before being put into operation. This is necessary in order to exploit the raw data collected by the space instrument once in orbit. Further, the performance of the instrument has to be determined to serve as a reference for the beginning scientific exploitation. The means for the full characterization

is a complex and comprehensive test bed developed during the second year of the thesis, its operation and the analysis of the obtained data.

Chapter four focuses on the description of the ground segment of the time transfer by laser link scheme, what consists in satellite laser ranging stations.

The fifth chapter finally exploits the obtained experimental data in order to build a comprehensive budget in terms of time transfer performance. This budget serves as comparative value needed for the performance assessment of the T2L2 operation in orbit.

The first part of the thesis closes with a conclusion and some outlook for future evolutions of the scheme.

The second part of the thesis is oriented towards a common instrumental research activity between two groups at the Observatoire de la Côte d'Azur having complementary competences in interferometry and time-of-flight distance measurement.

Chapter seven therefore focuses on giving an introduction on different ways of implementation of these two distance measurement techniques for use in space. It further introduces the central keystone of the following technology project, the frequency comb.

The eighth chapter discusses the ILIADE project aiming at unifying both interferometry and time-of-flight measurement in a single approach using frequency combs. This combination would yield high resolution absolute distance measurement on arbitrary scales without any ambiguity. After an introduction into the scheme, first preliminary experimental work is presented that aims for reaching wavelength resolution time-of-flight measurement in order to bridge the gap to interferometry. The ILIADE part closes with a discussion of the first obtained results that promise that the following technology generation, right now under development, may reach the targeted objective.

A final concluding chapter sums up the achieved results of some of the most advanced time and space measuring technologies, T2L2 and ILIADE.

The work of the thesis was carried out in the RDM group (Recherche & Développement en Métrologie) of the GEMINI laboratory (UMR CNRS 6204) of the Observatoire de la Côte d'Azur, under the supervision of Etienne Samain and Pierre Exertier.

The GEMINI lab merged into the Géosciences Azur laboratory (UMR 6526) and the RDM group into the AstroGéo group beginning 2008.

Part I.

The "Time Transfer by Laser Link" experiment

Zeit ist das, was man an der Uhr abliest.

(Albert Einstein)

1. Time transfer

1.1. What is time transfer?

1.1.1. What is time in the first place?

Before touching on time transfer, one should take a step back and contemplate what one is dealing with: What is time? The answer to this very fundamental question is very tough and it is for this reason that I cited one of the most brilliant physicists, Albert Einstein, very famous for his popular dictums, who answered with a twinkle in his eye, "Time is what you read on your clock", meaning that he evidently had no clue about the true nature of time.

There are two aspects that drive the perception of time: Directivity and periodicity.
The first notion refers to the observation that time, and with it the universe, evolves in a single direction. This matter is often termed "Arrow of time". Generally, the laws of the universe, in their mathematical formulations, do not distinguish between a forward or a backward direction of time. However, following Hawking [1], there are at least three different indications that there is some sort of arrow of time. The most famous is probably the fact that disorder increases with the time going by. This is simply due to the fact that there are much more states of disorder than states of perfect order. If a closed system, initially in an ordered state, undergoes some variations, it is very probable that it is in a state of higher disorder later. This observation was first formulated by Rudolf Clausius, based on the work of Sadi Carnot, in the second law of thermodynamics, adapted to heat engines. In a closed system, entropy would always increase. Entropy is often equated with the measure of disorder, following the concept of Ludwig Boltzmann as a measure for microscopic configurations that result in the observed macroscopic description of the thermodynamic system. Today it is commonplace to state that the entropy in the universe increases with time.
The second arrow of time stated by Hawking [1] is of psychological nature: People remember the past and not the future; in fact, this psychological arrow is bound to the thermodynamic: The process of producing a state of higher order in a human brain (or a computer memory) consumes a lot of energy, increasing entropy.
The third arrow of time is the cosmological arrow, reflecting the fact that the universe is in expansion rather than contraction. The reason for the collinearity of the thermodynamic and the cosmological arrow of time is that intelligent beings can only exist in the expanding phase of the universe [1].
Hence: Time evolves in a certain direction. The perception of the way it evolves was profoundly unsettled in the beginnings of the last century. In history, time, together with space had always been at the basis of the laws of the universe, somehow directing other processes but itself invariant to the laws. Einstein finally inverted this situation: Time, along with space is also subject to the laws of the universe. Time and with it other processes evolve differently in a moving system as compared to a system at rest. Time and space are coupled to gravity. Today, we are used to describe physical processes in a four-dimensional space-time, itself subject to the laws of relativity.

But how to measure time? For space we may conveniently use a meter, but what meter exists for time? The answer refers to the second point I mentioned above, periodicity, and the transposition of the measurement of time in the measurement of some other quantity. Henri Poincaré postulated (cited in [2]): "La durée de deux phénomènes identiques est la même; ou, si l'on aime mieux, les mêmes causes mettent le même temps pour produire les mêmes effets."[1] As we will see in the following, this relation was used throughout the millenia of human history to produce meters for the measurement of time, chronometers.

1.1.2. The measurement of time

Throughout the history of humanity, people used basic processes to measure time or to situate events in a time frame. People used the movement of sun, moon and earth to establish calendars. One conclusion must have been drawn very early: The measurement of time is the more accurate, the smaller the time between the periodic events or the more frequent the events. The smallest natural event observable by eye, apart from tides, is the movement of the sun in the sky: The oldest known sundial dates from over 1,500 B.C., build in the ancient Egypt.
But one had to divide the day into even smaller pieces, what lead to different types of mechanical clocks, like water meters (clepshydra) or sand clocks, which were used, together with the sundial into the ages of enlightenment when the first pendulum clock was build in 1656 by Christiaan Huygens, certainly inspired by the work of Galileo Galilei and his son Vincenzo.

Since then, mechanical clocks have been constantly ameliorated. In 1735, the carpenter and autodidactic watchmaker John Harrison resolved the problem of maritime longitude measurement by building a clock of unprecedented accuracy. In 1923, the automatic clock

Figure 1.1.: The first Harrison chronometer H1 (1735) and his masterpiece H4 (1759). Captain James Cook took an exact copy of the H4, Kendall's K1, on his second journey into the south Pacific and ascertained its excellent quality to the British admiralty, what finally led to the recognition of the "Longitude Prize" to Harrison. Photographs © National Maritime Museum, UK

(wristwatch with pendulum flywheel mass) was developed by John Harwood. The need for

[1] The duration of two identical phenomena is identical, or, if one prefers, the same causes take the same time for producing the same effect.

winding up mechanical clocks was further taken care of by electric motors or by electromagnetics.

Finally, after the discovery of the Piezo-effect in 1880 by the brothers Jacques and Pierre Curie, the way to the quartz clock was in reach: In 1929, the first quartz clock was developed by Warren A. Marrison in the Bell labs. In 1932, the two physicists Adolf Scheibe and Udo Adelsberger produced a proper quartz clock and measured for the first time the irregular rotation of the Earth. The electric behavior of a quartz resonator is equivalent to a serial connection of a capacitance, inductor and resistance. Quartz oscillators may be used in nearly all LC - oscillator circuits[2], and replace the LCs partially or completely. Today, modern circuitry demands nearly everywhere for fast and precise clock generators. So the quartz technology is not only omnipresent in timing applications but in all information technology. Quartz resonators are further secondary frequency etalons providing highly stable (on the short term) frequencies for other types of clocks, like atomic clocks.

Into the years of the 1950s, quartz clocks had played the role of time keepers in the national standards laboratories. The need for ever more accurate and also more stable clocks led to the development of atomic clocks. The devices use the energy levels between the different levels of the hyperfine[3] structure of a certain atom species. Certain transitions are preferred to others due to their better stability, insensitivity to external effects or simply better ease of implementation.
Today, the SI second is based on the transition between the two hyperfine Zeeman levels of the ground state of the Cesium 133 atom (exactly 9,192,631,770 cycles of the hyperfine structure transition frequency).

A typical Cesium clock of today (for example the commercial HP 5071A) is based on a jet of Cesium atoms in the lower energy level E_1 that is introduced in a resonant cavity; this cavity is excited by a radio frequency signal coming from a quartz oscillator that is multiplied as close as possible to the transition frequency of 9.19 GHz. The better the accordance of the supplied radio wave, the bigger the number of atoms that will pass into the excited state E_2. After the exit of this so-called "Ramsey-Cavity", a magnetic state selector separates the atoms in state E_1 from the ones in E_2. A detector produces a signal proportional to the number of atoms in E_2. A control loop permanently adjusts the oscillator frequency in order to maximize the number of Cesium atoms in the excited state E_2 and thus to produce at best the desired transition frequency.

A hydrogen maser, however, is based on stimulated emission of radiation and thus produces the electro-magnetic radiation itself.
For this purpose, only Hydrogen atoms in the excited state E_2 of the hyperfine transition of 1,420,405,751.768 Hz (this is achieved by some state selection process) are fed in a high quality factor microwave cavity, thus generating a population inversion. Some of the excited atoms may now decay into the lower energy level by emitting some microwave radiation; the resonant cavity confines the radio waves which generate stimulated emission of the other atoms, leading to a standing wave in the cavity. A small fraction of this radiation is coupled into a coaxial cable and fed to a coherent receiver which amplifies and divides this signal

[2]Inductor-capacitor oscillating circuits.

[3]The hyperfine structure goes beyond the fine structure of atomic energy levels due to the weak magnetic interaction between electrons and nucleus; the order of magnitude of this type of spectral splitting is about 1,000 times lower than for the fine structure, which in turn is about a factor of 10^4 lower than the gross structure (energy difference of electronic orbitals). Therefore, the hyperfine transitions lie in the radio frequency or microwave domain.

with a series of phase-lock-loops and quartz oscillators.

Both types of atomic clocks offer a high degree of frequency accuracy: Today, commercial Cesium clocks attain less than 10^{-14} and masers about $5 \cdot 10^{-14}$. In Cesium fountains the atoms are cooled and launched on a ballistic trajectory to overcome perturbing effects, thus reaching 10^{-15}.

Today, researchers are aiming to further reduce the time interval of the transition in order to achieve higher accuracy. This is done with atomic transitions in the optical domain (at some hundreds of THz instead GHz). For a long time this option could not well be exploited since there was no connection between the generated optical frequency (e.g. by a laser) and the microwave world of atomic clocks, quartz and electronics. Optical frequencies could only

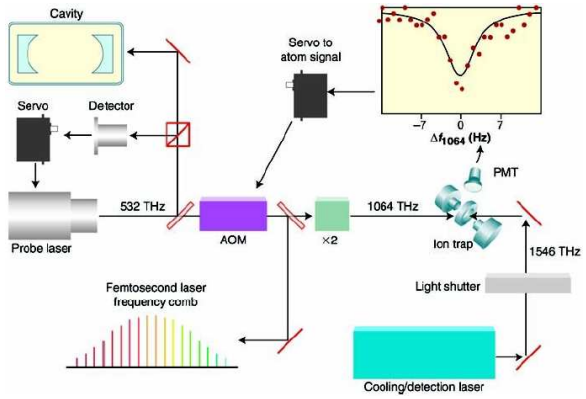

Figure 1.2.: Basic layout of an optical atomic clock (sketch taken from [3])

be compared to Cesium clocks by employing very large and complex multiplication stages with all sorts of lasers.

Then came the invention of the optical frequency comb for what Ted Hänsch and John Hall received the Nobel prize in 2005. The frequency comb, or femtosecond laser, features a set of narrow individual spectral lines (corresponding to the modes in the oscillator) in the spectral domain and a pulse train (of short durations) in the temporal domain. With the self-referencing technique, the offset frequency f_0 of the spectral lines may be controlled. The repetition rate f_{rep} determines the comb spacing with $f_n = n \cdot f_{rep} + f_0$. The comb thus serves as a ruler for optical frequencies referenced by the laser rate what may be controlled by an atomic clock.

In an optical atomic clock, the principle works the other way round: A highly stable laser (issued from a highly stable mechanic cavity) is locked onto a certain optical atomic transition (698 nm for Strontium, for instance). This radiation is fed to a frequency comb which, in turn, is locked with one tooth on this line; the adapted repetition rate is now locked on the optical transition allowing for higher accuracy (10^{-16}) and stability.

For a general overview of clock development a review article by Scott Diddams from NIST [3] may be recommended by the author.

1.1.3. Clocks and time scales

There are a whole bunch of different time scales, all having a goal in common: To situate physical elements in time and space in a most precise and accurate way. The nature of the used time scale is therefore adapted to the respective application.

As an example, the Universal Time N°1 (UT1) is based on Earth's rotation; it indicates the true angle between the Greenwich meridian and the astronomical vernal equinox - the users are mainly geoscientists and astronomers. UT1 is obtained through observations with Very Long Baseline Interferometry (VLBI), Satellite and Lunar Laser Ranging (SLR, LLR) and GPS. The International Earth Rotation and Reference Systems Service (IERS) synthesizes all these measurements and publishes the actual earth orientation data in a monthly bulletin, by giving the difference of UT1 from UTC (see below), known as dUT1.

The different national standard labs generate proper time scales based on their best atomic clocks, called TAF in France or TA(PTB) in Germany, for instance. All these clocks are combined (over 250 clocks in more than 50 labs) to form the international atomic time TAI, which is under the responsibility of the Bureau International des Poids et Mesures (BIPM). This bureau publishes monthly a bulletin of the individual differences between TAI and the respective TA(k). As it could be guessed, the creation of such a time scale needs some sort of comparison; this is done with time transfer, as we will see in the next section.

A combination of the astronomical Universal Time and TAI is the UTC (Universal Time, Coordinated): UTC is based on TAI but adapted to UT1 by inserting leap seconds whenever $dUT1 \geq 0.9$ s. It is the basis for all civilian and military activity like air, sea and space traffic, science, internet and so forth.

There are a lot more of very adapted time scales like the hypothetical Geocentric Coordinate Time (GCT), the Terrestrial Dynamical Time (TDT) and GPS time which is established by the Global Positioning System.

1.1.4. Comparison of clocks and time scales: Time transfer

As mentioned above, both the generation and the dissemination of time scales (no matter if they are produced with one clock or one thousand) needs a means of transportation of the temporal information over space. This function is fulfilled by the technologies of time transfer.

Today, most time transfer systems rely on the comparison of the "ticks" of the respective clocks, which have an absolute origin rather than comparing directly the frequency of the clocks. This means that a frequency difference of two clocks appears as a temporal offset since the last time they have been synchronized.

The different time scales above, in particular TAI/UTC and GPS time, are established with the use of the GPS signals and TWSTFT (Two-Way System for Time and Frequency Transfer) which are very common methods today. Both systems are described in the following chapter.

1.2. Actual time transfer systems

1.2.1. Time dissemination with GNSS

Today there exist many satellite based positioning systems in the world. The GPS-NAVSTAR is probably the most common and most used, but there are other systems relying on the same principle and employing analogue technology, like the operational Russian GLONASS and the Chinese COMPASS systems and the European GALILEO system in its development and experimentation phase.

As a matter of fact, these Global Navigation Satellite Systems (GNSS) provide first and foremost a time dissemination service. The principle of positioning is performed by analyzing the time information of several satellites: Each satellite basically sends a time "tick" from his local clock along with some correction information about the orbit and the clock (navigation message). A user on ground, air or space, seeing at least four satellites is able to calculate its position and time.

The following section shows the most famous navigation system that is used for today's time transfer around the world.

1.2.1.1. Principle of GPS

The current GPS satellite fleet consists of 31 satellites in MEO orbits (20,183 km); these are partitioned into six orbital planes (rotated about 60° one to another), with an inclination of 55°; by this means one achieves that a user on ground always has at least four satellites in his view.

Depending on its type, such a two-ton GPS satellites carries two to three atomic clocks (Rubidium and Cesium), that provide reference signals at 10.23 MHz. A GPS satellite provides signals on two frequencies, issued by multiplication with 154 and 120 of the reference signal: L1 on 1.575 GHz and L2 on 1.228 GHz. The C/A-code (Coarse Acquisition) for all

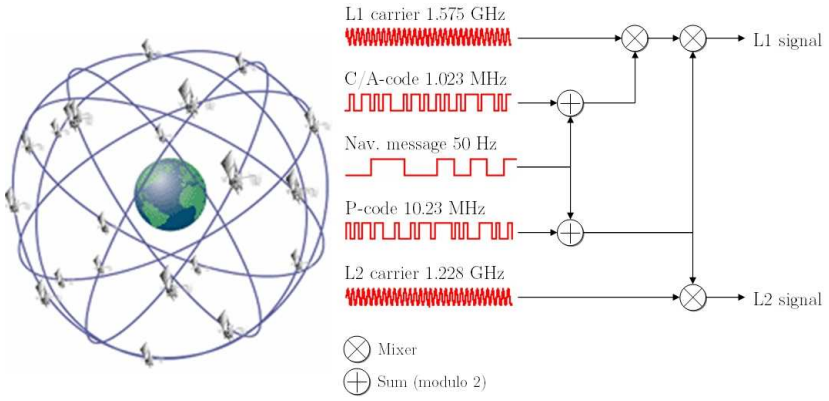

Figure 1.3.: The GPS constellation and its emitted signals

civil applications modulates the L1 carrier, as shown in Fig. 1.3. The C/A-code is a 1,023 bit (here called chip) pseudo random code and is different (orthogonal) for each satellite; by this means, all satellites may use the same frequency, but use different parts of the spectrum (spread spectrum technique or CDMA, Code Division Multiple Access). The CDMA pseudo random code which is of the Gold code family and has a chipping frequency of 1.023 Mcps,

encodes a slower signal (at 50 bits/s), the navigation message that contains all information about orbit prediction, estimates of the respective satellite's clock offset to GPS time, satellite health and so forth. The L1 carrier further contains a second, orthogonal P-code (JPL type at 10.23 Mcps).
The L2 carrier is always encoded by the P-code, and selectively also by the C/A-code. There are currently added new satellites to the fleet that provide further signals.

Today, in the contrast to the past, when the P-code was encrypted and only accessible to authorized users, GPS users may use both frequencies to obtain a better positioning by directly estimating the ionospheric delay.

1.2.1.2. Time transfer with GPS

As mentioned in Section 1.1.4, the GPS system has its own internal time scale which is, though, gently steered to UTC. The U.S. Naval Observatory (USNO) is in charge of a real-time realization of the universal coordinated time UTC(USNO). GPS time is specified to be maintained less than one microsecond apart from UTC(USNO), and in fact has been maintained to less than 22 ns within that specification since 1997 [4].

Time transfer with GPS is very straightforward: A GPS receiver has to be put up at a known position (which may also be measured by the receiver itself), and it will typically analyze the pseudo random code to extract the time information. There are some different configurations:

One way In the one-way configuration, one just retrieves the clock signal from the satellite. Receivers typically have an accuracy of about 1/100 of the code length. The real time is then calculated by applying the different corrections issued from the navigation message. As a result one obtains an information of one's clock as compared to GPS time and thereby to UTC(USNO).

Common view In common view mode, i.e. when two users, or timing labs see a satellite at the same time, they may directly synchronize their clocks. This has the advantage of removing the error of the satellite clock and reducing errors related to atmosphere and orbit and ionosphere estimations when the paths are common (small baselines). This procedure has been the primary means for the establishment of the TAI time scale for the last twenty years. Common view is about a factor two better [4] in terms of stability and accuracy as compared to the simple direct access.

Carrier phase An approach to also use the 1,000 times faster carrier frequencies as a temporal reference signal has been proposed a long time ago. However, the resolving of the carrier to code ambiguity needed big efforts; additionally, there were some instrumental problems since most receivers did not unambiguously lock their internal signal on the input signal.

Today, many institutions provide software that can solve for the carrier-code ambiguity. The most popular in the time community are probably the GIPSY (of JPL) and Bernese code. It has been shown that carrier phase measurement are very gratifying for averaging times smaller than 5 days [5]; however, ambiguities can still not be solved completely: This leads to the need for the processing of both code and phase measurements. The absolute clock offset is determined by the code, whereas the phase gives an indication on the fine signal evolution.

Table 1.1.: Typical r.m.s. performance of radio frequency time transfer systems (data from [4])

Type	Time stability 1,000 s	Time stability 24 h	Time accuracy 24 h	Frequency accuracy 24 h
GPS one way	5 - 10 ns	2 ns	3 - 10 ns	$4 \cdot 10^{-14}$
GPS common view	5 ns	1 ns	1 - 5 ns	$2 \cdot 10^{-14}$
GPS carrier-phase	20 ps	100 ps	1 - 3 ns	$2 \cdot 10^{-15}$
TWSTFT	$<$ 100 ps	100 - 200 ps	1 ns	$2 - 4 \cdot 10^{-15}$

The analysis of carrier-phase data allows to significantly ameliorate the GPS time transfer as compared to common view or one way. Table 1.1 summarizes the basic performance that can be obtained with GPS. However, the time transfer by GPS remains a one-way method which is unable to correctly assess the ionospheric and atmospheric delays; this may only be achieved by a two-way method where the carrier traverses the medium two times.

1.2.2. Two-way system for time and frequency transfer (TWSTFT)

Another radio frequency and satellite based method for time transfer is the TWSTFT, which is a two-way system (Fig. 1.4). Stations (1) and (2) emit, at prearranged dates,

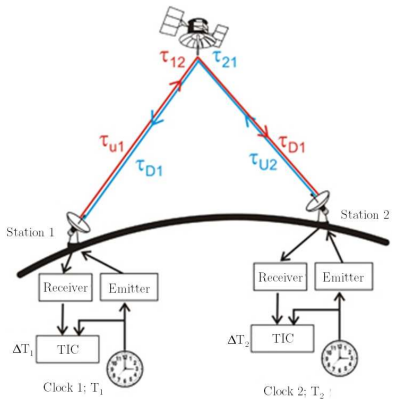

Figure 1.4.: Scheme of TWSTFT. Graphic © PTB, Germany

signals over a geostationary relay satellite and thus determine the time difference between the emission of the own and the reception of the other. Considering that both signals are really travelling at the same time, the time difference may be determined from the difference of the measurements independently from the position of the satellite. Stations (1) and (2) have to be equipped with a similar receive/transmit instrumentation. As the geostationary relay, typically commercial telecommunication satellites are used. On the transmit side, a one pulse per second (PPS) reference signal issued from the local temporal reference frame (local clock or clock ensemble) is coded onto a 70 MHz intermediate frequency (IF) by a pseudo random code. This signal is transformed into the K_u-band and sent towards the satellite; the satellite transponder receives the signal and emits it on another frequency. The receive scheme is equivalent. Both PPS pulses, local and remote are then fed to a time interval counter (TIC) that determines the difference.

Today, there exist some tens of Two-Way stations all over the world with networks in USA,

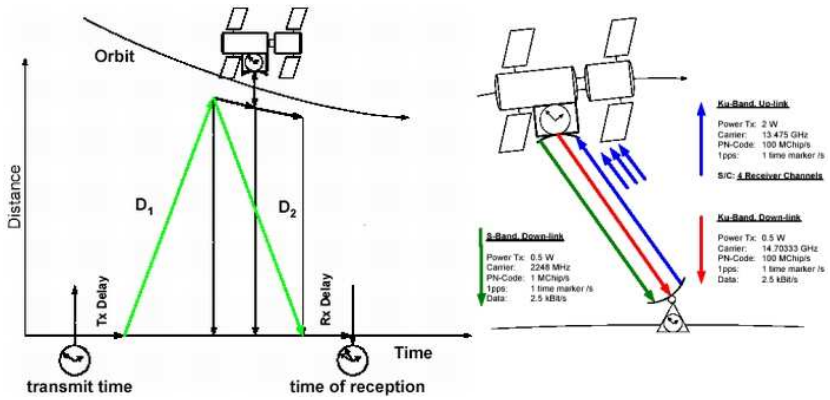

Figure 1.5.: The MWL bi-directional simultaneous link configuration and signals (sketches from [7])

Europe and Asia. The OCA time/frequency team performs these measurements since years and is today working on an Intelsat transponder in the K_u-band (12 - 14 GHz). TWSTFT allows for very precise and stable time transfer (as indicated in Table 1.1) and is used today for augmentation of the GPS based time transfer that constitutes TAI.
However, though being a two-way scheme, this fact is not fully exploited since the up/down frequencies differ what causes residual uncertainty in the ionospheric correction.

1.2.3. MWL of the ACES mission on the International Space Station

The Atomic Clock Ensemble in Space (ACES) is an ESA mission on the International Space Station ISS with mainly fundamental physics objectives [6]. It is composed of three segments: The PHARAO Cesium fountain clock, the SHM hydrogen maser and MWL (Microwave Link) that performs the time and frequency transfer between ground and space.

MWL consists of a similar receiver/transmitter assembly both on ground and in space and uses a two-way dual-frequency (K_u-band) signal that is emitted quasi-simultaneously aboard and on ground. This ensures that the system is rather independent from the actual link geometry and its variation over time. A third frequency in S-band is used in the down-link for the compensation of ionospheric effects. All signals are spread with a pseudo-random code that includes a one pulse-per-second (PPS) time marker and some housekeeping data of the system. The receivers and codes are designed such that they resolve the carrier-phase ambiguity; the time measurement is then performed on the reconstructed signal's phase as compared to the local time scale. Multipath effects on the carrier and on the code may suppressed by the correlation properties of the PN-code.

The MWL system is specified exhibiting a time stability of 230 fs at 300 seconds integration time and of 5.5 ps over a day. At the time of the compilation of this document, the MWL flight segment (FS) engineering model was build and tested and showed performances slightly exceeding these specifications with a time stability of about 100 fs after 20 to 1,000 seconds (depending on the applied signal to noise ratio [7]). These data do not yet include the ground terminal, the antennas and any errors due to troposphere, ionosphere or geometry.

The time transfer performed with MWL, once on the ISS, will represent the flagship of what is possible with radio frequency technology.

1.2.4. Other systems

There exist many other, older and less performing radio-frequency based techniques for time dissemination and time transfer. In particular there are the time dissemination systems on long wave like DCF77 (from Frankfurt in Germany) at 77.5 kHz and the American LORAN-C on 100 kHz which is in fact an enhanced navigation system dating from World War II. A very simple means is provided by the time stamp contained in public TV signals what permits time transfer down to the nanosecond level.

A very common method today is the Network Time protocol (NTP) in the internet. National time labs provide the respective time stamp online and the absolute travel time of the package (per UDP) to the user is estimated by using a hierarchical system of time servers. Typically, an accuracy of about 10 ms may be obtained with NTP.

1.2.5. Limitations of radio frequency systems

Fig. 1.6 shows the performance of actual operational time transfer systems [8]. In principle,

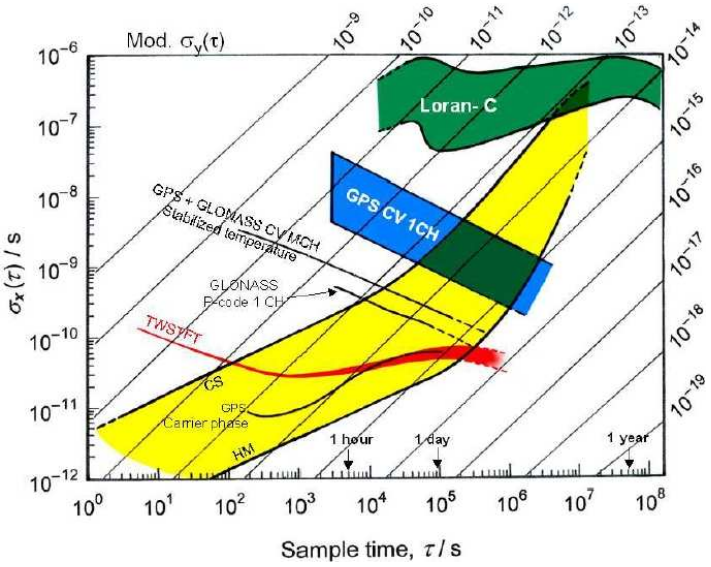

Figure 1.6.: Performance ranges of actual microwave time transfer systems (graphic from [8])

the performance of any time transfer system is physically limited by the phase measurement on the used signal. The latter is determined by the applied modulation frequency, which is of 10 MHz or better 10 Mcps for GPS P-code (1 Mcps for C/A-code) and between 0.5 and 20 Mcps for TWSTFT. Considering a comfortable relative precision of 1/100 of the chip length, one sees that the precision of a pure transmitter/receiver system is limited on the nanosecond level.

But there are other, much bigger contributions in the overall error budget, notably coming from the troposphere and the ionosphere; these may ideally be assessed on the same level of performance as the mono-channel system by using different carrier frequencies as it is performed with GPS (see GPS CV MCH in Fig. 1.6, meaning GPS common-view, mono-channel) and TWSTFT.

A means to enhance the precision of the always performed phase measurement is (1) to

increase the modulation or chipping frequency and (2), which is more effective, to use the carrier itself. Today, this is done quite regularly for GPS (see above) and has also been performed for TWSTFT showing remarkable sub-picosecond performance [9]. Still, there remain problems with the code-carrier phase ambiguity that are not simple to resolve.

The trend in radio frequency systems will thus be to further increase the frequency: TWSTFT is already working in K_u-band and MWL will do the same, so that it will just be a matter of time until K_a-band will be used, following the trends of communication systems. The following frequency ranges from EHF to THz radiation are, however, subject to very strong absorption by atmosphere and water (rain and vapor). Further, technology is not on the point to provide substantial equipment even if isolated projects develop high-speed data links on different frequencies (at 40 and 75 GHz, for instance).

1.2.6. The optical world

A frequency domain that is well exploited and where exists a considerable amount of technology is the optical domain and in particular the frequencies offered by lasers.

The visible and near-infrared domain offer carrier frequencies of some hundreds of THz. This theoretically allows for modulation frequencies much higher than the carrier frequencies we dispose of in the radio world. Today, lasers exists that modulate the carrier with picosecond to femtosecond pulses; even attosecond pulses have been demonstrated where the notion modulation is no more appropriate. The fiber-optic based communication industry today provides us with modulators that offer bandwidths of some tens of GHz allowing Gigabit data transfer.

T2L2 is such a system that exploits the advantages of the high frequency carrier that is modulated by GHz pulses. The T2L2 experiment has to be seen as "the first of its kind", together with LASSO (Section 2.1.1) that paved its way, a technology demonstrator (with scientific output too, though) that shows the feasibility of a space-based laser link time transfer.

T2L2's ground-based kinsman is the utilization of this laser pulse based time transfer with propagation in optical fibers. This is used today more and more commonly to distribute radio frequency clock signals (like the 10 MHz output of a commercial Cesium) over short to mean distances, instead of using coaxial cables. This method shows good performance, is however limited by the attenuation in the fibers.

Groups at the Observatoire de Paris (LNE-SYRTE) and the Max-Planck Institute for Quantum Optics (MPQ) therefore develop methods of direct frequency transfer with the optical carrier itself. This leads to a considerable reduction of the sensitivity to signal attenuation and continental distances become feasible. This method is not able to transfer time since there is no notion of an absolute phase, but the frequency of a certain clock. This is in particular interesting for the comparison of different high performance clocks, in particular optical clocks that may directly be compared to the optical frequency by the frequency comb.

In the same objective, coherent, continuous laser links from ground to space are proposed for future space clock missions as SAGAS (Search for Anomalous Gravity in Space [10]) or EGE (Einstein Gravity Explorer [11]).

1.3. The T2L2 scheme

1.3.1. T2L2 time transfer

The time transfer scheme of T2L2 is radically different from currently used time transfer methods such as GNSS or TWSTFT. It relies on the direct time comparison between two clocks: Basically, a clock A sends a laser pulse towards a clock B (compare Fig. 1.7); the emission time t_s (s for start) at A and the receive time t_b (b for board) at B are both timed in the respective clock reference frames. Upon arrival at B, the laser pulse is equally reflected and returns to A where it is timed a third time, t_r (return). By this means, the time offset χ between the clocks A and B may immediately be calculated with the date triplet $\{t_s, t_b, t_r\}$ by subtracting the round-trip-time from A to B:

$$\chi_{AB} = t_s - (t_b - t_{\text{trip}}) = \frac{t_s + t_r}{2} - t_b \tag{1.1}$$

In the first order we may assume, since the path is common, that the trip time is just the half of the round-trip time: $t_{\text{trip}} = \frac{t_r - t_s}{2}$.
In practice (in particular for a satellite-based system) there have to be added some correction factors, since the round-trip time is not perfectly symmetrical. The aim of the space-based

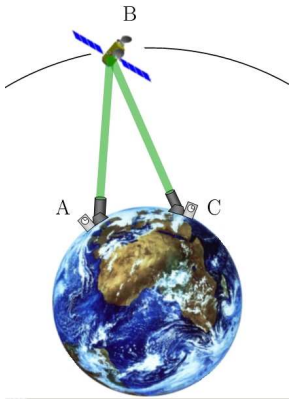

Figure 1.7.: The T2L2 scheme

T2L2 project is the synchronization (or the time transfer between) of remote ground clocks or between ground and space clocks. The overall scheme relies on a space and a ground segment.
The ground segment (detailed description follows in Chapter 4) has the role of the emission and detection of the laser pulses, in the temporal frame of the clock and is represented by a typical satellite laser ranging (SLR) station: A powerful laser emits short laser pulses which are sent through a telescope towards the satellite equipped with the T2L2 instrumentation. A highly precise event timer, connected to the clock to be synchronized, times the departure and return of the laser pulses on the picosecond level. So far, the scheme is identical to SLR, but whereas SLR determines distances and thus has to apply corrections for atmospheric delay, T2L2 only uses the temporal information.

The space segment consists in the T2L2 instrumentation, which is the central topic of the present work. Fundamentally, the T2L2 payload is composed of a clock, a retroreflector

and some detection and timing electronics. The instrumentation is addressed in detail in Chapter 2.

The time transfer between ground clock A and space clock B is performed when the satellite is in the visibility of the laser station; it's final precision is considerably ameliorated by averaging over a big number of measurements over the whole satellite pass: $\langle\chi_{AB}\rangle$. A time transfer between two ground clocks A and C is simply calculated[4] by the difference $\langle\chi_{AB}\rangle - \langle\chi_{CB}\rangle$.

1.3.2. Advantages of the optical scheme with T2L2

As compared to its radio frequency counterparts, the T2L2 scheme has some important advantages, whereof some shall be cited hereunder:
First, the optical carrier is not sensitive to the ionosphere what limits the accuracy of RF systems. The T2L2 scheme is a mono-carrier, true two-way scheme; this is a significant difference and advantage over TWSTFT which features a two-way scheme on two different carries (for the up and down link) inhibiting a full cancellation of ionospheric effects.

Further, due to its frequency elevated by at least four orders of magnitude as compared to microwave, it allows for a much higher modulation bandwidth, what is intrinsically an advantage for precise time transfer.
In the same logic the higher carrier frequency also permits much better defined spatial reference points leading to a better accuracy.
The elevated frequency permits also a high directivity for rather compact instrumentation.

On the other hand, the laser wavelength used in SLR suffers from absorption in water vapor (as in clouds) and T2L2 is therefore not an all-weather scheme.

[4] In fact, there are different methods for the data analysis, using single triplet pairs, the average etc. This aspect was addressed in [12] and is not part of the present work.

2. The Time Transfer by Laser Link project on the Jason 2 satellite

Since its first proposal in 1995 [13], this next concept of optical time transfer had been studied for a flight on various space missions (see the upcoming Section 2.1 for some details). The Science Program Committee of CNES has repeatedly advised to look for other flight opportunities. In 2004, the Prospective Science Seminar of CNES reaffirmed this position.

In fact, the idea of associating the time transfer experiment to some altimetry mission was not new: This mission type is in need of very precise orbit determination and, further, T2L2 would allow the independent characterization of the DORIS ultra-stable oscillator; in this context, T2L2 had already been under discussion for the Jason predecessor mission TOPEX/Poseidon and again for Jason 1.

But it should take until some still unresolved behavior of the DORIS oscillator with respect to radiation on Jason 1 and the abandon of the WSOA instrument by NASA. The Wide-Swath Ocean Altimeter is in fact an interferometric K_u-band radar, planned with two distinct antennas separated by a 6 m-baseline. Vis-à-vis mass and power constraints, the Jason 2 satellite seemed finally not to be the right carrier, only a demonstrator could have been embarked. This finally led to an abandon of the concept on Jason 2 and liberated a sufficient mass and power budget to accept three passenger instruments, thereunder T2L2.

A new feasibility study (phase A) for T2L2 on Jason 2 has been conducted in beginning 2005. A Jason 2 key point on May 10, 2005 finally validated the concept and the way was free for the detailed study of T2L2 on Jason 2 (what I will call T2L2J2 hereafter to mark the difference between the general T2L2 concept and its special implementation on the Jason 2 satellite.).
The phase B of the development started finally in September 2005. Details about its development will be given in the next section.

Generally, the T2L2 project at OCA was and is carried by E. Samain, its PI and my thesis advisor. My personal contribution to the instrument development itself covers some minor characterization experiments of the non-linear detector, an activity that is not presented in this thesis. The main contribution of mine to the T2L2 on Jason 2 project is described in Chapter 3. The T2L2 mission on the Jason 2 satellite is described in [14], which I had the occasion to present at the IEEE Frequency Control Symposium 2006 in Miami, and in [15].

2.1. The development of T2L2J2

2.1.1. Heritage of LASSO

The idea of optical space-based time transfer relying on satellite laser ranging technology dates back into the seventies. The project LASSO (Laser Synchronization from Stationary Orbit) had been proposed to ESA to fly on the Italian satellite SIRIO-2, in an Italian-French collaboration [16, 17]. SIRIO-2 was an experimental communications spin-stabilized

satellite to be placed on a geostationary orbit. Supported by the BIPM (at that time the BIH, Bureau International de l'Heure), the project was accepted and CNES was in charge of the instrument with Dassault Electronique as the prime contractor. Unfortunately, during its launch on September 10, 1982, the third stage of the Ariane-1 rocket, carrying SIRIO-2, failed and fell into the Atlantic Ocean.

After some time, the LASSO experiment was anew accepted, this time on the European prototype meteorological satellite Meteosat-P2 (which was, in fact, the third Meteosat, equally spin-stabilized and on a GEO orbit). The LASSO instrument on Meteosat-P2 con-

Figure 2.1.: The Meteosat-P2 satellite with the LASSO payload (front of main cylinder): The lower part is the retroreflector panel, the upper the detection system (photograph taken from [12]).

sisted basically of a retroreflector panel (340 × 155 mm with 98 corner-cubes), an optical detection system, an event timer and an ultra-stable oscillator. The detection systems featured two channels, both for red laser light at 694 nm (Ruby laser) and 532 nm (Nd:YAG laser), consisting of the respective interference filter, a lens, and a linear avalanche photodiode. The amplified and converted signal triggered the event timer that consisted in a counter and a vernier with 100 ps resolution.
Meteosat-P2 was launched on June 15, 1988 and placed on 0° longitude in order to replace Meteosat-2 whose radiometer had dropped out.

Yet another hitch complicated the scientific exploitation of LASSO: This time, nearly the whole laser ranging community had changed their laser technology from Ruby to YAG; the design of LASSO anticipated this evolution by offering two optical channels. Yet, the YAG lasers in use offered much less energetic laser pulses, making it difficult for the stations to reach a geostationary satellite. Only few stations, thereunder the Grasse Laser-Lune and Graz, Austria could perform time transfer with LASSO. Thereunto came different operational difficulties concerning software and the need to shoot into predefined time windows depending on the rotation period of the satellite. Nevertheless, some precious data could be acquired [12].

But to top all existing problems, in August 1991 the satellite was transferred to another position, to 50° West in order to support the American satellite GOES-E. Only the Laser-Lune continued to receive echoes from Meteosat-P2 and some campaigns have been performed with McDonald, Texas and Greenbelt, Maryland [18]. End of 1989, the satellite was put back to Europe before definitely being transferred to 50° W again in autumn 1991. During the time over Europe, comparisons between the different time transfer systems GPS, TWSTFT and

LASSO had been carried out [19, 12].

Even though the obtained data from LASSO is very sparse, the mission itself represented a success in terms of the demonstration of time transfer based on laser links.

2.1.2. T2L2 feasibility studies

The concept of T2L2 was first proposed in 1994 to fly on a Russian meteorological satellite (Meteor-3M), together with a hydrogen maser and another time transfer system, PRARE-TIME based on the PRARE (Precise Range And Range-Rate Equipment) satellite tracking system.
In 1996 it was again proposed in a Russian-French collaboration and a first specific phase A study by CNES and OCA was conducted the year after: A French-Russian mission to the space station Mir should install the T2L2 instrumentation on one of its modules [20]. Unfortunately, the whole mission had finally to be abandoned.

In a next step, T2L2 was proposed (1997) in the framework of the ESA project ACES (Atomic Clock Ensemble in Space) on the International Space Station ISS. It would have been a complementary time transfer scheme to the microwave based MWL, in order to perform picosecond time transfer with the atomic fountain PHARAO and the hydrogen maser SHM. Due to some budget constraints concerning the whole ACES mission, T2L2 in ACES had finally to be abandoned, after a successful B phase.

As mentioned above, T2L2 had been discussed for some altimetry satellites, like TOPEX/ Poseidon and Jason 1. T2L2 had also been proposed to ESA to complement the Galileo mission, in particular for the precursor satellite missions GIOVE. In 2002, CNES conducted a study for an implementation of T2L2 on its proper Myriade micro-satellite. This activity included also the study of a large hollow corner-cube retroreflector what would represent the ideal configuration in terms of geometry issues (with the detector in the apex).
Since the Myriade solution represented a high cost, CNES had finally to renounce to this opportunity.

In 2004 T2L2 was proposed to fly as a passenger instrument on the ocean altimetry satellite Jason 2, what was accepted by CNES in 2005.

2.1.3. Development phases for T2L2 on the Jason 2 satellite

The T2L2 concept and feasibility on Jason 2 had been validated in May 2005. This study included also some minor changes to the initial T2L2 architecture, notably the use of an external retroreflector instead of the mono corner cube developed previously. The second point was of course the use of the DORIS oscillator as the clock.

The phase B preliminary development phase of the space instrument was initiated not earlier than September 2005, with a projected launch in June 2008. This tight schedule left not very much room for misconceptions. Advantageously, due to the different conducted previous studies and some successful ground based prototype testing in 2004 [21], the concept was rather mature at that time. The preliminary definition of the instrument architecture and composition, conducted by OCA and the chosen industry partners, EREMS, subcontracting SESO for the optical part, was already finished in December 2005, with the PDR (Preliminary Design Review).

It dates also in this time when it was decided by E. Samain and the author to reorient the mainpart of the present thesis from the formerly principal topic ILIADE (see Part II

of this document) to the characterization of the T2L2 instrument. An immediate work was then the characterization of the chosen non-linear detector. The second, somewhat more substantial agreed topic was the definition, integration and operation of a test bed for the detailed characterization of the T2L2J2 instrument engineering and flight model (MI and MV).
After a detailed study of the requirements on the test bed, based on the needed tests to be performed [22], the basic architecture and components (as laser, pulse picker, energy bench etc.) were determined and presented at the PDR of T2L2J2 on December 21, 2005. The studies around the test bed were continued and refined and led to its detailed definition that was presented at the respective key point on April 13, 2006 and the CDR (Critical Design Review) on May 13, 2006 [23].

For the T2L2J2 instrument, following model philosophy had been chosen: For the electronics part, the French space electronics manufacturer EREMS would produce prototypes, an engineering model and a flight model. For the optical part, to be supplied by SESO, it was opted to go for a proto-flight model without any prototype or engineering model.
The electronics prototypes were evaluated and troubleshooted from January to April 2006, then, after the conclusion of the C-phase (detailed definition) mid-May 2006 with the CDR, the construction of the engineering model was begun.
After its detailed design, the integration of the optical subsystem (SSO) started already in February 2006; after some tests during the summer 2006, including the mechanical verification tests, the optical subsystem was ready in autumn.
End of July, beginning August 2006 we performed a detailed evaluation of the engineering model of the electronics subsystem (SSE); this aimed at the detailed definition of some parameters as well as the comply to specifications in terms of metrology.
After this preliminary test campaign, carried out with a partial implementation of the test bed, the construction of the flight model (MV) was started. With some small delay, the instrument (SSE and SSO) was delivered to CNES by end of February 2007 (end of production phase D). The Qualification Review (QR) was held mid March 2007.

At that time, the integration and test of the associated test bed had also been concluded and the flight instrument could be subjected to a detailed characterization campaign aiming at the calibration and the determination of the final performances of the instrument. These tests, including their preparation, are the main part of the present work and are presented in Chapter 3.
After the first evaluation campaign in the CNES facilities (March/April 2007), the T2L2J2 flight instrument was finally handed over to THALES Alenia Space who is the prime contractor for the integration of the satellite Jason 2. A second performance verification campaign was conducted during the integration (Section 3.1.2.8), in June 2007. The integration of the Jason 2 satellite was completed in August, followed by the usual satellite-level verification test series (mechanical, acoustic, EMC and thermal). These were successfully finished at the end of 2007, and the satellite was shipped to Vandenberg Air Force base during April 2008. The Jason 2 satellite has been successfully launched on June 20, 2008 from Vandenberg Air Force Base in California.

For the scientific exploitation of the T2L2 on Jason 2 experiment, OCA and CNES have set up a designated working group federating the different user communities identified in the next section. After the preparation of the raw data download from the satellite by CNES, OCA is in charge of preparing the scientifically usable data. This role is represented by the Scientific Mission Center (CMS), implemented at OCA, Grasse.

2.2. The goals of T2L2 on the Jason 2 satellite

The objectives of the T2L2 experiment on Jason-2 may be classified in three groups, concerning the functional validation of the T2L2 scheme and its performances, scientific objectives based on the performed time transfer and complementary objectives in conjunction with the Jason 2 mission.

2.2.1. Validation of T2L2 scheme and its derivatives

Apart from the validation of the time transfer scheme by T2L2, there are two further concepts that may be proven by the mission.

Functional validation of T2L2: The T2L2 experiment on Jason 2 will allow for the validation of optical time transfer in terms of time stability and accuracy. A reference value is represented by the LASSO results, obtained in 1992 that should be ameliorated by two orders of magnitude in terms of time stability and one order in terms of accuracy. The metrological specifications on the T2L2 instrument are given in Section 2.3.2.

Validation of one-way laser ranging: The concept of one-way laser ranging is based on only the start date and the arrival time on a satellite. Differential distance measurements may be deduced from the clock readings at ground and aboard. This scheme is proposed (see TIPO [24]) for long-haul distance measurements (on solar system scale) where no return signal may be expected; the scheme evidently needs an extremely stable clock, but the concept may be analytically emulated with T2L2 by comparison of the different ranging methods.

More precise satellite laser ranging: The quality of the T2L2 ground segment, represented by a set of ameliorated laser ranging stations, allows for a gain in exactitude of classical two-way satellite laser ranging data. Further, the determination of the laser pulse energy in orbit in conjunction with its energy on ground (return pulse) will permit to ameliorate current atmospheric models.

2.2.2. Scientific objectives

The scientific objectives of T2L2 on Jason 2 are mainly represented by time/frequency metrology itself and fundamental physics.

Ground clock comparison: The main scientific purpose is the direct comparison of distant ground clocks. T2L2 will be able to compare today's best cold atoms clocks over long distances with a stability of some 10^{-17} over 10 days and an exactitude of less than 100 ps. For this purpose it is planned to displace mobile laser ranging stations to non-displaceable clocks such as Cesium-Fountain arrays at LNE-SYRTE in France or at PTB in Germany.

Calibration of RF time transfer systems: T2L2 will permit to calibrate classical microwave time transfer systems such as Two-Way (TWSTFT) or the Global Positioning System (GPS); the T2L2 scheme allows to calibrate these systems with an amelioration of at least one order of magnitude, the state of the art being the 1 ns level [25] for Two-Way. Through these calibrations T2L2 will also contribute to the construction of international time scales like TAI (Temps Atomique International).

Contribution to international time scales: Through the calibration of existing standard systems and by supplying clock data points in addition to those collected by the systems in place, T2L2 will allow to contribute to the construction of international time scales such as TAI. In particular, T2L2 will be able to give evidence of systematic errors committed by the actual employed systems, due to its radically different scheme.

Fundamental physics: Through the comparison of remote clocks based on various atomic species over the Jason 2 mission lifetime it will become possible to measure a possible drift in the fine structure constant $\alpha = e^2/h{\cdot}c$. T2L2 will further permit to measure the anisotropy of speed of light by comparing the laser pulse transmit/receive propagation times for different beam orientations.

VLBI augmentation: T2L2 may also contribute to Very Long Baseline Interferometry (VLBI) by an augmentation of the observation coherence time and determining independently the time offset between the different masers used in the stations.

2.2.3. Jason 2 mission related objectives

An asset for the selection of T2L2 to fly on Jason 2 was surely its possible contribution to the overall mission. The two main contributions are listed in the following.

Characterization of DORIS USO: The T2L2 experiment will further be used, in collaboration with the DORIS positioning system community, to characterize precisely the on-board ultra-stable oscillator. This includes generally the ultra-precise characterization of the DORIS oscillator whenever Jason 2 is tracked by an SLR station, and more specifically the evaluation of DORIS during its pass through the south-atlantic anomaly[1] (SAA). This may be performed by a campaign with the mobile laser ranging station FTLRS in Kourou, French Guyana.

Jason 2 altimetry: The T2L2J2 experiment may rigorously ameliorate the altimetry data. One part consists in the augmentation of the number of return dates on ground by reconstituting data triplets. Further, the effect of the LRA retroreflector may much better be modeled with the additional T2L2J2 data. As a last point, already mentioned in Section 2.2.1, the ameliorated accuracy of the T2L2 ground segment is of capital importance for the altimetry of the satellite.

[1] The SAA is an anomaly in the Earth magnetic field which is locally very low; this leads to an increased cosmic and solar radiation in this area.

2.3. The design of T2L2J2

2.3.1. Constraints and implications by the Jason 2 mission

As mentioned above, since T2L2 was accepted as a passenger instrument, its design had to subordinate the overall layout of the Jason 2 mission. This concerned not only mass or power constraints but in particular two vital subsystems of the original T2L2 proposal. As the Jason 2 primary mission, ocean altimetry, relies primordially on very precise orbit determination, it is equipped with several such systems, namely, DORIS, GPS and SLR. Since the new type of mono-corner-cube retroreflector (of the initial T2L2 proposal) would represent a too risky undertaking for the whole mission, it was decided that in turn T2L2J2 would use the retroreflector of the Jason 2 mission.
A second issue was the clock: Since both time and financial budget were too small for the development of a dedicated clock for the T2L2 experiment, the T2L2J2 version has to content with the local oscillator of the DORIS positioning system as a frequency reference.
After giving some insight in the Jason 2 mission in general, these two mission-originated quasi-subsystems will be outlined in the following sections.

2.3.1.1. The Jason 2 ocean altimetry mission

The Jason 2 satellite mission is a joint undertaking of CNES, NASA, EUMETSAT and NOAA and is intended to replace the Jason 1 satellite that, on its turn replaced the TOPEX/Poseidon (and actually has been flying some time in tandem with it). Together with SEASAT (1978), GEOSAT (1985), ERS-1 (1991), ERS-2 (1995) and ENVISAT (2002), these missions cover a wide field of oceanographic applications mainly through ocean topography. Ocean scientists use the ocean altimetry data for the establishment of sea surface current charts, the study of their intra-seasonal to seasonal variations and the observation of climatic anomalies through the understanding of oceanic signatures [26].

Figure 2.2.: Exploded view of the Jason 2 satellite and its main payloads. The T2L2 optics are mounted on the boom that holds the LRA (image center); the T2L2 electronics are mounted on the X+ wall of the satellite, next to the DORIS system.
Sketch © CNES, France

Satellite The Jason 2 satellite, also known as OSTM (Ocean Surface Topography Mission) in the U.S., carries five primary payloads for the altimetry mission and three passenger

instrument:

Poseidon-3 dual frequency radar altimeter: The radar altimeter emits 100-microsecond pulses at two frequencies (K_u and C-band) in order to simultaneously determine atmospheric electron content, what affects the radar signal path delay. These two frequencies also serve to measure the amount of rain in the atmosphere.

AMR Advanced Microwave Radiometer: The AMR is a passive receiver collecting microwave radiation reflected by the oceans at frequencies of 18.7, 23.8, and 34 GHz. These radiations depend on various factors such as ocean surface winds, ocean temperature, salinity, foam, absorption by water vapor and clouds, etc. The main goal of AMR is the determination of the water vapor content in the atmosphere in order to perform a correct path delay correction for Poseidon-3.

Scientific GPS for precise orbit determination: The GPSP is a dual-frequency GPS receiver, tracking up to 16 satellites at once. It permits to perform pseudo-range measurements with an accuracy of about 10 centimeters.

DORIS positioning system and LRA: These two will be addressed below.

CARMEN-2: This passenger instrument studies space radiations and their effects on electronic components. It allows the measurement of charged particle fluxes with a set of fully depleted solid state Silicon detectors; it further measures the effects of these particle fluxes on electronic components.

LPT: The Light Particles Telescope is a contribution of JAXA, also studying radiations.

T2L2: Time Transfer by Laser Link.

Orbit The orbit of Jason 2 is identical to those of TOPEX/Poseidon and Jason 1. The altitude of 1,336 kilometers is a trade-off between the radar scheme and a minimum "disturbance" of the orbit by gravitational potential variations. The orbit inclination of 66° was chosen to cover most of the Earth's unfrozen oceans. The orbit features a repeating ground track reiterating its cycle every 9.9 days (with 254 passes per cycle). This geometry leads to an orbital velocity of 7.2 km/s and a ground track velocity of 5.8 km/s.

Launcher The main contribution to the Jason 2 mission from the American side is the supply of the launcher; the satellite will profit from the unique luxury to be launched completely solitary in a Delta II launcher from Boeing. The launch site is the SLC2 West launch pad of Vandenberg Air Force base on the Pacific seaside of California.

2.3.1.2. The Laser Retro-Reflector Array (LRA)

The T2L2 project on Jason 2 uses the LRA (Laser Retroreflector Array) retroreflector of the original Jason 2 mission as its reflection device.
The LRA, designed by JPL and manufactured by ITE Inc. is the retroreflector array for precise orbit determination through satellite laser ranging. Its design is identical to the reflectors of Jason 1, GFO-1, ICESat and the Japanese ADEOS-2 satellite. The LRA design was usually intended for lower orbit missions, such as the latter three, but has finally been

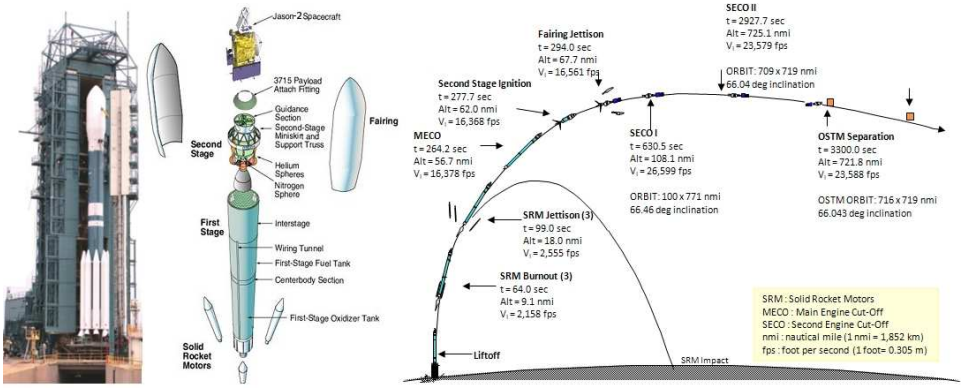

Figure 2.3.: The launch of Jason 2 with a Delta II launcher. Sketch © CNES, France

adopted for the Jason series as well. For this reason, the effective cross section is, depending on the incidence angle, of less than $1.8 \cdot 10^6$ m^2, what is a fairly low value for the Jason orbit. The array consists of nine corner cubes made of Suprasil quartz, with a diameter of 31.75

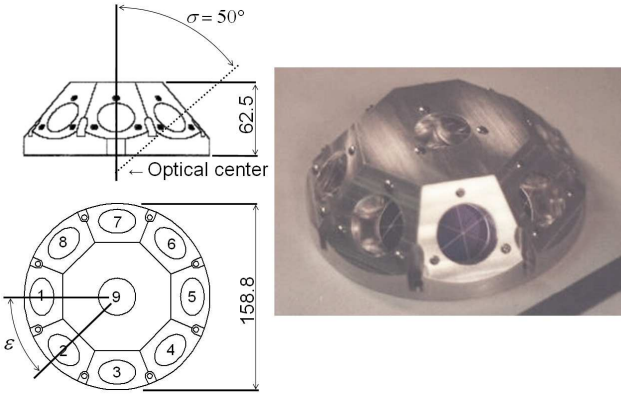

Figure 2.4.: The Jason 2 retroreflector array LRA. Images © JPL, USA

mm. The eight equally spaced peripheral cubes are oriented at 50° with respect to nadir. The reflective faces of the corner cubes are silver coated and the front faces are coated with MgFl2, optimized for 532 nm laser wavelength [27]. The array is mounted on a special boom on the X- wall of the satellite. Representing both the closest location and the easiest to be implemented, this boom was decided to equally carry the T2L2J2 optics. By this means the distance between the reflection and detection reference points may be as close as ≈12 cm what minimizes any timing errors due to attitude errors.

2.3.1.3. The ultra-stable oscillator of the DORIS positioning system

The T2L2J2 instrument uses the signal provided by the DORIS ultra-stable oscillator (USO) as a frequency reference. The DORIS USO is part of the DORIS positioning system package of the Jason 2 primary mission and further provides its signal to other payloads as a reference, like T2L2 and Poseidon.
The French positioning system DORIS relies, as an counter-example to GPS, on a passive

satellite payload. Ground-based beacons emit continuous signals towards the satellite receiver. Due to the relative motion of ground beacon and satellite, the signals' frequencies are shifted (Doppler-effect); the on-board receiver compares the received frequencies to its reference: With this data, a precise orbit determination may be performed.

The DORIS system typically works on two frequencies: 2036.25 MHz and 401.25 MHz. The 2 GHz frequency is less sensitive to ionospheric disturbances and serves as primary signal. The latter frequency is used for ionospheric correction and is also modulated in order to transmit messages containing an ID number, timing information, meteorological and housekeeping data of the ground transmitter. The French geodetic service IGN (Institut Géographique National) and the CNES have deployed more than 60 autonomous DORIS beacons throughout the world as depicted in Fig. 2.5. Three so-called master-beacons (Toulouse,

Figure 2.5.: DORIS permanent ground station network in 2007. Image © IDS/CNES, France

Kourou, Harthebeesthoek) make the link of the whole network to the International Atomic Time TAI. Many of the DORIS beacons are collocated with other geodetic position resolving equipment like GPS, SLR and even VLBI; Table 2.1 gives a summary [28]. In the framework

Table 2.1.: Geodetic instruments collocations with DORIS (2006)

Collocation	N° of sites
DORIS & GPS	37
DORIS & SLR	9
DORIS & VLBI	7
DORIS, GPS & SLR	8
DORIS, GPS & VLBI	7
DORIS, GPS, SLR & VLBI	2

of the projected precise monitoring of the DORIS oscillator with T2L2 it is also planned to install a beacon on the OCA facilities at Caussols.

The DORIS space equipment consists of an omnidirectional antenna, a frequency reference (ultra-stable oscillator, USO) and the main equipment for frequency comparison, the MVR (Mesure de vitesse radiale). In the last generation of the DORIS equipment, the latter two systems are integrated into one, the DGxx, shown in Fig. 2.6. The DGxx features a quartz oscillator working at 5 MHz, together with a cold redundancy. The signal is then doubled and fed to a distribution circuit that distributes it to the two internal users, the 2 GHz and

Figure 2.6.: The DORIS satellite payload on Jason 2: On the left, the combined 2 GHz and 400 MHz antenna, on the right the DGxx (USO and receiver).
Photographs and CAD-view © CNES, France

400 MHz receivers and to the external users, Poseidon-3, WSOA and T2L2. The DORIS space payload finally stores the frequency measurements and downloads them to the ground stations during visibility. The DORIS control and processing center SSALTO (Segment Sol multimissions d'ALTimétrie, d'Orbitographie et de localisation précise) located in Toulouse, performs the orbit calculations from various missions that are equipped with the DORIS system as Topex/Poseidon, Jason 1 and Envisat-1.

In general, the DORIS positioning system has been used in seven space missions and will be used in some future satellite missions as Jason 3 and Cryosat. The primary application, for what it is designed, is the precise orbit determination needed for altimetry missions like Jason. Through the vast and well dispersed network of the DORIS beacons, the system makes also a contribution to other fields, especially geodesy and geophysics: It measures the continental drift, monitors geophysical deformations, determines Earth rotation and gravity parameters and contributes to international reference systems. Moreover, with the addition of the DIODE (Détermination Immédiate d'Orbite par DORIS embarqué) in the recent DORIS payloads, it contributes to the real-time orbit determination of the satellite.

Though being a powerful and complementary alternative to the ubiquitous GPS, the DORIS positioning system features some singular problems that have been discovered on the Jason 1 satellite, with the need for some investigation: Especially for beacons located in the southern atlantic region the orbit determinations are somewhat perturbed; it is believed that this is related to the pass of the satellites through the SAA (South Atlantic Anomaly), an anomalous region of the Earth's magnetic field, with a local weakness that leads to a higher cosmic and solar radiation. T2L2 on Jason 2 will allow to follow precisely the on-board oscillator in that region (with a dedicated campaign of the mobile laser ranging station FTLRS at Kourou, for instance) while making the link to the radiation measurements provided by the other passenger instruments Carmen and LPT. This monitoring of the USO, not limited to the SAA, has been declared a primary complementary mission objective of T2L2 on Jason 2.

2.3.2. Specifications on the T2L2 instrument

The implementation of the T2L2 instrument for the Jason 2 satellite has been contracted to EREMS, a company near Toulouse with experience in building electronics payloads for space applications. The main specifications are defined in [29]. These include both functional and performance specifications.

The functional specifications cover aspects as the mission lifetime (2 years), details about the operations, and particular points about the implementation of the timer and photodetection.

The performance specifications cover direct time/frequency performance parameters as well as indirect points that warrant the effective exploitation of the instrument. In the following, the most important points (relevant in this document) will be cited from the specification document [29] (using the same nomenclature).

Detection

E 4.2.1-1 The dynamic of the two optical detection channels (see next section) must cover at least 80 dB.

E 4.2.1-2 The instrument has to be able to detect and time-tag laser pulses as defined in the Link Budget Document [30], in presence of Earth reflected solar flux. The non-linear detection channel has to be compatible to a detection threshold of the single-photon type.

E 4.2.1-3 The precision of the non-linear detection channel has to be inferior to 25 ps.

E 4.2.1-8 The ratio of the luminous flux collected by the linear and the non-linear channel has to be constant (within 10%), for all incidence angles, its polarization and the instrument temperature.

Timing

E 4.2.2-1 The timing precision has to be inferior to 5 ps.

E 4.2.2-2 The resolution of the event timer has to be inferior to 1 ps.

E 4.2.2-3 The time stability of the T2L2 instrument (detection and timing), referenced by the DORIS USO and including all internal error sources has to be equal or inferior to:

$$\sigma^2_{x,\mathrm{T2L2}}(\tau) \leq K_1^2 \cdot \tau^{-1} + K_2^2 \cdot \tau \tag{2.1}$$

with $K_1 = 12.6\ \mathrm{ps}\sqrt{\mathrm{s}}$ and $K_2 = 12.6\ \mathrm{fs}/\sqrt{\mathrm{s}}$, resulting in a time stability plot as depicted in Fig. 2.7.

E 4.2.2-4 In order to identify linear phase drifts of clocks, the uncertainty over a time interval τ_0 has to be inferior to the time stability $\sigma_{x,\mathrm{Clock}}(\tau_0)$ of the considered clocks. For this purpose, T2L2 has to permit to identify a linear phase drift of clocks characterized by a time stability of:

$$\sigma_{x,\mathrm{Clock}}(\tau) = 40 \cdot 10^{-15} \times \tau^{1/2} \tag{2.2}$$

or expressed as root of Allan variance:

$$\sigma_{y,\mathrm{Clock}}(\tau) = 10^{-13} \times \tau^{-1/2} \tag{2.3}$$

These primary metrological specifications will be confirmed throughout the document.

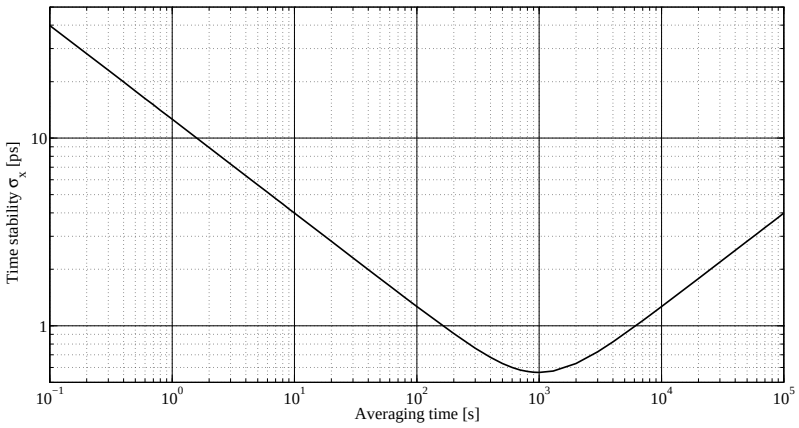

Figure 2.7.: Time stability specification of the T2L2J2 instrument

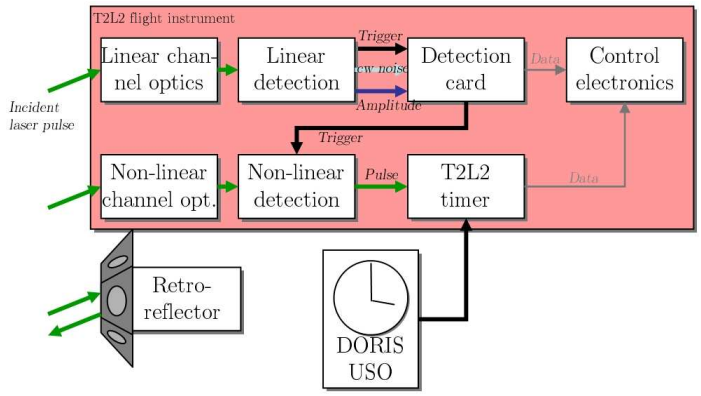

Figure 2.8.: Synopsis of the T2L2J2 instrument and its main parts

2.3.3. T2L2 on Jason 2 instrument synopsis

The general layout of the T2L2 instrument as it is designed for the Jason 2 satellite is depicted in Fig. 2.8. The incoming laser light falls into two optics, the linear and the non-linear channel (for the significance see below). The linear detection system has a triple purpose: It triggers the non-linear channel, measures the laser pulse amplitude and the continuous background illumination (noise). It further permits to set a detection threshold. The non-linear channel, situated behind a delay line in order to give some time to the linear channel to react, detects the laser pulse and transforms it into an electronic signal. This signal in turn triggers the event timer, which is working in the reference frame of the DORIS USO, generating a date t_b. All data, as the date, the pulse amplitude and the noise level are fed to the control electronics, that stores them together with a set of operational data. These data are assembled into packages and sent to the PROTEUS platform which is in charge for the download to Earth via the usual radio link.

Parallel to the detection, a part of the laser pulse is reflected by the LRA retroreflector. The following chapters highlight in more detail the different functions of the instrument and their implementation.

2.3.4. The optical architecture of T2L2J2

The main purpose of the optics in T2L2 is the transformation of the incident optical pulse into an electronic signal able to trigger the event timer. In classical SLR, today mostly Silicon Avalanche Photodiodes (APD) come into play as detectors, for following reasons: they have a very fast rise time (down to some tens of picoseconds), usually a good quantum efficiency (up to 60%) while providing a good precision over a large dynamic, notably including single photon detection, in comparison to, however still widely used, Photo-Multiplier Tubes (PMT), who come short in detection of very weak signals.

In order to reduce noise and consequently false trigger signals, in particular for weak return signals, in typical laser stations various filter techniques come into play. Usually, a spectral filter around the laser line is employed; further, a spatial filter (usually a pinhole) rejects noise from the target-surrounding background and finally a temporal filter is used that activates the detector only when a return is expected. This last temporal filter, represented by an APD working in the so-called "Geiger" mode [31], is activated on a return epoch estimation based on relatively precise satellite ephemerides and the start date.

To come back to T2L2, it is evident that it has to face the same problems associated to noise as typical laser stations. However, the latter two of the powerful employed filter techniques are difficult to implement for a spaceborne instrument. From an organizational point of view, it is laborious to determine in advance which laser station will fire at what time towards Jason 2. This excludes a spatial filter[2] and in turn, even drives the constraint to consider any possible location on Earth as a source and hence take into account the whole globe. For the matter of a temporal filter: Even in the case we knew perfectly at what time of day a specific SLR station wants to participate to T2L2 (or simply to Jason 2 altimetry), there is no possibility to know in advance the time of arrival of a specific laser pulse on the nanosecond level as most actual laser stations are working with asynchronous flash lamp (or diode) pumped Nd:YAG lasers that cannot be tied on a reference signal such as a clock[3].

From these constraints follow the required functionalities of the T2L2J2 optics:

- Imaging of earth globe onto detector and
- implementation of an internal trigger.

The first requirement implies a field of view (FOV) of $\pm 55.77°$ that has to be imaged onto the detector(s). The second requirement can be fulfilled by employing a first detection by an APD in linear gain mode (that is not sufficiently precise to be useful for the envisaged time transfer level of performance) that triggers a second APD operating in Geiger regime. The respective laser pulse has to be sent onto a delay line in order to arrive some nanoseconds (the electronics response time) later on the Geiger diode.

[2] Of course, there is the possibility to include such a type of filter, for instance by the use of a liquid crystal matrix that becomes opaque in areas where no participating laser station is expected. However, this solution has not been considered for reasons of implementation complexity and the mentioned planning uncertainty.

[3] Since newly there are some laser stations that are equipped with lasers based on resonant cavities that are in principle able to be synchronized on an external reference signal such as a clock signal. As an example, the Austrian SLR station Graz [32] is right now able to perform such synchronous laser pulse emission. To give a further example for different implementation, the Chinese time transfer experiment "Laser Time Transfer" (LTT [33]) is designed such way: Laser stations have to adapt their time of fire, what makes operation difficult but takes out a source of complexity in the instrument design.

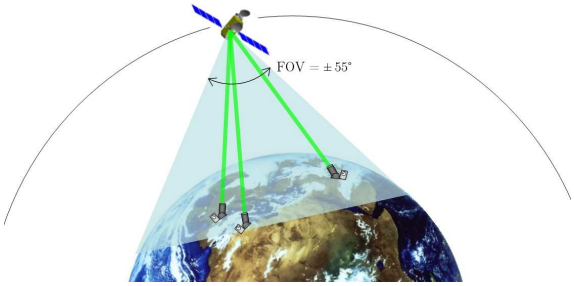

Figure 2.9.: The field-of-view of the T2L2 instrument on the Jason 2 satellite (determined by the orbit altitude)

Another important point is the expected dynamic of the laser pulse energy met in orbit: It is a function of the station - satellite distance to the square and the atmospheric transmission over the satellite pass. In order to roughly equalize the laser energy over a pass (this inhibits a date signature), the optics should slightly attenuate laser beams coming from the nadir direction and perfectly transmit beams coming from extreme directions (low elevations). This is possible by converting the 55° FOV into a parallel beam that falls on a neutral density filter that features a radial optical density distribution. Nadir originated rays (inclination $i = 0^\circ$) stay in the center of the beam whereas rays from the extremities ($i = 55^\circ$) pass through the outer perimeter of the optics. The form of the distribution should be the

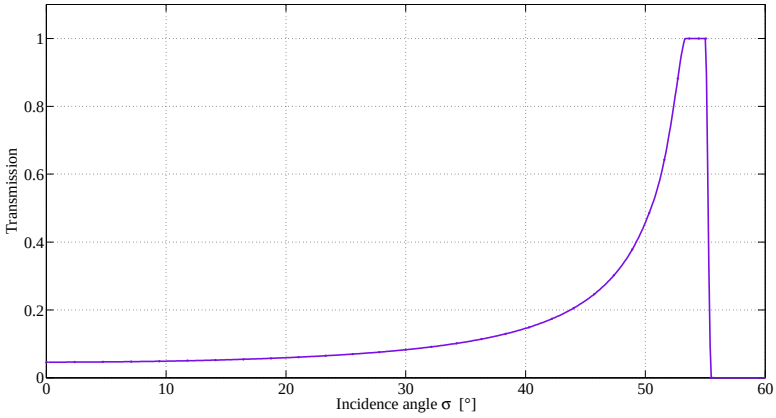

Figure 2.10.: Relative transmission of the radial neutral density filter as initially specified by OCA

inverse of the distance square and the atmospheric transmission function as depicted in Fig. 2.10. SESO studied several solutions for implementing this type of filter, namely a sphere calotte or a similar form of absorptive colored glass together with its negative form to overcome aberrations; this solution seemed to risky to be correctly implemented with respect to molding and gluing difficulties. Another possibility, discrete chrome depositing was rapidly discarded for similar reasons. SESO finally opted for a continuous chrome deposit, together with a specific rotating mask in order to attain the desired distribution. This option included some change of the form of the filter distribution given in Fig. 2.10, what was accepted by OCA.

It was decided to fulfill the internal trigger requirement by creating two channels, one for creating the trigger (that features also additional functions; see in the respective section),

called "linear channel" and a "non-linear" channel for accommodating the Geiger detection. These two parts, also known as "BOLI" for "Boîtier Linéaire" and "BONL" for "Boîtier Non-Linéaire" are described in the following sections.

2.3.4.1. The linear detection channel

The linear detection channel consists of an optical part (BOLI) and an opto-electronic part.

BOLI optical frontend The optics have following functions:

- Collimate the specified FOV of 55 ° into a parallel beam in order to
- illuminate the radial density filter and
- the spectral filter,
- concentrate the beam onto the detector.

The resulting beam condenser has to be designed such that the initial FOV of ±55° is concentrated into some acceptance cone of the diode. In fact, the selected photo diode (RCA 902STC, see next paragraph) sees luminous flux over nearly 2π sr but previous studies by E. Samain showed that the differential sensibility of the diode silicon towards orthogonal polarization (s and p) was acceptable only up to an angle of 30° from the optical axis. From conservation of energy follows the principle that the product of pupil and solid angle stays constant in an optical system:

$$\Omega_1 \cdot S_1 = \Omega_2 \cdot S_2 \tag{2.4}$$

where Ω_1 and Ω_2 are the FOV and the diode acceptance angles, and S_1 is the virtual pupil surface corresponding to the considered detector surface S_2. With a magnification[4] of 3.2, one finds a photometric pupil D_1 of 160 µm[5]. The function of generating a parallel beam is fulfilled by a set of three lenses made of synthetic fused silica who form the intermediate image (diameter: 10 mm) of the ±55° field onto the front face of the radial filter. Figure 2.11 shows the optical layout of the BOLI system along with a ZEMAX simulation. The zoom on the right bottom indicates the presence of an aberration causing an increased pupil size of about 650 µm (data SESO) what has been confirmed in the test campaign (see Section 3.2.2.4).

The beam passes then on the spectral filter for noise suppression. As the optical part BOLI is necessarily located at the outside of the satellite and therefore outside the platform's thermal control system[6], the system will undergo important thermal variations. Narrow spectral interference filters suffer considerable variations of their characteristics, notably the bandpass line center and the linewidth, if temperature changes. This is due to variations of the refractive index and the absorption of the employed materials. It was decided to be less stringent on the permitted noise level (and hence the filter linewidth) and thereby give a comfortable margin on any temperature induced variation. The used filter (product of SAGEM) is a higher-order interference filter in order to obtain a rectangular shape instead

[4] SESO considered a planar angle instead of a solid angle what modifies the outcome of this ratio. $\frac{\Omega_1}{\Omega_2} = 3.2$ for solid angle instead of 1.83 for a planar angle.

[5] Instead of 270 µm calculated by SESO.

[6] The T2L2J2 outside optics also feature a small thermal control system, but uniquely composed of heaters. The thermal variations are considerably higher than in the satellite body.

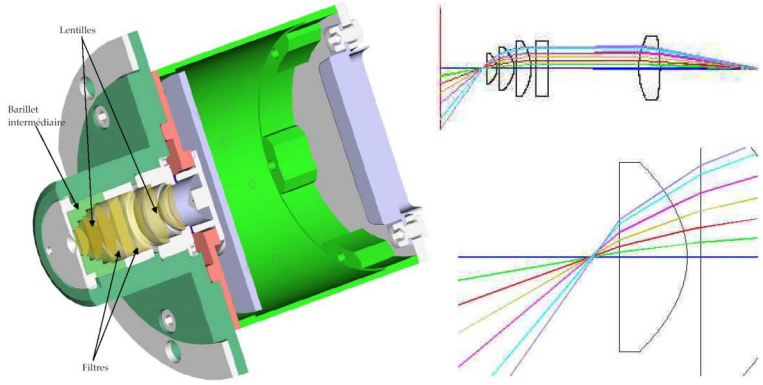

Figure 2.11.: The mechanical and optical layout of the linear channel. CAD-view and ZEMAX simulation © SESO, France

of Gaussian. Fig. 2.12 shows the spectral response of the employed 10 nm wide interference filter, centered at 532.1 nm. After the filter the intermediate image is concentrated onto

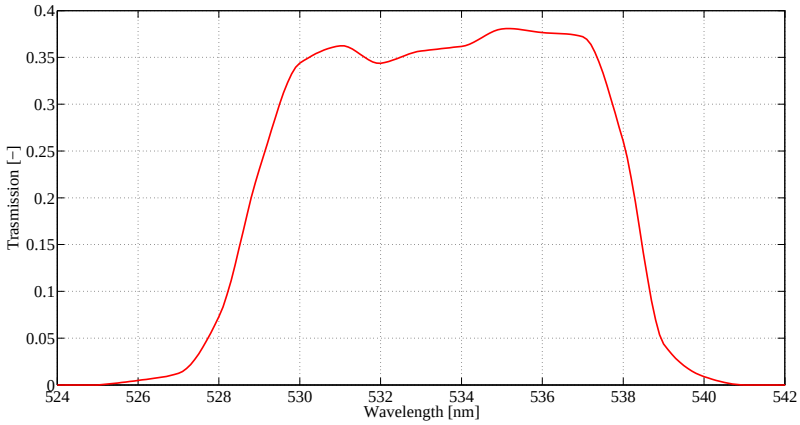

Figure 2.12.: Spectral response of the linear channel interference filter (data provided by SESO)

the 500 µm diameter surface of the linear APD by means of two spherical lenses. In order to respect the specified transmission budget and to minimize polarization effects, all optics, except the first surface, are covered with an anti-reflection coating.

Opto-electronics of the linear channel Despite the role of providing an internal trigger, the linear detection channel has two further functions:
One additional function is to measure precisely the energy of the laser pulse; this is necessary because the non-linear detection (see below, 2.3.4.2) is afflicted with an important time walk, that is, a dependence of the detector internal delay on the amount of energy contained in the optical pulse. Knowing the laser pulse energy, one may, a posteriori, correct the time walk afflicted dates with an appropriate value.

This pulse energy measurement is performed by an electronic circuitry that features a sample-and-hold module that is, a little bit tricky, in turn triggered by the non-linear detection signal (as this is the most precise trigger signal). The hold signal is then digitized by a 16-bit analog-to-digital converter (ADC).

The second additional function is the measurement of the continuous luminous background level. This luminous background, provoked by sunlight that is reflected by Earth atmosphere, oceans and land masses (Albedo), is not constant. The higher the background flux, the higher the corresponding DC part of the signal and consequently the noise level on the trigger output (proportional to the root of this flux). The knowledge of the continuous part of the diode output permits to adjust the detection threshold, the voltage to which the diode output signal is compared in order to allow a trigger.

The output of the linear APD is filtered, and a low-frequency or DC part is measured by another 16-bit ADC. The T2L2J2 control electronics (see below 2.3.5.1) permit to set different detection thresholds, even threshold automatics: A fixed threshold, a list with three threshold cases and a threshold based on the DC level (calculated on the base of the square root of the background signal).

The main functions as the provision of the three signals trigger, pulse and continuous are located on a small proximity electronics PCB (called ProxL, see figure 2.13). This board, holding equally the detector, is mounted in the BOLI mechanics. The chosen detector, as

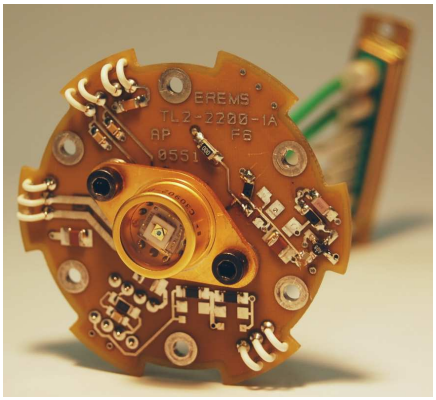

Figure 2.13.: The linear 902S detector and its electronics

mentioned above is an C30902STC, manufactured by Perkin-Elmer (formerly RCA). This APD, with a bandwidth of 1 GHz (pulse response: FWHM = 600 ps), has very good characteristics in terms of noise (noise equivalent power NEP = 1 fW/Hz$^{1/2}$, dark current I_{dark} = 15 nA), quantum efficiency (ρ up to 75% and 40% at 532 nm) and bandwidth.

All signals are routed through a harness from the satellite's LRA boom into the interior of the satellite, in the T2L2J2 electronics box (section 2.3.5) and on the "Detection Card", which is in charge of signal conversion, routing and measurement.

2.3.4.2. The non-linear detection channel

As stated above, the optical signal, i.e. the laser pulse has to be retarded to give some time to the non-linear detection chain to be armed. For this reason a fibered delay line is employed. The T2L2J2 design profits from this delay line by putting the more sensitive optics and opto-electronics in the inside of the satellite. The front optics of the non-linear detection channel are thus divided in one part located outside of the satellite, on the LRA boom, and a second part consisting of the fiber delay line, the rest of the optics and the detection, located in the T2L2J2 electronics box. These elements are called "BONL" (for "Boîtier Non-Linéaire") and "OCTO".

Collimation optics BONL The BONL optics concentrate, just as BOLI does for the linear detector, the specified FOV of ±55° into the optical fiber. The chosen optical fiber, a multimode graded index fiber, has a maximum numerical aperture NA of 0.29 and a core diameter of 100 µm. The chosen acceptable NA, corresponding to an acceptance of a 25%-level of luminous flux is 0.20 (an maximum incidence angle of 11.5°). The magnification ratio, expressed in solid angles, is 21, resulting in a virtual pupil of only 10.6 µm.
A first set of three lenses, in fact the same arrangement as for BOLI, creates a parallel beam in order to illuminate the same kind of radial density filter as for BOLI (see figure 2.14). A single spherical lens then concentrates the beam into the ±11.5° acceptance angle of the fiber. Once outside the BONL mechanics, the fiber is protected by a copper shielding and

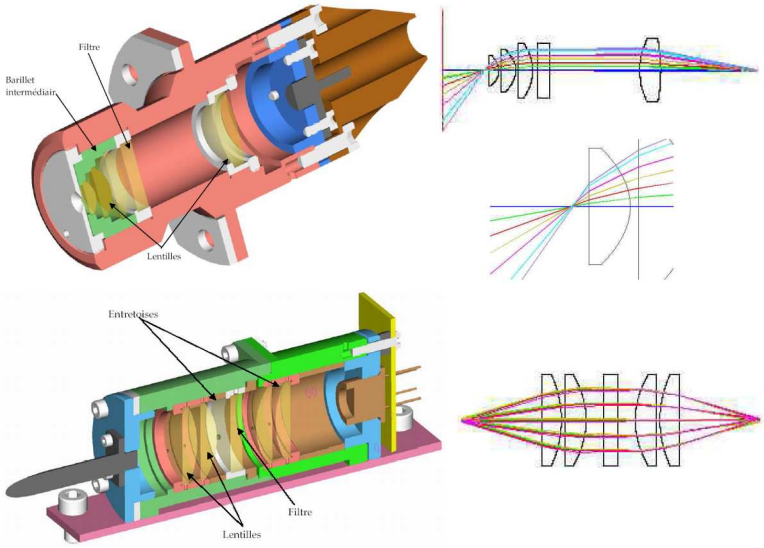

Figure 2.14.: The collimation optics BONL of the non-linear detection channel located outside the satellite body and the coupling optics OCTO located in the electronics unit.
CAD-view and ZEMAX simulations © SESO, France

some layers of lead tape. Together with the coaxial cables of BOLI the fiber is guided via a harness into the T2L2J2 electronics box.

Detection optics OCTO In the T2L2J2 electronics box is located a further delay line, constituted of the same kind of optical fiber coiled on a 120 mm ring. This delay line serves for retarding the laser pulse while the non-linear detection chain is electronically armed (application of Geiger voltage); this process takes some nanoseconds. After passing through the delay line, the light exits the fiber in the same numerical aperture of 0.29 corresponding to 17°. This divergent beam is transformed into a parallel beam by a group of two lenses in fused silica and transmitted onto a narrow (FWHM = 1 nm) interference filter. As already mentioned, this narrow filter is preferably located in the better protected (and less temperature variant) electronics box than at the outside of the satellite.

Another set of lenses, identical to the first stage, concentrates the light onto the detector. The detector has a diameter of 200 µm, but in order to preserve a better timing (lower dispersion), the illuminated spot on the junction should measure less than 160 µm as was derived in an exhaustive characterization test. Given the same optical layout for both ex-

panding and concentrating part and the 100 µm core diameter of the optical fiber, there is sufficient margin for alignment error.

The non-linear detector consists in an APD in Geiger mode that is triggered, or better: armed, by a signal issued from the linear detection. This "trigger" means the application of a voltage slightly above the break-down voltage of the diode. During "off" conditions, a voltage below the breakdown is applied; when triggered, the detection electronics (see below 2.3.5.1) applies a small DC voltage on top of that. In that condition, only one electron-hole pair in the junction is sufficient to engage the multiplication process and to generate an avalanche. This first electron-hole pair may be generated either by a laser photon, a noise photon or thermally. This extreme sensibility is the reason why the so-called "Geiger-Voltage" has to be applied a very short time before (about 4 ns in the case of T2L2J2) the arrival of the laser pulse that has to be detected. The photodiode used in T2L2J2 is the K14 SPAD of Czech design (PESO Consulting), and widely used in the SLR community. It has several peltier stages for cooling, the optimum operation temperature being at -10°C. Together with some read-out electronics for the fabrication of the Geiger-voltage and a comparator in order to produce a logical signal (throughout the electronics the ECL standard is used) for the event timer, the diode is mounted on a small proximity electronics board (called "ProxNL").

2.3.5. The electronics architecture of T2L2J2

2.3.5.1. Signal forming and management: Detection board

All management, conversion and comparison of the different signals are implemented on a separate PCB, the "Carte Détection"; a synopsis with the most important functions is given in Fig. 2.15. The pulse output of the linear detection, coming from ProxL, is fed to a fast

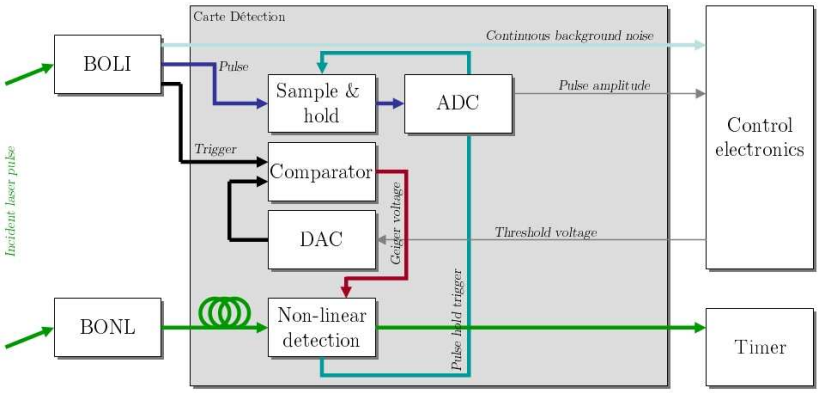

Figure 2.15.: Synopsis of the detection board

sample and hold circuitry; this, in turn, is triggered by the non-linear detection, as it is more precise, and thus there is less dispersion on the hold signal. The constant signal is then digitized by a 16 bits digital-to-analogue converter (DAC) which send this data to the control electronics.

The trigger output of the linear diode is first compared to a threshold voltage if it has to be regarded as a valid event. The reference threshold voltage value comes from the control electronics where is implemented the comparison to the continuous noise measurement: There a three possibilities: A fixed threshold, a list with three cases depending on the noise

level and a function depending with the square root on the noise level.
If the trigger signal is higher than the threshold it is transformed into a (Geiger) voltage that is applied on the non-linear detector.

The delay line in the non-linear channel is designed such that the detector receives the photons approximately four nanoseconds after its own activation by the trigger (Geiger) voltage. The generated avalanche is transformed into a logical signal and sent to the event timer.

The sun noise measurement simply transverses the detection board. There are additional functions fulfilled by this board such as the thermal regulation of the two detectors as well as the generation of their respective polarization voltages.

2.3.5.2. The T2L2J2 event timer

The T2L2J2 event timer consists basically of a frequency synthesis, a programmable logic array (FPGA) and a double vernier.

The frequency synthesis generates a 100 MHz signal based on a low-noise quartz oscillator of the company AR-Electronique, with a phase-lock-loop (PLL) on the 10 MHz reference signal delivered by the DORIS USO. A time constant of 300 Hz insures very low short term phase noise (compare Fig. 2.16), which amounts to less than 100 fs in terms of jitter. The frequency synthesis provides this reference signal to both timer subsystems, the FPGA

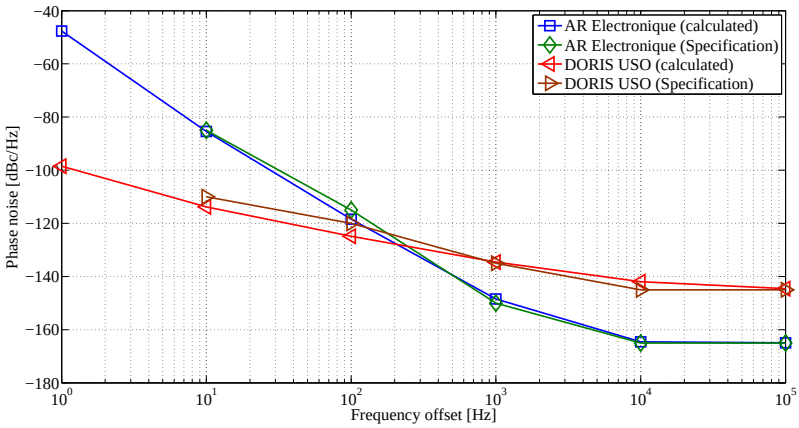

Figure 2.16.: Combined phase noise of DORIS oscillator and event timer local oscillator AR Electronique

counter and the vernier.

The FPGA serves as a coarse timing device: It runs on 100 MHz and in each cycle increments its register by one, thus permitting timings with a resolution of 10 ns. The autonomy of the FPGA counter is on the order of two years before it starts at zero again.

The vernier is the heart of the precise timing by resolving events with a resolution of 100 fs and a dynamic of 20 ns. The precision of the vernier stage and thus of the whole timer is on the order of two picoseconds.

2.3.5.3. Other electronics

There are two further electronics boards in the electronic subsystem. One is the overall control electronics: It manages the communication and data interchange with the other boards as the timer and detection board and the satellite MIL Std 1553 communication bus. It writes the raw timings, together with other instrumental parameters as the pulse amplitude, noise level and temperatures etc. into data frames, and sends them to the PROTEUS platform computer.

The other electronics are just the respective power supply in order to properly generate the voltages needed by the different electronics from the PROTEUS supplied 28 V.

All electronics, except for the photodetector board of the linear channel, are housed in a single electronics box, as depicted in Fig. 2.17.

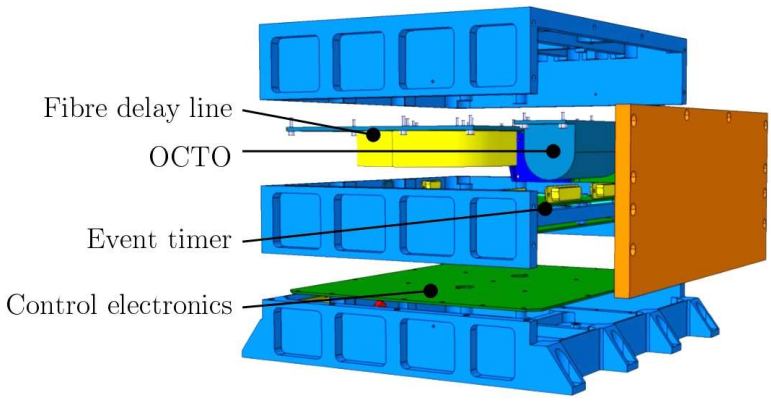

Figure 2.17.: Exploded view of the T2L2J2 electronics subsystem SSE. CAD-view © EREMS, France

2.3.6. T2L2 on Jason 2 budgets

This section summarizes the overall resources of the T2L2J2 payload on the Jason 2 satellite.

Mass: The T2L2 electronics subsystem (SSE) consists of a single box of 8 kg, mounted on the X+ wall of the satellite. The outside optics BOLI and BONL are mounted on an interface plate with an overall mass of 1.2 kg; this ensemble is in turn fixed on the LRA boom.

Volume: The SSE represents a cubiod with a footprint of 270 mm × 280 mm and a height of 150 mm. The overall volume of the optics subsystem may be described by a block-shaped envelope of 160 mm × 116 mm × 103 mm.

Power: The power consumption is of 42 W on the PROTEUS delivered 28 V supply.

Data: The T2L2J2 instrument is equipped with an internal memory for immediate storage of the generated measurements; during operation it emits continuously its housekeeping and scientific data over the MIL Std 1553 bus to the Jason 2 main computer. The three passenger instruments T2L2, LPT and Carmen share a total of 128 Mbits of memory; the alloted data rate for T2L2 is of 40 Mbits per day. Jason 2 uses three ground stations in Europe for its data download.

3. Characterization of the T2L2J2 instrument

The T2L2J2 flight instrument had to undergo a detailed calibration after its delivery by the industry prime contractor EREMS. The data retrieved in orbit would not be fully exploitable without this calibration. It is thus of vital importance to achieve the mission goals.

Furthermore, the final performance of the instrument in terms of time/frequency metrology had to be determined in great detail; on the one hand, these results provide information to what extent the instrument development itself is a success and on the other hand they deliver evidence of what may finally be expected from the whole T2L2 time transfer system.

For these two points, the OCA team developed a metrological test bed, to which the author largely contributed in all phases from concept, detailed design, implementation, test and operation. The following section describes this test bench; then, both the calibration and the performance experiments that were conducted on the T2L2J2 flight model are described.

3.1. A metrological test bed for T2L2J2

3.1.1. Scope and demands on the test facility

The metrological test bed simulates all instrumental and experimental parameters that are important for the derivation of calibration parameters and metrological performance of the T2L2J2 instrument.

The T2L2J2 instrument receives two main input signals:

- A reference signal from a clock; in the case of T2L2 on Jason 2, this signal comes from the DORIS ultra-stable oscillator.
- The laser pulses coming from the different laser stations: They may characterized by following four parameters:
  - The laser wavelength: In the actual design, only green 532 nm laser pulses can be considered.
  - The laser pulsewidth: This parameter depends on the actual configuration of the laser used in the SLR station; The trend in the SLR community is of course to shorten the pulse length to a minimum in order to ameliorate precision. For the test bed it was decided to choose 20 ps as the required value, as it represents both a representative value and is sufficiently low for determining highest precision.
  - Pulse power: This parameter varies from zero to arbitrary values. Expected values on the Jason 2 orbit, considering the MéO and the FTLRS station and different elevation angles, have been determined in A and B-phase of the T2L2 on Jason 2; they are described in the link budget[1] document [30].

[1] Please note that an examination of the link budget is not part of the present work.

  - The polarization of the incoming light wave: The polarization of the laser beam may be considered as an arbitrary value; based on different polarization configurations in the laser stations (linear or circular), and after propagation over various optical elements in varying geometry, it is difficult to predict the polarization state at arrival on the satellite level. For the tests, the polarization should thus be held in one fixed arbitrary state.

In addition to these two rather straightforwardly definable signals, there are further issues that have to be respected:

- Varying attitude: During a pass over a ground station, the geometry of the laser beam with respect to the T2L2J2 optics constantly changes; as the incidence angle has some (also volitional) repercussions on the propagation of the beam inside the optics and interacts with the polarization, this geometrical aspect has also be regarded in the test bed. A variable laser beam incidence angle over the whole FOV cone (two axes) has to be implemented.

- Background noise: The T2L2J2 optics image the whole earth onto the detectors; this leads to a large amount of continuous noise, coming from all directions and from anywhere in the solar spectrum (since the noise is basically sunlight reflected by Earth's atmosphere, oceans and land masses). This noise source has to be simulated.

- Other parameters: The environmental conditions in space, even protected by a satellite body, are very harsh. The test bed does not aim to reproduce these conditions (since this is a topic of space industry). The test bed should on the contrary work under best laboratory conditions in order to perform the tests on the highest level of performance. One aspect that should be regarded anyhow is the response of the instrument towards temperature since the satellite may only guarantee to keep it in a certain range.

As we will see in the next few sections, these few requirements are sufficient to demand a very complex, heterogeneous and demanding setup. In fact, the test bed represents, on a laboratory scale, the whole T2L2 experiment scheme, with SLR stations (laser and clocks), orbit and satellite (geometry mechanics) and the instrument itself; the difference is that all parameters are, or have to be, much better mastered than in the real world systems.
Further, as this document is not a technical report, it will not provide an exhaustive list of all intended calibration and performance tests; these are described in detail in [22].
The projected evaluations of the T2L2J2 flight instrument were to be performed in two steps:

- A first, main test campaign on the T2L2J2 instrument flight model (MV) alone for a detailed calibration of all instrumental and operational parameters and the determination of its performance in terms of time metrology. This campaign was scheduled directly after the integration and delivery of the instrument by the prime contractor EREMS to CNES.

- A second campaign for the determination (or the verification) of the flight instrument's performances in conjunction with all associated satellite equipment, primarily the PROTEUS (satellite bus) power supplies and the DORIS oscillator. This campaign had to be performed in the THALES Alenia Space plant in Cannes, since the company is the prime contractor for the PROTEUS platform and satellite integration.

3.1.2. Design and composition of the test bed

The following section describes in detail the different subsystems of the test bed. The whole test bed may be seen as an ensemble of four subsystems: the main part, an optical bench, that comprises the laser system, optics and some mechanics; an associated energy calibration bench for control and monitoring of the provided laser pulse energy; a reference timing subsystem with clocks, event timers, frequency synthesis and signal distribution; and finally a control equipment, consisting of computers and the equipment associated to the different previously cited units.

The development of this complex panoply of metrology and control devices was carried out by a team, part of the RDM group, namely by Dominique Albanese, Aurélien Dréan, Franck Para, Etienne Samain[2] and me. My responsibility therein covered, of course in collaboration with the team, a big part in the study, concept and design of the optical bench (next section) and other parts. The development of the test bed gave rise to two publications [34][3] and [35].

3.1.2.1. Test bed optics: Laser and optical architecture

This section will describe the major design issues that had to be addressed in the layout of the optical architecture of the test bed. The optics comprise the laser system, the general beam architecture and some other optics for monitoring and control of laser power and reference timing.

Laser system As mentioned earlier, the primary demand on the test bed is to imitate at best the functionalities of an SLR station. The central constraints on a laser system were therefore the used wavelength (mostly 532 nm and particularly true for T2L2J2) and a short pulse length (on the tens of ps scale). The latter is less well defined throughout the SLR community (ranging from 20 to 300 ps), depending on the respective employed laser technology and has a secondary importance (as compared to wavelength), so it was decided to take the value of the MéO station's laser (that is, 20 ps) as a specification[4]. In order to qualify the T2L2J2 instrument at the highest level and not to bias the measurements by noise generated by the test apparatus itself, further requirements were added: In order to decouple the timing from the laser system the laser pulse energy should not vary from one pulse to another. Further, the laser pulse length shall remain constant and single pulses should be guaranteed (In actual diode or flash lamp pumped Nd:YAG laser systems there is often generated a train instead of a single pulse.). In order to study the instrument's dependence on the repetition rate, the laser system should also offer the possibility to generate pulses from DC (single shot) to the kHz level. But in order to use the laser also for later experiments like fast event timing (see Iliade in Chapter 8.3) we augmented this requirement voluntarily to at least 1 MHz. As a final (in fact, quite stringent) demand the laser's repetition frequency should be able to be synchronized to an external reference frequency in order to perform synchronous measurements.

[2] At this place I already like to express my gratitude for the congenial collaboration and fruitful discussions with all of them.

[3] The presentation of the poster during the TimeNav'07 conference in Geneva was rewarded by the "IEEE FCS/EFTF Student Poster Award".

[4] An FWHM of 20 ps is also the lower limit imposed by the spectral bandwidth of the lasing crystal Nd:YAG and by atmospheric dispersion due to spectral broadening.

Shortly after the determination of these specifications a vast search in industry offerings was started. After some iterations including several redefinitions of the optical beam architecture (see below) we disposed of a first selection of laser models that fulfilled at least most of the specified criteria. These systems are summarized in Table A.1 in the Appendix.

Many or most of the considered lasers are based on a passive mode locking system what leads to a very high, fixed repetition rate depending on the cavity length ($f_{\mathrm{rep}} = c/2L$, some tens to hundreds of MHz). In order to work with low repetition rates as used in SLR, we had to consider a pulse selection by some kind of optical modulator. The requirement on this type of modulator is to be transparent during the time of the laser pulse and to be opaque during an arbitrary number of pulses; in other words, for a pulsed laser with a given repetition rate, say 100 MHz, the modulator should switch from one state to another in less than 10 ns, but stay in one of the states for an arbitrary time. Many acousto-optic and electro-optic modulator systems offering this short rise time are eliminated by this last requirement because they mostly work in a resonant mode. A number of different products including fibered modulators based on fiber Bragg gratings have been considered; this type of product of the communication technology does in fact represent an ideal choice for selecting single short pulses in a dense pulse comb, but unfortunately does not resist the mean power of the laser that had to be employed in the test bed.

After sorting out the different alternatives we concluded that, with respect to our specifications, a combination of the HighQ Laser Picotrain together with ConOptics pulse picker system would represent the best choice. We specified to HighQ a repetition rate of 100 MHz, a pulse width of 20 ps[5] and an average power of 1.5 W (HighQ finally delivered 3.5 W). Further we opted for the synchronization option[6] and the physical separation of the frequency doubler[7] from the cavity. The laser cavity of 1.5 m length is in a zig-zag configuration and passively mode-locked by an saturable absorbing mirror (SESAM, based on a semiconductor material), while the Nd:YO_4 slab is continuously pumped by a red laser diode (at 808 nm) producing a 100 MHz train of infrared pulses. One cavity end mirror sits on a displaceable piezo stage controlled by a phase lock loop electronic comparing the laser rate (by an internal photo diode) with an external reference frequency.

Pulse pickers A set of two pulse pickers of ConOptics is used on the laser's native 1064 nm beam. A "pulse picker" is an electro-optic modulator based on birefringent crystals (in this case LTA) and a Glan polarizer. The birefringent crystals decompose the incident laser light into two orthogonal rays, the ordinary and the extraordinary ray.
In the ConOptics setup, as in Pockels cells in general, these crystals (and with it their ordinary and extraordinary axes) are mounted turned by 45° with respect to the incident linear laser polarization. This allows to decompose the light (or its electric field vector) in order to make it travel on the two crystals axes, the so-called slow and the fast axis. As the names states, the particularity of the two axes is that they feature different indices of refraction.
In addition, this birefringence is subject to applied electrical fields (the so-called Pockels

[5]The Nd:YO_4 material allows for transform-limited pulses with a FWHM of about 7 ps. The longer pulses are obtained by an intra-cavity etalon in order to reduce the spectral bandwidth.
[6]HighQ announced a jitter of less than 1 ps, jitter being the unique noise notion throughout all industry products; see Section 3.1.3 below for the characterization in terms of stability.
[7]Second harmonic generation from the intrinsic wavelength of 1064 nm of the Nd:YO_4 lasing crystal to 532 nm.

effect). The two components of the light's electrical field thus travel at different speeds through the crystal; at its output, the resulting electrical field vector is build by the vector sum of the two components: By this means, the polarization of the light (i.e. its electrical field vector) may be manipulated by playing on the different refractive indices of the crystal (i.e. its birefringence). This is performed by mounting the crystals in a capacitor setup and applying extremely high electrical fields on them. Hence, the polarization of an incident laser pulse may be turned by an arbitrary amount. The way of pulse selection is then done by employing an additional polarizer (a Glan prism as mentioned above): The wanted pulses are not polarization-turned and pass through; the unwanted pulses are turned in polarization (by 90°) and are rejected by the Glan prism. As one sees, the performance of the system depends directly on the angle (and its repeatability) by which the polarization is turned.

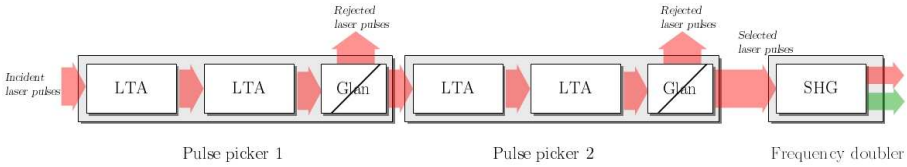

Figure 3.1.: The pulse picker - frequency doubler assembly (LTA: birefringent crystal, Glan: polarizer, SHG: second harmonic generation)

In our setup, the pulse selection (see Fig. 3.1) is performed on the IR beam in order to enhance the pulse pickers' extinction ratio (E.R.): The IR beam is frequency doubled in order to obtain a 532 nm beam. Both the selected pulses as well as the residual, not sufficiently suppressed pulses are transformed into green light; though, the frequency doubling is a highly non-linear process, i.e. the efficiency is very low for low optical power (as have the residual pulses) and higher for higher powers. By this means the ratio between selected to suppressed pulses is efficiently enhanced.

Figure 3.2.: The HighQ laser and the set of two pulse pickers as configured in the test setup

The reason for employing two pulse pickers rather than a single one is outlined in the following: If one considers an initial E.R. of 1/100 (specification given by ConOptics), which is enhanced by the non-linear doubling efficiency (giving a final E.R. of 10^{-4}) at a low repetition rate (like 10 Hz) and with a 100 MHz laser, means that the (quasi-continuous) power contained in the residuals of the suppressed pulses is still 1,000 times higher than the power

contained in the primary, selected pulses what would lead to a serious bias in the T2L2J2 measurements. In fact, in order to have a power ratio (residuals to primary) of, say, less than 10% we find (for small repetition rates): E.R. $\leq 0.1 \times \frac{N_{\text{rep}}}{N_{\text{las}}}$, that is 10^{-8} for the HighQ laser.

A set of other solutions to enhance the E.R. had been studied, mainly by use of saturable absorbers. A saturable absorber could absorb the residual pulses in a pulse train prepared by a pulse picker and transmit the primary "picked" pulses that are above some threshold. Meanwhile, experiments on the saturable absorbing dye used for mode locking of the MéO station's laser (see Section 4.1.1.1) did not bring satisfactory results: An enhancement of the E.R. by a factor of only 4 was obtained, what is probably due to this type of dye; for mode locking only small differences of "absorbed" to transmitted powers are necessary.

Another saturable absorber was proposed by the small spin-off company BATOP of the University of Jena in Germany: It offers a resonant saturable absorber mirror (RSAM), just designed for this purpose, cleaning a pulse picker output for E.R. enhancement. Above a certain laser fluence, the semiconductor-based saturable absorber material becomes transparent and the light is reflected by a mirror located behind the absorber. Unfortunately, this

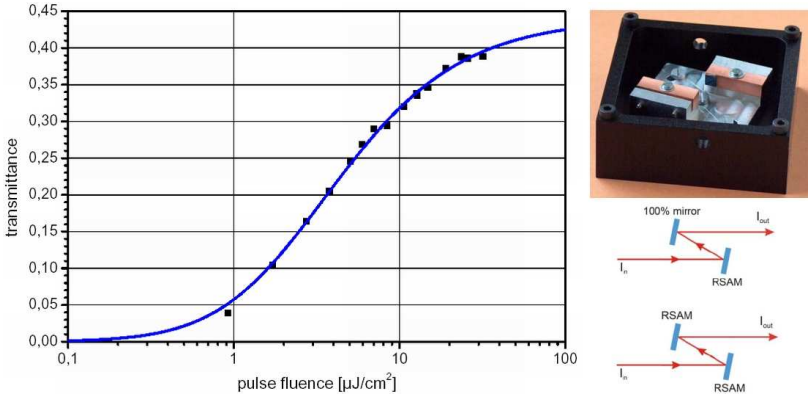

Figure 3.3.: Transmittance of a BATOP-supplied saturable absorber as a function of laser pulse fluence. Setup photo. The device exists in two versions, with one or two resonant saturable absorber mirrors. Images © BATOP, Germany

device requires an extremely high fluence (about 10 µJ/cm^2) in order to obtain a transmittance of about 0.4 as depicted in Fig. 3.3. The RSAM device principally represents a very interesting technology, but some detailed verification studies would have been necessary. It further entails a more complicated optical architecture with a serious beam compression to get the right fluence.

In order to meet the temporal constraints and taking into account the rather fine performance of the first pulse picker we decided to opt for the acquisition of a second pulse picker of the same type. With this arrangement of two pulse pickers followed by the second harmonic generator an extinction ratio of about 2.8×10^{-9} in the green could be shown.

Beam architecture The very early philosophy of the test bed optical architecture was to investigate both the T2L2 instrument and the LRA retroreflector simultaneously, as they would be mounted on the outside of the Jason 2 satellite. Besides the difficulties to obtain a mockup of the LRA or at least some technical information (by the time of the test bed

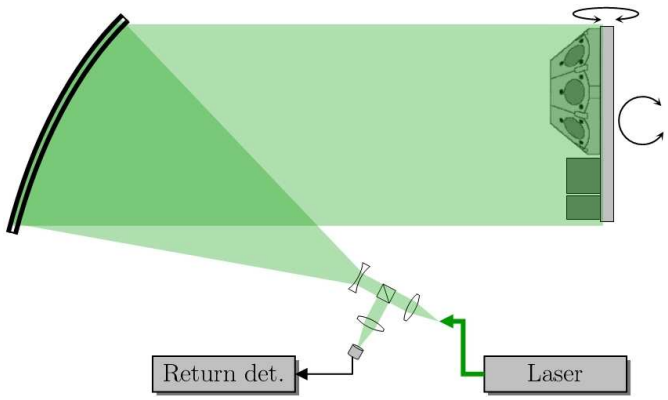

Figure 3.4.: Parallel beam generation with an off-axis parabolic mirror: The initially fine laser beam passes through a cube separator and is then expanded onto the parabola. Some of the returning photons (reflected by the LRA) are then branched off onto a return detector. The LRA and the optics are turned in two axes in order to simulate the geometry of the laser beam with respect to the satellite.

design) in order to build a copy, we had to face the problem of available laser power: in order to characterize both T2L2 and LRA simultaneously, e.g. for the determination of the detection and reflection equivalent points, one would have to illuminate the whole LRA with the attached T2L2 optics, leading to a beam diameter of about 30 cm. This may be achieved by expanding the laser beam onto a parabolic mirror which creates a parallel beam, like depicted in Figure 3.4. Still, laser beams feature a Gaussian power distribution, which is mainly preserved by the different optics: we would illuminate the center of our 30 cm beam with the maximum power, whereas the T2L2J2 optics, mounted on the rim of the setup would obtain a very low fraction of the laser energy. A quick laser power budget shows that this option would necessitate the use of high power amplification stages in order to provide the necessary laser pulse energy in front of the T2L2J2 optics. This is not reasonable for this purpose, from a cost and implementation as well as from a laser security point of view[8].

As will be pointed out in Section 3.1.2.9, this concept of T2L2J2 SSO and simultaneous LRA evaluation had to be abandoned. However, the power offered by most of the lasers given in Table A.1 do even not allow to illuminate the T2L2J2 optics with a circular beam. A concept to economize laser power in, at least, one dimension is to create a type of rectangular or elliptic beam. This may be obtained by the use of a set of cylindrical lenses in order to expand the beam more in one dimension than the other. In one version, a diverging beam (e.g. beam exiting a monomode fiber) is further diverged in the vertical direction by a first cylindrical lens (i.e. horizontal cylinder axis) whereas in the horizontal direction the beam is made parallel or converging (see the ZEMAX simulation conducted by G. Martinot-Lagarde in Fig. 3.5). For reasonable cylindrical lenses found on the market one may obtain an elliptic spot (with semi major axis of 32 mm and semi minor axis of 1.6 mm corresponding to the $1/e^2$ point of the beam power distribution) which features light rays that are inclined of about 8° to the normal in the vicinity of the T2L2J2 apertures. In order to overcome this

[8] As we will see in Section 3.1.2.9, this configuration employing a parabolic mirror in order to generate a parallel beam will be used for the characterization of the LRA. A high laser power is not needed for this experiment as all reflected energy will be collected by the same optics again before passing onto a detector.

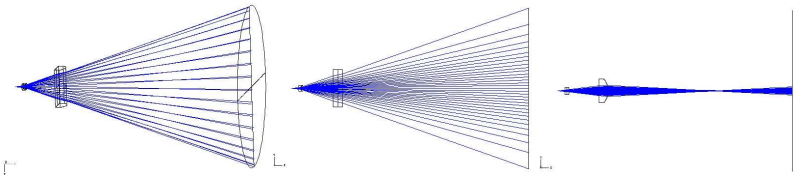

Figure 3.5.: ZEMAX simulation of an elliptic beam formed by cylindrical lenses (left: 3-D view, middle: side view, right: top view)

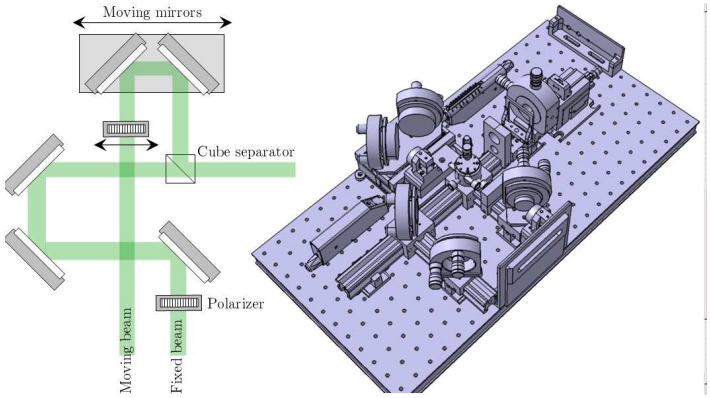

Figure 3.6.: Two parallel beams are produced by a moving mirror assembly. The whole setup (right) is mounted on a small breadboard that itself is installed on a translatable sledge.

ray inclination, as it would seriously complicate the measurements (or at least, the analysis) with respect to incidence angles (see below), one would have to employ a third, quite big cylindrical lens with the bulbous dimension on the order of 64 mm. This type of lens is not a standard product and would have to be manufactured on purpose.

These different considerations concerning laser power budget, beam quality, delivery time, cost and ease of implementation were iterated with the different types of lasers and modulators mentioned before and led finally to the implementation of two narrow, circular, parallel laser beams that illuminate BOLI and BONL separately.

Beam distribution Another requirement on the two laser beams is that they are displaceable. As we will see in the next paragraph, in order to simulate different incidence angles, the T2L2J2 optics are mounted on a two-axis gimbal mount and may thus be rotated on a horizontal and a vertical axis. The laser spots then have to follow the T2L2J2 apertures, that is to say their projection on a plane perpendicular to the laser beam[9]. The use of two beams following the T2L2J2 pupils takes care of a problem that has not yet been evoked above: For one beam it is already difficult to guarantee the same power density on both pupils; further, during a rotation both pupils traverse the (Gaussian) distribution. It would be delicate to govern the power density in each point, especially employing energy detectors that have a finite size (see Section 3.1.2.2).

[9]Of course, the implementation of two fixed beams covering just the range of the aperture displacement was also considered; however, stating a rotation of 55° one would end up with only the half of the power density as compared to the cylindrical solution mentioned before.

The distance between the two parallel beams may be modified by an optical layout depicted in Fig. 3.6. An incoming laser beam is split in two by a cube separator, one half is directed on a motorized assembly of two mirrors (at 90° one to another): when this stage moves, the outgoing beam is displaced with respect to the incoming. The other half of the beam has to be fed through a small delay line in order to equalize the two path lengths (the laser pulses should arrive at the same time). Finally, the powers of the two beams are equalized by two polarizer assemblies ($\lambda/2$ and polarizing cube separator). One of them has to be movable since an implementation upstream is not possible because the polarization may be deteriorated by the mirrors.

All this instrumentation is mounted on a small optical table which itself is mounted on a moving carriage. As we will see in Section 3.1.2.2, this sledge permits to swap the laser beam between the T2L2J2 optics and the reference energy detectors permitting a regular monitoring of the laser energy.

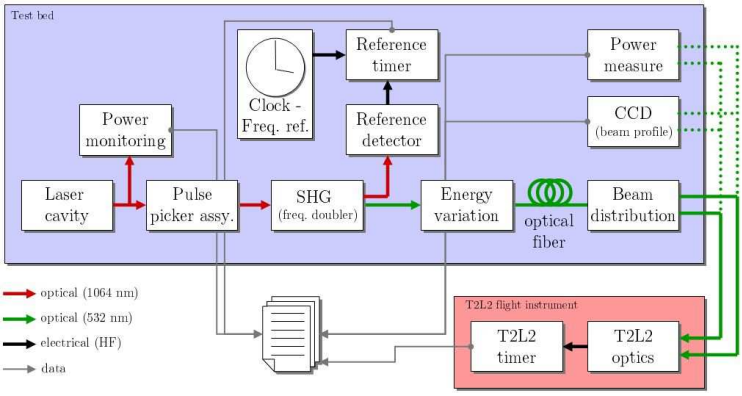

Figure 3.7.: Synopsis of the main parts of the test bed

Simulating varying incidence angles We already heard the T2L2J2 optics were designed such that they are able to "see" the whole earth surface from the Jason 2 orbit, resulting in a field of view of ±55.6° (compare to Fig. 2.9). By this means, the instrument is capable of performing a time transfer on global scale (please refer to Chapter 2.3 for details). Hence, the optics have to be tested with respect to various viewpoints like propagation (in the optics) differences for different angles of incidence, the characterization of the radial neutral density filter and so forth.

The T2L2J2 optics being a quite compact assembly, it seemed obvious to put them on a rotation stage instead of creating a movable laser beam architecture. After some industry survey we decided to use an existing gimbal mount of the MéO station. On the first sight perhaps seeming over-designed in terms of size, load and torque, it represents the best in terms of precision and repeatability (on the order of 0.001°). The T2L2J2 optics are mounted such that, for a rotation around the horizontal axis[10] the apertures stay at their place (collinear axis), and for rotations around the vertical axis, the aperture of the linear

[10]The horizontal axis, its angle denoted as ϕ, is the line connecting the two apertures, whereas the vertical axis designates the axis perpendicular to the latter and to the detector line-of-sight going through the BONL pupil.

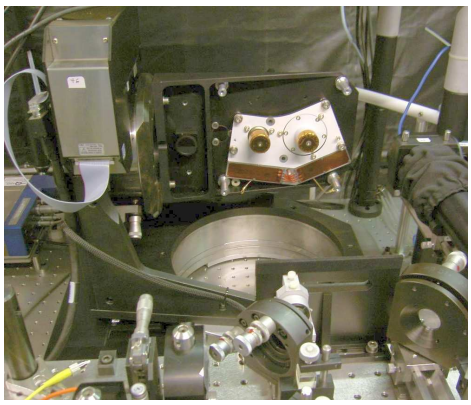

Figure 3.8.: The two axis gimbal mount used for incidence angle measurements, with the T2L2J2 SSO installed; in the foreground, part of the beam distribution system.

channel moves whereas the aperture of the non-linear channel stays in place[11]. Fig. 3.8 shows a photo of the T2L2J2 optics flight model on the "AltAz" mount. The interface plate on which is mounted the T2L2J2 optical assembly is equipped with two mirrors, one for alignment and another for a measurement of return pulses (instead of the LRA). The mirror plane of the first is parallel to the reference plane of the T2L2J2 optical assembly relying on the mechanics produced by SESO. The second mirror is coplanar with the apertures of BOLI and BONL and adjustable so as to reflect the laser pulses back into the beam distribution system where they are directed into an optical fiber (cube separator) that leads to the return reference detector (see Section 3.1.2.4).
The two Newport rotation stages of this two axis mount are controlled by a Newport XPS motion controller (see Section 3.1.2.5).

In the following, there should not be given the contemplation of each and any mirror or lens employed in the test setup, but two systems should anyhow be mentioned.

Laser power control As mentioned in the first paragraph, the laser pulse energy (and hence the mean power) should be variable in order to perform measurements for all expected levels of laser pulse energy (from single photon to some tens of thousands of photons). This functionality can easily be obtained by a very common setup using polarization: The linearly polarized laser beam is passed through a half-wave polarizing plate that is mounted on a motorized rotation stage. The polarization of the beam is thus turned by the double angle between initial polarization and polarizer axis. The beam is then passed through a second polarizer, a Glan-Thompson prism that transmits only vertical polarized light, the rest being rejected. By this means, the laser beam power may be precisely controlled.
The power control system is completed with a mechanical shutter in order to interrupt the laser beam in a secure manner.

[11] This solution is preferred to the opposite because the laser pulses will arrive at the very same time in the BONL aperture for all rotations (good for timing comparison) whereas a slight delay or advance (some ps) for the linear detection is not supposed to considerably alter the outcome of the measurement. At least, it is of no importance for the incidence measurements.

Table 3.1.: Characteristics of the Nufern single-mode polarization maintaining fiber 460-HP

Operating Wavelength	[nm]	450 – 600
Mode Field Diameter	[µm]	3.5 ±0.5 @ 515 nm
Second Mode Cut-Off	[nm]	430 ±20 nm
Attenuation	[dB/km]	30 @ 515 nm
Core Numerical Aperture	[-]	0.13

Monomode fiber A drawback of the use of the pulse pickers is the degradation of the beam due to impurities in the LTA crystals and non-parallelism in the applied electrical field. Fig. 3.9 shows a picture of the beam power distribution after the two pulse pickers, taken with a CCD camera. A solution to spatially "clean" the beam consists in passing it

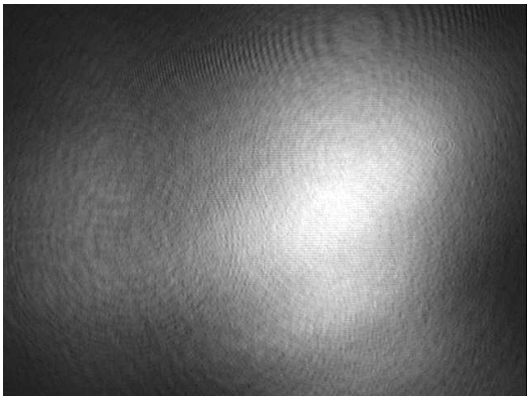

Figure 3.9.: Laser beam power distribution at the output of the pulse pickers

through a pinhole. A quite analogue means is the use of a monomode fiber; as a fiber is very convenient to handle, this solution was adopted to transport the laser light from the optical table to the movable beam distribution system. In order to preserve its polarization, a polarization maintaining fiber of the Panda type of Nufern (see Table 3.1) was employed. After passing through the laser power control, a lens concentrates the laser beam into the fiber core. On the displaceable sledge of the beam distribution the beam is anew expanded and collimated.

This concept is also adopted for the test bed setup for the measurements on satellite level (AIV) as pointed out in Section 3.1.2.8.

3.1.2.2. Reference energy measurement

In order to calibrate the measurements for laser pulse energy, a highly precise energy or power measuring device has to be employed. In addition to this functionality, the power distribution in the laser beam has to be monitored. To fulfill these needs, it was chosen to use two different devices, a set of Silicon PIN detectors associated to a read-out meter and a high fidelity CCD camera.

Laser power monitoring For the regular power measurements, mainly one detector was used: The Newport 818-SL is a large-area planar-diffused PIN silicon detector for integration

of weak continuous or quasi-continuous signals with a current output. As mentioned before, the detector is mounted next to the T2L2J2 optics (with a baffle for stray light protection); the laser beam distribution system, mounted on a displaceable sledge, may be moved in front of the detector permitting regular power measurements. As this type of detector is designed

Table 3.2.: Characteristics of the Newport detector and power meter

Weak signal detector 818-SL		
Spectral range	[µm]	400 to 1,100
Av. power max.	[W/cm^2]	2
Max. pulse energy	[mJ/cm^2]	1
Calibration uncertainty	[%]	1 (visible)
Uniformity	[%]	±2
Linearity	[%]	±0.5
Responsivity	[A/W]	0.1 to 0.5
NEP	[W/$\sqrt{\text{Hz}}$]	$5.5 \cdot 10^{-13}$
Active diameter	[mm]	10
Power meter 1935-C		
Sampling rate	[kHz]	250
Measurement rate	[kHz]	10
Accuracy	[%]	±0.1

for continuous signals, the repetition rate for power measurements is raised to its maximum of 1 MHz (which is imposed by the control electronics, see Section 3.1.2.5). At this rate, the fact of having discrete pulses instead of a continuous level is negligible[12]. The 818-SL detector is read out by a versatile power meter (Newport 1935-C) that calculates the optical power out of the current supplied by the detector; it hereby relies on a calibration unit that contains any information concerning responsivity of an individual detector. The energy per pulse is finally derived by the quotient of integrated power and number of pulses.
For some singular measurements at high power (directly at the laser cavity output, e.g.) a Newport 818-P came into use.

CCD camera It was decided to use the highly precise and low noise ANDOR DW 436 N for the spatial beam analysis. This camera had been acquired by OCA for various applications in the future MéO station, like astronomy or optical space debris tracking. At the time of T2L2 preparation, this instrument was in its testing phase and had already been used in some calibration experiments for the T2L2J2 phase B.

The readout noise being extremely low, the quasi non existing dark noise, the large dynamic of pixel readout, the exceptional quantum efficiency (over 0.9 for 532 nm) and the high number of pixels makes this camera a very precise instrument for the measurement of low optical energies and its spatial distribution.

Like the Newport detector, the camera is installed next to the T2L2J2 optics, together with an opaque baffle in order to avoid any stray light. The final measurement procedure includes the acquisition of flats, darks and the imaging of the laser beams. A "flat field" means the determination of the gain of each pixel in the CCD by illuminating it with a

[12]The bandwidth of the 818-SL is less than 200 Hz.

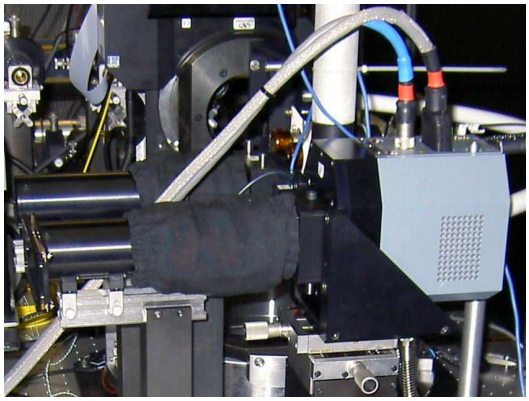

Figure 3.10.: Reference power and energy measurement bench: In the foreground the Andor CCD camera used for detailed beam analysis, in the background the Si PIN detector 818-SL. Both detectors are protected against stray light by some opaque baffles.

Table 3.3.: Characteristics of the ANDOR DW 436 N camera

Sensor type	[-]	Marconi CCD42-40
Sensor size	[-]	2048×2048
Pixel size	[µm]	13.5
Readout noise	[e^-]	1.6 (r.m.s.)
Min. shutter speed	[ms]	30
Min. temperature	[°C]	-96
Digitization	[bits]	16
Depth	[e^-]	100,000
Linearity	[%]	$<$ 1 over 16 bits
Response uniformity	[%]	< 0.11
Minimum dark noise	[e^-/pix/s]	$1.26 \cdot 10^{-4}$

source that features an extremely uniform (i.e. "flat") spatial intensity distribution. This measurement was performed at the begin of the test campaign (there is not much reason why the gain of the pixels should change during the campaign, if not damaged) by employing a LED source behind a whole set of highly diffuse filters.

A "dark" is the acquisition of the actual light background (as it will be during the beam exposure) without any laser light. After the exposure of the beam (what is performed at a laser repetition rate of 100,000 kHz for having reasonable exposure times), the dark image may be subtracted and the final image be corrected for the individual pixel gain by applying the flat field. A software finally calculates the power distribution out of the image data.

Further laser power monitoring To monitor the laser power at different spots in the optical setup, some low-bandwidth (in order to have a continuous output at 100 MHz) photodiodes came into use. They were located at the output of the laser cavity (some light branched off by a beam sampler) and at the reject output of the two pulse pickers, that is to say the output where the "suppressed" pulses are directed. By this means, a very good monitoring of the extinction ratio is assured.

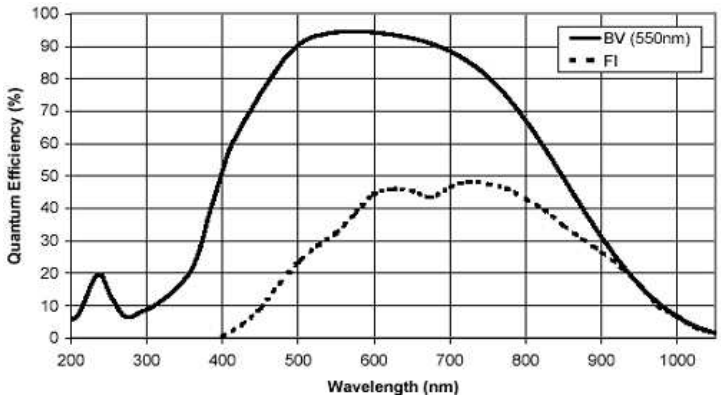

Figure 3.11.: Quantum efficiency ("BV") of the Andor DW 436 N camera (graph from [36])

3.1.2.3. Sun noise generation

During operation in orbit, the T2L2 instrument will be exposed to a high level of background noise, resulting from the sun irradiation that is reflected (albedo) by Earth atmosphere, oceans and land masses (refer to Section 2.3). The T2L2J2 optics have to be tested against these circumstances. Therefore an apparatus had to be conceived that features the main characteristics of the sun-generated background noise, that are:

- the dynamic range (from zero, to about 250 W/m^2),
- the rather uniform Lambertian[13] illumination over the whole field of view of over 110° (if we consider the worst case of a totally cloudy hemisphere),
- and the spectral distribution of the Earth albedo. In order to keep it simple we may approximate the spectral distribution of the Earth albedo by that of the sun (the actual albedo spectrum in space of course shows numerous absorption lines etc. but these features are not of importance for the present regard.).

Additionally, laser measurements have to be performed at the same time, that means one is in the need of a light source (that should have dimensions of about 35 cm by 30 cm at a 10 cm distance from the T2L2J2 optics) featuring two holes for the laser beams.

What comes first to mind when asking for simulating sun irradiation, are of course solar simulators, like employed by satellite manufacturers in their vacuum test chambers. These are mainly based on halogen lamps, mounted on a big reflector. For cost and time reasons, an assembly with tens of these lamps and an reflector build on purpose was not envisageable for this type of rather isolated measurement. Simpler solutions had to be found:
The same type of lamps can be found in small industrial solar simulators (like of Edmund Optics or Newport Oriel). In order to provide a large field-of-view illumination we would have to employ a Lambertian reflector or diffuser screen (lamp illumination from front or back). For assuring a good Lambertian emittance, reflectors tend to be very granular and thus feature a rather low reflectance, whereas diffusers like milk glass suffer low transmittance.

[13] A Lambertian emitter (or reflector) is characterized by the fact that it emits uniformly in all directions. A very well known Lambertian reflector is the moon since it appears completely uniformly luminous.

Concerning the spectral specification: The sun is well characterized as a black body emitter with a temperature of about 6000 K what not only describes the width of the emitted spectrum but also its emissivity distribution. The spectral intensity follows the well-known Planck law:

$$I(\nu)d\nu = \frac{2h\nu^3}{c^2}\frac{1}{\exp\left(\frac{h\nu}{kT}\right)-1} \tag{3.1}$$

with $I(\nu)d\nu$ being the spectral radiance with the unit [J/s/m^2/sr/Hz]. The sun spectrum is depicted in Fig. 3.12. On the other hand, lamps, LEDs and other kinds of lighting devices

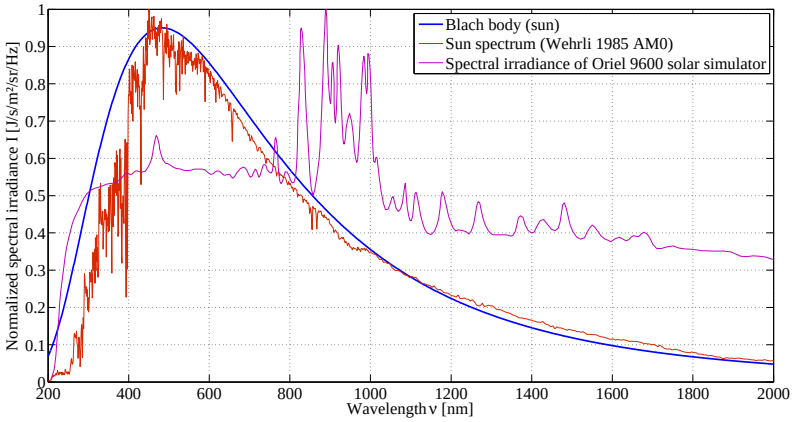

Figure 3.12.: Sun spectrum: Black body curve (at 6000 K), real conditions above the Earth's atmosphere (Wehrli 1985 AM0 [37]) and Oriel solar simulator 96000.

are mostly specified by a color temperature. Still, this doesn't mean that the respective lamp features a spectral emission following the Planck law for the specified temperature.

In the illumination market, this specification says that the emitted light provokes a similar color impression in the human eye (and brain) as would have done a Planck emitter having the specified temperature. This color impression is based on experiments performed with so-called standard observers, as stated in the CIE norm 1931. Fig. 3.13 shows the commonly employed x,y-color space chart by CIE. Thus, a color temperature of, say 6000 K may be produced with a completely arbitrary spectral distribution, as for example just the three colors red, green and blue. The offered spectrum of lamps called "solar simulators" offer at least a continuous spectrum, but this does not necessarily follow very much a Planck distribution. Further, they feature some strong emission lines, what may be used for calibration of spectral devices. The rule is simple: The better accordance to Planck, the more expensive (compare "Oriel 96000" of Fig. 3.12).

Weighing all the implementation issues (diffuser, reflector, optics, lamp) and the cost against the importance of the sun noise measurement we came to the conclusion that still an easier solution should be found. On the rapidly growing and developing market of illumination may actually be found other interesting products. One of them that has been studied by our group is an electro-luminescent panel, having the advantage of being able to be cut in arbitrary forms. So the problem of drilling holes in a light source for passing the laser beams would be resolved. The price being low, we acquired two of the panels and first experiments concerning the Lambertian emissivity showed quite good results whereas the emitted radiance was found to be much too low.

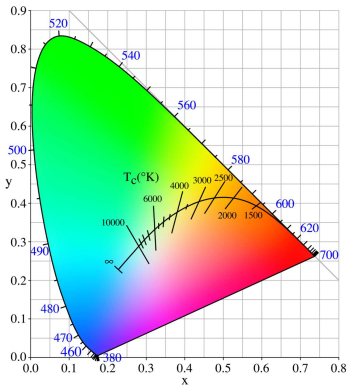

Figure 3.13.: The CIE x,y-color space

The most emerging product of the last years on the lighting market is for sure the LED, now available in all colors and white. White in this sense means real white with a spectral distribution covering all colors, and not the combination of three colors in order to make white-light impression on the human eye. Even though ready-made white LED arrays are available on the market (we acquired one for performing the flat fields for the Andor camera), none of them fulfilled the criteria of Lambert and the right size. A suitable LED for proper implementation in a grid was found to be the OSRAM Hyper TOPLED LWT67C, with a spatial emission very close to a Lambertian and a good white spectrum. One has to admit

Table 3.4.: Characteristics of OSRAM Hyper TOPLED LWT67C

Color temperature	[K]	5600
Chromaticity coordinate (CIE 1931)	[-]	x=0.33, y=0.33
Optical efficiency	[lm/W]	22
Luminous intensity	[mcd]	355 to 710
Luminous flux	[lm]	1.6
Technology	[-]	InGaN

that the spectrum (Fig. 3.14) does not really hold to that of the sun, but still this LED is a good compromise for all specifications. A grid of the OSRAM LEDs was designed,

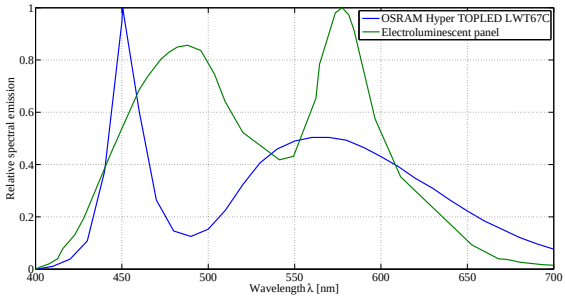

Figure 3.14.: Relative spectral emission of OSRAM LED and electroluminescent panel

approximating uniform illumination by regular spaced discrete light points. The dimensions

are such that it fills the whole field of view of T2L2J2; it further features two holes for the laser beams (see Fig. 3.15). The number of LEDs had to be limited to a "human level"[14] what finally resulted in a grid of 151 LEDs. The luminous flux provided by the ensemble of

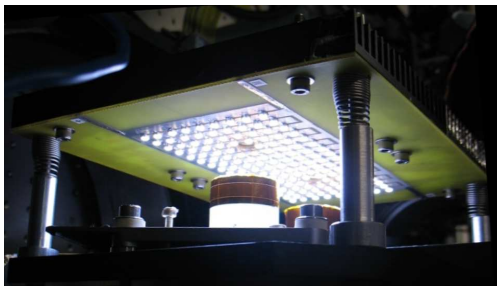

Figure 3.15.: The white LED grid for wide field sun noise simulation mounted in front of the T2L2J2 optics

LEDs is not able to cover the whole expected dynamic of sun noise irradiation (only up to a fourth). Hence the sun noise experiment is separated into two parts: The LED grid covers the spectral, Lambertian and wide field aspects, whereas the dynamic is covered by a simple green, continuous laser.

This continuous diode-based laser is, whenever necessary, mixed to the pulsed laser beam by the means of a cube separator in front of the moving-mirror beam distribution.

3.1.2.4. Reference timing and reference signals

Another central metrology keystone apart from the laser source is the timing reference. The equipment used for the test bench were some high-bandwidth photo detectors and a set of Dassault event timers. All of the devices described below were already in the hands of OCA; some are regular laser station experimentation equipment, others prototypes for T2L2 instrumentation; some minor hardware changes had to be performed.

Detectors In order to compare the T2L2J2 timings to a reference, the reference detection should largely outperform the T2L2J2 detection. For this purpose we used a 3 GHz bandwidth InGaAs avalanche photo diode for infrared light mounted in an electronic circuitry and featuring an ECL comparator. The system has been in use for years and proven a precision of about 2 ps and a good stability (see Section 3.1.3). In the test bed, it is used as the "departure" (in equivalence to a laser ranging ground station departure time tag) diode and mounted at the IR output of the laser frequency doubler (using the residual IR output). Its ECL output signal is directed to the first stage of the Dassault event timer.

Also in equivalence to a laser station's "return" signal, a return detector was employed in order to time the laser pulses reflected by the reference mirror of the mount that holds the T2L2J2 optics (described in 3.1.2.1). We employed the T2L2J2 non-linear detection prototype photo diode (K14) and circuitry (ProxNL); the laser pulses, reflected by the reference mirror are concentrated in a single-mode optical fiber; the fiber transports the flux to a 19" drawer (see Fig. 3.16) where are housed the ProxNL electronics, some other electronics for the K14-diode cooling Peltier control and some special optics. These optics, called

[14] At this place many thanks to Olivier Dupont for his nice soldering work.

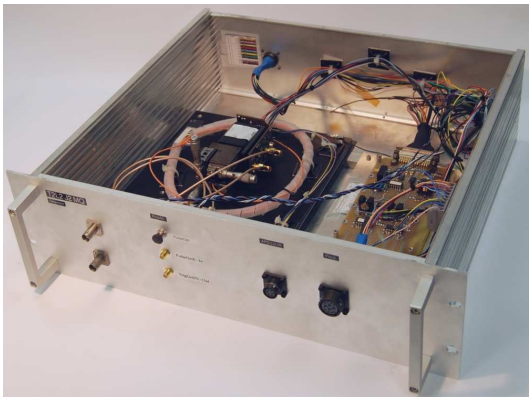

Figure 3.16.: The single-photon reference detection system based on the T2L2J2 prototype

OCTO-OCA have been specifically designed for the engineering model measurement campaign; they concentrate the fiber output into a narrow spot[15] on the diode. The K14 is mostly operated in single-photon mode giving a precision of about 22 ps and connected to the second stage of the Dassault event timer.

Event timer A double stage Dassault (today THALES) event timer is used for reference timing. The present Dassault, in possession of OCA since 1998, offers an augmented performance stage (with 2 ps precision), a second timing stage (with 5 ps precision) and an associated 200 MHz frequency synthesis. The device is piloted by some OCA-build electron-

Figure 3.17.: Event timer Dassault Det1

ics that communicates directly with the control PC (see 3.1.2.5) of the test bed.

Clocks During the diverse test campaigns, a whole set of different clocks or frequency standards with different performances was employed:

- A DORIS USO engineering model,

[15] Compare to the specifications deduced in Chapter 2.3: The laser beam has to be collimated into a spot of 160 µm diameter in order to feature best timing performance.

- a GPS disciplined Rubidium clock,
- a Hydrogen maser supplied by CNES,
- a Cesium beam frequency standard of OCA.

The DORIS clock, an engineering model of some previous CNES mission employing a DORIS USO, was mainly used to get an impression of this type's of clock behavior and to validate the concept of the DORIS measurement to be performed with the real Jason 2 DORIS space clock by T2L2J2 (see 3.2).

The Rubidium clock was mainly used for casual measurements, where the metrology is not affected by noise introduced by the clock. It is an ExacTime 6000 of Datum Inc. (today Symmetricom), a GPS disciplined Rubidium cell oscillator. In any case, most of the timing tests are common-clock experiments where both device under test and reference suffer the same noise; second-order noise processes are considered to be negligible.

For more sensitive measurements, as mid- and long-term stability measurements, both a maser and a Cs standard HP5061A came into play: The maser was supplied by CNES for the test campaign in their facilities: It is an EFOS-B of the Observatoire de Neuchatel, located in the Time/Frequency service of CNES, what is about 1 km apart from the lieu of the test campaign. The clock signal is transported via an optical fiber link produced by RFPA (type RFO 201000-DFB).

For the AIV campaign in the THALES Alenia Space facilities, OCA supplied one of the Cesium frequency standards HP 5071A that are operated in its time/frequency laboratory. The quality of these devices is summarized in Section 3.1.3.

Reference electronic signals In order to evaluate the T2L2J2 event timer alone, the flight instrument was even designed with an auxiliary ECL input (and with an output of its 100 MHz frequency synthesis) solely dedicated for electronic evaluation.
To supply an ECL signal to the T2L2J2 instrument and to the reference timing, an output offered by the National Instruments Data Acquisition Card (NiDAQ, see Section 3.1.2.5) was used; this card has the advantage of being controllable by the overall control PC (start, stop and frequency). In order to reduce the temporal jitter to a useful "metrological" level (for synchronous measurements), the signal is passed to a high-speed ECL D-type flipflop circuit driven by the 10 MHz reference clock signal of the master clock (see next paragraph). The output is thus re-synchronized to the reference clock signal.
The resulting temporal precision of this signal is expected to be better than the Dassault reference timer's stability given in Fig. 3.27 (i.e. a single shot precision of < 2 ps and a flicker floor of well below 100 fs for integration times around 1,000 seconds).

Frequency synthesis and signal distribution The synchronization electronics of the HighQ laser needs a 100 MHz signal; for this purpose we once again reused some prototype boards of T2L2J2. The event timer card features an own frequency synthesis at 100 MHz by a high quality Wentzel quartz oscillator (see Section 2.3.5.2) that is phase-locked to the 10 MHz reference signal. This analogue signal is split in two by a simple resistive T, and one part is fed to the HighQ synchronization control. The other part is fed back into the frequency synthesis circuitry, filtered and converted into a logical ECL signal and divided by ten in order to form another 10 MHz logical clock signal. This latter 10 MHz logical signal is used as a reference signal in a distribution card (called DD005) issued from a former

OCA-implemented T2L2 timer prototype (T2L2 ground simulation [21]). It consists in a whole set of flipflops, distribution and conversion circuits based on the ECL family 100 EL, and serves for distributing the clock signal for various other applications, in ECL or TTL levels; another feature is the re-synchronization of electronic pulses that was described in the previous section.

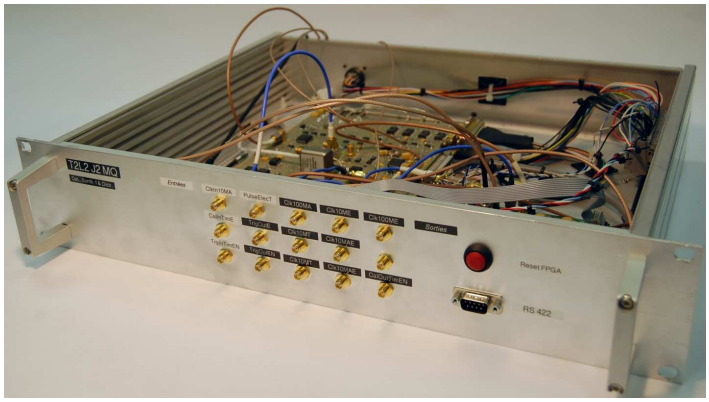

Figure 3.18.: A versatile frequency synthesis and signal distribution device based on T2L2 prototype boards

Together with the prototype timing card of T2L2J2 (in fact only the frequency synthesis functionality is used) the whole assembly represents a very useful and versatile signal and frequency conversion and distribution device. The photo (Fig. 3.18) shows this assembly how it is integrated into a 19" drawer.

For some other measurements, namely for asynchronous measurements (e.g. for the event timer's vernier examination) further a Marconi 2023 general purpose signal generator was employed: It provides a frequency synthesis from 9 kHz up to 1.2 GHz, based on an internal 10 MHz TCXO or an externally supplied 1 or 10 MHz signal.

3.1.2.5. Data acquisition and control of the test bed

One of the premises of the projected detailed flight model evaluation laid in the demand for high reliability of the whole test apparatus and its operation. Considering the extent of configurations and the number of tests that had to be performed, it was clear that only a highly automated test procedure could lead to the requested results.

A detailed description of the employed hardware and software would go far beyond the reach of this document (and is not part of the author's work), but for consistency, a short synopsis of the overall control electronics and informatics should anyhow be given.

Control PC The control PC assures the communication with all the control and measurement devices; for this purpose, it houses a set of electronic interface cards. One of the central used electronics cards is a National Instruments data acquisition (NI-Daq) card: It gathers the data of four thermocouples that are installed on the optical table of the test bed and it reads three analogue voltages of the three laser power monitoring photo diodes described in Section 3.1.2.2. The card accepts a 10 MHz reference signal as an external clock. The NI-Daq further offers some TTL-outputs whereof one is used for the generation of a reference timing signal (in phase with the external reference), as described above (Section 3.1.2.4). The other

is used for the piloting of the two pulse pickers, as will be explained below. Another signal is used for commanding the mechanical shutter between laser source and the beam distribution optics.

Four RS 422 ports permit to communicate with the Newport power meter 1935-C described in 3.1.2.2, with the Dassault event timers, with the HighQ Laser control electronics and with the T2L2J2 instrument.

A fast digitization (1 GHz bandwidth) card of Acquiris represents a computerized oscilloscope and is used for detailed analysis of the laser pulse profiles, especially for analysis and monitoring of the extinction ratio through the pulse pickers. It is connected to a secondary (pulsed) output of the departure photo diode that was described in Section 3.1.2.4.

The Andor camera of the reference energy monitoring assembly is controlled and read out by a proprietary card of Andor.

A central keystone of the control of any locomotive device in the test bed is the Newport XPS unit. The Newport XPS is in fact a PC apart (TCP/IP communication with the control PC) that controls the diverse motorized stages via dedicated control and amplification cards. The test bed uses seven Newport motorized stages (depicted in Fig. 3.19): The laser power controller ($\lambda/2$ waveplate-Glan polarizer assembly, Section 3.1.2.1) uses a PR-50 small rotation stage. The displaceable beam device (beam distribution) uses three small LTA series precision motorized actuators; one moves the $2 \times 90°$-mirror assembly (Fig. 3.6), the second moves the corresponding polarizer (that has to move two times faster than the mirror assembly) and the third permits to insert a beam blocker. The beam distribution unit itself is

Figure 3.19.: The Newport XPS motion controller pilots four types (and a number of seven) of different motorized stages: LTA motorized actuator, PR-50 small rotation stage, IMS linear stage and RV high precision rotation stage (from top left to bottom right, different scales). Photographs © Newport Corporation, USA

mounted on a movable sledge in order to swap between T2L2J2 laser exposition and energy reference measurement: This is performed with a big Newport IMS translation stage. The T2L2J2 optics are finally mounted on a two axis gimbal (heritage of MéO): This mount is composed of two high precision Newport RV rotation stages.

Apart from piloting the different devices, the control PC gathers all their corresponding housekeeping data.

Control and analysis software BT2Studio The software BT2Studio was prepared by OCA and the software company Phusipus Integration especially for the T2L2J2 metrological eval-

uation. It permits not only to read and control the various employed instruments described just above, but also offers automated measurement procedures (like geometry and energy variation and regular energy calibration) that greatly enhance the effectiveness of the tests. For this purpose it proposes different measurement families.

As a third feature the software performs real-time analysis (like the comparison of dates returned by the T2L2J2 and reference Dassault event timers) in order to facilitate the operation and control of the whole test setup and the experiments.

Pulse picker control In order to provoke the transition of the pulse pickers' birefringent crystals from one state to the other at the right time, a reliable phase relation between the laser pulses and the piloting signal has to be established.

In the test bed configuration (Fig. 3.20), a clock supplies a 10 MHz reference signal, what is fed to the frequency synthesis and signal distribution unit described in Section 3.1.2.5, p. 57. This unit produces a 100 MHz signal out of it which is fed to the HighQ laser synchronization unit. The latter receives equally a 100 MHz signal from an internal monitoring photodiode of the HighQ laser cavity, whose intrinsic repetition rate is governed by its cavity length. The synchronization unit performs a phase comparison of the two signals and feeds the error signal back to the cavity; the cavity length is then adjusted, by the means of a combined linear motorized stage (coarse displacements) and a piezo stage (fine). By this means, the laser pulses are locked to the external reference clock phase. The distribution unit further

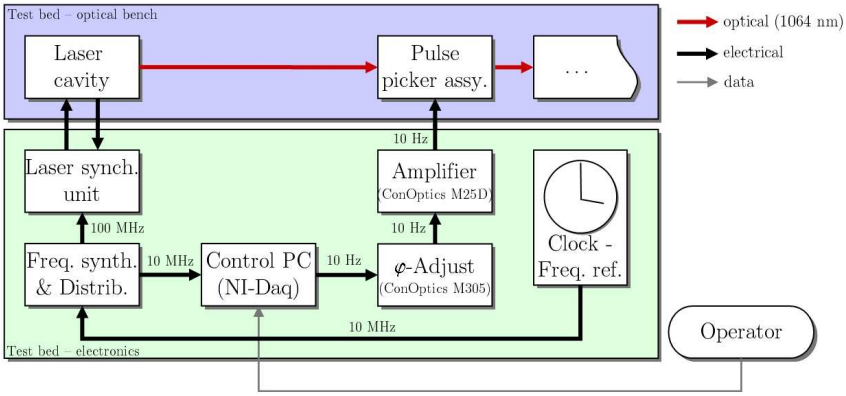

Figure 3.20.: Synopsis of the pulse picker control scheme

provides a 10 MHz signal that is fed to the NI-Daq card of the control PC (see above). This one provides a TTL signal in phase with this reference, of a rate chosen by the operator (of 10 Hz, for instance). This TTL signal is given to a phase-adjusting unit (equally supplied by ConOptics[16]), in order to properly select the laser pulses. The phase delayed signal is then given to the ConOptics M25D that amplifies the some nanosecond short electronic signal to some hundred volts (drive voltage) in order to provoke the right birefringence in the crystals. Both the drive voltage and the bias voltage (to adjust some zero point) may be adjusted manually.

[16]The ConOptics M305 usually serves both the purpose of downdividing the laser reference signal for the production of a manually chosen pulse picking rate and the phase adjustment of the control signal. In the test bed configuration, we just use the phase functionality, since the other may better be automated in the control PC.

In a stable temperature environment (as it was the case for the test campaigns), the pulse picker assembly showed a very good stability without a frequent adjustment of the bias voltage.

3.1.2.6. General architecture

Optical layout This section highlights how the different parts of the test setup described above are assembled together. Fig. 3.21 depicts the general layout: All optical parts are installed on a 1 × 2 m optical table (typical steel plates with honeycomb reinforcing). The HighQ laser cavity emits a 100 MHz pulse train of IR pulses; the average power output is monitored, selectively by a Newport 818-P detector or by a low-bandwidth photodiode (see Section 3.1.2.2). After passing a mirror, the linear polarization is anew redressed in order

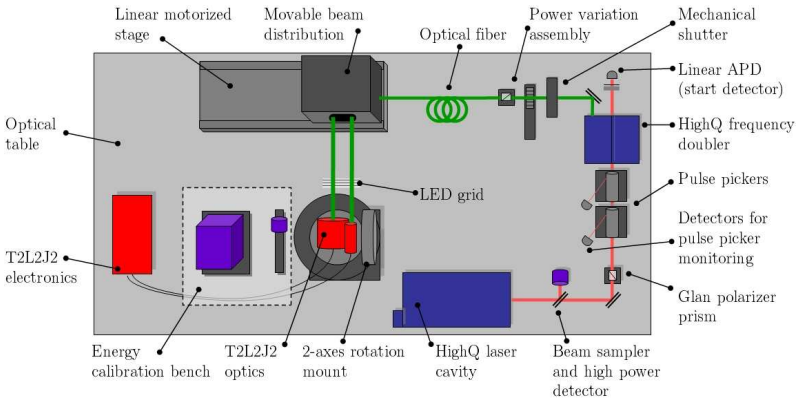

Figure 3.21.: Overview of the main parts of the optical part of the test bed

to be optimally configured for the pulse picker assembly. The pulse pickers downselect the laser rate to an adjusted value. The dismissed pulses are rejected by a Glan-Thompson polarizer prism (inside the two pulse pickers) and fall onto two additional power monitoring photodiodes, what permits a good surveillance of the respective extinction ratio. After the pulse pickers, the laser beam is frequency-doubled by the second harmonic generator (SHG), equally supplied by HighQ laser. A fraction of the IR pulses, that is not doubled due to the limited effectiveness of the process, is guided onto a fast APD (start detector) that serves for the reference detection (see Section 3.1.2.4).

The green beam passes through the $\lambda/2$-waveplate-Glan-polarizer assembly that serves for power adjustment and is finally concentrated into a single-mode polarization maintaining fiber. This fiber transports the flux into the beam distribution unit (see Section 3.1.2.1) where it is again expanded, collimated and divided into two beams, whereof one is displaceable with respect to the other. These two beams each pass once again through a waveplate-polarizer in order to perfectly redress the linear polarization and are then transmitted onto the two optics of the T2L2J2 instrument. The optics subsystem is installed on a two-axis mount permitting a rotation around the vertical and the horizontal (perpendicular to the laser beam) axis; by this means, all possible incidence angles with respect to the optics' lines of sight may be scanned. In order to simulate simultaneous background noise, a LED grid may be mounted in front of the T2L2J2 optics.
The energy calibration bench is located next to the two-axes mount: The whole laser beam

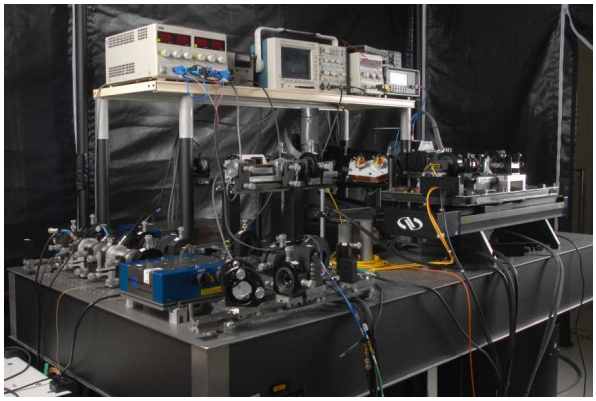

Figure 3.22.: The optical part of the test bed implemented at CNES, Toulouse

distribution system may be displaced in front of the two detectors, a continuous power detector and a CCD camera for beam profile analysis.
The T2L2J2 electronics unit is also located on the optical table and connected to the optical subsystem by its harness.

Of course, this is just a simplified synopsis: The whole complexity is well pictured in the Photo of Fig. 3.22.

Electronics infrastructure The active devices of the optical bench, such as measurement devices and mechanics, feature an electronic counterpart in the form of some computer board as pointed out on page 58. The optical table was thus complemented by a set of six 19" racks containing all associated control and additional devices.

It should be noted that for the operation of the T2L2J2 flight instrument a separate EGSE (electronic ground support equipment) was supplied by EREMS, consisting of an appropriate power supply for the electronics unit, some signal distribution unit, the CNES supplied DORIS USO engineering model and a PC with a MIL Std 1553 bus communication interface. This permitted to control the T2L2J2 instrument settings from the EGSE computer, while the produced data could (in parallel to the EGSE) directly be retrieved towards the test bed PC, via its RS422 port.

Temperature evaluation: Thermal chamber Section 3.1.1 stated the need for an evaluation of the influence of the temperature. Since it seemed too precarious to heat and cool both optics and electronics subsystems, it was decided to perform the respective tests only on the electronics unit. CNES provided a large thermal chamber for cooling and heating (it can be seen on Fig. 3.23, the big blue box to the right of the tent).

3.1.2.7. Test bed implementation at CNES

One central requirement on the metrological test campaign on the T2L2J2 flight model had been identified by the CNES product assurance: Optical tests would have to be performed in a clean room environment (class 100) in order to protect the T2L2J2 optics from an deterioration due to dust deposit. Different solutions had been studied: An installation of a clean-room environment in the OCA facilities at Grasse or Calern, a campaign in the

premises of EREMS or a campaign at CNES in Toulouse. The second option had quickly to be discarded for not being feasible in terms of available space. The option of performing the tests at OCA was, after several iterations, also abandoned. CNES proposed a class 100,000 clean room (Pronaos hall, previously used for the integration and test of high-atmosphere balloons) with a second structure (Fig. 3.23) enclosed in order to produce the requested class 100 cleanliness. This structure consisted in a 3×3 m blowing wall that supplied the needed filtered class 100 air in a horizontal laminar flux. A tent was attached to this wall in order to produce a slight excess pressure in the inside where the optical bench was set up.

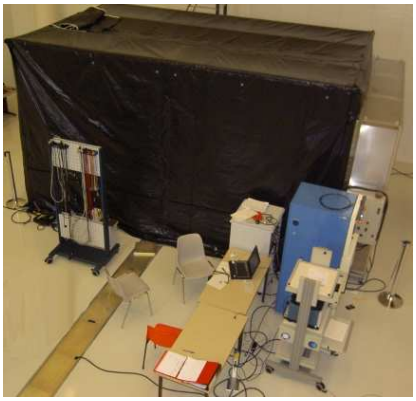

Figure 3.23.: View on the class 100 tent (blowing wall to the right) in the Pronaos class 100,000 hall

The planned execution of the metrological tests in the CNES facilities had of course some ponderous repercussions on their preparation: The test bed was first completely assembled in the OCA optical laboratory at Calern. It was troubleshooted and tested with the engineering model MI of the electronics subsystem SSE of T2L2J2 (mainly for the electronics infrastructure).
After successful operation it was disassembled, boxed and shipped to Toulouse in order to be reassembled anew. The first metrological test campaign at CNES finally started on March 13, 2007 and lasted for two months.

The obtained results of this main calibration and performance determination campaign are given in the Chapters 3.2 and 3.3. After the successful completion of this campaign, the test bed was then shipped to THALES Alenia Space in Cannes, and again set up with a slightly different architecture. This architecture is described in the next section.

3.1.2.8. Modified architecture for AIV measurements at Cannes

As mentioned in the first section of this chapter (3.1.1), a second campaign was planned to be performed during integration of the different scientific payloads on the Jason 2 satellite. By this means, the T2L2J2 instrument could be tested in the real satellite environment, notably in conjunction with the clock signal of the real DORIS oscillator and the definite satellite power supply.

Evidently, the operational constraints were not the same as for the stand-alone tests performed previously in the CNES clean room. A free exposure of the laser radiation in the giant integration hall of THALES Alenia Space in Cannes with several satellites at once being integrated, was not possible due to eye safety concerns. A workaround was found in

the propagation of the laser radiation in single-mode polarization maintaining fibers from the laser bench directly on the T2L2J2 optics. Since an attitude measurement was no more necessary (this part of the calibration had been completed), this concept was realized.

The laser setup was thus slightly modified (and simplified) in order to fit on a smaller optical table; motorized parts like the moving sledge with parallel displaceable beam distribution and the two-awes mount were no longer necessary. Fig. 3.24 shows the setup: From the laser cavity until the power variation it is similar to the one of the CNES campaign: The laser beam coming from the HighQ cavity passes through the two pulse pickers and the frequency doubler. It then goes through the mechanical shutter and the power control

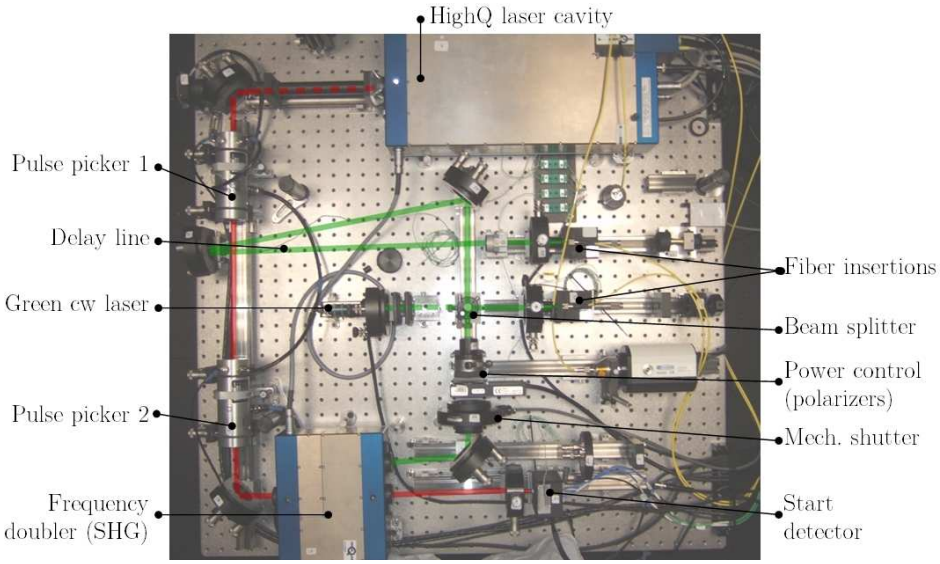

Figure 3.24.: The modified architecture of the test bed for use during the Jason 2 AIV process

(polarizer assembly). A cube beam splitter then separates the green beam into two beams (center of the photo): One is directed to the right side and concentrated into one fiber; the other travels straight, through a small delay line in order to take account of the different lengths of the two fibers[17], and is then equally concentrated into the second fiber. All the laser bench and the electronics were housed in a specially furnished room next to the satellite integration hall. The fiber, of a length of 30 m, transports the laser flux from the bench to the T2L2J2 optics already installed on the satellite. SESO had designed two small adaptation caps, consisting of a fiber connector and a lens, that produced two narrow parallel beams radiating in the optics of the T2L2J2 SSO.

The T2L2J2 electronics unit SSE, equally integrated in the satellite, was accessible, from a control point of view, only via the satellite computer. This was under the control of the THALES Alenia Space AIV personnel and strict test procedures had to be established prior to operation. The data produced by T2L2J2 could nevertheless directly be downloaded to the test bed control PC. Fig. 3.25 shows a photo of Jason 2 during integration in the integration hall of THALES Alenia Space.

[17] Optical fiber manufacturers typically do not guarantee the exact length of their fibers to less than some (tens of) centimeters.

Figure 3.25.: Jason 2 during integration in the THALES Alenia Space satellite integration clean hall: The LRA pyramid may be discerned in the center, left to the big Poseidon antenna. The T2L2J2 optics are situated just left of the LRA.

3.1.2.9. The evaluation of the LRA

Initially, an additional goal of the test series on the flight instrument was also the characterization of the retroreflector LRA, that is supplied by JPL as a part of the altimetry mission. As we will see in the Error Budget chapter (Section 5.1.4.2), due to its composition of discrete corner cubes, the LRA disperses incoming short laser pulses into a set of superimposed pulses. These patterns interact differently with each type of return detector of the laser stations.

Further, due to the distinct design of T2L2J2 and LRA, the detection and reflection reference point are not the same.

In order to assess these two aspects in detail, and in conjunction with attitude variation it was desirable to perform the respective tests in common. Though, three points conflict with this approach:

- First, in order to characterize the LRA properly, its entirety or at least a certain number of its corner cubes have to be illuminated with laser light. In order to produce a beam of this scale, a large parabolic mirror (or an off-axis parabola) has to be employed, as depicted in Fig. 3.4, p. 45. Ready-fabricated mirrors of the right dimensions (diameter and focal length) are rare on the market (if available at all) and extremely expensive. OCA thus decided to fabricate one such mirror itself with the constraint that it would not be ready at the right time for the T2L2J2 flight model test campaign.

- Second, the laser power constraints implicate in any event an optical layout as it finally had been implemented in the test bed (see Section 3.1.2.1).

- Third, at the time of the detailed study and implementation of the test bed, very few information about the mechanical and optical layout of the LRA could be obtained

from JPL or ITE Inc. (the manufacturer). Effort to obtain something like a mockup or an engineering model had been even less fruitful.

These points led to the conclusion that the tests on the T2L2J2 instrument had to be performed without the LRA in the first instance.
In the meantime, the parabolic mirror is completed and the respective mechanics are in preparation. As a next step, a mockup of the LRA, or a part of it, should be designed. For this purpose we identified some corner cubes that comply with most of the optical parameters of the ITE cubes. The LRA, installed on a two-axes mount like the T2L2J2 optics, may then be characterized with a similar setup as depicted in Fig. 3.4: The laser emits laser pulses and a part is timed by a start detector; the laser pulses are transmitted on the LRA and the return is detected by some other diode. By this means, the temporal position of each and any pulse part may be determined, depending on the attitude angles.
These tests shall be performed during the course of the T2L2J2 operation.

3.1.3. Performance of the test bed

This section summarizes some of the most important features that characterize the performance of the different subsystems that made up the two versions of the test bed; in order to properly determine the performance of the T2L2J2 flight model and to calibrate it on a sufficient level, the test bed should feature better or at least similar performance as the instrument.

3.1.3.1. Laser system

Referring to the first section of this chapter (3.1.1), the laser pulses generated by the laser system are defined by following quantities: The wavelength λ, the pulse length, their power and the polarization.

For what concerns the wavelength of the laser system there is not much doubt that it is really 532.1 nm as specified since the technology is based on Vanadate (Nd:YO_4) which fixes λ. The polarization is equally well mastered in the test bed: Before being transmitted into the T2L2J2 optics, both beam pass through a polarizing beam splitter that typically features a rejection of more than 1:1,000.

A verification of the laser pulse length turned out to be somewhat more troublesome: HighQ Laser had specified a pulse FWHM of 18 ps (at 1,064 nm); HighQ had later repeated this measurement with a commercial autocorrelator of APE (Berlin). On our side, several attempts to measure the pulse length during the CNES test campaign had failed for various reasons, be it some misalignment of the non-linear T2L2 prototype detection system or some trouble with a high-speed oscilloscope supplied by CNES. It was not until January 2008, that we could really verify the laser pulse width with a combination of a New Focus 1004 fast photodiode and a LeCroy WaveExpert 9000 with a 50 GHz sampling head.

Concerning the laser pulse energy, it is rather difficult to measure the energy of single pulses, except for a system like T2L2J2 itself. Lacking such a system, we have to rely on the T2L2J2 instrument: Section 5.1.2 states a precision of less than 6% for the linear pulse measurement - this includes both the contribution of laser/pulse picker system and the T2L2J2 linear detection. The energy measurement of the test bed informs us about the longer-term energy stability. Due to the low bandwidth detector (818-SL) and the mean power integration performed at rates of 1 MHz, all pulse to pulse variations (possibly

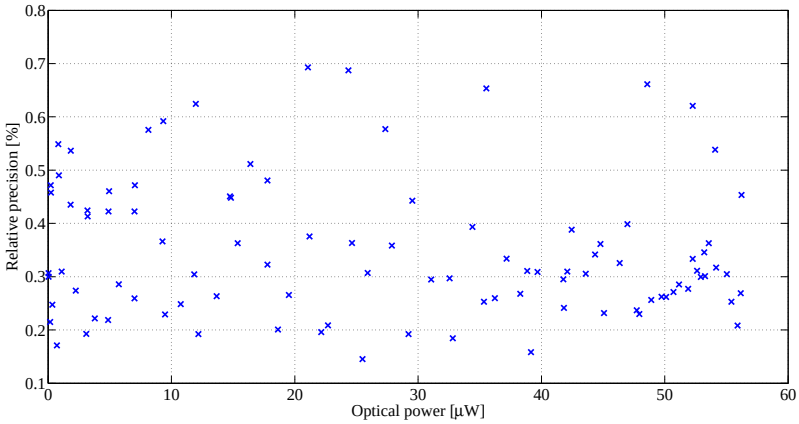

Figure 3.26.: Relative dispersion of the power measurement performed with the 818-SL detector on the laser beam

originating in the pulse picker system) are already averaged out. Nevertheless, Fig. 3.26 gives an indication of the quality of the energy stability: For the whole range of measured power levels, the relative precision is below 0.7%.

3.1.3.2. Timing precision and stability

Reference event timer The Dassault Electronique timer represents a reference in commercially available event timers. It has an excellent precision, a very small non-linearity and a good stability. For the test bench, two timer stages were used, together with the appropriate frequency synthesis; one of the two timer stages is an enhanced version, attaining higher precision.
The single shot r.m.s. of the two Dassault timer stages are of 2 and 5 ps, respectively. The specification of the Dassault timer is given in Fig. 3.27.

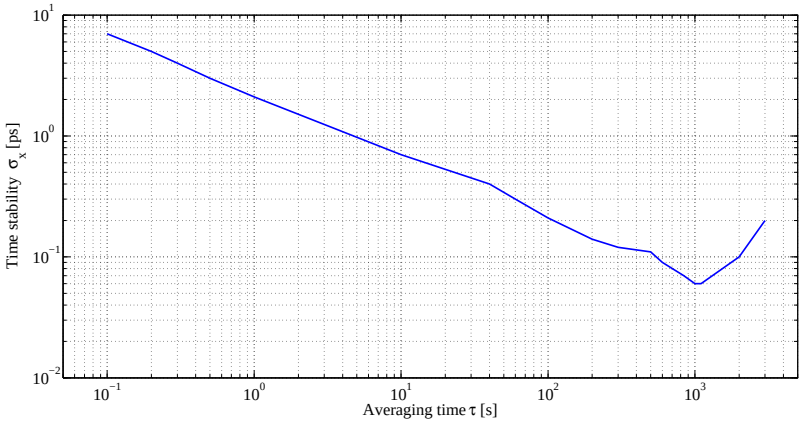

Figure 3.27.: Time stability of Dassault Electronique event timer

Frequency standards To assess the quality of the utilized frequency standards with respect to a reference, following experiment was performed (Fig. 3.28): A phase comparison is carried

out by referencing the event timer to one of the clocks. The other clock provides its 10 MHz signal to a flipflop circuit that is reset at a low rate (usable by the timer). The reset signal

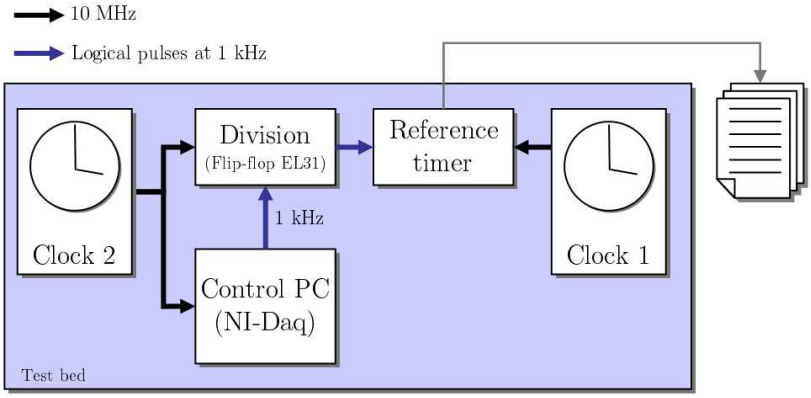

Figure 3.28.: Measurement scheme to compare different clocks via their phase evolution

comes from the NI-Daq card in the control PC that is as well running on the second clock signal. By this means the 10 MHz clock signal is divided to a low rate pulse train, in this case at 1 kHz, which is then timed by the Dassault.

Finally, we calculate the time stability from the phase data, represented in Fig. 3.29. Further, data of the H-Maser EFOS-B is given which has been used in the CNES test campaign (from final acceptance test at Observatoire de Neuchatel); the performance of the RFO optical fiber link transporting the Maser signal from the CNES time/frequency lab to the test bed had previously been assessed by CNES in the framework of the PHARAO development since it is an integral part of its performance verification system [38]. The fiber

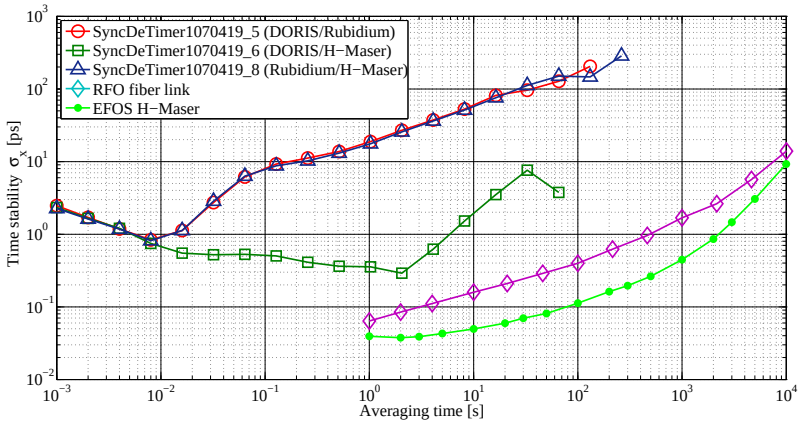

Figure 3.29.: The different clocks used in the test bed compared to another

link slightly deteriorates the Maser performance but this system combination still represents a good reference as compared to the other clocks. During the test campaign, the Maser further featured a fractional frequency offset of less than 10^{-11} (determined by comparison to the CNES time/frequency clock ensemble) and a fractional frequency drift of less than 10^{-14} per day [39].

Start detection The quality of the start detection is of vital interest for all optical measurements with T2L2J2 since all timings are referenced to this start epoch. The setup for its stability determination is pictured in Fig. 3.30, it is identical to the one used for the T2L2J2 operation: The HighQ laser cavity is synchronized to the clock frequency and thus emits synchronous laser pulses, which are detected by the start detector and finally timed by the reference timer that is also slaved to the clock signal. In fact, the overall outcome of this

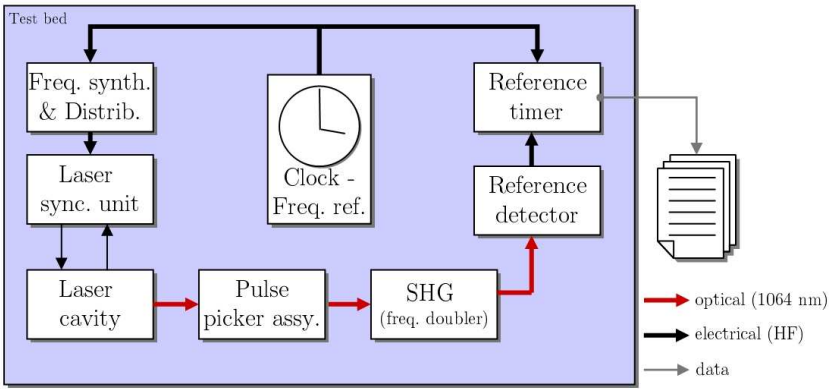

Figure 3.30.: Test setup for the determination of the start detection stability

experiment includes a further factor, despite the detector stability: The stability of the laser synchronization.

The influence of a possible laser pulse energy variation due to the laser itself or rather the pulse picker assembly is suppressed by driving the detector in a saturated mode and thus making its response rather independent from energy variations. The experiment revealed a

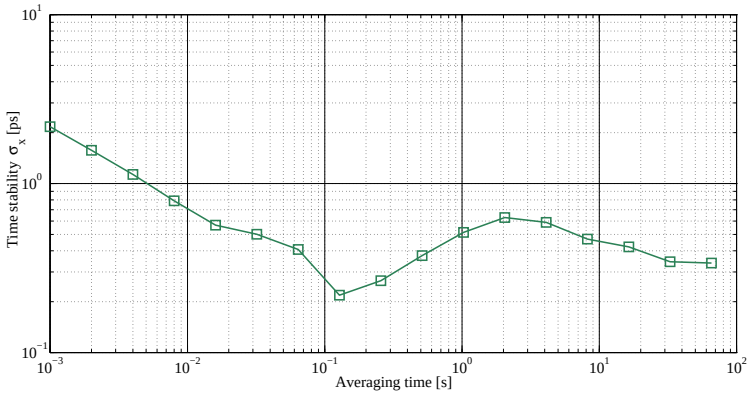

Figure 3.31.: Time stability of start detection

performance of 2.2 ps precision, with a phase flicker floor of 220 fs (Fig. 3.31). This floor and the subsequent increase in stability is probably imputable to the HighQ laser synchronization.

Reference return detection The reference return detection (described in Section 3.1.2.4, see Fig. 3.16) serves as a performance reference for T2L2J2 non-linear detection channel.
Its proper timing performance has been evaluated at different occasions during the test campaigns.

The experiment synopsis is depicted in Fig. 3.32: The laser setup emits pulses on both the start detector (see above) and the T2L2J2 prototype-based non-linear detection. The detectors are connected to the two timer stages of the reference timer Dassault which is referenced to a clock. The precision of the return detection is then determined by the

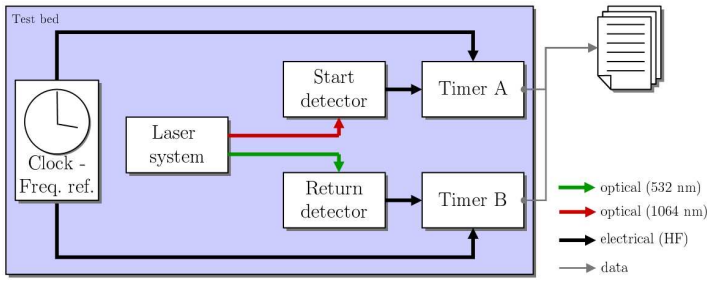

Figure 3.32.: Experiment setup for the return detector qualification

difference of the epochs on timers A and B.

The measurements shown here were performed at a laser rate of 1 kHz, for different laser levels. The non-linear detection prototype setup features a precision of 22 ps in single-photon mode as shown in Fig. 3.33. Its precision at higher photon levels is well below 6 ps

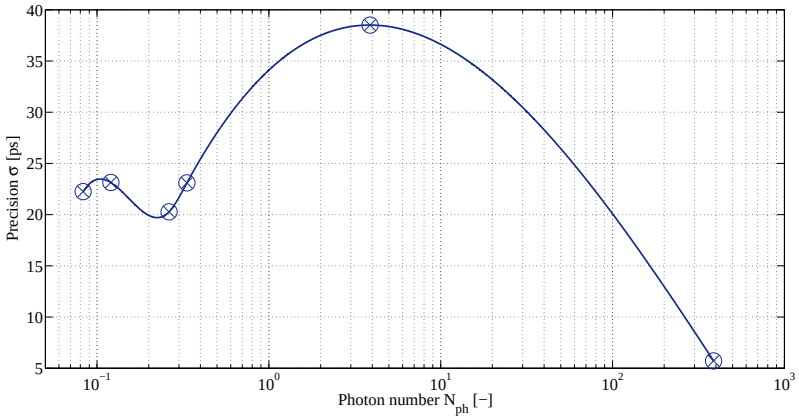

Figure 3.33.: Precision of the non-linear return detector as a function of photon number N_{ph}

(probably around 2 ps); in the setup the measurement is limited by the two timer stages and the start detection that alone account for 5.7 ps. The measured points in the graph are connected by a spline to highlight the typical precision in single to few-photon operation. In this condition, the detection probability follows Poisson statistics and is determined with $P_{\mathrm{det}} = 1 - \exp(-\rho\ N_{\mathrm{ph}})$, with ρ being the quantum efficiency of the detector and N_{ph} the actual mean photon number (as in the graphic). The maximum value of precision is then attained when the probability of two-photo-electron events increases (for some photons, or $P_{\mathrm{det}} \to 1$).

Fig. 3.34 shows the time stability of two acquisitions in single and multi photon mode. Both sets have been measured at 1 kHz, but the effective measurement frequency of the single-photon acquisition is considerably degraded due to the detection probability (here $P_{\mathrm{det}} \approx 8\%$), entailing a τ_0 of 12.5 ms instead of 1 ms.

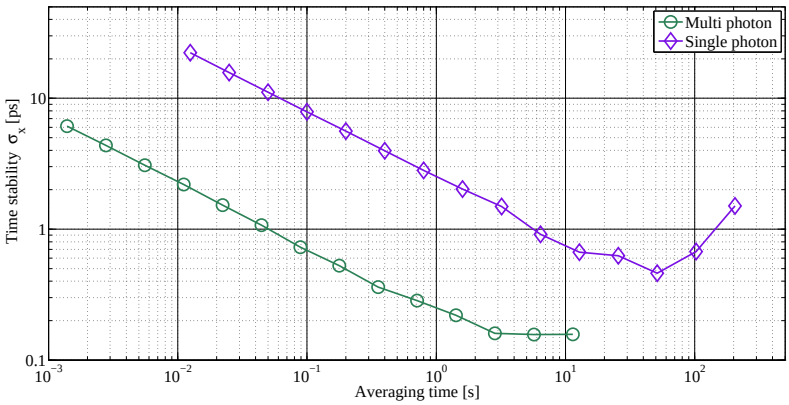

Figure 3.34.: Time stability of two acquisitions on the reference non-linear return detector

The electronic architecture of this prototype-based detection system is basically the same as of the flight model except for the power supply which is of linear type here as compared to the T2L2J2 instrument which uses a switched-mode supply. The optical architecture, which focuses the optical fiber output on the K14 APD, has been designed by OCA for the tests on the MI (engineering model) to replace the second part of the non-linear optical subsystem OCTO (since it has not been available for these tests). Hence, the measurements on this prototype may serve as a reference for a comparison for the T2L2J2 flight model non-linear channel detection.

This detection system served further for the verification of the overall stability of the optical setup of the test bed: As described on page 56, the reference mirror mounted next to the T2L2J2 optics (on the two-axes mount, p. 48) may reflect the laser radiation backwards where it is concentrated in an optical fiber and thus transported to the return detector.

3.1.4. Conclusion test bed development

3.1.4.1. From development to operation

The development of the test bed represented a substantial activity in the RDM team at OCA lasting over one year. It started with a vast requirements study, passing through several iterations. This was followed by an extensive industry search for various components, in particular the laser system. The acquisition of the material was not always easy due to budgetary bottlenecks[18] and exceeded delay times. The whole test bed development process was accompanied by countless designs and implementations of mechanics. Hereby we should thank our concerned technicians, in particular Aurélien Dréan who spent numerous hours with CATIA, and the Calern mechanics factory people Richard Brunet, Xavier Martin and Christian Munier who always did an effective and high quality job.

A first, partial version of the test bed had been implemented in July 2006 for the evaluation of the engineering model[19] (MI) of the T2L2J2 instrument. At the end of the year 2006, the test bed had finally being implemented in its "CNES-version" (Section 3.1.2.7) in the Calern

[18] These were in particular due to the disappointing organization of the CNRS/INSU administration (this has to be stated at least once!) with respect to the budget flow from CNES to our lab.

[19] This activity is not described in the present document.

optical lab. End of February 2007 it had then been disassembled and moved to Toulouse, for the execution of the flight model stand-alone tests.

After completion of the tests at CNES, the needed subsystems of the test bed were shipped to THALES Alenia Space for the implementation of the AIV version (Section 3.1.2.8). This campaign was then performed during June and July 2007.

The measurements employing the test bed on the T2L2J2 instrument had been performed by Dominique Albanese, Philippe Guillemot (of CNES), Franck Para, Etienne Samain and myself, in different compositions.

Generally, the test bench was a high-fidelity metrology system in its own, representing nearly all aspects of an extremely well-equipped satellite laser ranging station, but on a lab scale. It performed compliant to the requirements and expectations producing large amounts of high-quality data for the determination of the T2L2J2 performance and high-fidelity calibration (Chapters 3.2 and 3.3).

3.1.4.2. Performance

The performance of the test bed has been highlighted (for the most important parts) in Section 3.1.3. Generally speaking, the test bed has been developed in order to determine the performance of the T2L2J2 flight model. For this reason, the quality of the metrology characteristics had to be better than the specifications of the T2L2J2 instruments.

This has been the case for all systems such as the clocks, the start detection and the laser power monitoring. However, as we will see in the Performance chapter (3.2), in some points, the T2L2J2 instrument eventually outperforms the test bed equipment (as for the timer). In this special case, the measurement is limited by the test equipment; this does not represent a weak point in the test apparatus, but rather an extraordinary achievement in the design of the T2L2J2 instrument.

3.2. Performance of the T2L2J2 instrument flight model

This chapter focuses on the metrology performance of the T2L2J2 flight instrument. These have been determined during the two main test campaigns at CNES and THALES Alenia Space.
The analysis of the derived test data has been carried out by Etienne Samain and the author; Etienne Samain mainly concentrated on the evaluation of the T2L2 event timer data whereas the analysis of the optical experimental data is covered by the present thesis work. The following chapter subsequently treats the T2L2J2 timer, the optical subsystem (SSO) and the DORIS USO aboard Jason 2.
As this document is not intended to be a technical report, only the most important quantities that have been determined shall be highlighted. A full description is given in the documents [40] and [41].

3.2.1. The T2L2J2 event timer

The part that drives the performance of the event timer evidently is the fine timing stage; once the counter (FPGA) does correctly its job, it is not of concern for the precision of the measurement.
The timer's quality thus depends on two main components: The frequency synthesis that provides the reference signals, and the vernier. The performance of the frequency synthesis may be determined separately what is addressed in the following section. The quality of the vernier reference signals that are derived from the frequency synthesis is addressed in Section 3.3.1 in the calibration chapter.
The performance of the vernier, though, may only be assessed taking the timer as a whole, what follows in Section 3.2.1.2. The quality of the internally generated calibration signals for the determination of the residual non-linearity of the vernier reference signals is investigated in Section 3.2.1.3.

3.2.1.1. Frequency synthesis

For the determination of the timer's frequency synthesis quality, the instrument was deliberately provided with a test output of the reference signal. For the test purposes, the phase of the generated 100 MHz signal (issued from the AR Electronique local oscillator, then transformed into some ECL logical signal) is compared to the phase of the underlying reference clock signal. Following tests were performed:

- Temperature sensitivity
- Influence of the reference oscillator noise
- Functioning with respect to the frequency of the reference clock
- Dependence on the clock signal power

Test setup The experiment is carried out in a common clock configuration as depicted in Fig. 3.35. A clock (or frequency reference) provides a 10 MHz reference signal for the T2L2J2 instrument and the reference event timer, as well as for the control PC. The 100 MHz (logical) signal coming from the T2L2J2 frequency synthesis is divided by some ECL

flipflop component that is reset at a rate adjusted by the control PC's NI-Daq card, usually at 100 or 1,000 Hz. The outgoing signal is then in phase with the 100 MHz of T2L2J2, but at a user-defined rate; the noise of the ECL component may be regarded as negligible as compared to the frequency synthesis'. The phase comparison is then performed by the

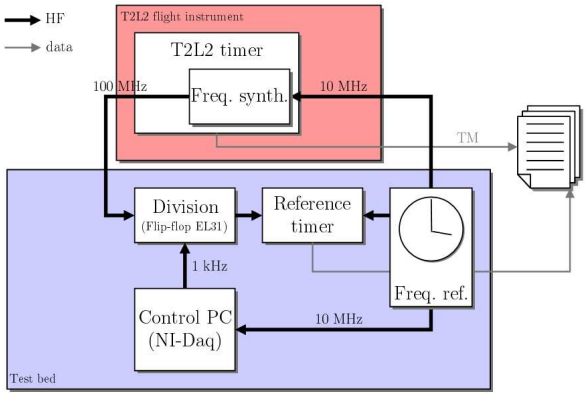

Figure 3.35.: Measurement scheme for the determination of the frequency synthesis' performances

reference event timer, in synchronous mode, by timing the signals coming from the flipflop. For all measurements, the T2L2J2 electronics unit (SSE) is placed in the thermal chamber and operated at some temperature levels. For the determination of the influence of the reference's noise, different clocks are employed as a reference: An H-Maser, supplied by CNES, a small Rubidium clock, a Marconi signal generator and the DORIS USO engineering model (see Section 3.1.2.4). The Marconi signal generator was also used for determining the possible input frequency range. For the influence of different signal powers, some attenuators were used.

Results The temperature sensitivity of the frequency synthesis's phase is of about 0.5 ps/°C. Fig. 3.36 shows the time stability of the phase comparison between the T2L2J2 frequency synthesis and the H-Maser for some temperatures. The stability curves are basically the

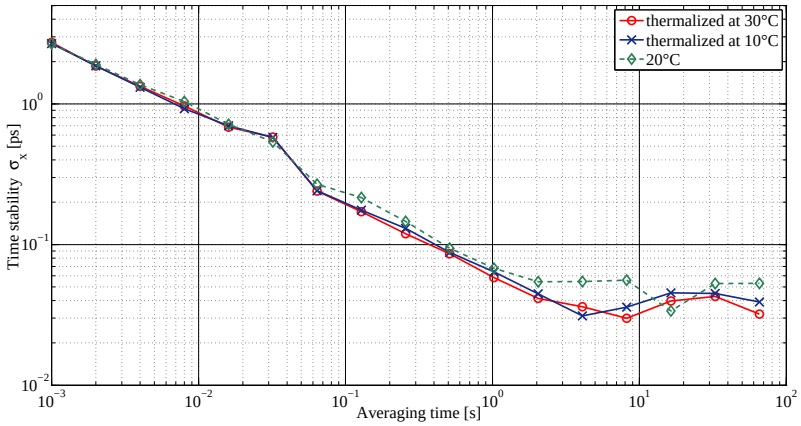

Figure 3.36.: Time stability of the T2L2J2 frequency synthesis phase compared to reference phase

same (the plot of 20°C corresponds to a dataset of a somewhat less thermalized experiment)

what indicates that there is no noise evolution with temperature (at least in the range of 10° to 30°).

Another interesting exercise is to find out to what extent the frequency synthesis, i.e. the local oscillator and the phase-lock-loop (PLL) are disturbed by noise introduced by the reference frequency. Since first-order noise processes cancel out in the common-clock scheme of the current experiment, only non-linear noise processes appear in the phase comparison. Fig. 3.37 shows such a comparison between the different clocks of the test bed. We find that

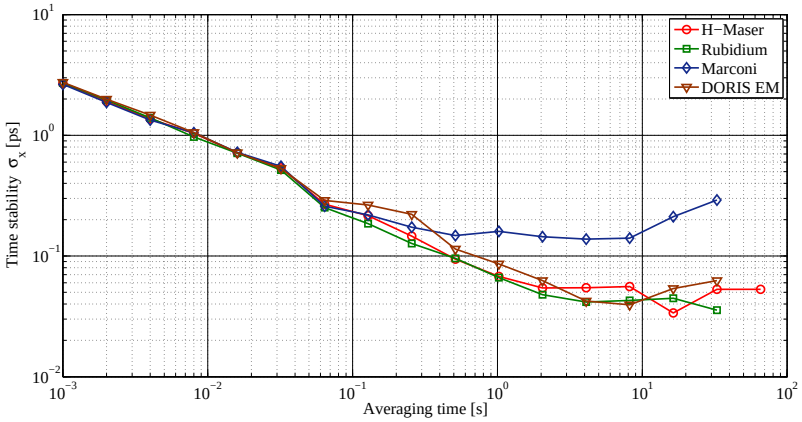

Figure 3.37.: Influence of different clocks and their noise properties on the frequency synthesis

for all clocks, except the Marconi signal generator (known to be of modest noise characteristics), the time stability looks very similar; this is an indication that the frequency synthesis is not very susceptible to the applied noise processes. In particular, the DORIS oscillator seems not to alter the synthesis' performance, what is of primordial importance.

The frequency range accepted by the synthesis was determined to be 150 Hz, what complies with specifications. The needed input signal amplitude is also complying to specifications.

Discussion The time stability of the T2L2J2 frequency synthesis reaches its phase flicker floor on the range of some tens of femtoseconds, relatively independent of the applied frequency reference or the operating temperature. This level represents also the limit of the reference timer (Dassault) in synchronous mode; one may expect that the frequency synthesis time variance would even go beyond this level. This level surpasses the specifications and represents a remarkable performance in itself.

3.2.1.2. Timing

Experiment setup The performance of the event timer is assessed by comparison to the Dassault reference timer by sending events to both timers. These may be in phase with the reference signals (i.e. synchronous) what doesn't reflect the operation reality, though, or asynchronous, i.e. in a random manner with respect to the reference. Fig. 3.38 depicts the two corresponding setups. The control PC (i.e. the NI-Daq card) generates events that are fed to the signal distribution unit, that puts them in phase with the applied reference signal when working in synchronous configuration. For asynchronous operation, the computer card is left running freely what leads to randomly distributed events. The signals are then routed

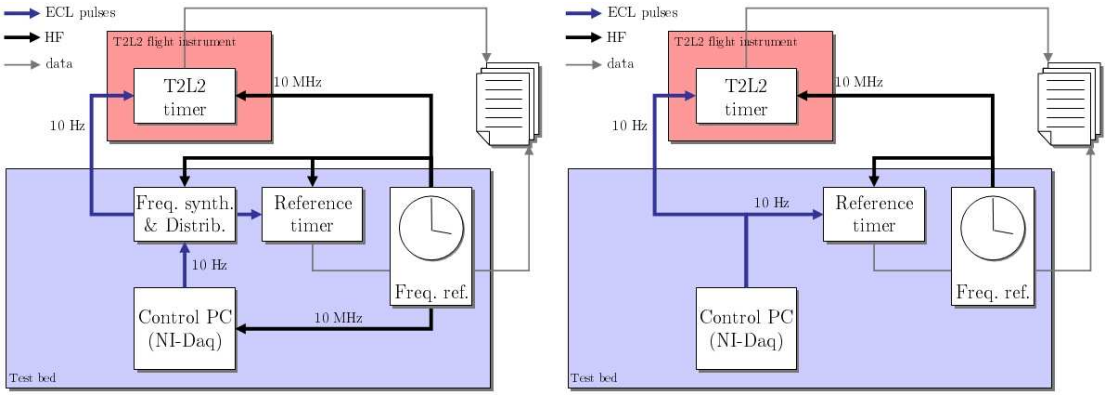

Figure 3.38.: Experiment setup for synchronous (left) and asynchronous (right) timing

to both timers, T2L2J2 and Dassault. The performance is then evaluated by the difference of the two generated events which is transformed into time variance.

Results Throughout the test campaigns various acquisitions have been performed, with different repetition rates and over different time periods. Fig. 3.39 shows some representative acquisitions. The one featuring the best stability, `ChrES070419_3` exhibits a pink noise floor of about 50 fs, even with an initial standard deviation of about 5 ps (what is due to some imperfect calibration). The precision has generally be determined to be below 2 ps

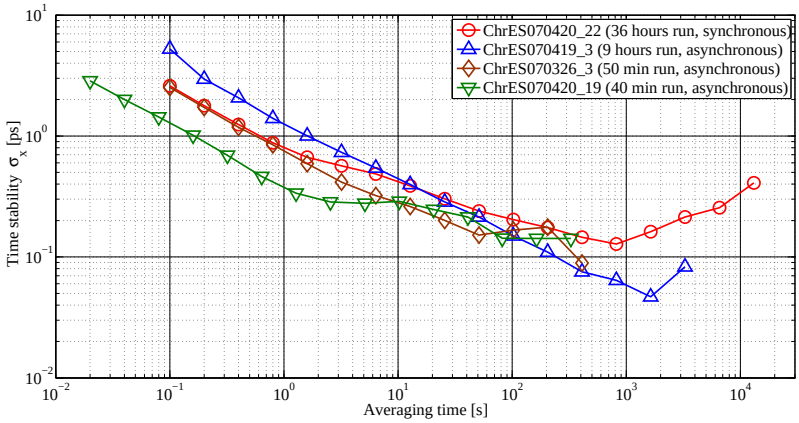

Figure 3.39.: Stability of event timing in synchronous and asynchronous mode

(resolution below 1 ps) confirming specifications [E 4.2.2-1] and [E 4.2.2-2] of Section 2.3.2. The synchronous acquisition (red, circles) suffers some other than white noise as compared to the other curves: This is due to the vernier non-linearity whose error averages out for asynchronous, random events, but not for synchronous, where each event retrieves the same deviation.

The drift of the timer dates could be measured to be about 0.7 ps/hour under normal operation conditions. For very stable operation, this value could even be lowered to values of less than 0.1 ps/hour. The overall drift will generally be governed by the drift due to temperature evolution (0.5 ps/°C); however, the epochs may then be corrected for the

temperature induced drift.

Discussion In general, the timing performance is as expected, with a single shot r.m.s. of less than 2 ps and a white noise behavior over more than 1,000 seconds making it principally possible to average out to levels of less than 50 fs.

3.2.1.3. Internal calibration signals

The event timer itself generates calibration signals. These are referenced to, because issued from the reference clock signal (see Chapter 2.3). These fixed calibration signals are routed back to the vernier in order to be timed. The event timer allows to perform an arbitrary number of such internal calibrations during normal acquisition (with a priority for optical dates) allowing the calibration data to average out onto a sufficient precision; the gain through a good calibration has then to be pondered against sufficient optical events while facing a limited data storage volume as well as a limited data rate for earth download.

The quality of the internally generated calibration pulses is of vital interest for a longer independent operation of the timer. In the test campaign at CNES, this topic was addressed by exploring following issues:

- The temporal distribution of the calibration pulses (i.e. their precision)
- The long-term evolution of their temporal position
- Thermal sensitivity of the calibration pulses

Experiment configuration The respective test setup is rather straightforward: The T2L2J2 event timer is left running independently: The timing of the internal calibration pulses is performed by the timer itself. For the analysis of the long-term behavior, the different date sets are compared after intervals of some days. For the thermal sensitivity analysis, the SSE is heated or cooled in the thermal chamber of the test bed and the respective dates are compared.

Analysis, results and discussion Fig. 3.40 shows the distributions of the four calibration pulses on the two verniers. All pulses show an r.m.s. of about 9 ps what is in accordance with the specifications.

A comparative study of different calibration pulse timing datasets over a period of about ten days reveals however a rather important variation of two of the four pulses (with a common origin) what may be imputed to the design of the pulse generation circuitry. This variation, or long-term drift may cause difficulties in the timer calibration in orbit. Nevertheless it seems feasible to develop sophisticated analysis methods to counteract this phenomenon.

The same observation was made for the temperature sensitivity analysis: The same two pulses with a common origin show a temperature-related drift. This variation has to be borne in mind when establishing new calibration datasets from the internal pulse calibration when acquired with a temperature variation.

In general, the calibration works roughly according to specifications but great care has to be taken when re-calibrating the timer with a new set of pulse calibration data: There may be a drift related to aging *and* temperature.

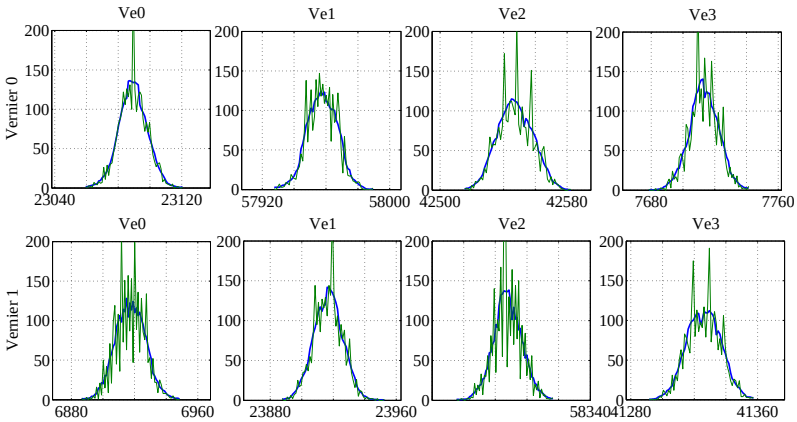

Figure 3.40.: Temporal precision of the generation of the four internal calibration pulses as determined with the T2L2J2 event timer itself (abscissae scale in ps), representing their position in the vernier timescale

3.2.2. The T2L2J2 optical subsystem

This section presents the main experimental results on the optical and in particular the photodetection part of the instrument. Essentially, the results of the most important components for time metrology are given: The performance of the non-linear detection. After that, another important issue is addressed: The coupling, i.e. the optical throughput efficiency of the two optical channels.

3.2.2.1. Non-linear photodetection: Precision as a function of photon number

Test setup One of the central measurements to investigate the performance of the T2L2J2 photodetection is the determination of the temporal precision. The measurement is performed by sending laser pulses both on the T2L2J2 optics and on a reference detector, as depicted in Fig. 3.41. The latter is operated in a high power, saturated mode yielding a precision of 2 ps (see Section 3.1.2.4).
The electric pulses generated by the detectors are timed by the T2L2J2 and the reference event timer, respectively. Both are driven by a common frequency reference, in this case a Rubidium clock. In order to sweep over the whole possible dynamic of laser power, the laser

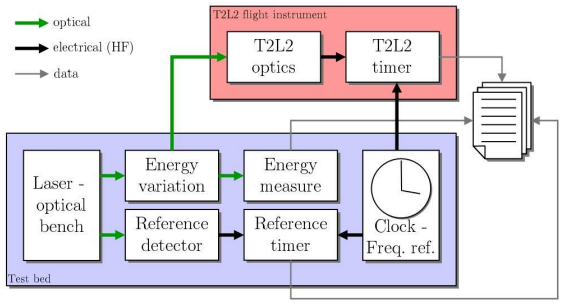

Figure 3.41.: Measurement setup for the determination of the non-linear detection's precision as a function of incident laser pulse energy

beam is attenuated by a controllable energy variation setup (Section 3.1.2.1). In order to cover even more than the four possible decades of this device, this particular experiment was additionally performed with some neutral density filter in front of the T2L2J2 optics. The two series were combined afterwards.

The whole experiment is piloted by the autonomous control software: At a laser rate of 50 Hz, it performs a set of acquisitions during 80 s. After each set, the laser power is varied and measured by the reference energy detector and the beam profiler (Section 3.1.2.2) by moving the beam distributor carriage in front of the detectors. Then, the carriage returns and the timing measurement continues.

Results The measurement outcome is finally a table with the calculated differences between the T2L2J2 and the reference timings, averaged over one set: MeanDiff=$\langle t_{\mathrm{T2L2}} - t_{\mathrm{Ref}} \rangle$ with the corresponding r.m.s. value. The reference timer is always considered as a perfect reference. Attached to each value, the respective number of events N_{eve} per set and the laser power and beam profile measurements are supplied.

The determined precision (r.m.s. values) as a function of the photon number impinging on the detector is given in Fig. 3.42. The photon number is determined by statistical methods:

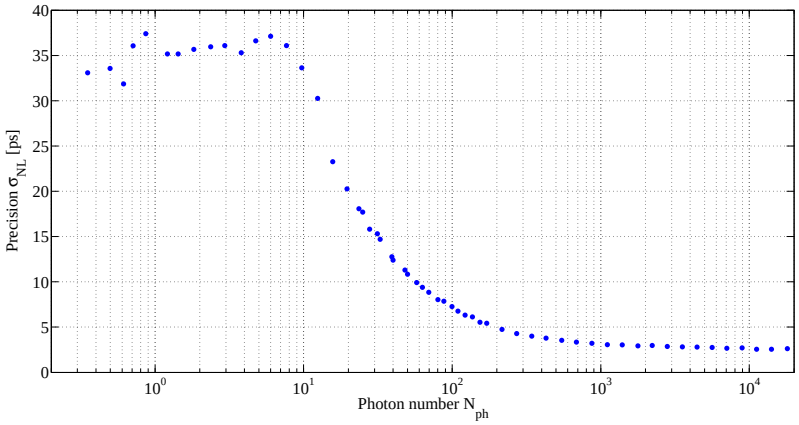

Figure 3.42.: Precision of the non-linear detection as a function of impinging photon number

For low photon flux, the detection probability P_{det} follows Poisson statistics with $P_{\mathrm{det}} = 1 - \exp(-N_{\mathrm{ph}}\rho)$, where N_{ph} is the actual photon number and ρ is the quantum efficiency of the detector. The photon number N_{ph} is then calculated from the number of events N_{eve} per set; for higher photon numbers, the photon number is determined by the respective ratio of the measured laser powers.

Discussion The precision in single-photon mode is higher than expected; values of about 23 ps can be obtained with the K14 photodiode. These values were also confirmed by the T2L2J2 non-linear detection prototype that was assembled with some optics by OCA in order to serve as a single-photon reference (compare to Section 3.1.3). This reference detection systems shows no significant difference in its architecture as compared to the T2L2J2 optics except for the beam concentration optics.

An explanation of this deteriorated precision could be an inadequate coupling of the optical fiber output onto the detector (refer to the architecture in Section 2.3.4.2): It had been

specified that the beam should fall in a centered spot of 160 µm diameter on the diode active region to allow an optimum precision and a constant value of time walk; the experimental results give an indication that this specification could not be hold. Another confirmation of this assumption is given in Section 3.2.2.4.

This deteriorated performance in single-photon mode will not have much influence on the general performance of the instrument except for weak signal time transfers (with small or kHz laser stations). As we will see below (Section 3.2.2.4), this deteriorated precision comes along with an attenuation of the non-linear channel sensitivity of a factor of 5 as compared to specifications. These two points let suspect a misalignment of the non-linear detector (probably a spot spilling over the detector's physical extent).

For photon numbers over 10, the precision falls below 25 ps, complying to specification [E 4.2.1-3] (refer to Section 2.3.2). The dynamic of the non-linear channel covers nearly fives decades (100 dB) what further complies to specification [E 4.2.1-1]. The same dynamic is featured by the linear channel what will be shown in Fig. 3.53 of Chapter 3.3.

3.2.2.2. Long term stability of the non-linear detection

The time stability of the T2L2J2 event timer has been tested to be very satisfactory: starting from an initial precision of less than 2 ps, it features a white noise behavior of over 1,000 seconds: This allows to average a whole set of dates acquired over a complete orbit pass over a laser station.
But the precision of the timing depends principally on the photodetection as shown in the previous section. This part investigates the noise behavior of the non-linear detection by determining the long-term time stability of the optical acquisitions.

Test setup In order to determine the time stability of the photodetection, several short, mid and long term acquisitions were performed. The test setup is somewhat simpler than in the previous section: Laser pulses are sent onto the T2L2J2 and the reference detector. Both T2L2J2 and reference event timer are again referenced to a common clock in order to determine the difference of the time tags. The laser power is set on a fixed value beforehand.

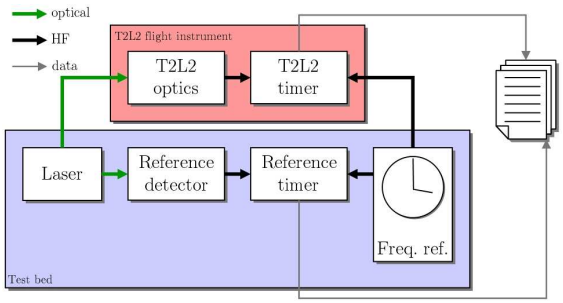

Figure 3.43.: Test setup for stability measurement

In the case of the measurement series regarded here, it is set to single-photon level. The experiment is conducted over nine hours.

Analysis The obtained data is filtered in order to reject events that are too far off from the most frequent value (see Fig. 3.44: Upper left before and lower left after filtering); a typical

distribution of dates acquired in single-photon mode is shown in Fig. 3.44: The abscissa is the elapsed time (or simply the date number) and the ordinate (in ps) the difference of the T2L2J2 timing measurement to the reference timing (which does not work in single-photon mode and thus features a good precision). Points above zero are timed events before the real arrival of the laser pulse on the detector; these correspond mostly to detector avalanches generated spuriously by the impressing of the Geiger voltage some nanoseconds before the optical event. Events in between these early events and zero are due to noise photons (thermal or exterior) or electrons that trigger an avalanche. The shown acquisition was performed in darkness, so the noise event rate is very low; acquisitions performed with overlaid background illumination evidently show a higher noise density.

Most events are around the (arbitrary) zero value but, in fact, many avalanches may arrive some nanoseconds later, due to the stochastic carrier multiplication from one pair (generated by one photon) to a detectable signal, in particular at the beginning of the process. Only very few (with the same density as before) correspond to noise-provoked events (when no laser photon arrived). This type of distribution is typical of single-photon avalanche photodiodes. In order to arrive at a reasonable precision, these late events have to be dismissed by regarding them as outliers. A very common technique is to calculate the distribution (right

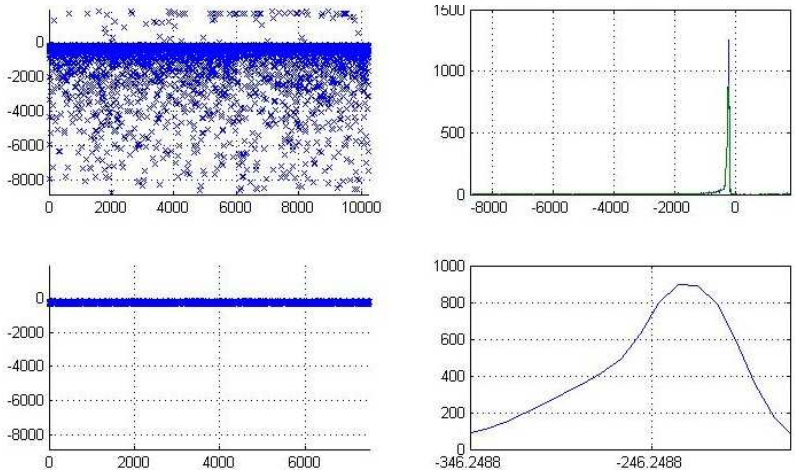

Figure 3.44.: Filtering of the raw dates: Raw dates show big dispersion for single-photon mode (above). After filtering at 10% the too far off dates are rejected (below) giving an acceptable dispersion.

upper graph in Fig. 3.44) of the whole acquisition series and, after some data smoothing, dismiss those events that appear with an occurrence below a chosen threshold. This threshold is typically set to 5 or 10% relative frequency, 10 % is used throughout the data analysis of T2L2J2. The filtered data points are shown in the lower left graph, whereas the lower right graph depicts the zoom on the main event.
By this means a certain precision may be attributed to a single-photon detector[20]. Incidentally, the quantum efficiency of such a detector usually comprises also this filtering.
After the filtering of the dates, the time stability is calculated over the remaining points.

[20] And to be consistent, the filtering occurrence threshold should be given along with the precision.

Results The longest acquisitions series, and thus the most trusty for the calculation of time variance on the long term, are shown in Fig. 3.45. Both acquisitions were performed

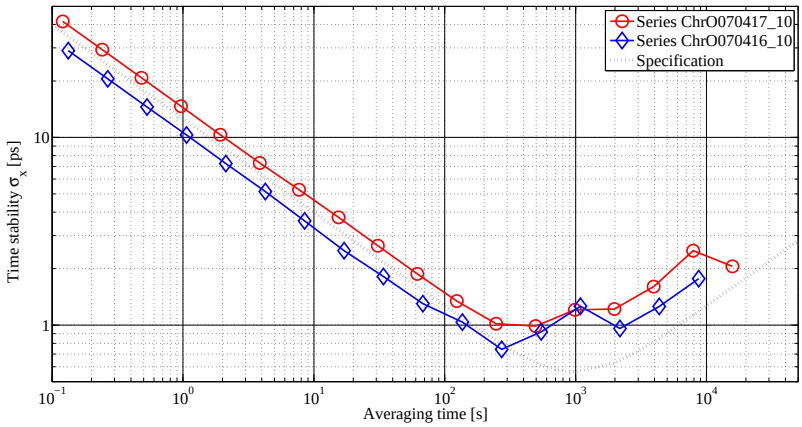

Figure 3.45.: Time stability $\sqrt{\text{TVAR}}$ of the T2L2J2 optical timing in single-photon mode

in worst-case conditions, i.e. in single-photon mode; nevertheless, they both show a very smooth $\tau^{-1/2}$-slope over some hundred seconds indicating the presence of solely white noise before attaining the flicker floor level on the ps-level. The graphic also shows the specification as defined in [29]; one sees that even in single photon mode, the specification is nearly fully fulfilled. We may hereby infer that the instrument complies to specification [E 4.2.2-3] for higher photon levels (see Section 2.3.2), starting at lower precision values. Though, a long term stability measurement on a higher photon level, what would directly prove the compliance to the specification, has not been performed[21].

The drift of the optical events could be measured to be about 1 ps/hour; the optical subsystem thus does not seem to significantly deteriorate the value of the timer (compare to the value of the event timer solely of 0.7 ps/hour, page 77).

Discussion The different acquisitions performed over a sufficiently long time period show a very pure white noise behavior over some hundred seconds. This is in full accordance with the needs and the specifications of the T2L2-scheme. Note that the here presented results include the contribution of the timer (and its calibration), which is negligible, though.

3.2.2.3. Influence of laser repetition rate

In order to assess the influence of the repetition rate on the time stability and thus its shape on shorter averaging times, the upper experiment was repeated (over shorter intervals) with different laser repetition rates. The experiment configuration is the same as indicated in Fig. 3.43. The time stability graphs for four analyzed repetition rates (10, 50, 200 and 1,000 Hz) are shown in Fig. 3.46.

It is clearly visible that they all feature pure white noise behavior on the short term. The measurement series' lengths do not permit to calculate time variance values for longer

[21] This was due to some deterioration of the first pulse picker (too high incident power density) during the tests: The final usable laser power was on a very low level when we finally performed this type of measurement (at the end of the CNES campaign).

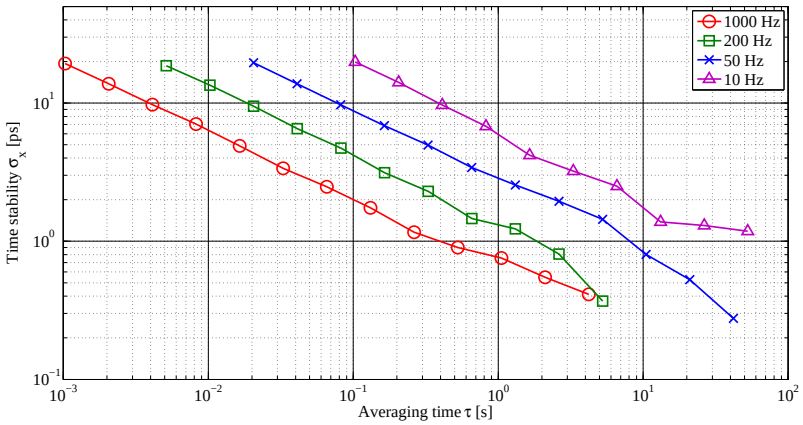

Figure 3.46.: Short term time stability of optical timing for different laser repetition rates

averaging times than some seconds to some tens of seconds; nevertheless, the time stability graphs of the faster acquisitions (50, 200 and 1,000 Hz) indicate that it is possible to attain a minimum time stability of some hundred femtoseconds before rejoining the values of the 10 Hz acquisition on the longer term (some hundred seconds).
The little smooth look of the four curves (in particular to their end) is due to the real physical nature of the measurement and the decreasing confidence of the time variance calculus for longer averaging times[22].

3.2.2.4. Coupling efficiency of the optics

This part treats the coupling efficiency of the optics of the linear and non-linear channel. As this does not directly concern T2L2J2's performance in terms of metrology, it may rather be regarded as a test of the compliance with the specifications. Only a description of the test of the non-linear channel will be given here, since the analysis of the linear channel is a somewhat complex undertaking what would lead too far.

Test setup and analysis During the test campaign at CNES, two partially complementary methods in order to determine the coupling efficiency of the non-linear channel have been performed. Both are based on the measurement of the ratio of incident light falling into the T2L2J2 optics and the quantity of light after the optics.

The first test concerns solely the front optics of the non-linear channel BONL (compare to Section 2.3.4.2 and Fig. 2.14); the fiber of the harness that transports the laser light from BONL to OCTO in the inside of the electronics unit is guided onto the reference power detector of the test bed. The amount of light transmitted into the BONL optics is equally measured by the power detector.
By this means, the throughput of the BONL optics and of the fiber are evaluated (Fig. 3.47).

The second test encompasses all BONL, the harness and delay line fiber and the OCTO optics located in the electronics unit. The laser pulse energy falling into the BONL aperture

[22] Here, the longest used averaging time τ_{max} accounts for one third of the total duration of the acquisition and thus a rather low confidence on the calculated time variance.

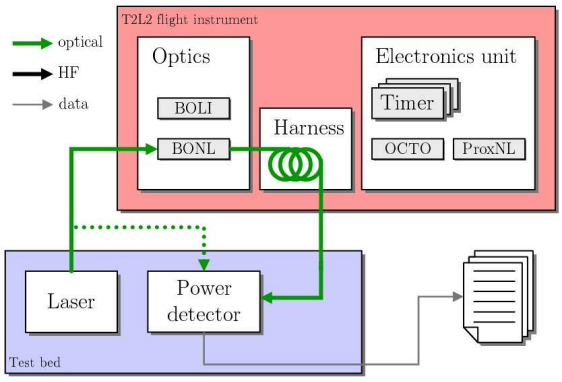

Figure 3.47.: Test setup in order to determine the optical throughput of BONL and the harness fiber

is measured by the reference power detector. The laser pulse energy that finally, after the transmission through all T2L2J2 internal optics, falls onto the non-linear detector is statistically assessed, in single-photon mode. Single-photon mode is a statistical process: The mean number of incident of photons is so low (below unity) that most of the time there are no photons at all; sometimes, a single photon is encountered, and the probability of two or more photons is still lower. The whole process is described with Poisson-statistics. The

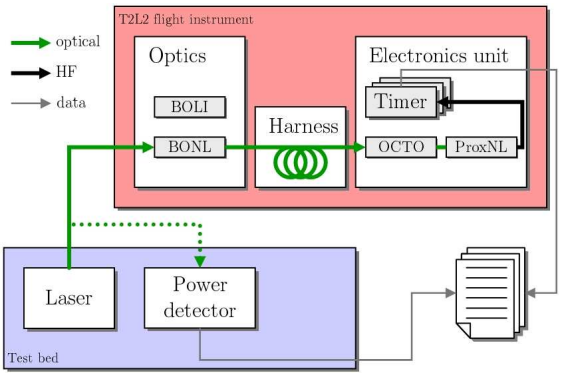

Figure 3.48.: Test setup in order to determine the complete coupling efficiency of the non-linear channel optics

laser power is reduced such that the detection probability of T2L2J2 is around 7, 20 and 30% (for three measurement sets), assuring single photons arriving on the K14 diode. The mean number of photons N_{ph} is determined from the detection probability: $N_{\mathrm{ph}} = -\frac{\ln(1-P_{\mathrm{det}})}{\rho}$ with ρ being the quantum efficiency of the detector ($\rho \approx 0.4$).
The transmittance of the optics may be quantified by an effective pupil surface, following Equation (2.4), instead of in transmission optical density. The effective pupil radius $R_{P_{\mathrm{NL}}}$ of the optics is given by:

$$N_{\mathrm{ph}} = \left(\frac{R_{P_{\mathrm{NL}}}}{R_{\mathrm{spec}}}\right)^2 \cdot N_{\mathrm{tr}} \cdot T_{\mathrm{RD}} \cdot T_{\mathrm{NL}} \tag{3.2}$$

with R_{spec} being the pupil radius specified to SESO, T_{RD} the transmittance of the radial filter (at the used incidence angle) and T_{NL} the general transmittance of the BONL optics.

N_{tr} is the number of photons transmitted into the optics calculated from the reference power measurement.

Results The first method reveals a slightly deteriorated transmittance of the BONL optics and the harness fiber: Instead of the specified 10.6 µm one finds 7.3 µm for $R_{P_{NL}}$. This induces about 50 % less flux at the output of the fiber than specified.

The second method unveils a further deterioration by more than a factor 2 in the second part of the non-linear channel optics: The statistical method yields $R_{P_{\mathrm{NL}}} = 4.9$ µm.

The performed measurements yield a total abatement of sensitivity of the non-linear channel of a factor of 4.7 as compared to the specifications. The parallel deterioration of the precision in single-photon mode, illustrated in Section 3.2.2.1 above, suggests a misalignment of the beam concentration cone on the APD: The beam may spill over the detector effective surface or just be decentered.

A further outcome of the study above, that was not addressed so far, is a "dark" spot in the center of the non-linear channel radial filter, reducing further the transmittance budget for incidence angles of 0°; this conclusion will be confirmed by the assessment of the radial filters that will be addressed in the calibration chapter (Section 3.3.2.2). Generally, this defect, due to the manufacturing procedure, will not have any effect on the performance of T2L2, since a 0° incidence is very improbable (and not feasible for most azimuth-elevation mounted telescope of laser stations) and in any case, the respective transmittance is known.

Linear channel coupling As mentioned in the introduction of this section, the coupling of the linear channel is not addressed in this work. Since there is not the possibility to measure directly the light throughput of the BOLI optics, its transmittance has to be estimated via the electronic signals generated on the linear 902S photodiode. Displaying the different steps of the coupling assessment would be more confusing than helpful; at this point, it should just be stated that the gain (or the photometric effective pupil) of the linear optics is in accordance with the specifications even though the geometric extent seems to be larger than the expected 250 µm; this is probably due to aberrations that are generated by the imperfect optics elements, diluting the geometric pupil. This suspicion was also confirmed by an additional geometrical test, with a narrow probe beam scanning over the pupil.

The relative coupling, or the coupling ratio of the linear to the non-linear channel k was thus determined to be 1,250 instead of the specified 150.

Discussion The coupling analysis shows that the non-linear channel's sensitivity suffers a reduction of about a factor of 4.7 as compared to the specifications. This will lead to a shifting of the operation of T2L2J2 towards lower photon levels what entails a degradation of precision for stronger signals and a degradation of detection probability for faint signals (as compared to the specifications).

3.2.3. Time stability of the DORIS USO

The DORIS ultra-stable oscillator (USO) of the Jason 2 mission has unfortunately not been directly available to OCA or CNES for a detailed long-term characterization in terms of time stability. We performed some measurements on an older engineering model that CNES could supply but the representativity of the respective tests is minor since each quartz oscillator

differs a lot from another. It was not until the tests in the THALES Alenia Space facilities that we finally could physically test the Jason 2 mission oscillators.

Test configuration The test setup has to be quite tricky since there wasn't any free signal output available at DORIS. We therefore used the T2L2J2-generated 100 MHz reference signal slaved to the DORIS oscillator, thus "looking through" T2L2J2. Considering the DORIS USO and the overall measurement setup, this contribution may be neglected. The

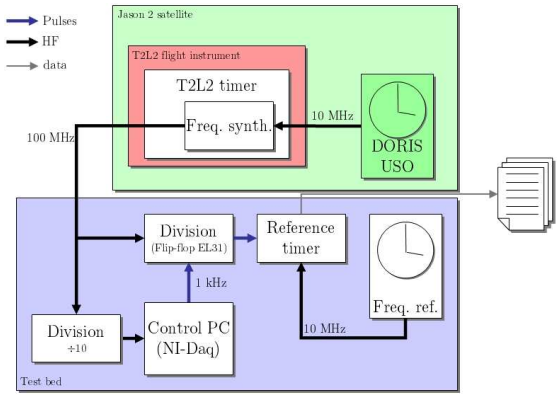

Figure 3.49.: Measurement for the determination of DORIS USO characteristics

T2L2J2 100 MHz signal was then fed to the same EL31 flipflop as used in Section 3.2.1.1. The 100 MHz signal was equally divided by ten and supplied as a reference to the control PC that sent a low rate of logical pulses to the Reset input of the flipflop. By this means, the 100 MHz signal was physically divided to a low rate pulse train (at 100 Hz, for instance) which was timed by the reference timer. The reference timer was referenced to another clock, in this case the OCA-supplied Rubidium frequency standard. By this means we performed a phase comparison of the DORIS space clock and the Rubidium.

Analysis and results The analysis of the different performed acquisitions that were performed with both USOs of the DORIS payload proved to be a rather laborious task: Due to some misadjustment of the commutation point of the flipflop circuit, it once triggered on the n^{th} rising edge of the 100 MHz logical signal and once on the $(n+1)^{\text{th}}$; This led to a separation of the phase data into two distinct curves in the file, as shown in Fig. 3.50 (a small zoom on the data, linearly adjusted for some frequency offset). The full procedure of this data treatment shall not be shown here[23].

By the analysis of the slopes of the raw data one finds for the frequency accuracy of the two DORIS oscillators[24]:

- DORIS PMA: $E = -19 \cdot 10^{-9}$ and
- DORIS PMB: $E = +18 \cdot 10^{-9}$

[23] This analysis has been performed by E. Samain.

[24] The DORIS space segment on Jason 2 features two distinct oscillators whereof one features as a backup; one is called PMA, the other PMB.

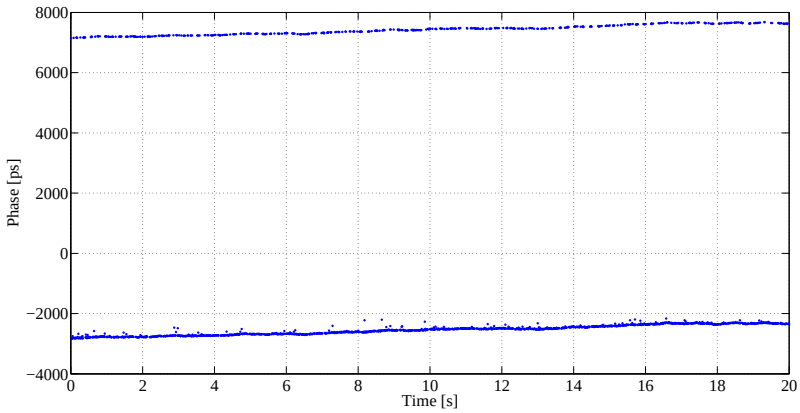

Figure 3.50.: Illustration of the phase data file: Two distinct curves, separated by 10 ns

After subtraction of the linear term for the frequency offset, the data still shows a residual parabolic feature, indicating a linear frequency drift. Since during the measurement the DORIS oscillators still were in their warm-up phase, this drift diminishes over time. The phase deviation was found to be of the order of:

- DORIS PMA: 2.4 ns/100 s after 1 h 30 min of stabilization and 0.12 ns/100 s after 7 h 30 min of stabilization and
- DORIS PMB: 1 ns/100 s after 1 h 30 min, and 0.2 ns/100 s after 7 h 30 min stabilization.

In terms of oscillator frequency, this indicates a frequency drift 0.096 µHz/s for PMA and 0.16 µHs/s for PMB after 7 h 30 min of thermalization.

In order to calculate properly the time variance, the linear frequency drift term (parabolic phase evolution) has to be subtracted from the epochs. This is carried out with a 2nd order polynomial. Further, the deceleration of this drift should be taken into account what is done with a third order polynomial. These corrections, and especially the last, represent of course something artificial, since one cannot distinguish between the effect of thermalization and any other process, like a noise process that we would like to uncover with the calculation of the time variance.

Discussion The result (in root of TVAR) is represented in Fig. 3.51; please note that the time stability is deteriorated on short term scale (up to about 100 s) due to the misadjustment of the measurement equipment that introduces a large (white-noise type) dispersion and the used Rubidium frequency standard. The figure also shows some time stability long-term extrapolation from phase noise spectral density data supplied by the manufacturer Rakon Ltd. One sees that the thermalization correction is necessary to approach the curves towards the expected performance level but still only PMB does the job. This proves the deterioration of the mean-term time stability by the thermalization process.

For what concerns the frequency exactitude and the frequency drift, these quantities comply to specifications (Rakon) or expectations. In terms of long-term time stability we can hope (but not anything more) that the DORIS USO performances will finally reach the expected performance level (extrapolation in Fig. 3.51) during nominal operation.
Still, the time stability level of some hundreds of picoseconds over some hundreds of seconds

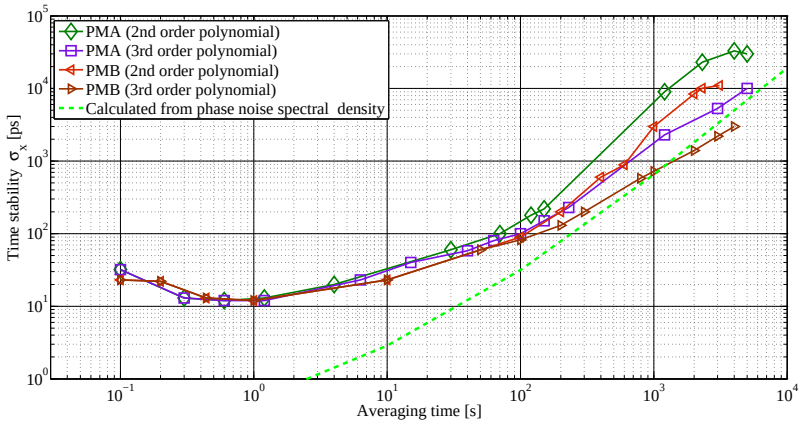

Figure 3.51.: Time stability of both DORIS USOs (PMA and PMB), corrected for thermalization and not

integration time does not promise the same excellent performance for time transfer in non-common view as compared to common view. This aspect is addressed in Section 5.1.3 of the error budget chapter.

3.2.4. Conclusion T2L2J2 final performance

The previous sections highlighted the most important features of the two subsystems of the T2L2J2 instrument (SSE and SSO) and the DORIS ultra-stable oscillator in terms of optical time metrology. In general, we could observe that the T2L2J2 flight instrument almost fully complies to the specifications. Apart from some functional topics, that have not been mentioned in this work (FIFO memory, software etc.), some minor metrology-related issues have been identified in the generation of the internal calibration pulses of the event timer and in the coupling of the non-linear channel optics.
The timer calibration problem may under certain circumstances complicate the necessary regular re-calibration of the timer in orbit, what seems manageable.
The deteriorated optical throughput of the non-linear channel will shift the operation of non-linear detection to lower photon levels.

To summarize, the T2L2J2 main metrology components, the event timer and the detection device show a level of performance that reflects the expectations:
The event timer has an intrinsic precision of less than 2 ps and permits a minimum time stability of 50 fs for an integration time of 1,500 s (compare to Fig. 3.39). The optical timing scheme permits a 30 ps precision in single-photon mode with a time stability on the picosecond level (or even below) after an integration time of some hundreds of seconds (Fig. 5.2) what corresponds to a typical satellite pass over a ground station. The design and performance of the T2L2J2 optical subsystem has been summarized in a SPIE publication [42] and its overall performance in [43] and [44].

3.2.5. Lessons learned

All T2L2J2 development phases from conception over design to production of the instrument have been subject to a very tight schedule (less than 1.5 years for the B-, C- and D-phases).

Further, all three concerned parties, CNES, the OCA team and the industry partners had no comparable experience in the development of such a radically new spaceborne system (as compared to more recurrent systems such as Poseidon or DORIS, to take just two neighboring systems on Jason 2 as examples).

The successful development and implementation of the T2L2 space segment is already a big achievement. A second big success is the performance of the instrument complying to the specifications. Another positive outcome of the T2L2J2 activity hitherto is the know-how acquisition of all three partners CNES, OCA and EREMS/SESO. In fact, the technology and know-how transfer from research institutes to industry is a very important aim of the CNES philosophy.

From these points we can draw some conclusions: (1) The performance of the T2L2J2 flight instrument shows that industry partners are actually capable of the production of high-fidelity metrology optics, opto-electronics and electronics for optical time and frequency metrology.
(2) However, both encountered problems (calibration pulses and optical coupling), originating in both EREMS and SESO responsibility may finally be traced back to lacking development time: The slightly deficient generation of the calibration pulses is due to some timing errors in the FPGA that generates the signals; this could easily have been avoided with more repeated feedback between OCA and EREMS. The coupling deterioration could probably have been avoided by another than proto-flight model philosophy and by employing alignment methods that are currently only available to OCA. To put it in a nutshell, a longer development time would certainly lead to still better results in terms of metrology.

3.3. Calibration of instrumental parameters of T2L2J2

The following section will highlight some of the numerous performed calibration measurements performed on the T2L2J2 flight model. These calibrations are vital to reduce the raw data obtained during operation in orbit and to correct them to the specified level.
Like in the previous section, for legibility some of the performed measurements are omitted and only the most important are presented. As for the performance test, the data analysis has been carried out by Etienne Samain and myself where the aspects of the event timer were covered by Etienne and the aspects of photodetection by me.
The last two sections, dealing with the influence of the incident laser wave polarization and the influence of Earth albedo noise are less calibration issues for data reduction than estimations of impact on the experiment; nevertheless it seemed more consistent to mention them here since the previous section was more oriented to performance in time metrology.

3.3.1. Event timer: Vernier calibration

The calibration of the vernier of the T2L2J2 event timer consists in the complete characterization of the vernier reference signals. The detailed determination of these characteristics is a vital start point for all future re-calibrations that will be performed during operation. These re-calibrations will be performed by the built-in calibration pulses and some statistical analysis.

During the two-months campaign at CNES, the detailed calibration by the means of an external reference timer had been performed several times.

Experiment setup and analysis The experimental setup is the same as for the performance determination[25] of the timer in asynchronous mode. This was explained in Section 3.2.1.2 (refer to Fig. 3.38, right scheme): Both T2L2J2 timer and reference timer are connected to a common clock; some source (here the NI-Daq card of the control PC) generates asynchronous events that are timed by both timers.

The outcome of this test, a complete characterization of the vernier reference signals (which is stored in a correction file) then represents the basis for the correction of the dates: A date is initially calculated with the counter number and the vernier value. This date is then corrected for its non-linearity by some coefficients derived from the correction file (see an example file in the Appendix, Table A.3).

Results and discussion Once the calibration performed (and the necessary corrections applied), the timer should work perfectly, only subject to statistical noise processes generated in the electronics. In this configuration the timer features the precision and stability as it was highlighted in Section 3.2.1.2.
A variation in the vernier parameters is detected by the internally generated calibration pulses, except for the signal harmonics.

These may be determined by statistical calibration: The orbital motion of the satellite permits a quite good random distribution (with respect to the vernier) of the events. By this means, and for a sufficient number of events, the vernier signals are completely scanned.

[25] Evidently the calibration is performed before the performance test in order to provide a good data correction base.

Table 3.5.: Excerpt from a reference timer file of T2L2J2

```
1 : Date1970 (fraction jour)
2 : DateRef(DE) (ps)
3 : ModuloDateRef (ps)
4 : Origine Datation T2l2j2
5 : Co (N x 10ns)
6 : Co E/O
7 : Ve0 (bit)
8 : Ve1 (bit)

Réalisé par le programme BT2Studio version 1.2
*** *** *** *** *** *** *** *** *** *** *** *** ***
PCTime1970       TimeR                MTimeR  Org Co                E/O Ve0     Ve1
39192.494340     663064484442459592   19592   0   1088595752517     1   46214   9962
39192.494340     663064504442556650   16650   0   1088597752526     0   22149   7282
39192.494340     663064524442651539   11539   0   1088599752536     0   8266    42650
39192.494340     663064544442733038   13038   0   1088601752544     0   5779    30402
39192.494340     663064564442825637   5637    0   1088603752553     1   50644   53751
```

One is then similarly able to deduce all correction parameters except for phase as there is no phase reference.

For illustration of the overall quality of the vernier reference signals a plot of the determined harmonics' amplitudes is given in Fig. 3.52. The power contained in the first harmonics is

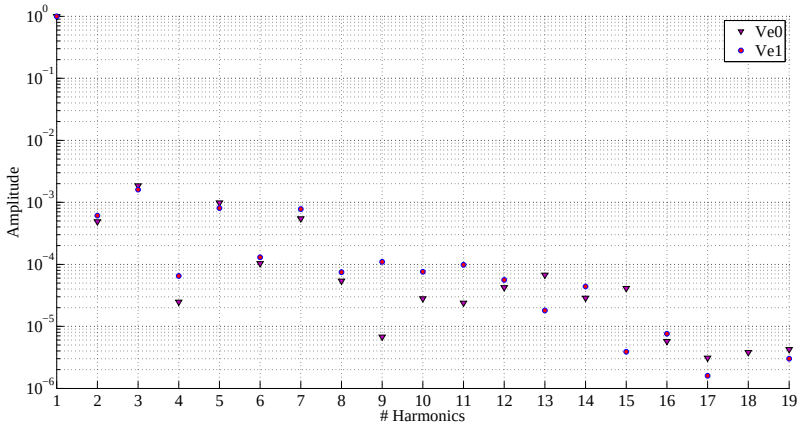

Figure 3.52.: Amplitude of the harmonics of the vernier reference signals

more than 60 dB inferior to the principal, what represents a remarkable spectral purity.

3.3.2. Optical subsystem

3.3.2.1. Detection: Determination of the time-walk and pulse measurement linearity

The most important calibration measurement of the optical part of T2L2J2 is the determination of the laser pulse energy dependent time walk of the non-linear photodetection. Another is the response of the linear pulse energy measurement. Both issues are determined in the same experiment.

Setup and analysis The experiment is the same as for the determination of the precision of the non-linear detection, described in the performance chapter (Section 3.2.2.1). The optical bench transmits laser pulses on both the T2L2J2 optics and on the reference start detector (Fig. 3.41). The automated test sequence performs an ensemble of measurement sets over the whole energy dynamic (dictated by the energy variation device); this dynamic is manually extended by further attenuating the power with neutral density filters.

Both devices time-tag the respective events; the difference of the dates over the laser power is the time walk. The measurement of the laser pulse energy by the linear channel is acquired simultaneously.

Results Fig. 3.53 presents the results of this experiment. The abscissa has been transformed into laser energy density in front of the T2L2J2 optics (as it will be in orbit) by calculating the energy density in a small circle of the Gaussian beam (of the test bed optical bench) in the vicinity of the optics aperture. The upper graph, showing the time walk, shows a very smooth trend over nearly five decades of laser energy. In general, the curve corresponds very well to the expected behavior of a K14 diode. The lower chart shows the "linearity"

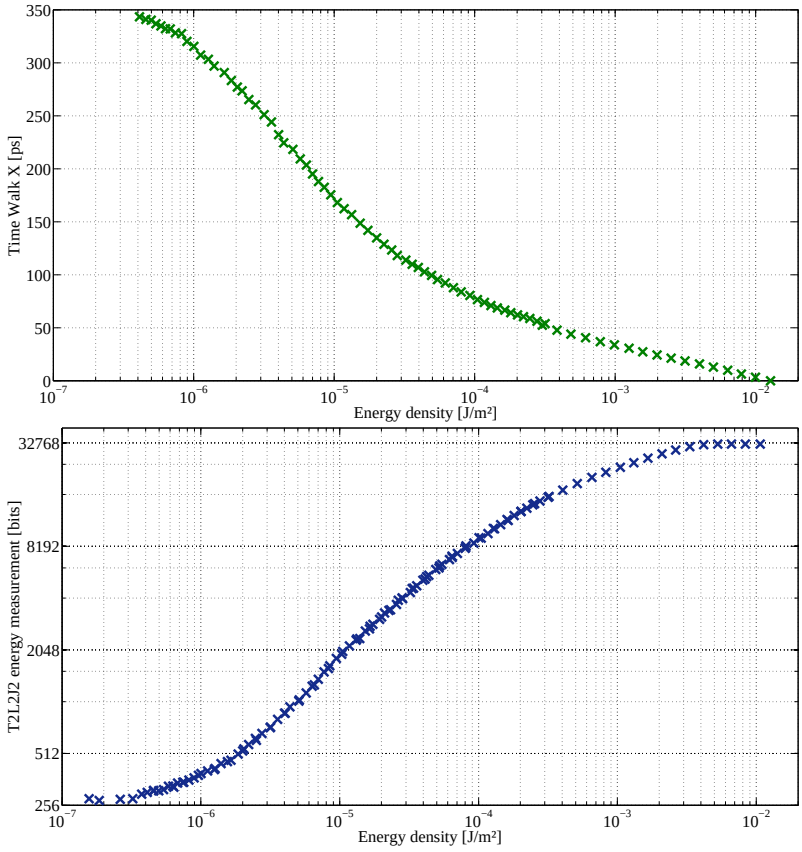

Figure 3.53.: Time walk of the T2L2J2 non-linear detection system (above) and pulse energy measurement of the linear channel

of the pulse measurement. It also features a very smooth trend starting from a minimum of 280 bits what corresponds to the electronics noise applied on the ADC (analog-to-digital converter). The maximum value is attained at an energy 34,000 times higher, when the

pulse measurement enters into saturation: The maximum value is defined by the half of the ADC's 16 bits dynamic.
The pulse measurement features an exploited dynamic of nearly five decades what shows the compliance to specification [E 4.2.1-1] of Section 2.3.2.

A further analysis of the pulse measurements reveals an extraordinary precision of 20 bits r.m.s. at low energies to 80 bits r.m.s. at high energies. The relative precision is shown in the Error budget, on Fig. 5.4. It varies from values of about 6% for photon numbers of around 1,000 (on the linear channel) down to less than 0.5% for photon numbers of about 1 million.

All measurements have further been performed for five different polarization voltages of the linear detector, ranging from -140 V to the nominal -206 V (the respective results are not plotted here). During nominal operation, the default voltage will be used a priori, but other values are also possible; both time walk and pulse response may be interpolated for polarization voltages in between, with the datasets obtained for the different voltages, if necessary.

The measurements have also been performed for some different values of the linear detection threshold[26]. The different curves of the pulse measurement superpose quite well, what proves the independence of this measurement from the threshold.
The time walk curves are also quite well superposed, yet with some shifts of maximally 10 ps. In the first order, these "offsets" may be neglected in the data analysis; for a more sophisticated data analysis, the different time walk curves as a function of the threshold may be taken into account.

3.3.2.2. Optics calibration for incidence angle

The linear pulse energy measurement is the central keystone of the time-walk correction. Yet, this energy measurement is performed by another optics, distinct from the non-linear channel. In a perfect world, both the transmission of the non-linear and linear channel would have the same behavior over attitude. The linear pulse measurement could directly be applied to correct the time walk.
However, due to some implementation and design issues (like the completely different optical layout), the transmissions over attitude are not equal; further, the two specially developed radial filters are not equal either. For this reason, both radial filters have to be characterized in great detail in order to construct the correct transfer function from measured energy on linear channel to applied time walk correction.

Experiment description The laser bench provides pulses for both the reference start detector and the T2L2J2 instrument. The energy is held on a constant level and from time to time monitored by the reference energy detectors. The T2L2J2 optics, mounted on the two-axes motorized mount are exposed to the laser beam under a number of different incidence angles. Two basic scanning modes were performed: Circles, with a fixed incidence angle σ and a varying revolution angle ε, and straights, with a fixed revolution angle and a varying incidence angle (see Fig. 3.54 for angles denomination).

For the determination of the linear channel filter curve, the linear pulse measurements are used. For the non-linear filter, a somewhat more delicate measure of the incident energy

[26] Reminder: The linear detection threshold is the voltage, to which the detection (photodiode and amplifiers) output is compared to in order to decide whether a correct laser event has occurred or not. The threshold is adjusted as a function of the incident continuous background noise illumination.

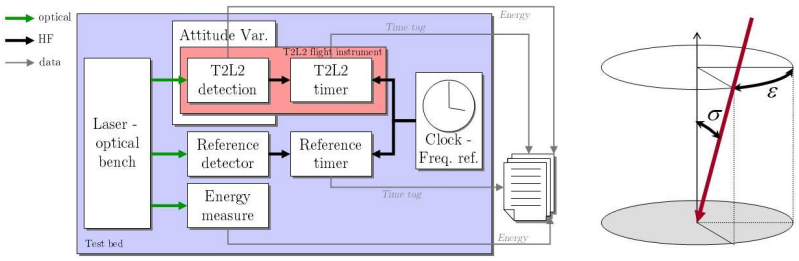

Figure 3.54.: Measurement scheme for the characterization of the two radial filters

is represented by the time walk. Both quantities are compared to their fixed reference counterparts, the reference energy measurement and the reference timing of Dassault, giving relative transmission. All possible incidence or revolution angle dependent defects of the other optics are as well attributed to the radial filters.

Results and discussion With the different datasets of circles and straights acquisition complete maps of the filters may be established, using appropriate interpolation techniques. Here, only the filter curves over the incidence angle σ, at ε=0° are presented. The analysis of

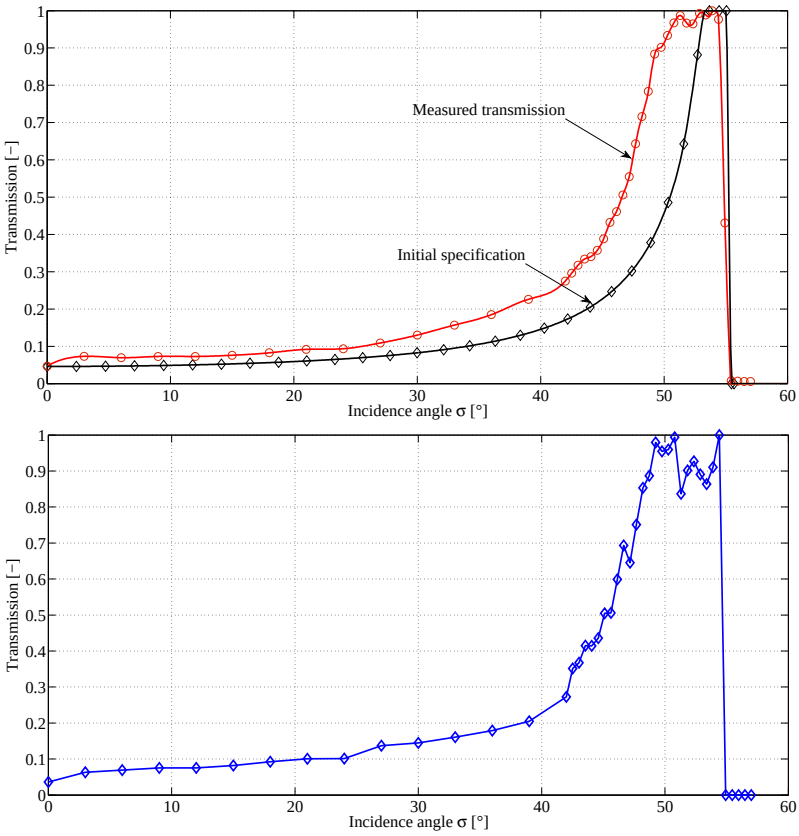

Figure 3.55.: Radial filter transmission for BOLI (above) and BONL (below)

the different acquisitions revealed in particular an important dependence of the transmission

on the revolution angle: Especially BOLI features quite big discrepancies, what may be explained by a possible misalignment of the filter itself with respect to the optical axis and some aberrations created by the lenses. A negligence of this fact would entail an error in the time walk correction on the order of 4 ps; otherwise, both the incidence angle AND the revolution angle would have to be used for the mapping of pulse measurement to time walk correction as a function of attitude.
The BONL filter also shows this revolution-dependent feature, but in a smaller extent.

A further discovered defect is a "dark spot" in the center of the filter, probably due to the production process; this will not influence the operation or performance of T2L2J2 at all.

Fig. 3.55 further shows the initial specification of the filter as the inverse function of station to satellite distance to the square, the atmospheric transmission and so forth, as pointed out in the description of the T2L2J2 instrument (Section 2.3.4). After assessment of some fabrication alternatives, SESO finally concluded that this specific form was not possible to be manufactured with the methods at hand. OCA and CNES eventually consented that the actual form would be sufficient. In this perception, the filter curves fully comply to the specifications.

3.3.2.3. Influence of polarization and incidence angle

At the level of the satellite, the polarization of the incoming laser beam is not known and may be regarded as random given the different processes that govern the polarization (initial state, laser station architecture, atmosphere and geometry). Unfortunately, the polarization may have several interactions with the optics and the detectors that may disturb both the pulse measurement and the timing. We may identify two major effects:

- A slight anisotropy of the optics' material (as a function of polarization and incidence angles) leads to a modification of entry/exit angle. This modifies the light ray trajectory in the optics, leading finally to a different time of arrival on the detector. (This effect concerns only the non-linear detector.)
- The Fresnel reflection on the optical surfaces alters the laser pulse energy as a function of polarization and incidence angles: This leads to a modified measured laser pulse energy and a modified time walk.

Both effects may in part mutually cancel or build up and are not distinguishable. The evaluation of the polarization issue is a rather complicated undertaking.

Experiment setup The setup is basically the same as for the evaluation of the filters as a function of incidence angle, described in the previous Section 3.3.2.2. Yet, the experiment pictured in Fig. 3.54 is repeated a second time with a modification of the incident polarization. Throughout the present tests, the incident polarization was always linear vertical, assured by the polarizing cube separators depicted in Fig. 3.6. These cubes are now turned by 90° to provide horizontal polarization.
Then, three straights (scanning over the incidence angle σ) at $\varepsilon = 0°$, 45° and 90° were conducted.

Analysis and discussion Now, in order to have some comparable quantity for both channels, the time walk on the non-linear and the pulse measurement on the linear were transformed

into transmitted power (or energy density, some arbitrary quantity) in front of the optics apertures by applying the filter curves derived in the last section. Of course, these are already affected by the polarization issue. To overcome this at least partially, only the filter curves of $\varepsilon = 0°$ were used for all other revolution angles and both polarizations; this, on the other hand, introduces some error due to the non-perfect rotational symmetry, what is minor as compared to the polarization effect, as we will see later.

Now, the resulting two times six curves (couples polarization - incidence angle for BOLI and BONL) showed something like linear trends of the calculated incident laser energy over the incidence angle (with some fluctuations).
Yet there was found a clear contradiction in the data: One expects that the mutual behavior of the curve couple H-0° (horizontal polarization and $\varepsilon = 0°$) and V-90° should be the same as for H-90° and V-0°; though this is not the case, for both BOLI and BONL.
We have to assume that the measurement set with vertical polarization is affected with some other systematic error (alignment error, for instance, what is not very improbable) and thus reject it.

Thus, in the following, only the horizontal polarization series are used. Fig. 3.56 shows the respective curves for BOLI and BONL; for more intelligibleness, I only show a linear fit of the different curves (that are subject to some fluctuations). The graph shows a mutual

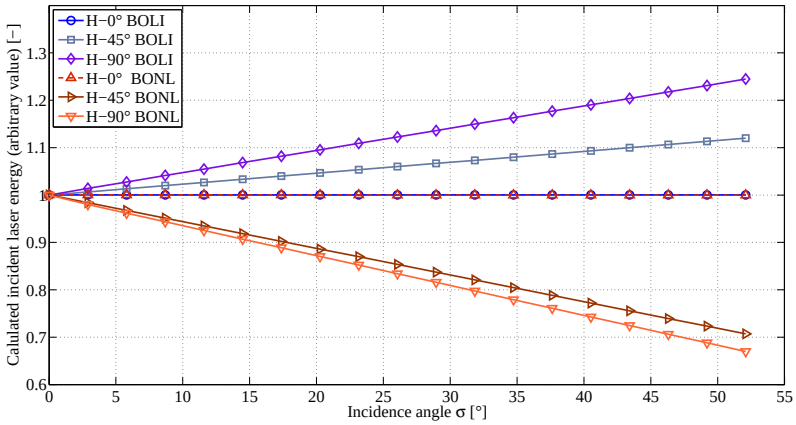

Figure 3.56.: Evolution of the apparent incident energy on BOLI and BONL over the incidence angle for revolution angles σ of 0°, 45° and 90°

behavior of BOLI and BONL in terms of energy measurement that goes apart like a pair of scissors; evidently, the mutual error is rather small for small incidence angles (less than 10% for $\sigma < 10°$ in the worst case H-90°) but grows up to 40% for $\varepsilon = 45°$ and 57% at high incidence angles (worst case $\varepsilon = 90°$).

This is yet a very big error that may occur in the linear pulse measurement as compared to the time walk and it is not sure that this outcome is exclusively due to the polarization or still some other effect (in particular related to the experiment setup itself). In any case we may claim that if ever polarization has an effect on the two optics BOLI and BONL, then it will be smaller or equal to the one shown in Fig. 3.56.

In order to assess the impact on the overall T2L2J2 measurement performance, we proceed: Assuming that neither very small incidence angles (close to nadir) nor very big ones (low elevations, low over the horizon) are very common during operation in orbit we may reduce the maximum error of $e_{\mathrm{pol}_{\max}} = 57\%$ with a normal distribution.

The polarization angle, however, has to be accounted for with a rectangular distribution since all angles are equally probable. This leads to an uncertainty of the linear energy measurement with respect to the non-linear measurement (i.e. time walk) [45]:

$$u_{\mathrm{pol}} = \frac{1}{3\sqrt{3}}\, e_{\mathrm{pol}_{\mathrm{max}}} = 10\% \tag{3.3}$$

Conclusion The results of the polarization experiments that we carried out on T2L2J2 turned out to be contradictory and difficult to analyze. Nevertheless, they permitted to put some upper bounds on the error introduced by the polarization. In the previous paragraph, the influence of the unknown state of polarization has been assessed to reach maximum worst values of 57% when comparing the chronometry measurement to the linear pulse measurement (the time walk should be corrected by the latter).
However, the error may be estimated to be smaller than 10% for the general time walk correction performance; this issue is addressed in more detail in the error budget (Chapter 5.1.2).

Generally, the analysis may be inaccurate due to the numerous assumptions: Yet it may be stated that the impact of the unknown polarization state will be below the mentioned level.

3.3.2.4. Effect of wide-field albedo irradiation

The T2L2J2 optics are designed to cover the whole visible Earth calotte with its FOV (field of view). This leads to an integration of an important amount of constant background photon flux due to the Earth's albedo, depending on weather conditions (cloud cover) and overflown region (oceans, land masses); the budget was even increased by the non-perfect neutral density of the radial filters due to the manufacturing process (see Fig. 3.55) as compared to the initial specification.

There is yet another apprehension that the noise budget could further be increased, due to the optics design:

- Multiple reflections in the optics (walls etc.) could cause more flux to be integrated by the detectors than specified;
- an effective FOV bigger than the specified $\pm 55°$ could further increase the integrated flux;
- both previous effects may lead to light rays with a steeper inclination than specified, notably on the interference filters; the latter are well less effective for higher inclination angles what entails a larger amount of noise background.

The wide field white noise source was designed just for assessing this topic.

Test setup, analysis and results The experiment setup is rather straightforward as depicted in Fig. 3.57. In a first experimental variant (on the left), the LED grid emits its radiation onto the T2L2J2 optics; the applied current is varied in order to cover some ten values of luminous flux. The actual flux generated by the LED under the different currents had previously been calibrated. The same exercise should have been repeated with the small diode based cw laser, i.e. the irradiation with different levels of laser power (on the right). Yet, this acquisition had inadvertently not been performed. However, in this context another

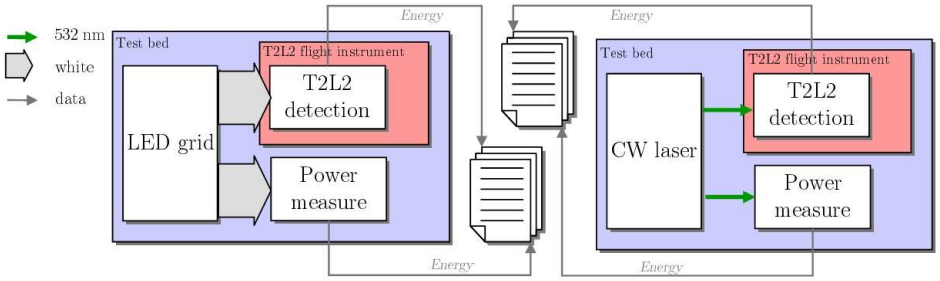

Figure 3.57.: Measurement scheme for the assessment of wide field white noise illumination

experiment is used, that employed the cw diode laser at a constant power, but with variable attitude. The corresponding "simulated" power variation is found by applying the BOLI filter curve.

The assessment of the wide field effect is carried out by the comparison of the T2L2J2 continuous signal measurement (TM_{CW} for cw telemetry) for the two different sources, wide angle and collimated. For the comparison, an equivalent measure of the flux has further to be calculated: Whereas the LED light is spectrally and spatially dispersed and thus will suffer from the spectral and radial filter, the laser light undergoes nearly no modification.

For the LED grid we first calculate the flux in the BOLI pupil (a theoretical pupil of 250 µm is used as a reference for confining the incident flux). During the design and test of the LED grid the luminous flux of one LED has been determined to be 1.4 lm (at 20 mA) instead of 1.6 lm as stated in the specifications (Table 3.4); this is not surprising given the actual operation temperature in the grid as compared to the suggestion of OSRAM. These luminous 1.4 lm correspond to 0.2 mW in radiometric terms, what had to be determined in a quite laborious calculus since information thereof could not be obtained from OSRAM.
The flux encountered in the pupil is calculated from the sum of all contributing LEDs:

$$\Phi_{\text{grid}} = \sum_i d\Phi_i = I_{\text{LED}} \cdot dA \cdot \sum_i \frac{\cos\sigma_i}{r_i^2} n_i \tag{3.4}$$

where I_{LED} is the luminous intensity of one LED, dA the small BOLI pupil, σ_i the incidence angle of the rays from LED i (like in Fig. 3.54), r_i the respective distance from pupil to LED i and n_i the number of LEDs in the i-configuration.
One calculates a luminous flux of 1.5 mlm (at 20 mA per diode) in the 250 µm pupil of BOLI, what corresponds to a radiometric flux of 4.9 µW. This means a flux density of 27.8 W/m^2 in the vicinity of the BOLI and BONL apertures.

For the analysis, we now proceed to the calculation of an equivalent flux by taking into account both the spectral filter (transmissivity T_{SAGEM} depending on the emitted spectrum of the LEDs and the filter response) and the radial density filter (T_{RD} depending on the incidence angle σ) and modify Equation (3.4) in the following way:

$$\Phi_{\text{grid}_{\text{eq}}} = I_{\text{LED}} \cdot dA \cdot T_{\text{SAGEM}} \cdot \sum_i \frac{\cos\sigma_i}{r_i^2} T_{\text{RD}}(\sigma_i) \cdot n_i \tag{3.5}$$

Only a third of the initial flux passes through the radial filter and the overall transmission of the whole LED spectral flux through the SAGEM line filter is of 3.75% (compare to Fig. 3.58). The equivalent flux is now: 0.35 W/m^2 (at 20 mA per LED). At this operation

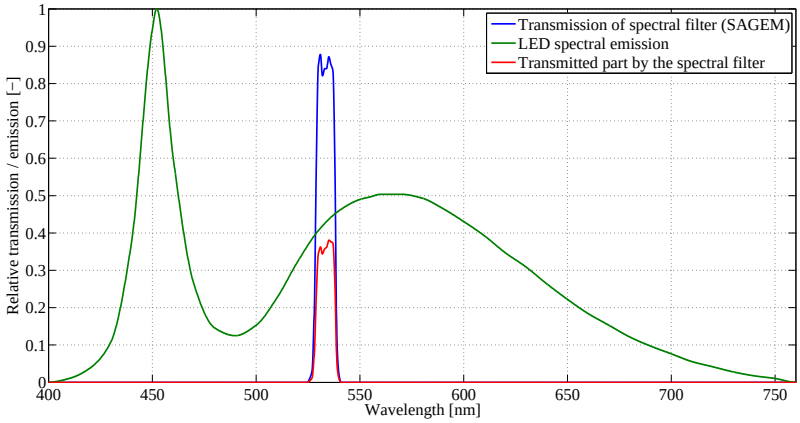

Figure 3.58.: Spectral emission of the OSRAM LED and spectral transmission of BOLI spectral filter

point of the LED grid, the T2L2J2 instrument measures a cw flux with $\mathrm{TM_{cw}} = 0.15$ V. The different luminous levels of the grid are plotted in Fig. 3.59 (circles), along with the respective T2L2J2 measurements.

For cw diode laser, a similar equivalent flux has to be calculated, only taking into account the geometry of the laser beam (Gaussian distribution)

$$\Phi_{\mathrm{las_{eq}}} = T_{\mathrm{SAGEM}} \cdot T_{\mathrm{RD}}(\varepsilon = 0) \cdot P_{\mathrm{total}} \left(1 - \exp\left(-2\frac{R^2_{\mathrm{BOLI}}}{w^2}\right)\right) \tag{3.6}$$

with P_{total} being 92 µW and the beam waist $w = 3.6$ mm.
This gives an equivalent flux density of 0.21 W/m^2. For this point, the T2L2J2 measurements gives: $\mathrm{TM_{cw}} = 0.071$ V.

We may finally trace all acquired data points of the two different acquisitions, what is depicted in Fig. 3.59. As mentioned above, the measurements at different Firefly-laser power levels were materialized by a variation of the incidence angle σ (and hence T_{RD}) instead of a variation of the power itself.

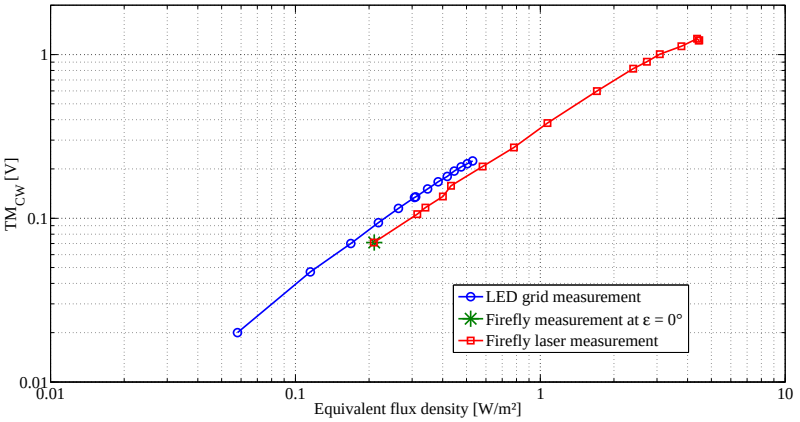

Figure 3.59.: Comparison of the cw flux measurement of T2L2J2 from LED and laser sources

It is clearly visible that there is an offset of about 20% between the measurements performed by T2L2J2 for the LED irradiation as compared to laser irradiation.

Discussion Yet, before drawing conclusions, one has to admit that the concordance of these two different measurement schemes of less than 20% is already an achievement. There is a whole set of error sources in the measurement and in the calculation of the LED irradiation, starting from the determination of the effective luminance, its conversion in radiometric quantities over the geometric calculus of the grid to the equivalent flux; the analysis of the laser is somewhat more straightforward, but the substitution of a power variation by an attitude variation does not help to improve the outcome.

The same philosophy as in the last section shall be applied by putting some bounds on the investigated effect: If ever there is an effect, it will be lower or on the order of what we see in Fig. 3.59: T2L2J2 measures about 20% more flux when irradiated with a spatially and spectrally extended source as compared to a collimated single wavelength source.
This entails that there seems to be an effect as described in the beginning of this section, like multiple reflection in the optics or a wider FOV than specified. Yet, the effect is not very important and will not represent the least problem during operation.

3.3.3. Conclusion of calibration measurements

The calibration tests, mostly performed during the test campaign at CNES, permitted to dispose of a huge set of high quality measurement data that will be employed for the reduction of the raw data of T2L2J2. They further allow to ameliorate the T2L2J2 data to a high degree. The obtained data pool is very rich and will provide a basis for investigation when unexpected problems appear during the exploitation of T2L2J2.

These calibrations, whereof the ones described here represent only a part, together with the determination of the performance of the T2L2J2 instrument allow to state that the test campaigns represented a genuine success in the development cycle of the T2L2 on Jason 2 experiment.

4. The T2L2 ground segment: Laser station

4.1. Three examples of laser stations

The ground segment and its performance is of equal importance in the T2L2 scheme as the space instrument itself. Its impact on the quality of the time transfer is assessed in the Error Budget, Chapter 5. This chapter gives a short illustration of its composition and functioning.

Since there is, apart from the need to provide full data, no principal difference to a standard satellite laser ranging (SLR) station, only a short introduction will be given, without going into too much detail of the instrumentation (the ground segment of T2L2 is neither part of the present thesis work).

In the first part some examples shall be pointed out: First, MéO station of OCA will be described since it is the reference station of the T2L2 scheme. Then OCA's mobile station FTLRS (French Transportable Laser Ranging Station) will be addressed; the FTLRS may be displaced to some location where are located interesting clocks (a campaign with the Observatoire de Paris is in preparation). Last, the German Wettzell station will be addressed. Then some indications about needed calibrations of the respective stations shall be given (Section 4.3); this is an ongoing activity but is not treated in the present thesis.

4.1.1. MéO on the Plateau de Calern

The MéO laser ranging station on the Plateau de Calern is the rejuvenated Laser-Lune station that permitted over nearly thirty years to range the moon and geodetic satellites with unequaled precision and accuracy.

In the framework of an operation for the evolution of satellite laser ranging at OCA, it was decided that the Laser-Lune station should undergo some modifications and enhancements. This activity concerns primarily the motorization (azimuth and elevation) of the telescope in terms of speed in order to follow low earth orbit satellites and to increase the covered field around the zenith direction[1]. A further goal of the motorization and control modification is an aimed pointing amelioration; this is necessary in order to improve lunar laser ranging (LLR) and a prerequisite for interplanetary (one-way) ranging. I should not fail to mention the renovation of the dome of the telescope that proved to be absolute necessary; this operation further includes the dome motorization (the dome has to follow the azimuthal movement of the telescope) as well as a new concept of wheel bearing.

Another aspect of the renovation is the migration of the former three distinct lasers onto one common setup on one optical table (for regular operation) as well as the provision of

[1] For azimuth-elevation mounted telescopes satellite passes near the zenith are difficult to track since the azimuth has to turn very rapidly when the object passes at the highest point of the track (culmination). This usually leads to "dead" zones that cannot be covered by the system; after losing track of the object around the zenith, these systems usually catch up the object on its way down towards the horizon.

dedicated labs with access to the telescope for a profound R&D activity in different sectors. The MéO team has further an ongoing instrumental research activity concerning fast commutation between the laser receive and return paths.
A further activity is the adaptation of the existing informatic infrastructure to the needs of SLR and the R&D aspects.

At the time of the preparation of this document, this rejuvenation operation is in full progress. This activity will stretch over some more time, but a partial implementation became ready for the early operation with T2L2 on Jason 2. In the following, the MéO station as it will be configured for operation starting in July 2008 will shortly be described.

4.1.1.1. The laser(s)

The MéO station presently disposes of two flash-lamp pumped mode-locked Nd:YAG resonators with a common amplifying stage. The basic principle is as follows: The cavity basically consists of an Nd:YAG rod (the lasing material) between two mirrors (M1 and FP1 in Fig. 4.1). The optical pumping creates a population inversion in the rod and the appearance of laser light that is reflected back and forth between the mirrors. This light builds plane standing waves (or axial modes) with the resonator length L being an integer multiple of the wavelength: $L = q\frac{\lambda_q}{2}$ $(q = 1, 2, 3...)$. In free-running operation, the axial modes in a laser cavity have statistic and temporally variable phase relations to each other. Constructive and destructive interference of the intensity amplitudes may provoke strong intensity fluctuations that are even more amplified by the amplification in the laser rod. It is possible to force a constructive interference of adjacent axial modes in order to, for each resonator round-trip, constructively superpose the intensity amplitudes in one point: By this means it is possible to fabricate short pulses with high intensities. Equation (4.1) gives the time dependent intensity amplitude of the electrical field, composed of a sum of N adjacent axial modes with the frequency f_q [46, p. 303]:

$$E(t) = \sum_{q=q_0}^{q_0+(N-1)} E_q \ \cos(2\pi f_q t + \varphi_q) = \sum_{q=q_0}^{q_0+(N-1)} E_q \ \cos\left(2\pi q \frac{t}{T} + \varphi_q\right) \tag{4.1}$$

with the resonator round-trip time $T = 2L/c$. For $\varphi_q = 0$ and a big number N of modes, a single short pulse is reflected back and forth by the resonator mirrors.
The pulse width of the laser pulse is limited by the time-bandwidth product:

$$t_{\mathrm{FWHM}} \geq \frac{K}{\Delta f} = \frac{K}{N}\frac{2L}{c} \tag{4.2}$$

with the factor K being dependent on the form of the wave packet (≈ 0.44 for Gaussian pulse form) and the number $N = \Delta f \frac{2L}{c}$ of modes in the given laser line width Δf of the material.

The typical mode-locking techniques rely on the principle of increasing the losses of uncoupled modes with respect to those who contribute to the constructive interference. One of the two resonators of the MéO station works with a double technique, an active-active modelocking. This high-power 200 ps laser is intended for use in Lunar laser ranging.

Shorter pulsewidths may only be obtained with passive mode-locking techniques: The second MéO resonator is based on an active-passive scheme. The setup is depicted in Fig 4.1, the resonator is delimited by mirror M2 and a Fabry-Perot FP2; the Fabry-Perot both

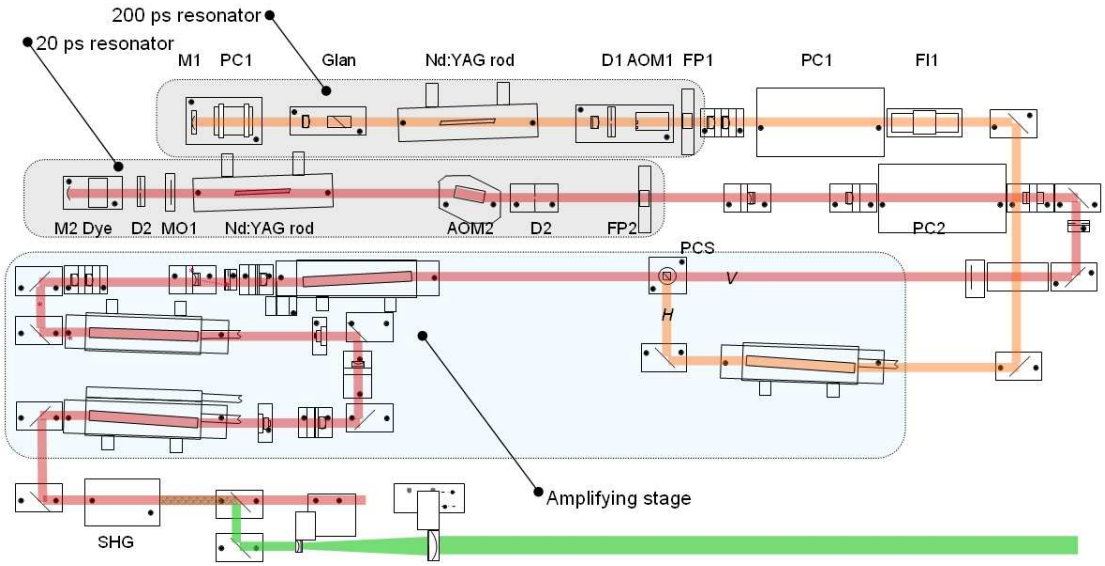

Figure 4.1.: MéO lasers for regular ranging operation on satellites and moon. The space in the lower part of the optical table is reserved for the projected commutation and detection setup.

delimits the number of possible modes N and serves as an outcoupling mirror of the pulses. An acousto-optic modulator (AOM2) is placed in the cavity that modulates the resonator losses with the frequency $f_{\mathrm{mod}} = \frac{c}{2L}$. The passive mode-locker is represented by the saturable absorbency of a dye, that is dissolved in a circulating liquid. If the light fluence exceeds some threshold, the dye abruptly becomes transparent and permits the preponderance of the right modes. By this means, the resonator delivers pulses whose length is only limited by the spectral width of the Nd:YAG material, that is 20 ps. The resonator further contains a diaphragm (D2) in order to select only the TEM_{00} transversal mode that features a Gaussian profile over the beam diameter. The emitted pulse train is also cut in single pulses by an EOM (PC2), before being transmitted in the triple amplification stage (consisting in some amplifier Nd:YAG rods).

Both lasers share the same amplification stage by the means of operating one resonator in vertical, the other in horizontal polarization: Both beams are then combined in a polarizing cube separator, that reflects horizontal and transmits vertical polarization. After amplification, the 200 ps pulses feature about 400 mJ energy whereas the 20 ps carry about 100 mJ due to their shortness. The pulses then pass in a frequency doubling crystal. The MéO laser uses a crystal of the KDP type (Potassium-Dihydrogen-Phosphate KH_2PO_4), with a doubling efficiency of up to 50%.

Finally, a dichroïc mirror (DM) separates the laser light into a green beam with either 200 mJ or 40 mJ pulses (depending on the resonator) and an infrared beam. In the actual configuration, the IR beam is not used but in the past, both IR and green delivered range data of the moon (despite the fact that the green detectors featured a better precision).
The green beam is then sent to the telescope base where it is directed into the vertical (azimuthal) axis.

A small fraction of the IR pulses is used to trigger the start detector, generating the start time tag t_s.

4.1.1.2. The MéO telescope and detection device on Nasmyth table

The MéO telescope is of common architecture for the transmit and receive path and of a Cassegrain-Nasmyth type with a focal distance of 32 m. Its primary mirror is of parabolic form and measures 1540 mm in diameter; the secondary mirror (hyperbolic) is suspended on a triple-legged spider at the output of the telescope tube and measures 290 mm. The tertiary, plane mirror (330 mm) is located in the elevation axis. Fig. 4.2 shows the path the laser light takes from the telescope base up to its output: The laser beam, coming from the laser laboratory, is directed in the vertical axis; then, via a mirror suspended from the telescope azimuth mount, it is directed through the telescope foot, until arriving at the elevation axis. Here, the laser beam falls on a rotating mirror (RM1) that swaps between transmit and receive path. In the transmit state, the laser beam is directed to the tertiary mirror of the telescope. In the receive state, the light arriving on the elevation axis

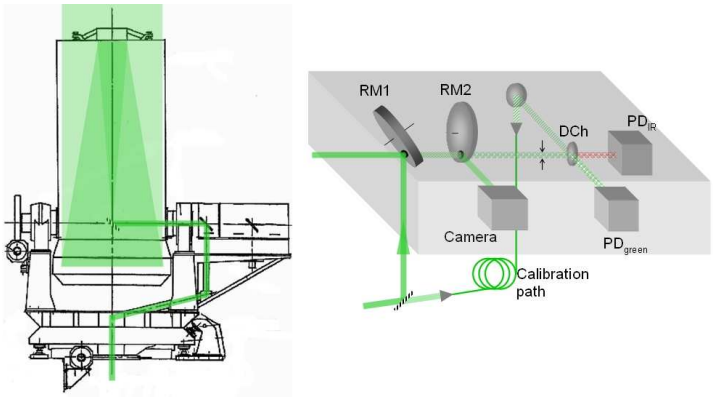

Figure 4.2.: Cross-Section of the MeO telescope and synopsis of the Nasmyth table

passes through a hole in the rotating mirror RM1. When an echo from a satellite or the moon is expected (this is calculated, see below), the returning photons pass through the hole of a second rotating mirror (RM2). After passing through an adaptable iris for field (and therefore noise) reduction, they fall on a dichroïc mirror (DCh). This mirror separates infrared from green photons (if IR light is transmitted) that, after passing narrow spectral filters for further noise reduction, are directed on the respective detectors. For the nominal green operation, MéO uses a Silicon Sensor APD (SSOAD230) in Geiger mode which has a precision of about 40 ps in single-photon mode. It is envisaged to implement a time-walk correction of this APD (or another) by measuring the photon level as in T2L2 [47] with a second, linearly operated APD.
Most of the time of the receive state, the second rotating mirror reflects the incoming light onto a camera that is used by the operators to manually re-align the telescope (with the aid of stars and additionally with moon craters for LLR).

In the framework of the laser ranging augmentation operation it is planned to relocate both the commutation assembly and the detection devices on the same optical table as the laser. The actual Nasmyth table that houses these two setups will be replaced by two separate Nasmyth benches that may be used for direct observation with the telescope (apart from laser ranging). A project with an astronomical camera (the Andor used for the T2L2 characterization) and image derotator is in preparation at OCA. Fig. 4.3 shows an overall view of the future MéO telescope.

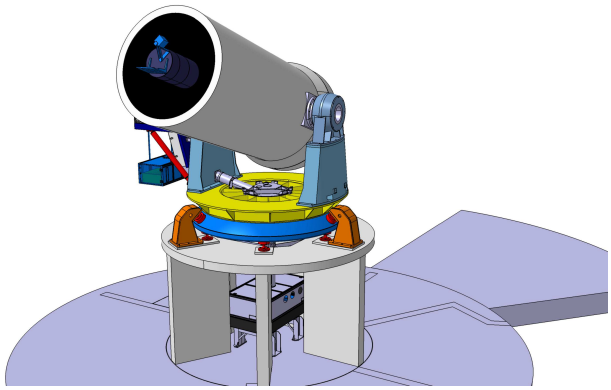

Figure 4.3.: View of the MeO telescope

4.1.1.3. Timing, time base and operation

All electronic signals from the detectors of the laser ranging scheme are directed to an ensemble of two event timers of Dassault Electronique (today THALES), giving the time tags of laser departure (start) t_s, laser return t_r and calibration t_{Cal} (see Section 4.2). The event timers rely on a 10 MHz reference signal coming from the OCA-Calern time/frequency laboratory's master clock, an HP 5071A Cesium standard. The event timers are also synchronized by the T/F lab, via a PPS signal. For absolute time transfer, as it is needed to perform calibrations of other time transfer systems such as GPS or Two-Way, the delay between the master clock and the SLR timer has to be known accurately. This calibration is outlined in Section 4.3.

The laser ranging (SLR and LLR) principle is as follows (and equally valid for time transfer): With the aid of very precise satellite (or moon) ephemerides[2] a set of observable passes is determined. On the specified time, a human observer prepares the telescope (pointing calibration) to follow the calculated pass; the operator has further the possibility to slightly modify the pointing in order to increase the photon return efficiency (when the prediction is not optimum).
Based on the start time $t_{s,i}$ of a laser pulse i and the ephemerides, the software calculates an expected return time $t_{r,i_{\mathrm{exp}}}$; the non-linear return detector is activated some 100 ns around the expected time of return of the photons: This is the third employed filter technique (apart from spatial and spectral filtering) in order to decrease noise events.
For a long time it has been usual to reduce the obtained data (the calculated round-trip time) into a "Normal Point" of several minutes (depending on the target) acquisition time. Today, as computer memory does not represent any problem, it should become usual to provide the so-called "Full-Rate Data". In order to exploit the time transfer, it is necessary to dispose of these full-rate data.

[2] These ephemerides usually are provided by the ILRS prediction centers of NASA or the BDL (Bureau des Longitudes).

4.1.2. The French mobile station FTLRS

The French transportable laser ranging station (FTLRS) may be called the exact opposite to the MéO station when it comes to its physical dimensions. The FTLRS [48, 49] was designed during the 90s aiming an extremely high mobility and to be operational after very short installation time.

The FTLRS features a common transmit/receive telescope of Cassegrain type with the tertiary mirror behind the primary thus ensuring a very short tube. The diameter is of only 130 mm. The laser, also of Nd:YAG type consists of an active/passive modelocked resonator and only one amplifier, but still ensuring green 20 mJ pulses of 30 ps length. As detector, a time-walk compensated SPAD is used. The FTLRS station has been largely used

Figure 4.4.: The mobile station FTLRS in Burnie, Tasmania

for the so-called CalVal campaigns of ocean-altimetry satellites such as TOPEX/Poseidon and Jason 1. It has successfully performed several such altimetry calibration campaigns in Corsica, Crete, Brest and Tasmania. The FTLRS will also be of a vital role for the T2L2 on Jason 2 experiment, notably with dedicated campaigns at timing labs (as the Observatoire de Paris: LNE/SYRTE).

Figure 4.5.: The Wettzell WLRS station in Germany and its telescope (photographs taken from [50])

4.1.3. Wettzell laser ranging station

The WLRS system of the Fundamentalstation Wettzell is based on a 750 mm telescope in common transmit/receive scheme. It has been designed to range to artificial satellites and to the moon.

The diode-pumped Nd:YAG laser provides 80 ps pulses of 360 mJ at repetition rates of 10 to 20 Hz and 30 mJ at 50 Hz. The systems features a triple detection system, offering three types of detectors, a micro-channel plate, a photomultiplier and an APD.

4.2. Calibration of a laser station

Just as any instrumentation, and especially as the T2L2 instrument, also the ground instrumentation undergoes variations. These are principally due to thermal variations of the employed electronics (detectors, circuits and timers) that entail alterations of the transit time. There are further effects like variations in the laser power or in the polarization voltages of the detectors that may result in further instrumental biases.

A regular calibration of the instrumentation is therefore employed in order to overcome these instabilities. In classical SLR one simply measures a well-known distance that may be delimited by an additional target (retroreflector). One distinguishes between internal and external calibrations: In internal calibrations, the reference is located somewhere in the optical instrumentation; very often a corner cube retroreflector is located in the telescope tube to redirect a fraction of the laser pulse on the return path. External calibrations use retroreflectors that are some tens or hundreds meters off the station.
In both cases, the distance between the station reference point and the target are determined with another technique; internal targets are often simply measured with a meter, whereas external targets are measured by employing a geodetic survey. In laser ranging stations, the geometrical reference point is typically the axes crossing of the telescope.
By the means of this geometric calibration all time delays between the start and the return detection are subtracted from the overall measurement; this means that the resulting round-trip-time refers to the distance between the station's reference point (the telescope's axes crossing) and the satellite reflector.

Throughout the SLR community, the calibrations are performed in different manners, depending on the ease of implementation and operation of the respective method. Very often, both internal and external calibrations are feasible, but one technique is preferred over another.

MéO The MéO station features both a double internal technique as well as external targets: Though the telescope is equipped with a corner cube mounted on the spider of the secondary mirror, this technique may not be used in real-time since multiple reflections inside the tube (on other objects) exacerbate distinguishing the return signal, especially when working in single-photon mode[3]. A second internal method is employed on a regular basis, parallel to each satellite ranging acquisition: An optical fiber collects the spill-over of the transmit pulse through the Nasmyth mirror and directs it onto the return detection. There are further several external reference targets on the Plateau de Calern, located at 330 m, 1.5 km, 2.5 km and 8 km[4], respectively and in different directions. Their distances have last been determined in the years 1998/99 on a centimetric or subcentimetric level by the IGN. From time to time, the different techniques are compared.

[3] In order to perform the calibration properly and to account also for the return detector's time walk, the return detector has to be operated on the same photon level as for the satellite measurements. This is another point the (human) operator of the SLR has to respect and to monitor: Many Nd:YAG based laser systems feature an evolution of the output power especially during warm-up, what can lead to an unwanted bias in the calibration measurement; also here, the operator usually has to put in neutral density filters in order to attenuate the power on the return detector.

[4] The last mentioned target may not be employed for an accurate calibration since the atmospheric propagation is less understood then necessary [49].

FTLRS The mobile station of OCA also features an internal calibration, with a small displaceable corner cube at the telescope exit. Though giving good results in terms of measurement dispersion (r.m.s. of 70 ps and a stability of 20 ps after 30 min of operation [49]), its operation is too demanding to be employed in a systematic manner: It is necessary to diminish the laser energy by modifying the fluorescence between the oscillator's and the amplifier's Nd:YAG rods and inserting neutral density filters in front of the amplifier; further neutral density filters have to be put in front of the return detector.
As a consequence, an external calibration is performed. For an external calibration it is necessary to put up a retroreflector and to measure its distance with a geodetic survey. A set of external calibration acquisitions is usually performed before and after a set of satellite passes. During the last campaign in Burnie, Tasmania, the two techniques, internal and external, agreed on a level of about 3 mm what corresponds to an uncertainty of 20 ps (see Section 5.2 in the Error Budget).

WLRS The situation of the WLRS is quite similar to MéO's: The operation of an internal target in the telescope tube is complicated by multiple reflections. The Wettzell team uses also an optical fiber to extract a fraction of the transmitted laser pulse from the back of a mirror; in contrast to MéO, this is performed shortly after the laser, before the coudé of the telescope. The geometrical distance from this point to the axes crossing is measured with a meter and assumed to be invariant over time and telescope movement.
Some external targets are also available to perform regular comparisons between the two methods.

The calibration measurement yields four measurement quantities: the usual start time tag t_s, the calibration return t_{Cal}, the geometrical distance d_{Cal} and the index of air n_{Air} that has to be assessed in more detail the more distant the reference target is located. The quantity $t_{\mathrm{Cal}} - t_s$ is usually averaged over a certain time; in the time transfer Equation (1.1) of T2L2 it may be subtracted from the laser pulse round-trip-time $t_{\mathrm{Roundtrip}}$ from telescope axis-crossing to the satellite reflector:

$$t_{\mathrm{Roundtrip}} = t_r - t_s - \langle t_{\mathrm{Cal}} - t_s \rangle - \frac{2\ d_{\mathrm{Cal}} n_{\mathrm{Air}}}{c} \tag{4.3}$$

Recommendation In order to perform time transfer with T2L2 on a high level of accuracy, the procedure of a reliable SLR system calibration is, together with the following section, of preponderant significance. Apart from preventing biases due to non-perfect operation (non-single photon on the return detector, for instance) it is noteworthy that the geometric distances d_{Cal} have to be known on a sub-centimeter scale in order to fit in the envisaged uncertainty budget of some tens of picoseconds (compare to Chapter 5.2). In this context it seems reasonable to re-evaluate these values.
A workaround for this measurement could be to make this d_{Cal} common for both calibrations, the SLR system calibration and the inter-calibration between the time/frequency equipment that is described in the next section.

4.3. Calibration of time/frequency system vs. laser station

This section highlights another, new problem that has to be addressed when aiming to perform an accurate time transfer with T2L2 and in particular when aiming to calibrate existing RF time transfer techniques.

In most space geodetic institutes, the time infrastructure (clocks, distribution and comparison as GPS/TWSTFT) and the SLR timing systems (start and return event timer) are located in separate and remote places.
The clock signal (PPS) issued from the local time frame (a local UTC, for instance) or directly from GPS equipment is mostly distributed by a coaxial cable or an optical fiber. The delay Δt_{PPS} between departure from the time/frequency physical reference point (connector of a distribution amplifier, e.g.) and arrival at the event timer of the SLR system is mostly evaluated with a precision on the 10 ns to 100 ns level (by measuring cable lengths). This means that the epoch at what the timing was performed is known at this level of exactitude what is sufficient for satellite laser ranging.
In order to compare local timescales of different SLR stations (like UTC(IFAG) in Wettzell or UTC(Calern)[5]) or singular clocks in an exact manner, one has to determine this delay Δt_{PPS} very accurately. The goal is an uncertainty of less than 50 ps.

OCA proposes a dedicated calibration campaign associated with dedicated equipment. This calibration will allow to determine exactly the temporal distance between the two different four-dimensional reference points of the time/frequency and the laser ranging systems as given in Table 4.1:

Table 4.1.: The different nature of the reference points of a time/frequency lab and an SLR system

Reference	T/F lab	SLR system
Spatial	Connector (BNC)	Telescope axes crossing
Temporal	PPS pulse $t_r > 20$ ns	Laser pulse $t_r \approx 10$ ps

4.3.1. Time/frequency laboratory

In this section, the typical architecture of a time/frequency lab is presented by means of an example. Fig. 4.6 shows the layout of the physical realization of UTC(IFAG) in the Fundamentalstation Wettzell. Typically, as presented in the schema, one Cesium frequency standard (usually the most stable) is selected to work as the Master Clock. The Master Clock performs a time comparison via GPS (in this case). All other clocks (Cesium standards and H-Masers) are compared to the Master via a time-interval counter. All these comparisons are stored and regularly reported to the Bureau International des Poids et Mesures (BIPM). The BIPM that calculates the Coordinated Universal Time (UTC), regularly publishes the temporal offsets between UTC and UTC(k) in its Circular T (a sample of this Circular T is given in the Appendix, Table A.2 on page 199). The phase of the Master Clock signal is regularly steered with the aid of a phase microstepper in order to smoothly follow UTC.

In the case of UTC(IFAG) the regular time transfer is performed via GPS (TTR6 monochannel) and thus with UTC(USNO) (USNO is in charge of the GPS time). In another time laboratory this could be performed with another GPS receiver (multi-channel) or with

[5]Note that officially, an UTC(Calern) does not exist, albeit it is physically implemented.

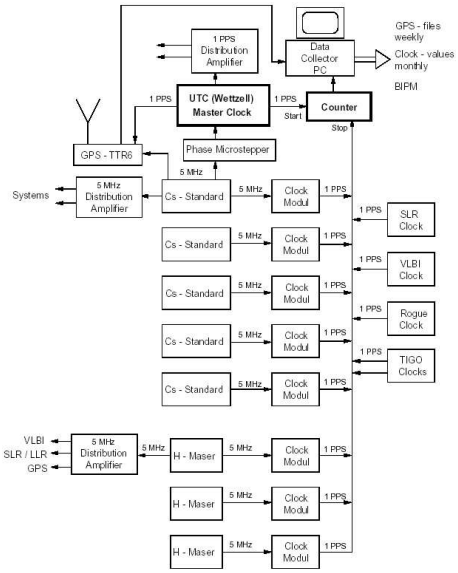

Figure 4.6.: Overview of the physical realization of UTC(IFAG) at Wettzell (from [50])

Two-Way (TWSTFT).
In any case, for the calibration of these techniques with T2L2 it is interesting to know the aforementioned spatial reference point. The GPS receivers employed for time transfer usually feature an internal time-interval counter and determine the Δt between the PPS decoded from the GPS signal and the PPS coming from the external Master Clock. These systems are regularly calibrated by additional calibration GPS receivers of the BIPM that travel from time lab to time lab (for internal, cable and antenna delays, for instance).
The reference point that may bu used by T2L2 for an additional, optical calibration is therefore the input PPS (clock) connector of the GPS (or other) receiver. The next section will show how this reference may be attached to the SLR system.

4.3.2. Calibration equipment

The calibration may be performed in several ways, with a passive method profiting from the station's laser pulses or with an active method. The preparation of some calibration equipment is right underway at OCA but is not a part of the present document.

4.3.2.1. Passive calibration method

The passive calibration scheme consists in the timing of both the PPS (of the Master Clock) and of the transmitted laser pulse in their respective reference points and to determine the temporal delay between the two events in an absolute manner.

The first difficulty is to transform the PPS signal into some temporally better defined signal that may be fed to an event timer (in the case of the Dassault used by OCA, the signal format is a negative ECL pulse). This is because the PPS signal is of a rather asymmetric form with a very slow rise time: Fig. 4.7 shows the leading edge of a typical PPS pulse of the OCA time lab. The length of the pulse is around 10 µs. It is difficult to define where exactly the temporal reference point is situated when it comes to picosecond

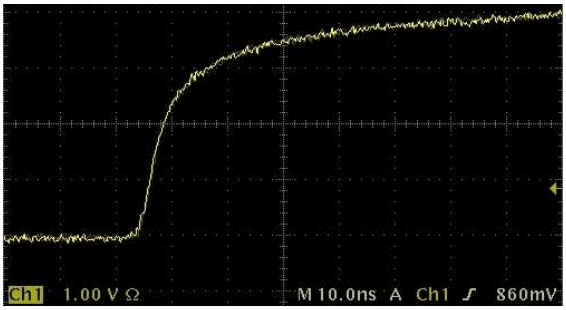

Figure 4.7.: Leading edge of a typical PPS pulse (abscissae division is 10 ns)

resolution. It may defined as the signal crossing of the half pulse value (half of top voltage minus lower voltage) or as well the point of steepest slope. A more viable reference is of course represented by the zero-crossing of the 5 or 10 MHz output of the clock, but the PPS has at least to be referenced once against this signal since it represents the temporal reference of the time transfer (this method was used for the LASSO comparisons to GPS and TWSTFT). Furthermore, the very flat signal slope of 100 ns of the clock sine signals would give a very noisy measurement.

Another feat will be represented by the accurate determination of the transit time of these PPS to ECL conversion electronics: This may be performed by the use of extremely fast circuits (tens of GHz bandwidth) whose transit and reaction times are well specified by the manufacturer. This approach may be complemented by some experiments on the employed circuits with a high bandwidth oscilloscope (50 GHz) that OCA acquired for the development of similar electronics in the ILIADE project (see Chapter 8.1).
Along with the electronics, all cable delays have to be determined. It is further preferable to transport the PPS pulse only over a short cable length before it enters the timer in order not to alter it too much (The PPS pulse has a very complex spectral response which is distorted by the propagation through a cable.)

The second, more complex difficulty is the timing of the laser pulse: Also here, all transit times in the used photodetector and associated electronics and cables have to be determined; defying any direct measurement, the transit time in the active region of a detector has to be modeled. The most straightforward detector to model is probably a photo-multiplier tube, since the process is rather simple. However, these devices are of rather big dimensions, so any relative errors become equally important. A semiconductor-based detector, such as a PIN photodiode may be of a very small size, such insuring smaller modeling errors. Equation (4.4) gives an approximation of the typical rise time t_{rise} of PIN photodiodes [51, p. 10].

$$t_{\mathrm{rise}} = \sqrt{t_{\mathrm{transit}}^2 + t_{\mathrm{RC}}^2 + t_{\mathrm{diff}}^2} \tag{4.4}$$

with t_{RC} being the time constant of the terminal capacitance C_{t} of the diode and the load resistance R_{L}: $t_{\mathrm{RC}} = 2.2\ C_{\mathrm{t}} \cdot R_{\mathrm{L}}$ and t_{diff} the diffusion time of carriers generated outside the depletion region. Since the rise time is governed by the transit time t_{transit}, it is therefore preferable to work with a fast PIN diode. Besides, its architecture is simple and its active area is small, thus ensuring smaller errors on the model. The use of a PIN over an APD is further advantageous because the multiplication process in an APD is more delicate to model than the simple relation between incoming photon number and generated carriers in

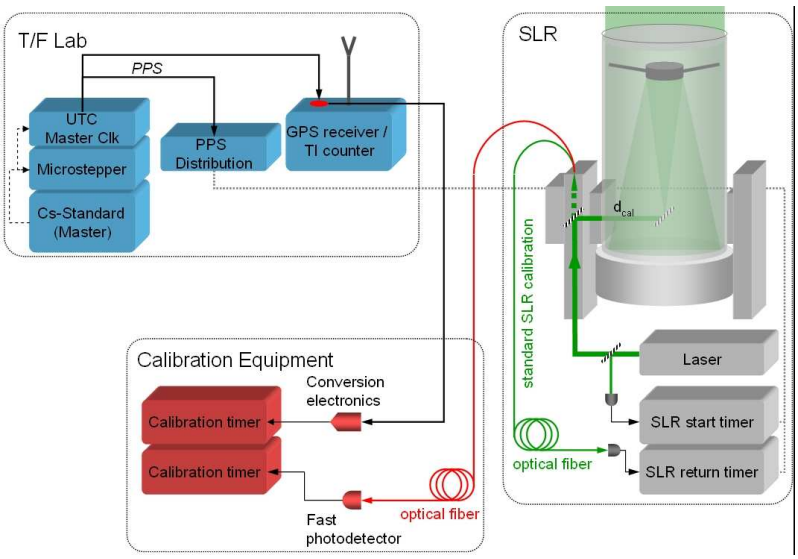

Figure 4.8.: Passive calibration method for absolute referencing of the SLR system to the time/frequency system

a PIN.
In any case it would be desirable to compare different detector types for their models along with comparative, relative transit times measurements.
The output of the detector (similarly to the PPS pulse) has to be fed to a comparator circuitry whose transit times have to be determined as described above. Further, since it is desirable to locate the event timer assembly close to the PPS reference point (and source), it seems reasonable to collect the laser pulse at the SLR's reference point (for instance the telescope's axes crossing) and to propagate it in an optical fiber until the detection circuitry. As mentioned at the end of the previous section, it is preferred to gather the laser light at the same spot as for the SLR calibration thus removing the geometrical distance d_{Cal} from the error budget.

By the means of this procedure, the complete time transfer is referenced to the PPS, both in time and geometrically. Fig. 4.8 shows the synopsis of this calibration scheme:
The SLR system (here MéO) performs its proper calibration by extracting a part of the transmit laser pulse at the Nasmyth mirror - this fraction is guided to the return detection and timing giving finally t_{Cal} (see previous section). The calibration between the time/frequency and the SLR systems may use the same spot for extracting a further fraction to be timed by a fast photodetector whose transit time is known on a picosecond level. The PPS pulse is also transformed by some electronics whose transit time is perfectly known and timed. By this means the complete SLR system is referenced to the time/frequency system.

Table 4.2 gives a summary of the proposed equipment.

4.3.2.2. Active calibration method

A second method is, instead of using the conventional SLR laser pulse, to employ a fast modulated laser diode situated in the SLR reference point. A pulse generator triggers the diode to produce a laser pulse that travels to the SLR return detector. Both the pulse from the generator and the PPS are timed with an event timer, as in the passive scheme.

Table 4.2.: Needed equipment for the calibration and special requirements besides the absolute knowledge of their transit times

System	Equipment	Special requirements
Time/frequency	Coaxial cables	Short
	Conversion electronics	High precision on PPS
	Event timer	-
SLR	Insertion optics	-
	Optical fiber	Low thermal expansion
	Photodetector	Fast rise time
	Electronics	Short reaction & transit time
	Cables	Short
	Event timer	-

This method represents an alternative but also here, some serious modeling work has to be performed. It seems even more delicate to model the transition time in a laser diode than the transit time in a photodiode. Hence, this solution is regarded as a possible back-up in the case any inconsistencies between microwave and T2L2 calibration may occur.

4.3.2.3. Status

A calibration equipment of the passive scheme is, at the time being, under development at OCA. Utilizing the synergy between the ILIADE development and T2L2, it profits from the same fast electronics and detectors as employed in the envisaged fast timing scheme of ILIADE.

5. T2L2J2 error budget

This chapter focuses on the stability and uncertainty budgets of the time transfer performed with the T2L2 instrument on Jason 2. The quality of the T2L2 scheme is not fully evaluated until all contributors in the time transfer chain are rigorously budgeted.
The establishment of these budgets partly relies on some work carried out by Jonathan Weick [52] who did some error assessment studies in the phase B of the T2L2J2 development.

The chapter first treats all aspects of the T2L2J2 instrumentation, i.e. the T2L2J2 instrument itself and all associated equipment, the retroreflector array LRA and the DORIS oscillator; further, any implications of the T2L2 on Jason 2 mission as the geometry and relativity issues are addressed. In a second part, the contribution of the respective laser stations are assessed; since not all laser stations participating in T2L2 can be analyzed here, only representative stations are discussed.
In general, the calculation of this overall performance budget relies in part on recently performed measurements and in part on assumptions and older data. This is for two reasons: the characterization of the T2L2J2 instrument is an integral part of the thesis at hand whereas the characterization of other contributors was not possible until now (e.g. the LRA) or already performed earlier (like for the MéO laser station).

This chapter intervenes on both measurement precision and uncertainty.
The dispersion of the performed measurements is analyzed employing the calculation of the time variance as shown in the performance and calibration chapters before. The determination of the uncertainty of the measurement is carried out employing both random-type contributors and systematic contributors. Following typical guidelines as given by the GUM of ISO (summed up in [45], for instance), the first component, "arising from a random effect" is denoted as a type A uncertainty. An example is the standard deviation of the mean of a series of data; in other words, the white noise of the measurement has been removed. The second uncertainty component, "arising from a systematic effect", is denoted type B.

The combined uncertainty may then be calculated by the squared sum of all type A and type B contributors. The different contributors of the whole T2L2 time transfer scheme are addressed one after another in the following chapters. Chapters 5.3 and 5.4 give the summary of the performed analysis.

5.1. Contribution of the T2L2J2 instrumentation and other mission related constraints

5.1.1. Event timer

When perfectly calibrated, the T2L2J2 event timer was found to have a very good precision and stability starting from 2 ps with white noise behavior over at least 1,000 seconds. Hence, the event timer contribution is of marginal importance in the time stability budget as compared to the contribution of the T2L2J2 photodetection system (see next section and Fig. 5.2).

$$\sigma_{x,\mathrm{T2L2_{Timer}}} \ll \sigma_{x,\mathrm{T2L2_{Det}}} \approx \sigma_{x,\mathrm{T2L2}} \tag{5.1}$$

This leads also to the conclusion that the type A uncertainty (standard deviation of the mean) is negligible.

The type B uncertainty covers biases and errors such as a drift due to the evolution of the timer's reference signals. Under stable conditions the residual drift of the event timer has been determined to be less than 0.7 ps/hour. This drift will appear alongside with the drift of the DORIS oscillator, but with seven orders of magnitude less ($2 \cdot 10^{-16}$), thus completely negligible. The common view time transfer accounts of any drift in the timer and the clock anyway.
For non-common view time transfer, an unknown drift would bring in an error; however, with the stated magnitude of 0.7 ps/hour it still remains negligible as compared to the oscillator.

Generally, for the error budget follows:

$$u_{A,\mathrm{T2L2_{Timer}}} \approx 0 \text{ and } u_{B,\mathrm{T2L2_{Timer}}} \approx 0 \tag{5.2}$$

5.1.2. Photodetection

5.1.2.1. Precision and stability of optical timing

The incoming laser pulses are timed by the non-linear detection channel. All processes that lead to any imprecision, like the temporal noise or the photon level dependence of the trigger (Geiger) signal, any noise on the non-linear detection threshold or of the comparator may be accounted for by the precision $\sigma_{\mathrm{T2L2_{Det}}}$ that was determined in Chapter 3.2. It was determined to be of about 35 ps in single photon level, falling down to 3 ps for photon numbers of around 1,000 (see Fig. 5.1).

Fig. 5.2 shows the time stability of the T2L2 event timing in optical mode. As stated above, it includes both the precision and stability of the photodetection as well as of the event timer (which is negligible as compared to the single-photon precision). The two acquisitions of Fig. 5.2 were performed in single photon mode, representing the worst case of optical timing and at a laser pulse rate of 10 Hz, typical value for laser ranging stations. The spike around some hundred seconds of averaging time is believed to be due to the test equipment. Therefore, the worst-case time stability of the whole T2L2J2 instrument (including photodetection and timer) may be approximated by following equation:

$$\sigma^2_{x,\mathrm{T2L2}} = \left(K_{\mathrm{T2L2},1} \cdot \tau^{-1/2}\right)^2 + \left(K_{\mathrm{T2L2},2} \cdot \tau^{1/2}\right)^2 \tag{5.3}$$

with $K_{\mathrm{T2L2},1} = 10.6 \text{ ps} \cdot \sqrt{\text{s}}$ and $K_{\mathrm{T2L2},2} = 19 \text{ fs}/\sqrt{\text{s}}$ for single photon mode.
For multi-photon operation of the T2L2 detection, the stability may be modeled with following factors: $K_{\mathrm{T2L2},1} = 3 \text{ ps} \cdot \sqrt{\text{s}}$ and $K_{\mathrm{T2L2},2} = 6 \text{ fs}/\sqrt{\text{s}}$. Comparison to Equation (2.1)

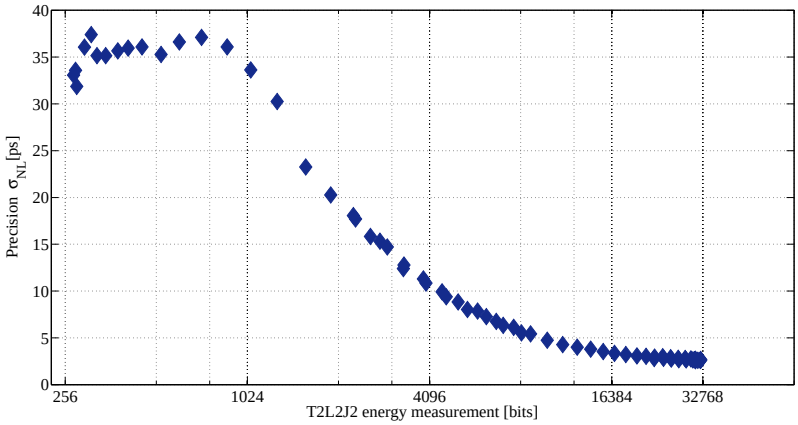

Figure 5.1.: Precision of the non-linear detection over laser pulse energy measured by the linear channel (photodiode output voltage converted into bits)

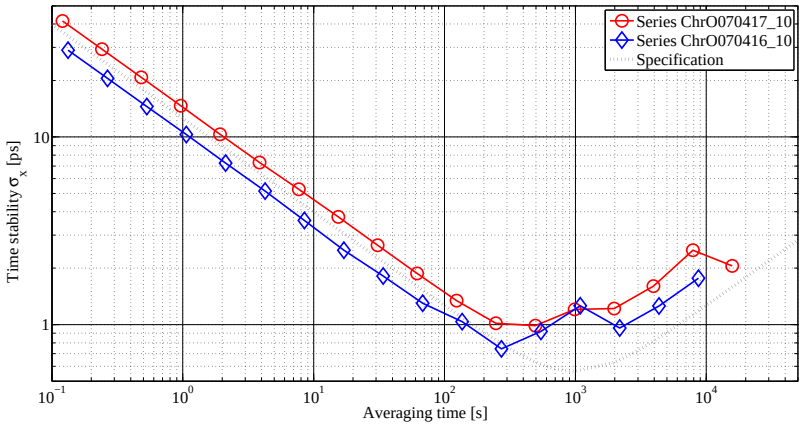

Figure 5.2.: Time stability of two series of optical timing in single photon mode

and Fig. 2.7 emphasizes the compliance to specification [E 4.2.2-3].
The lowest flicker floor that could be measured with the T2L2 flight instrument is 135 fs after an integration time of 20 s and at a laser rate of 1 kHz.

5.1.2.2. Uncertainty of the time-walk correction

The non-linear detection features a time walk depending on the photon number, as shown in Fig. 5.3.
In the data analysis on ground, this time-walk is corrected through the measurement of the incoming laser pulse energy by the linear detection channel: The pulse energy on the non-linear detector E_{NL} (or the photon number $N_{\mathrm{ph}} = E_{\mathrm{NL}} \cdot \frac{\lambda}{h \cdot c}$) is calculated from the measurement of the laser pulse energy E_{L} in the linear channel, applying factors for relative gain of the two channels k (see Chapter 3.3) and for relative transmission T_{rel} depending on the incidence angles. The corresponding time-walk value is then subtracted from the respective date.

$$E_{\mathrm{NL}} = \frac{E_{\mathrm{L}}}{k} \cdot T_{\mathrm{rel}} \tag{5.4}$$

The time-walk t_{tw} may be expressed by a logarithmic function; for better match with the measurements, a series of logarithmic functions is used (as depicted in Fig. 5.3):

$$t_{\mathrm{tw}} = \alpha \cdot \lg(N_{\mathrm{ph}}) + t_{\mathrm{tw},0} \tag{5.5}$$

with the following coefficients:

Table 5.1.: Time-walk of the non-linear photodetection over photon number: Logarithmic approximation for uncertainty determination

Range	Photon number N_{ph}	α [ps]	$t_{\mathrm{tw},0}$ [ps]
A	Single photon	-48	334
B	1 to 50	-133	344
C	60 to 600	-60	214
D	above 600	-31	135

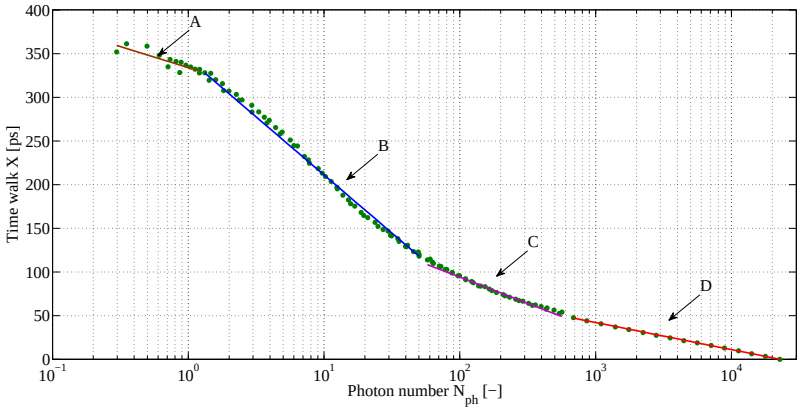

Figure 5.3.: Time walk of the non-linear detection as a function of impinging photon number N_{ph}

Any errors on the calculated pulse energy E_{NL} lead to an error in the time-walk correction or a type B uncertainty of the T2L2J2 detection as follows:

$$u_{\mathrm{T2L2_{Det}}} = \left| \frac{dt_{\mathrm{tw}}}{dE_{\mathrm{NL}}} \cdot \Delta E_{\mathrm{NL}} \right| = \left| \frac{\alpha}{\ln(10)} \frac{\Delta E_{\mathrm{NL}}}{E_{\mathrm{NL}}} \right| \tag{5.6}$$

We see immediately that this uncertainty depends, through the slope α, also on the encountered photon level and from Table 5.1 may be deduced that it will be five times lower for a high photon level (slope D) than for an intermediate (slope B).

In the following, the different sources for the error ΔE_{NL} will be discussed.
From Equation (5.4) follows:

$$\Delta E_{\mathrm{NL}}^2 = \left(\left| \frac{\partial E_{\mathrm{NL}}}{\partial k} \right| \Delta k \right)^2 + \left(\left| \frac{\partial E_{\mathrm{NL}}}{\partial E_{\mathrm{L}}} \right| \Delta E_{\mathrm{L}} \right)^2 + \left(\left| \frac{\partial E_{\mathrm{NL}}}{\partial T_{\mathrm{rel}}} \right| \Delta T_{\mathrm{rel}} \right)^2 \tag{5.7}$$

For convenience, expressed as a relative error:

$$\begin{gathered} \left(\frac{\Delta E_{\mathrm{NL}}}{E_{\mathrm{NL}}} \right)^2 = \left(\frac{\Delta k}{k} \right)^2 + \left(\frac{\Delta E_{\mathrm{L}}}{E_{\mathrm{L}}} \right)^2 + \left(\frac{\Delta T_{\mathrm{rel}}}{T_{\mathrm{rel}}} \right)^2 \\ u_{E_{\mathrm{NL}},\mathrm{rel}}^2 = u_{k,\mathrm{rel}}^2 + u_{E_{\mathrm{L}},\mathrm{rel}}^2 + u_{T_{\mathrm{rel}},\mathrm{rel}}^2 \end{gathered} \tag{5.8}$$

These three contributors to the uncertainty of the time walk correction are discussed in the following paragraphs:

Relative coupling between linear and non-linear channel For the term $\frac{\Delta k}{k}$ we may consider the uncertainty $u_{k,\mathrm{rel}}$ on the determination of k that has be assessed to be less than 1% (k has been determined to 1,250); otherwise, the error e_{tw_k} is common for all timings in the "linear" areas A to D of $u_{\mathrm{T2L2_{Det}}}$ from Equation (5.6). If we can guarantee that the laser pulse energies from stations A and B feature the same level[1], the errors through k will naturally subtract in the transmit/return scheme of the ground to ground time transfer. Yet in the general case the k-error has to be considered with $u_{k,\mathrm{rel}}$.

Another point is the possible radiation-induced deterioration particularly of the optical fiber of the non-linear channel and the consequent evolution (augmentation) of k. If this modification takes place, it will be in a very slow manner what will be completely imperceptible over, say, an orbit pass. This modification will generate an error in the time-walk correction, in the same way as described above, by the different slopes present in the correction curve (except for cancelling out in the described conditions). It is therefore crucial to re-evaluate this factor k in regular intervals in order to preserve the initial performance of the instrument.

The approach would be to emit laser pulses while guaranteeing the single photon mode on the non-linear channel; the factor k may then be deduced by the comparison of the detection statistics on the non-linear detector, and thus the photon level, and the pulse energy measurement performed on the linear channel.
Another method consists in comparing the residual signature of the time walk to the energy measurement; this may be obtained by fitting a short orbit arc (the orbit is not expected to vary abruptly over short time scales) on the measured on-board dates.

Linear pulse energy measurement In order to assess the error induced by the measurement of the laser pulse energy E_{L}, the determined r.m.s. precision may be transformed into an uncertainty by arbitrarily choosing the 1σ level, meaning that with 68% probability the error is less than $\sigma_{E_{\mathrm{L}}}$. Fig. 5.4 shows the relative uncertainty[2] of the pulse energy measurement. It varies from values of about 6% for photon numbers (on the linear channel) of around 1,000 down to less than 0.5% for photon numbers of about 1 million. The low dispersion for high energies is partially explained by the fact that the measurement is nearing saturation (approaching the max value of the ADC, i.e. 32,768 bits) and consequently the dispersion gets more and more truncated. At the point where we are, we may give several values for $u_{E_{\mathrm{L}},\mathrm{rel}}$, corresponding to the four zones given in Table 5.1: for A, one may account 6%, for B 5%, for C 1% and for D 0.5%.

Relative transmission of the non-linear to linear channel A possible source of uncertainty in the relative transmission lies in the fact that the two radial density filters of the linear and the non-linear channel are not identical (compare to Section 3.3.2.2). In the calculus

[1] Note that this condition is quite difficult to fulfill, since the laser pulse energy levels are expected to be a completely random outcome of the turbulence induced speckle features in orbit. An exception could be possible through working innately with very low laser level or collocation of similar stations (same atmospheric effects).

[2] Note that the dispersion of the laser pulse energy was determined to be less than 0.35% in Section 3.1.3, thus is negligible as compared to the energy measurement by T2L2J2.

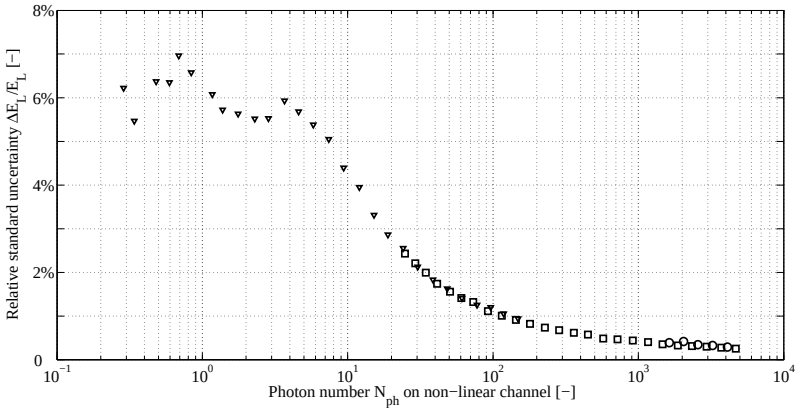

Figure 5.4.: Relative precision or 1-σ uncertainty of the linear pulse measurement. It is given here over the corresponding photon number N_{ph} on the non-linear channel. The photon number present on the linear channel is more than 10^3 higher.

of the laser pulse energy present on the non-linear diode, this is represented by $T_{\mathrm{rel}} = \frac{T_{\mathrm{NL}}}{T_{\mathrm{L}}}$. This relative transmission is a function of both the incidence angle to the boresight σ and the revolution angle ε; additionally, it has to account for the unknown polarization angle ρ. Fig. 5.5 shows T_{rel} as a function of the angles σ and ε as determined with the respective measurements on the BOLI and BONL radial filter (compare to Fig. 3.55).

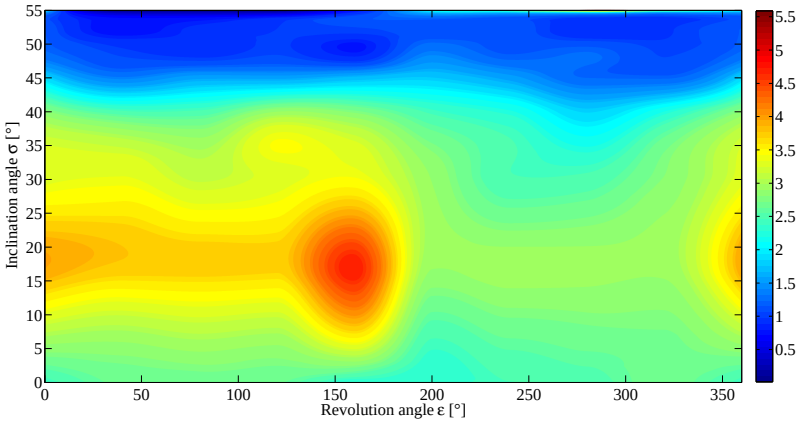

Figure 5.5.: Relative transmission T_{rel} of the radial filters of the non-linear and linear channel

The uncertainty in $T_{\mathrm{rel}}(\sigma, \varepsilon, \rho)$ originates in:

- the imprecision of the attitude measurement performed by the Jason 2 platform and thus inducing imprecision on σ and ε;
- an unknown misalignment between the respective attitude sensor (star sensor) and the T2L2J2 optics;
- the lack of knowledge of the polarization axis of the incoming laser light with respect to the optics and

- the uncertainty on the filter transmissions; even though the two radial filters have been examined in great detail, there still remains a certain uncertainty of the measurements of the transmissions T_{NL} and T_{L} themselves.

The uncertainty ΔT_{rel} may thus be expressed as follows:

$$\begin{aligned}\Delta T_{\mathrm{rel}}^2 = &\left(\left|\frac{\partial T_{\mathrm{rel}}(\sigma,\varepsilon)}{\partial\sigma}\right|\Delta\sigma\right)^2 + \left(\left|\frac{\partial T_{\mathrm{rel}}(\sigma,\varepsilon)}{\partial\varepsilon}\right|\Delta\varepsilon\right)^2 \\ &+ T_{\mathrm{rel}}^2\cdot\left(u_{\mathrm{Pol,rel}}^2 + u_{T_{\mathrm{NL}},\mathrm{rel}}^2 + u_{T_{\mathrm{L}},\mathrm{rel}}^2\right)\end{aligned} \tag{5.9}$$

Attitude: The first two terms are evaluated by building the partial derivatives of the relative transmission along the two angles[3] ε and σ; this is represented in Fig. 5.6. Along

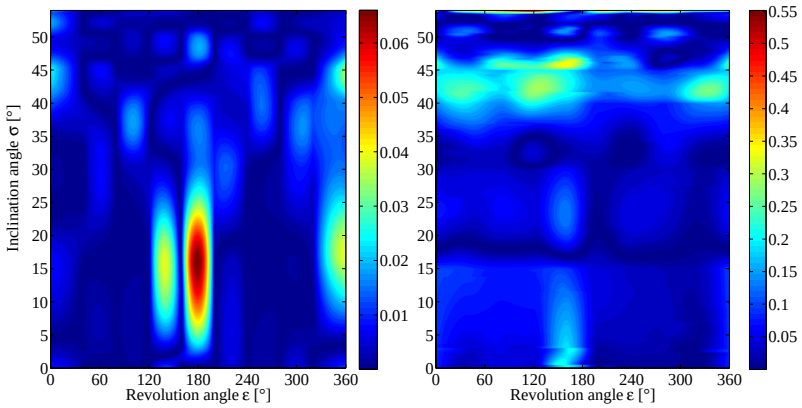

Figure 5.6.: Partial derivatives of the relative transmission T_{rel} along the revolution angle ε and the incidence angle σ: $|\partial T_{\mathrm{rel}}/\partial\varepsilon|$ on the left graph, $|\partial T_{\mathrm{rel}}/\partial\sigma|$ on the right.

the revolution angle $|\partial T_{\mathrm{rel}}/\partial\varepsilon|$ stays below 0.1 1/° for all angles.
Along the σ-direction, the slope $|\partial T_{\mathrm{rel}}/\partial\sigma|$ stays below 0.4 1/° for all values of σ smaller than 54°.

CNES, the operator of Jason 1 and Jason 2, states an r.m.s. pointing precision of Jason 1 (Jason 2 is expected to perform on the same level) of 1 mrad; the attitude determination precision may be estimated to be at the same level, if not much better. This gives an uncertainty of $\approx 0.06°$ (random, type A), evaluating at 1σ. This is negligible compared to a mechanical integration alignment uncertainty (systematic, type B) of 1°. The latter alignement uncertainty may be directly put in for $\Delta\sigma$ and $\Delta\varepsilon$ in Equation (5.9).
Polarization: Even though the laser systems of the respective SLR stations emit with a defined polarization, linear or circular, the alteration of the polarization axis at the various optical surfaces in the station and its evolution over the orbit pass (with variation of azimuth and elevation) is quite complicated to determine for each and every participating laser ranging station. Due to the different rotating elements in a station, all polarization angles ρ may be considered as equally probable over a pass.

The polarization of the incident light wave has different effects on the optics of the T2L2J2 instrument: all optics may suffer an attenuation of the perceived laser pulse energy as a result

[3] The angle σ denotes the inclination angle with respect to the optical axis, thus the nadir direction, and is thus calculated from both the roll and pitch angles of the satellite. The angle ε may be directly accounted for by the yaw angle.

of Fresnel reflection on the optical surfaces as a function of the polarization angle with respect to the incidence angle. This assumption holds true for the whole linear channel including the photodetector and implicates a detection of a modified laser pulse level.
On the non-linear channel, the optical fiber does not preserve the polarization state: the non-linear detector may be considered to receive unpolarized light, but the possible attenuation of the laser pulse in the front optics pulse may provoke an unknown value of higher or lower time-walk of the detector.

But the non-linear channel may still suffer another effect: the optical material could feature a slight anisotropy as a function of polarization and incidence angles what would result in modified optics entry and exit angles; this would finally modify the light ray trajectories in the optics and culminate in a modification of the measured time of arrival of the laser pulse on the non-linear diode as a function of polarization and incidence angle.
It is apparent that the different effects on the non-linear channel are difficult to discern, they may either mutually add up or cancel out. In any case, the polarization state will not have exactly the same effect on the linear as on the non-linear channel. During the metrological evaluation of the T2L2J2 flight instrument, see Section 3.3, there could be put some bounds on the error induced by the unknown polarization state.

It was determined (Section 3.3.2.3) that the deviation $\Delta E_{\mathrm{L-NL,rel}}$ between the laser pulse energy measured by the linear and the non-linear channel[4] may be quite good approximated by a linear trend over the incidence angle for a given polarization state[5], with a maximum discrepancy on the order of 57% for orthogonal[6] polarization (13% for 45°) and very high incidence angles (55°).
We may assume that the effective incidence angles in orbit have a normal distribution and consequently also the errors; thus, we may transform the maximum error into a standard deviation, giving: $\sigma_{\Delta E_{\max}} = 18\%$.
For the polarization angle, we have to consider an equal probability of all angles, meaning a rectangular distribution; for the polarization contribution u_{Pol} of the relative transmission uncertainty, Equation (5.9) it thus follows [45, 53]:

$$u_{\mathrm{Pol,rel}} = \frac{\sigma_{\Delta E_{\max}}}{\sqrt{3}} = 10\% \tag{5.10}$$

Uncertainty on the radial filter characterization: The knowledge (or confidence) of the determined filter transmissions is governed by the precision of the used observables and the mathematical model to interpolate values from discrete measurements. Consequently, the relative uncertainty on the linear channel radial filter $u_{T_{\mathrm{L,rel}}}$ is calculated with the precision of the linear pulse measurement $\sigma_{E_{\mathrm{L}}}$ of T2L2J2 itself, ameliorated by the number of performed measurements N_{meas}.

The relative uncertainty on the non-linear channel radial filter $u_{T_{\mathrm{NL,rel}}}$ is calculated with the temporal precision σ_{NL} of the non-linear diode, as the time walk is used as a measure of laser energy, and the number of measurements N_{meas}. Further, the energy dispersion of the laser pulses has to be taken account of (compare to the test bed performance, Sec. 3.1.3), but this can be considered to cancel out for both filters when the curves are determined with the same dataset, as the noise is common on both linear and non-linear channel and

[4] The time-walk of the non-linear photodetector is used as a measure of laser pulse energy.
[5] This polarization state, here a linear polarization, is chosen with respect to the "nominal" polarization axis at what all reference measurements were performed.
[6] See precedent footnote.

sufficiently small to be supposed to introduce a linear error. Additionally, two factors for the contribution of the chosen mathematical model have to be added. The two uncertainties read:

$$\begin{aligned} u^2_{T_{\mathrm{L,rel}}} &= \frac{1}{N_{\mathrm{meas}}} \cdot \sigma^2_{E_{\mathrm{L,rel}}} + u^2_{\mathrm{model,rel,L}} \\ u^2_{T_{\mathrm{NL,rel}}} &= \frac{1}{N_{\mathrm{meas}}} \cdot \sigma^2_{E_{\mathrm{NL,rel}}} + u^2_{\mathrm{model,rel,NL}} \end{aligned} \tag{5.11}$$

The measurements for the filter curve determination have been performed at a laser rate of 50 Hz and an exposition of 100 s per position, giving a measurement number N_{meas} of 5,000.

The uncertainty of the linear filter curve measurements $\frac{1}{\sqrt{N_{\mathrm{meas}}}} \cdot \sigma_{E_{\mathrm{L,rel}}}$ may be evaluated from Fig. 5.4 to be less than 0.1%. The uncertainty of the non-linear filter measurements $\frac{1}{\sqrt{N_{\mathrm{meas}}}} \cdot \sigma_{E_{\mathrm{NL,rel}}}$ has been deduced to be less than 0.5% for high photon numbers (> 50) what has been the case for the filter evaluation ($\approx 1\%$ for single photon mode).

A rather empirical means for an assessment of the error induced by the interpolation process between measured points of the transmission curves is to compare between different datasets: For some revolution angles (i.e. at 0°, 120° and 240°) measurements with much more points were performed. In order to assess the magnitude of the error, simply the difference between the datasets with many points (and fewer interpolation errors) and the datasets with fewer points (and bigger interpolation errors) may be calculated. This procedure is shown in Fig. 5.7 with the linear channel filter curve already shown in Section 3.3. One

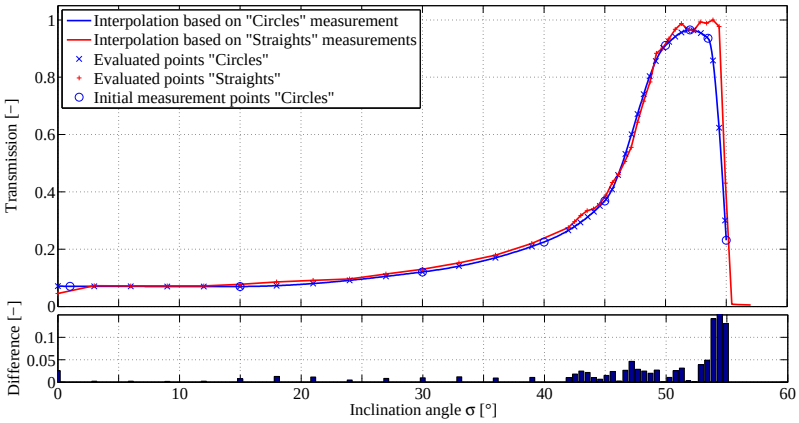

Figure 5.7.: Assessment of the error induced by interpolation between filter curve measurement points: Linear channel.

sees that the difference is mostly below 2%, but may rise to more than 5% (even up to 15%) for higher inclinations, where the discrepancies of the filter are higher. In order to be representative of the T2L2J2 operation in orbit, we may consider 2% for $u_{\mathrm{model,rel,L}}$ with a rather clear conscience.

For the non-linear channel, a similar analysis reveals a magnitude of interpolation errors of about 5% for $u_{\mathrm{model,rel,NL}}$; the higher error on the non-linear channel radial filter is due to the much more delicate calculus of the transmission based on the time-walk of the diode.

5.1.2.3. Summary T2L2J2 photodetection

For the time stability budget of the ground to ground time transfer with T2L2J2, the contribution of the T2L2J2 instrument was already given by Equation (5.3).

In order to assess the uncertainty on the time walk correction (the uncertainty contributor of the T2L2J2 photodetection system), Equation (5.6) was set up; any errors on the calculation of the laser pulse energy on the non-linear channel E_{NL} lead to an error $u_{B,\mathrm{T2L2_{Det}}}$ in the time walk correction.
The error enters exclusively through the term $\frac{\Delta E_{\mathrm{NL}}}{E_{\mathrm{NL}}}$. Equations (5.7), (5.8) and (5.9) designate the different contributors, relative coupling $\frac{\Delta k}{k}$ between linear and non-linear channel, linear pulse measurement uncertainty $\frac{\Delta E_{\mathrm{L}}}{E_{\mathrm{L}}}$ and the uncertainty about the relative transmission $\frac{\Delta T_{\mathrm{rel}}}{T_{\mathrm{rel}}}$ between the two different radial filters in the linear and the non-linear channel. Table 5.2 summarizes these three different contributors.

Table 5.2.: Contributions to the uncertainty of the time walk correction

Contributor	Term	Photon level			
		A	B	C	D
Relative coupling	$\frac{\Delta k}{k}$	1 %			
Linear pulse measurement	$\frac{\Delta E_{\mathrm{L}}}{E_{\mathrm{L}}}$	6 %	5 %	1 %	0.5 %
Relative transmission	$\left\lvert\frac{\partial T_{\mathrm{rel}}(\sigma,\varepsilon)}{\partial\sigma}\right\rvert \frac{\Delta\sigma}{T_{\mathrm{rel}}}$	0.4 %			
	$\left\lvert\frac{\partial T_{\mathrm{rel}}(\sigma,\varepsilon)}{\partial\varepsilon}\right\rvert \frac{\Delta\varepsilon}{T_{\mathrm{rel}}}$	0.1 %			
	$u_{\mathrm{Pol,rel}}$	10 %			
	$u_{\mathrm{T_L,rel}}$	2 %			
	$u_{\mathrm{T_{NL},rel}}$	5 %			
Sum	$\frac{\Delta E_{\mathrm{NL}}}{E_{\mathrm{NL}}}$	13 %	12.5 %	11.5 %	11.4 %
Uncertainty (B)	$u_{B,\mathrm{T2L2_{Det}}}$ [ps]	2.7	7.2	3	1.5

Evaluating Equation (5.6) with the found value of $\frac{\Delta E_{NL}}{E_{NL}}$ of about 12% for all different photon levels (slope α of Table 5.1) gives the type B uncertainty $u_{B,\mathrm{T2L2_{Det}}}$, equally given in Table 5.2.

The type A uncertainty is determined with the standard deviation of the mean of the dates. Considering a 1σ level, we determine from the precision $\sigma_{\mathrm{T2L2_{Det}}}$ (Fig. 5.1) of the optical timing:

$$u_{A,\mathrm{T2L2_{Det}}} = \frac{\sigma_{\mathrm{T2L2_{Det}}}}{\sqrt{N_{\mathrm{meas}}}} \tag{5.12}$$

with N_{meas} being the number of performed measurements, under the presumption that only white noise is present; as we saw in the time stability plot, this statement is true for a whole pass of the satellite over a ground station. Assuming some hundreds of measurements (anticipating Equation 5.28) the type A uncertainty falls to values of around 1 picosecond.

The combined uncertainty of the T2L2J2 photodetection is build by the quadratic sum of type A and B contributors:

$$u^2_{\mathrm{T2L2_{Det}}} = u^2_{A,\mathrm{T2L2_{Det}}} + u^2_{B,\mathrm{T2L2_{Det}}} \tag{5.13}$$

The result is given in Table 5.3. During nominal operation in orbit, any of the given photon numbers of Table 5.1 may be possible. Hence, we may further conclude that the overall

uncertainty averages out to some value representative of the photon number distribution present over a whole satellite pass. In the table are given weighted averages[7] taking account of the expected statistics in orbit. Weighted average 1 is a more conservative distribution, whereas weighted average 2 is more confident, corresponding to a powerful laser ranging station as MéO or Wettzell. During nominal operation, this statistic has to be re-evaluated

Table 5.3.: Uncertainty of the T2L2J2 detection system

Photon level	A	B	C	D
Type A: $u_{A,\mathrm{T2L2_{Det}}}$ [ps]	1.5	0.9	0.4	0.1
Type B: $u_{B,\mathrm{T2L2_{Det}}}$ [ps]	2.7	7.2	3	1.5
Sum $u_{\mathrm{T2L2_{Det}}}$ [ps]:	3	7.3	3	1.5
Uncertainty $u_{\mathrm{T2L2_{Det},av1}}$ [ps]	3.7			
Uncertainty $u_{\mathrm{T2L2_{Det},av2}}$ [ps]	3.3			

for each pass over a laser station in order to correctly assess the corresponding uncertainty of the time transfer.

Conclusion In this section the uncertainty of the photodetection has been determined. Table 5.3 summarizes the type A and type B contributors. In the worst case (steepest slope in the time walk plot, photon number case B) an error of 7 ps can be budgeted due to type B contribution. The major contributor for this error are the lack of knowledge of the polarization state of the incoming laser beam.

Table 5.2 gives the error in the relative transmission $\frac{\Delta T_{\mathrm{rel}}}{T_{\mathrm{rel}}}$ of about 11%. The specifications (Section 2.3.2) claimed 10%, but one may state that this is however acceptable (specification [E 4.2.1-8]).

The analysis performed in this section shows the high potential of the a posteriori time walk correction as performed in T2L2J2 by the simultaneous measurement of the laser pulse amplitude.

5.1.3. The DORIS oscillator

The T2L2 space instrument uses the 10 MHz sinusoidal signal issued from the DORIS ultra-stable oscillator as its reference signal. The DORIS positioning system's space instrument comprises, for redundancy and performance reasons, two quartz oscillators (one as a backup). Nominally, the two oscillators show equivalent characteristics (in the limits of the possible); on the basis of some criteria, one of them is chosen to provide the DORIS and general satellite 10 MHz reference signal.

During the test campaign at THALES Alenia Space the two oscillators could be measured by the intermediate of the T2L2J2 internal frequency synthesis (see Section 3.2.3). Fig. 5.8 shows the time stability plot of the DORIS PMB (one of the two USOs) phase when it was compared with an HP 5071A Cesium standard of OCA. Curve (a) is a theoretical expectation on the time deviation calculated from spectral data of the manufacturer. For curve (b), the

[7] Weighted average 1 assumes that, respectively, a quarter of all timings are performed in single-photon mode (case A), with photon numbers from 1 to 50 (case B), from 60 to 600 (case C) and with number above 600 (case D). The second weighted average assumes 10% in single photon mode (A), 20% for case B, 30% for C and 40% for D.

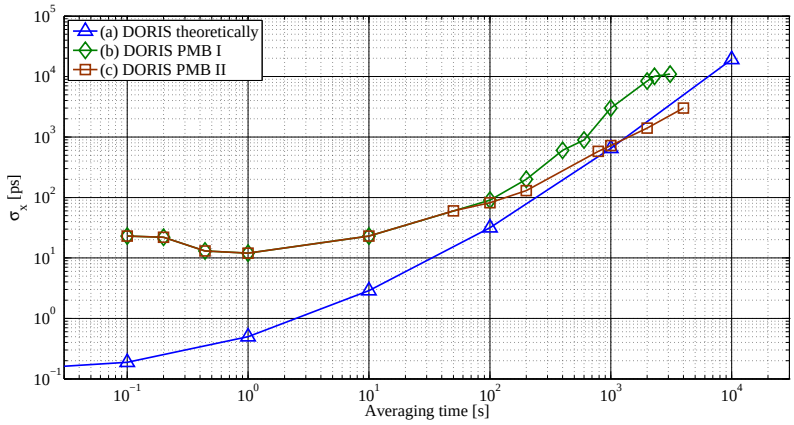

Figure 5.8.: Time stability of the DORIS local oscillator PMB aboard Jason 2

experimental phase data was corrected for a frequency offset and a linear frequency drift. During the measurement, the oscillator was still in its thermalization phase, i.e. in addition to a linear frequency drift, a frequency drift rate towards its nominal operation point was present: The phase dataset was thus corrected for this drift rate by a polynomial of the order three; the corresponding time stability is indicated by curve (c).

The DORIS oscillator contributes to the overall error budget due to the lack of knowledge of its actual frequency one has over longer time periods.
For a given pass of Jason 2 over a laser ranging station, the oscillator characteristics may perfectly be assessed through the ground-space time transfer itself. Periods when the DORIS oscillator is not monitored by a ground station represent a problem: This is the case for non-common view time transfer where the stations A and B do not share the same pass at the same time. In this case, the phase evolution of the DORIS/T2L2 ensemble has to be assessed with clock data acquired during the passes over stations A and B, what introduces an error. The cases of common-view and non-common view are addressed in the following paragraphs:

Common-view time transfer For ground to ground time transfer in common view, the noise of the oscillator intervenes only over very short intervals, that is for the time span that separates the time of arrival of the laser pulse from station A from the time of arrival from B. These intervals are on the order of 100 ms depending on the respective stations' laser rate and the detection probability on T2L2. The error committed on the time prediction (see below) on these time scales may be regarded as negligible.

$$\sigma_{\mathrm{DORIS_{CV}}} \approx 0 \text{ and } u_{\mathrm{DORIS_{CV}}} \approx 0 \tag{5.14}$$

Time prediction for non-common-view time transfer During non-monitored intervals, the DORIS oscillator evolutes in an unknown way. For a dead time τ_{AB} between the extremities of two subsequent passes over stations A and B, one may [54] simply write Equation (5.15) for the time prediction, or include an additional drift rate term [55], with (5.16):

$$\tilde{x}(t+\tau_{AB}) = x(t) + a_0\ \tau_{AB} + a_1\ \tau_{AB}^2 + \epsilon(t) \tag{5.15}$$

$$\tilde{x}(t+\tau_{AB}) = x(t) + a_0\ \tau_{AB} + a_1\ \tau_{AB}^2 + a_2\ \tau_{AB}^3 + \epsilon(t) \tag{5.16}$$

The terms a_0, a_1 and a_2 designate factors for frequency offset, frequency drift and drift rate. The term ϵ relates to all random fluctuations that are subject to power-law noise processes. The optimum predictor depends on the nature of the preponderant noise process for the considered time interval τ_{AB} [54]. For the DORIS oscillator one has therefore to determine which of the noise processes prevails for the expected dead times. Analyzing Fig. 5.8, one sees that for some hundreds to some thousands seconds the slope of curve (c) is proportional to τ indicating the presence of flicker frequency modulation noise. According to [54], the prediction algorithms are significantly the most difficult for flicker FM, but may be developed by using ARIMA[8] techniques. From the analysis of the measurements of Fig. 5.8 there remains some uncertainty about the really present noise nature: Curve (b), where only a quadratic correction of the phase data has been performed, exhibits a dependence more similar to $\tau^{3/2}$ what would mean a preponderance of random walk FM noise and induce a different time prediction algorithm.
This means that despite the performed measurements on the DORIS oscillator some detailed analysis of the oscillator still has to be performed, in particular in cooperation with the DORIS community.

However, the time prediction of the DORIS oscillator(s) for the not-covered gaps will prove to be different than predicting a clock into the future whereof one disposes only of historical (though recent) data. The continuous monitoring of the oscillator through the laser station and DORIS network allows to procure data in order to know on a relatively high level about its behavior. By this means, drifts and drift rates may more easily be approximated. The next paragraph, though, treats the time prediction error in a more conservative way.

A way to mitigate quite perfectly the drawback of a "not-so-stable" oscillator as it is DORIS on the long term (due to its nature as a quartz) is to employ intermediate laser ranging stations located between the stations A and B that perform the principal time transfer. Such a station does not need to participate directly, with a perfectly calibrated system, to the time transfer as long as it may provide absolute start and return dates t_s and t_r (determined with an event timer). Fig. 5.19 shows exemplary the locations and satellite passes of a time transfer between Grasse and Shanghai, supported by intermediate stations like Mendeleevo near Moscow, Russia or Maidanak, Uzbekistan.

Time-prediction error in non-common view time transfer According to [56] and [54] the committed error in the process of time prediction depends also on the kind of noise dominating the oscillator for the regarded time interval.

In the case of white and random walk FM noise one may calculate the committed error over a dead time τ_d by simply multiplying the value of the Allan deviation at τ_d with the regarded time interval $\delta t_{\text{pred}} = \tau_d \cdot \sigma_y(\tau_d)$. For white phase modulation noise, the time prediction error is lower: $\frac{\tau_d}{\sqrt{3}}\sigma_y(\tau_d)$. The most conservative or pessimistic estimate is for flicker FM noise: $\frac{\tau_d}{\sqrt{\ln(2)}}\sigma_y(\tau_d)$.
The error on the time prediction of the DORIS oscillator translates directly into uncertainty. The transformations between Allan and time deviations read:

$$\text{TVAR} = \sigma_x^2(\tau) = \frac{\tau^2}{3}\text{Mod}\sigma_y^2(\tau) \tag{5.17}$$

[8] ARIMA means AutoRegressive-Moving Average and is a common technique for time series analysis based on stationary, time-discrete stochastic processes. The use of these techniques is not subject of the present work.

and [57]:

$$\mathrm{MVAR} = \mathrm{Mod}\sigma_y^2(\tau) = 0.645 \cdot \sigma_y^2(\tau) \tag{5.18}$$

Supposing conservatively flicker FM noise (worst case) one obtains for the time prediction error δt_{pred} and therefore the corresponding uncertainty over a dead time interval τ_{AB}:

$$\delta t_{\mathrm{pred}} = u_{\mathrm{DORIS_{NCV}}} = \sqrt{\frac{3}{\ln(2) \cdot 0.645}}\, \sigma_x(\tau_{AB}) \tag{5.19}$$

In order to come to a reasonable precision, the two separate acquisitions over stations A and B have to be repeated over and over again in order to profit from the averaging with $1/\sqrt{N_{\mathrm{meas}}}$. This may be performed a couple of times since the Jason 2 orbit features always a set of consecutive passes around a given ground station[9]. For each unmonitored travel of the satellite between A and B, the DORIS oscillator will show another random behavior; nevertheless, the error on the prediction may always be quantified with Equation (5.19). Thus, the corresponding dispersion of the whole dataset of dates is also approximated by Equation (5.19).

Following table (5.4) gives the time prediction error (both uncertainty or dispersion) for some dead times: It is clearly visible that the dead times should be held as low as possible

Table 5.4.: Time prediction error of DORIS USO

Dead time τ_{AB} [s]	$\sigma_{\mathrm{DORIS_{NCV}}} = u_{\mathrm{DORIS_{NCV}}}$ [ps]
100	210
300	520
1000	1860
3000	5700

by encouraging other laser stations to participate in the time transfer project as shown with the France-China transfer and the Maidanak station. Evidently, this is not possible for all configurations, like for a transatlantic time transfer with Greenbelt, Maryland (the dead time with Grasse is about 350 s, but could be reduced by working with the Herstmonceux and Metsahovi laser stations).

5.1.4. Geometry of the T2L2J2 instrument and LRA retroreflector

Another contributor to the overall time transfer precision and uncertainty budget is the geometry of the T2L2J2 equipment aboard the Jason 2 satellite, including the retroreflector LRA.
One contribution lies in the uncertainty about the actual attitude of the satellite and the mechanical uncertainty about the integration of the T2L2J2 optical subsystem; this is discussed in the following Section 5.1.4.1.
Another contribution concerns the response of the LRA retroreflector with respect the actual attitude, what will be addressed in Section 5.1.4.2.

[9] The non-common view time transfer will be addressed in more detail in 5.3.2.

5.1.4.1. Attitude and mechanics

In the Jason 2 layout, the detection and reflection reference point are not collocated. The detection reference point may be (quite arbitrarily, but invariant with respect to the attitude) materialized by the center of the non-linear channel optics orifice. The reflection reference point may be attributed (likewise arbitrarily; detailed treatment of the problem in Section 5.1.4.2) to the center of the middle corner cube of the LRA pyramid.

Attitude determination uncertainty The uncertainty of the attitude measurement by the Jason 2 satellite was already mentioned in Section 5.1.2. This time we are dealing with a simple geometrical error in the correction $\Delta t = f(\text{Att})$ that has to be applied to the measured time tag as a function of the attitude. The detection and reflection reference points are separated by a distance $l = 120$ mm. The maximum error (B-type) intervenes

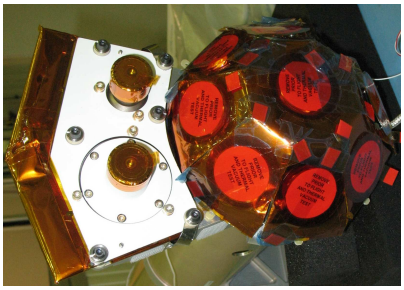

Figure 5.9.: The T2L2J2 optics and the LRA retroreflector mounted on the boom. On the photograph, the LRA is covered with protective caps (during integration).

when the laser pulse wavefront arrives perpendicular to the optics boresight axis, i.e. for zenith-near passes: $dl = l \cdot d\alpha$. With $d\alpha = 1$ mrad one determines:

$$u_{\text{A,Geo}} = u_{\text{Att}} = dl/c = 0.4 \text{ ps} \tag{5.20}$$

what may be neglected in the error budget.

Mechanical uncertainty about the relative position of T2L2J2 optics and LRA There is further some uncertainty about the distance l separating the reflection and detection reference points, due to the physical integration. Considering an 1-mm offset in each axis, a ballpark figure of the error is $e_{\text{mech}} = \sqrt{3}$ mm. Over an orbit pass this error varies [52] as presented in Fig. 5.10 for two different passes over a ground station, one with an orbit culmination at an elevation of 87° (near zenith, the closest pass to the MéO station) and a low pass culminating at an elevation of 19°. This evolution over the orbit is reduced to a standard deviation, giving for the uncertainty (type B since it is a systematic effect):

$$u_{\text{B,Geo}} = u_{\text{B,mech}} \leq 3 \text{ ps} \tag{5.21}$$

considering the 1σ level.

5.1.4.2. Retroreflector response with respect to attitude

As described in Section 2.3.1.2, the LRA consists of nine 31.75 mm diameter quartz corner cubes that form an octagonal pyramid with the ninth on top. The eight equally spaced

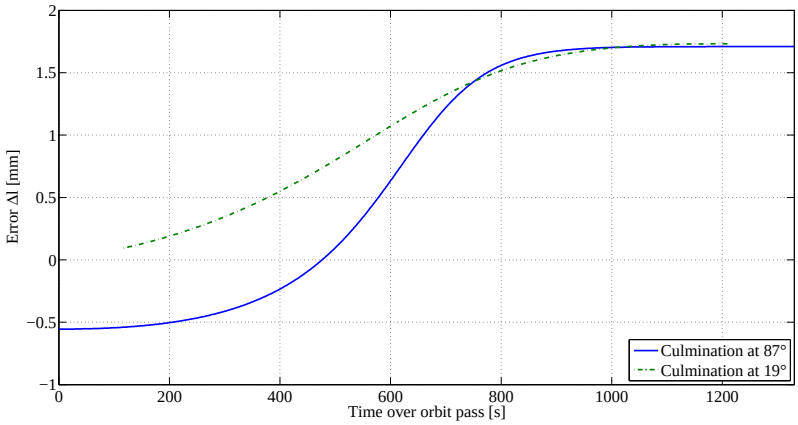

Figure 5.10.: Evolution of the error due to mechanical uncertainty of LRA and T2L2J2 optics

peripheral cubes are oriented at 50° with respect to nadir, see Fig. 2.4.
The incident laser pulse is nearly always reflected by more than one corner cube. As an example, facing the nadir cube normally, it provides 78.4% of the total reflecting area and the eight other cubes each provide 2.7%. When normal to one of the eight radially oriented cubes, that cube provides 65.5%, the cubes adjacent to it on the left and right each provide 16.1% and the nadir cube provides 2.3% of the total reflecting area.

ITE Inc. performed computer simulations [58] in order to determine the contribution of each corner cube to the return signal as a function of incidence angle σ and revolution angle ε. However, these simulations have not been performed in very high detail, since the goal was rather to analyze the discrepancies in the "range correction" for the different corner cubes. ITE calculates range correction values taking into account the actual far-field diffraction pattern and several apparent satellite velocities (for velocity aberration effects). The available data is not very exhaustive in terms of different orientations with respect to the LRA. Table 5.5 sums up the obtained range correction values (averaged for different velocities, referenced to the optical center) for orientations normal to each cube. Only two runs have been performed with an orientation between two cubes (at incidence angles σ of 25° and 50°). The last orientation with $\sigma = 25°$ and $\varepsilon = 22.5°$ is in between the three corner cubes N° 1, 2 and 9 and represents the extreme case: the actual optical depth of this arrangement is much lower (closer to the virtual optical center) than the other cases; this is due to the longer path before hitting the retroreflectors than when a cube face is normal to the laser beam.
In the absence of any more data about orientations in between the modeled cases we may assume an equal probability for any orientation and thus a rectangular distribution with a total span of 22.7 ps. Supposing eventually that no range correction is performed, we would obtain a standard uncertainty of 6.5 ps.

However, the range correction calculated by the reflector manufacturer does not adequately reflect the reality since it deals only with the theoretically determined optical depth of the corner cube arrangement. Yet there are two more aspects that come into play in real laser ranging as well as in time transfer:

- The laser pulses having a certain length, the different parts coming from different corner cubes superimpose to form a longer pulse or a pulse pattern.

Table 5.5.: Range corrections obtained for different corner cubes (ITE Inc.)

Cube N°	Inc. angle σ	Rev. angle ε	Range correction [ps]
9	0	0	161
1	50	0	157.3
2	50	45	158
3	50	90	157
4	50	135	157.3
5	50	180	157.3
6	50	225	157
7	50	270	156
8	50	315	155
1 & 2	50	22.5	155
1, 2 & 9	25	22.5	138.3

- One has to take into account the laser station's detector response vis-à-vis these pulse forms or patterns.

Generally, one has to examine the problem retroreflector/receive-detector in a common approach. Fig. 5.11 shows different superposed pulses for a laser pulse width of 35 ps, calculated by ITE (from [27]).

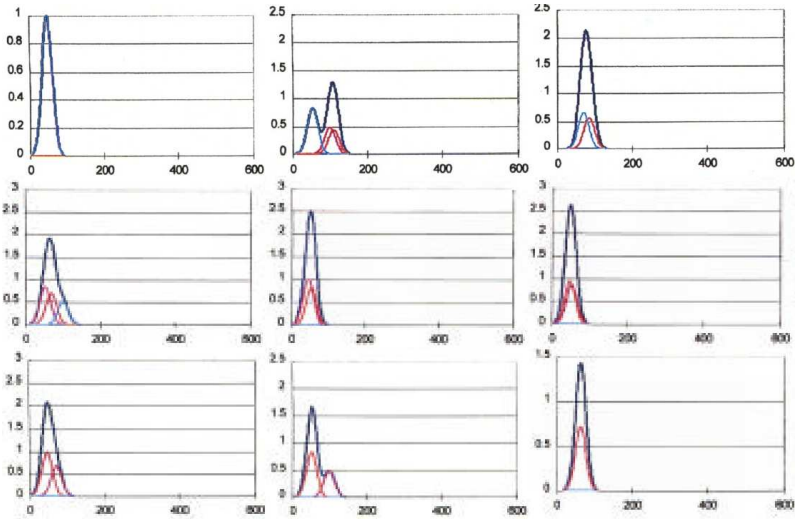

Figure 5.11.: Return pulses superimposed by the LRA's discrete corner cubes for 35 ps laser pulses

In Section 5.2, the combined problem LRA/station will be analyzed for different cases as the detection devices and the detection mode (single photon or multi-photon) play also a big role.

5.1.5. Atmosphere

Through its travel through the different atmospheric layers from laser station to satellite and back, the laser beam is refracted what leads to a slightly curved path instead of a straight. For

satellite laser ranging, in order to calculate a distance (in meters), the apparent path length is calculated with zenith delay and mapping functions for other elevations. Historically, the Marini-Murray model is used throughout the SLR community, but newer, more precise models (Mendes-Pavlis [59, 60]) are also available.

For time transfer, this study of the refractive index is not of importance in the first order, since the half round-trip time is subtracted in order to account for the actual distance from the station to the satellite. Therefore, systematic effects due to the atmosphere may be neglected.

However, the outward and inward bound optical paths are not perfectly equal, as a result of the motion of the station during the light pulse travel time; for the Jason 2 orbit, the round-trip time is on the order of some milliseconds during which the Earth surface (and the laser station) moves some meters[10].
Optical turbulence caused by turbulent mixing of air of different temperatures entails fluctuations of the air refractive index. The scale parameter of turbulence L_0 being often on the level of some meters, and the time constant of atmospheric turbulent structures evolution on the millisecond level, both aspects contribute to a variation of the refractive index between outward and inward path.

A very pessimistic estimate on the noise induced by this differential variation was given by [13] and [61] as a white noise of about 20 ps:

$$\sigma_{\mathrm{Atm}} = 20 \text{ ps} \tag{5.22}$$

For the uncertainty, this expression translates into:

$$u_{\mathrm{A,Atm}} = \frac{20 \text{ ps}}{\sqrt{N_{\mathrm{meas}}}} \tag{5.23}$$

The type B uncertainty may be neglected since no major systematic effects due to the atmosphere are expected.

However, the noise on the actual path length due to turbulence in the atmosphere should be studied in more detail; Equation (5.22) is of rather old and potentially obsolete origin. In 2005, a Czech-Austrian team measured one-way optical path delay fluctuations (from some kilometers to satellites) to be on the order of only 0.3 to 3 ps [62]. Currently, the SYRTE of the Observatoire de Paris is studying the influence of turbulence on the propagation of a coherent cw laser beam (Mini-DOLL project); it is possible that some part of this work could be of use in the T2L2 framework.

5.1.6. Relativity

There are several relativistic effects in the T2L2 time transfer scheme, concerning on the one hand the overall geometry and on the other hand the embarked clock. The geometrical issues are the Sagnac effect, i.e. the anisotropy of speed of light in a rotating reference frame; the second is the modification of the Euclidean distance between station and satellite due to the present gravitational potentials of Sun, Moon and Earth.
The difference in the gravitational potential between station and satellite and the speed of the satellite invoke a different clock rate than it would have on earth.

[10] Inducing path variations on the nanosecond scale, this movement is of course corrected from a geometrical point of view.

All these effects are very well mastered (see for example [63]) at the expected time transfer level. Errors in the modeling or through inaccurate data (like satellite coordinates etc.) may be neglected.

$$\sigma_{\mathrm{Rel}} \approx 0 \text{ and } u_{\mathrm{Rel}} \approx 0 \tag{5.24}$$

5.2. Contribution of the laser ranging station

The SLR (Satellite Laser Ranging) station represents, together with the clocks that have to be synchronized, the ground segment of the T2L2 experiment. The general layout of such a station has been addressed in Section 1.3. Nevertheless, the network of laser stations, federated in the ILRS (International Laser Ranging Service), is very heterogeneous. Though the overall employed technology relies on the same principles, the actual architecture of a specific laser station differs in many ways from another. It is therefore impossible to develop a global error budget by abstracting the instrumentation. Instead, it is chosen to give some benchmark data by selecting some representative stations that will be very involved in the T2L2 campaigns.

As a first station, the MéO station on the Plateau de Calern will be highlighted; the MéO station is the rejuvenated "Laser-Lune" station which will become fully operational only short time before the T2L2J2 exploitation. Therefore, no recent performance data does exist; nevertheless, since the main architecture stays the same (laser in the Coudé, detection in the Nasmyth focus, same detectors, same clocks and timers), we may assess its performance by formerly acquired data [57]. The second station is the mobile station FTLRS [48] of OCA and the third one the Wettzell station in south-eastern Germany.

For the precision and stability budget of the T2L2 time transfer, a laser station shows three contributors: The start detector, the return detector and the used event timer. Any biases in the system are typically accounted for by a continuous calibration that is performed in parallel to an SLR acquisition or interleaved between succeeding measurements. In order to perform accurate time transfer, a second calibration between the SLR system and the time/frequency infrastructure has to be performed.

Hence, the uncertainty budget is build with the type A contributions from the timing precision and the type B contribution of the calibrations.

5.2.1. Start date

The start detection of the laser pulse is of all the least delicate part of the time transfer. In most SLR stations a part of the laser IR output is directed onto the start detector; the photon number is sufficient to operate the start detector in a saturated, highly precise mode. Any bias due to laser power variations may thereby be neglected. The start detection is however sensible to variations of the laser pulse width: Since the detection is triggered by the rising edge of the pulse, a variation of the pulse width entails a shift of the start date. A statistic variation of up to 30% may occur in the warm-up phase of some lasers but this aspect is neglected here.

The precision σ_s may be accounted for by 5 ps [57]. The stability, considering a laser rate of 10 Hz, may be assessed with:

$$\sigma_{x,s}^2 = \left(K_{s1} \cdot \tau^{-1/2}\right)^2 + \left(K_{s2} \cdot \tau^{1/2}\right)^2 \tag{5.25}$$

with $K_{s1} = 1.6$ ps$\sqrt{\text{s}}$ and $K_{s2} = 3$ fs/$\sqrt{\text{s}}$ (see Fig. 5.13).

Hence we obtain for the uncertainty:

$$u_{\text{A},s} = \frac{5 \text{ ps}}{\sqrt{N_{\text{meas}}}} \tag{5.26}$$

with N_{meas} being the number of usable measurements that depend on the return rate (see below). This expression is true since the start detection features white noise behavior over sufficient long integration times.

5.2.2. Return date

The biggest contribution of the laser station to the error budget originates in the detection of the returning pulse. As mentioned in Section 2.3.1.2, one has to respect the couple retroreflector response - return detector. Following issues have to be considered:

- The retroreflector response consists of a pulse pattern or a longer superposed pulse as a function of attitude that may modify the detector behavior (compare Fig. 5.11) like an increase in imprecision and an additional bias.

- The received photon level is governed by various effects: The actual distance between station and satellite as well as the corresponding elevation create a clear signature on the laser return power.
  On top of that signature there are some other effects: The received photon level is a function of the attitude dependent effective cross-section of the LRA, which varies from 1 (normalized at nadir incidence) to 2.7. It is further governed by the speckle feature of the laser beam at satellite level: Atmospheric turbulence reduces the horizontal coherence length ρ_c well below the beam radius W_h (at atmosphere exit). These incoherent regions create an interference pattern, similar to speckles, with a scale $\varepsilon = \frac{\lambda\ H}{\pi\ W_h}$ between 0.5 and 20 m (with λ being the wavelength and H the orbit altitude). The expected scintillation factor due to this speckle feature is expected [64] to be $\alpha = 0.6$. The energy received by the T2L2 detector and reflector is then between $(1 \pm \sqrt{\alpha}) \cdot I$.
  The variances of the LRA cross-section and speckle feature being of the same order, it is not possible to distinguish between the two effects. Including other effects like variation of velocity aberration, laser fluctuations and pointing quality, the return energy may be regarded as totally random over the mentioned distance/elevation signature (due to distance and atmospheric attenuation).
  Since most photodetectors are afflicted with a time-walk (just as the T2L2 detector, compare Fig. 5.3) and a precision (compare Fig. 5.1) that both depend on the impinging photon number, the randomness of the return photon level is a major issue.

Most detectors feature a time walk that depends on the impinging photon number. In order to overcome this unwanted bias in the range measurements, several methods are used throughout the SLR community: First, working in single-photon mode what assures a constant photon level (meaning unity). Second, the use of a time-walk compensated detector. These two techniques are described in the next paragraphs by the means of the three laser station examples evoked above. Further, the effect of the LRA response is addressed.
A third technique consists in the analysis of the signal amplitude of the detector at each acquisition (possible for PMTs since the response is sufficiently linear) or by employing a second detector. The time walk is then corrected aposteriori, like in the T2L2 instrument. Yet, this technique is not commonly employed.

Single photon mode - Grasse MéO station The MéO laser ranging station of OCA uses a very common single-photon avalanche diode (SPAD), the Silicon Sensor SSOAD230, afflicted with a strong time walk of about 100 ps per decade (for photon numbers above 1).

A means to insure a constant return pulse energy level on the detector (to keep the time walk on a constant level) is to artificially keep the return rate down: For low photon flux, the detection probability P_{det} follows Poisson statistics with $P_{\text{det}} = 1 - \exp(-n\rho)$, where n is the actual photon number and ρ is the quantum efficiency of the detector. In practice, the operator holds the detection probability on a level of around 10% by putting neutral density filters in front of the return detection. This operation is significantly complicated by the fact that the speckle feature at the retroreflector level intrinsically causes a twinkle-like return rate, even when having a strong signal. Theoretically, the photon number may only be determined a posteriori. Practically, one has to rely on the experience of the respective operator in order to achieve an acceptable single-photon rate and at the same time ensuring a strong photon number on T2L2J2 (yielding that a depointing has to be avoided). A too high detection probability may lead to an increased portion of two-photon events what would generate a bias in the return detection.

A further advantage of working in single photon mode is the possibility to discern the signature of the LRA, as far as there are several pulses instead of a pulse superposition. With the 20 ps pulsewidth of the MéO station's laser and the optical depth of the LRA, this condition can be fulfilled for incidence angles close to 10° and 30° as shown in Fig. 5.12; in these cases, the barycenters of the two generated pulses are separated by about 50 ps.

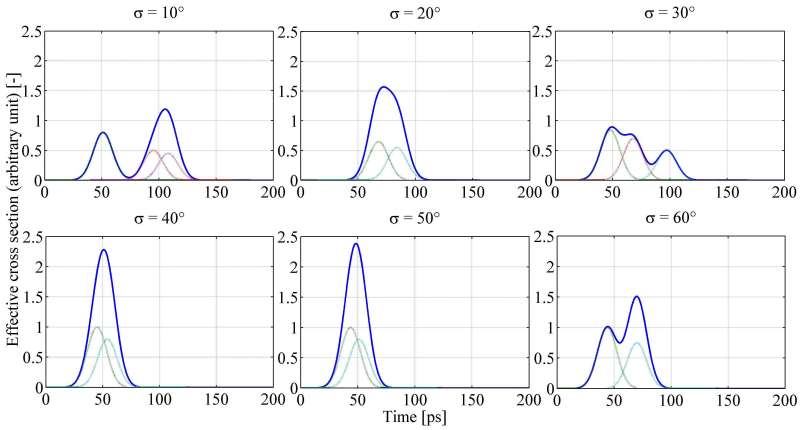

Figure 5.12.: Pulse pattern created by the LRA for laser pulse widths of 20 ps, attitude $\varepsilon = 0°$ with incidence angle σ varying from 10° to 60°. These pulse patterns have been recalculated based on the data provided by [27].

Generally, the detector's intrinsic precision $\sigma_{\text{SSO}} = 40$ ps is affected by an average return pulse width $\langle w_{\text{LRA}} \rangle$ of about 25 ps; the maximum generated pulse width is 38 ps for incidences about 30°.

$$\sigma_{r,\text{MeO}} = \left(\sigma_{\text{SSO}}^2 + \langle w_{\text{LRA}} \rangle^2\right)^{1/2} = 47 \text{ ps} \tag{5.27}$$

In order to assess the time stability of the return detection in single-photon mode, one has to take account of the effective return rate, which is considerably degraded:

$$R_{\text{return}} = \frac{1}{\tau_0} = f_{\text{rep}} \cdot P_{\text{det}} \tag{5.28}$$

Considering a reasonable detection probability of 10% in order to ensure single-photon operation, the stability may be modeled as follows:

$$\sigma^2_{x,r,\mathrm{MeO}} = \left(K_{r,\mathrm{MeO1}} \cdot \tau^{-1/2}\right)^2 + \left(K_{r,\mathrm{MeO2}} \cdot \tau^{1/2}\right)^2 \tag{5.29}$$

with $K_{r,\mathrm{MeO1}} = 47$ ps$\sqrt{\mathrm{s}}$ and $K_{r,\mathrm{MeO2}} = 28$ fs$/\sqrt{\mathrm{s}}$ (see Fig. 5.13).

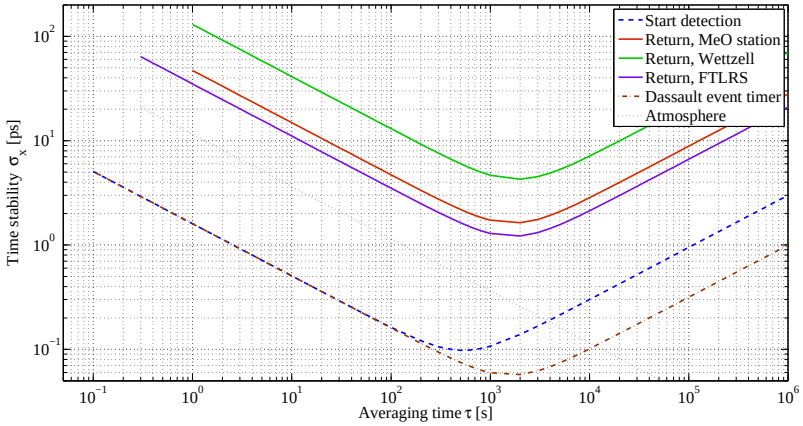

Figure 5.13.: Contributions of the laser stations and atmosphere to the time transfer stability budget

For the uncertainty follows:

$$u_{\mathrm{A},r,\mathrm{MeO}} = \frac{47 \text{ ps}}{\sqrt{N_{\mathrm{meas}}}} \tag{5.30}$$

The number of utilizable measurements N_{meas} is determined from Equation (5.28) and the length of the pass over the station (since the return detector features white noise on these time scales).

As we saw, the operation in single-photon mode has also some inconveniences, notably the rather difficult operation (artificial signal attenuation) and the resulting weak return rate. In the MéO development it is envisaged to operate the SSO SPAD (or a K14) together with a linear photodiode in order to perform an a-posteriori time walk correction as in T2L2J2. The big collection surface of MéO will definitely allow to implement this type of double detection for LEO satellites as Jason 2. By this means, the SPAD could be operated in multi-photon mode and at the full return rate, without deterioration by the (single-photon) detection probability.

Single photon mode - Wettzell WLRS station The WLRS station is equipped with three different detectors: An MCP with a precision of about 100 ps that is mostly used for LEO satellites as Jason 1, an APD with 70 ps and a PMT with 50 ps. For the reasons of rather poor quantum efficiency of MCP and PMT (about 5%) and time-walk issues, the detectors are usually operated in single-photon mode. The initial laser pulse width is of 80 ps, but this is slightly degraded (a similar calculation as for Fig. 5.12 has been performed) by the LRA signature to a value of $\langle w_{LRA} \rangle = 87$ ps. Considering the MCP, the precision reads:

$$\sigma_{r,\mathrm{WLRS}} = \left(\sigma^2_{\mathrm{MCP}} + \langle w_{\mathrm{LRA}} \rangle^2\right)^{1/2} = 130 \text{ ps} \tag{5.31}$$

This assessment is roughly consistent with the upper value of the Jason 1 Normal Point r.m.s.: These r.m.s. values are normally comprised between 30 and 130 ps, what means that the assumptions made above are rather conservative (The normal point data for the WLRS station is given in the Appendix, Fig. A.1.). With a typical return rate of 10% (ensuring single photons) it follows for a stability estimation:

$$\sigma^2_{x,r,\mathrm{WLRS}} = \left(K_{r,\mathrm{WLRS1}} \cdot \tau^{-1/2}\right)^2 + \left(K_{r,\mathrm{WLRS2}} \cdot \tau^{1/2}\right)^2 \tag{5.32}$$

with $K_{r,\mathrm{WLRS1}} = 130$ ps$\sqrt{\mathrm{s}}$ and $K_{r,\mathrm{WLRS2}} = 70$ fs$/\sqrt{\mathrm{s}}$ (see Fig. 5.13).

The uncertainty (type A) reads (for measurement times up to 1,000 seconds):

$$u_{\mathrm{A},r,\mathrm{WLRS}} = \frac{130 \text{ ps}}{\sqrt{N_{\mathrm{meas}}}} \tag{5.33}$$

Compensated detector - Mobile FTLRS station A very common method throughout the SLR community to overcome the time-walk issue is the use of a compensated detector [65], commercially available as the CSPAD. This detector uses the K14 avalanche photodiode (as in T2L2J2) together with an additional electronic circuit that applies an analogue time-walk correction. The electronics use the slope of the diode avalanche output signal to adjust the time-walk compensation.

Since the signal slope depends also on the slope of the incident laser pulse, the CSPAD is very sensitive to any variation of laser pulse widths as we observe with LRA signature. This effect has experimentally been studied at OCA[11], with the mobile station FTLRS and a set of three corner cubes emulating the LRA. The different LRA attitudes could be simulated by varying the distance between the FTLRS and the individual corner cubes. Usually, in multi-photon operation, the station's CSPAD detector has a precision of about 12 ps [49, p. 111] (with the laser's natural pulsewidth of 30 ps). The performed experiments showed a degradation of the detection precision on the order of 30 ps for the corner cube distance dynamic:

$$\sigma_{r,\mathrm{FTLRS_{exp}}} = 30 \text{ ps} \tag{5.34}$$

Theoretically, one derives for the LRA induced pulse broadening: $\langle w_{LRA} \rangle \leq 40$ ps, with a possibility to discern some of the pulse patterns around 10° of incidence. With the 12 ps precision this leads to:

$$\sigma_{r,\mathrm{FTLRS_{theo}}} = \left(\sigma^2_{\mathrm{CSPAD}} + \langle w_{\mathrm{LRA}} \rangle^2\right)^{1/2} = 42 \text{ ps} \tag{5.35}$$

These considerations don't account for the residual time walk of still 20 ps per decade [49, p. 108] that exhibits the CSPAD detector. This is somewhat better than the naked K14, but still introduces a dispersion of the dates due to random laser return energy[12]. In practice, the return rate is held on a level between 20 and 30% in order to reduce the dynamic of the return photon number and thus limit the residual time walk effect to a reasonable minimum. The last campaign in Burnie, Tasmania showed an average Normal Point precision of about 60 ps (compare to Fig. A.8.4 in the Appendix, showing the Normal Point precision):

$$\sigma_{r,\mathrm{FTLRS_{Burnie}}} = 60 \text{ ps} \tag{5.36}$$

[11] This experiment has been performed by E. Samain in 2005.

[12] In order to overcome the residual time walk and to provide most consistent data to the community, the English Herstmonceux laser station usually operates the CSPAD detector in single-photon mode as well.

In order to assess the performance in a conservative manner, it is chosen to use the data of Burnie rather than the laboratory or theoretical values mentioned before. Further experiments of J. Nicolas [49] on the FTLRS-CSPAD showed a flicker floor of about 1.2 ps; the stability may thus be written:

$$\sigma^2_{x,r,\mathrm{FTLRS}} = \left(K_{r,\mathrm{FTLRS1}} \cdot \tau^{-1/2}\right)^2 + \left(K_{r,\mathrm{FTLRS2}} \cdot \tau^{1/2}\right)^2 \tag{5.37}$$

with $K_{r,\mathrm{FTLRS1}} = 35\ \mathrm{ps}\sqrt{\mathrm{s}}$ and $K_{r,\mathrm{FTLRS2}} = 15\ \mathrm{fs}/\sqrt{\mathrm{s}}$ (see Fig. 5.13).
The uncertainty of the FTLRS return date is thus:

$$u_{\mathrm{A},r,\mathrm{FTLRS}} = \frac{60\ \mathrm{ps}}{\sqrt{N_{\mathrm{meas}}}} \tag{5.38}$$

5.2.3. Event timer

The SLR community uses a wide range of event timers or time interval counters with all kinds of precision. The three laser stations considered here, though, all use the commercial state-of-the-art event timers of THALES, former Dassault Electronique. It features a very good linearity, precision and stability. For all three stations, the (single shot) precision is around 5 ps and the stability may be modeled as (for 10 Hz repetition rate):

$$\sigma^2_{x,\mathrm{Timer}} = \left(K_{T1} \cdot \tau^{-1/2}\right)^2 + \left(K_{T2} \cdot \tau^{1/2}\right)^2 \tag{5.39}$$

with $K_{T1} = 1.6\ \mathrm{ps}\sqrt{\mathrm{s}}$ and $K_{T2} = 1\ \mathrm{fs}/\sqrt{\mathrm{s}}$ (see Fig. 5.13).

The type A uncertainty for both start and return timing reads:

$$u_{\mathrm{A,Timer}} = \frac{5\sqrt{2}\ \mathrm{ps}}{\sqrt{N_{\mathrm{meas}}}} \tag{5.40}$$

The systematics uncertainty (B-type) of the timing system may be considered as zero since any phase offsets or other biases (changed cable lengths) are cancelled by the internal calibration of the SLR system, what is addressed in the next section.

5.2.4. SLR system internal calibration

In Chapter 4.2 the calibration quantity was introduced with Equation (4.3). It is subtracted from each measured laser pulse round-trip time.

$$\langle t_{cal} - t_s \rangle + \frac{2\ d_{\mathrm{Cal}} n_{\mathrm{Air}}}{c}$$

The first term denotes the calibration measurement: It is usually performed over a longer period, parallel to the ranging acquisitions or before and after. The value is averaged over a period τ_{Cal} that features only white noise. The corresponding precision and type A uncertainty $\sigma_{x,\mathrm{Cal}}(\tau_{\mathrm{Cal}})$ is usually below the picosecond level and thus negligible in the stability budget.

In the uncertainty budget therefore appears only a type B contribution coming from the second term in the calibration quantity: This is mainly due to the measurement uncertainty about the distance d_{Cal}.

Since mainly internal calibrations come into play (for MéO and WLRS), the uncertainty about the refractive index of air n_{Air} may be neglected.
The mobile station uses an external target situated at a distance between 100 and 200 m: The uncertainty on the refractive index is on the millimeter level in this case. For the last campaign in Burnie, Tasmania, the combined uncertainty of d_{Cal} and n_{Air} has been confirmed to about 3 mm (meaning 20 ps) by the comparison of internal to external method. Table 5.6 summarizes the uncertainty of the three discussed stations:

Table 5.6.: Uncertainty of the calibration of the SLR instrumentation

Station	$u_{\mathrm{A,Cal_{int}}}$ [ps]	$u_{\mathrm{B,Cal_{int}}}$ [ps]
MéO	≈ 0	15
FTLRS	≈ 0	20
WLRS	≈ 0	15

5.2.5. Calibration between time/frequency and SLR systems

As pointed out in Chapter 4.3, OCA prepares a dedicated calibration equipment in order to measure the time interval between the PPS and the laser pulse passing through their respective reference points. This serves for attaching the time transfer measurement to the local time frame in an absolute manner of high exactitude.
This specific equipment consists mainly in an event timer, a high speed detector and electronics and an optical fiber. Table 4.2 summarized the projected parts of the equipment. In the following, a short assessment of the uncertainty in this calibration process is given. Please note that this assessment serves uniquely to determine the expected scale and is entirely based on assumptions; this exercise has to be rigorously re-iterated when the equipment has finally been built and tested.

Time/frequency part A delicate part in the calibration process is the timing of the PPS pulse; it has first to be converted into some logical signal that is accepted by the event timer. Preferably, this is carried out with a fast comparator. The problem is the definition of a temporal reference point what gives this calibration some arbitrary notion; however, if each participating station is calibrated in the same way, this is of no concern.
One has to define a level (in the PPS pulse) whereon the comparator should trigger. Considering the steepest part of the PPS rising edge (compare to Fig. 4.7, with an equivalent rise time of about 3 ns), one finds a slope of about 2 ns/V: With an r.m.s. of 1% of a reference voltage, one would obtain a jitter of at least 20 ps, meaning that the timing precision is governed by the PPS and not the comparator.
We then have some uncertainty (systematic) on the comparator response and transit time: Inphi (a high-speed electronics manufacturer) specifies for its latest 25 GHz comparator (25706 CP) around 100 ps propagation delay in the component; this number has to be evaluated employing a fast (50 GHz bandwidth) oscilloscope that OCA recently acquired. An error of 10% on this determination means a type B uncertainty of 10 ps.

Then, the physical (or better: temporal) lengths of the conductors on the electronics board (PCB) where the circuitry will be implemented has to be assessed; claiming a millimeter-level, an error of about 5 ps may be budgeted. Great care has also to be taken with respect to the thermal sensitivity of the used PCB material.

Finally, cable lengths have to be determined: Even though they may be precisely measured using a signal generator and an event timer, this is a delicate undertaking with respect to the spectral distribution of the actually used signal: The propagation times may not be the same for different signal forms; this is generally true for absolute signal delay determination when it comes to picosecond resolution. Further, connector margins account at least for some picoseconds. We may easily assign another 10 ps for these contributions of the cable lengths.
Since we opted for short cable lengths (timer and electronics assembly near the clock), a possible thermal expansion term may be budgeted to some picoseconds (typical coaxial cable propagation times are on the order of 3.9 to 5 ns/m and the thermal expansion on the order of 10^{-4} 1/°C).

Table 5.7.: Assessed uncertainty contributors of the calibration equipment

Equipment	Issue	$u_{\mathrm{B,Cal_{TF-SLR}}}$ [ps]
Comparator	Delay time	10
Conductors	Length	5
Coaxial cables	Length	10
	Thermal expansion	2
Insertion optics	Traversed distance	3
	Installation	15
Optical fiber	Thermal expansion	4
Photodetector	Transit time	4
	Optical architecture	3
	Sum	**25**

SLR part On the optical part, we first have to deal with some insertion optics and its geometrical layout: The distance traversed by the laser pulse may be determined on the mm-level; the position of this setup has to be ascertained with respect to the reference point of the SLR system (see Section 4.2). This brings in an uncertainty that will be on the same order as the one of the SLR calibration, thus 15 ps (see Table 5.6).

The length of the optical fiber, at least 200 m for a calibration of Wettzell or the Observatoire de Paris, may be determined employing the equipment of the T2L2 test bed, yielding a precision of about 3 ps and a negligible uncertainty when averaging sufficiently longtime. Being guided between different buildings, this fiber may undergo serious thermal variations. The thermal expansion of an optical fiber core is that of fused silica [66], $0.6 \cdot 10^{-6}$ 1/°C. For a length of 200 m and a temperature range of 10°C results an uncertainty of 4 ps.

Chapter 4.3 mentioned already that a most fast, simple and small photodetector should be employed. A good candidate is the time-domain optimized photodiode M1024 of New Focus with a rise time of 12 ps. The error on the transit time may be estimated to be below 4 ps when supposing a modeling error of 30%. When operated in a saturated mode, the detector precision should be well below the value of the one used in the T2L2 test campaigns (Section 3.1.2.4)[13]; further, its stability should allow to average below the picosecond level. The transit time uncertainty of the laser pulse in the optical architecture (fiber-pigtailed package) may be assessed with about 3 ps.

[13]Value for MéO and FTLRS; may be higher for WLRS since laser pulse width is 80 ps.

Finally, the subsequent electronics being of the same type (fast comparator etc.) as for the PPS pulse, the uncertainty may be assessed on the same order.

Table 5.6 gives the overall uncertainty budget that may be expected from the calibration. We assume that all type A uncertainty contributors (photodetection and PPS conversion precision etc.) may be averaged out to values below the picosecond.
It was shown that a level of 25 ps may be obtained through the use of appropriate equipment. It is obvious that the accuracy of the calibration depends mainly on estimations of signal delay (or propagation) times. These have to be verified in a very meticulous manner; further it has to be assured that the measurement conditions in the different laser stations are rigorously the same in order to perform a valid absolute calibration.

This present uncertainty assessment should be revised when the calibration equipment is build.

5.3. Summary I: Clock to clock time transfer stability

This section proceeds to the calculation of the overall time stability budget for a ground to ground time transfer. It first addresses the time transfer in common view mode, and then passes to non-common view.

5.3.1. Time stability budget for common view time transfer

5.3.1.1. Ground to space time transfer

From Equation (1.1) follows the overall time stability of a time transfer from a ground station A to the T2L2J2 instrument on the satellite S:

$$\begin{aligned}\sigma^2_{x,AS}(\tau) = \frac{1}{4}\left(\sigma^2_{x,s}(\tau) + \sigma^2_{x,r}(\tau) + \sigma^2_{x,\mathrm{Cal}}(\tau)\right) + \frac{1}{2}\sigma^2_{x,\mathrm{Timer}}(\tau) \\ + \sigma^2_{x,\mathrm{T2L2}}(\tau) + \sigma^2_{x,\mathrm{Atm}}(\tau) + \sigma^2_{x,\mathrm{Geo}}(\tau) + \sigma^2_{x,\mathrm{Rel}}(\tau)\end{aligned} \tag{5.41}$$

The contributions $\sigma_{x,\mathrm{Cal}}$, $\sigma_{x,\mathrm{Geo}}$ and $\sigma_{x,\mathrm{Rel}}$ have found to be negligible in terms of time stability. The other contributions have been determined with the expressions (5.25), (5.29, 5.37, 5.32), (5.39), (5.3) and (5.22). Fig. 5.14 shows the thus calculated time stability

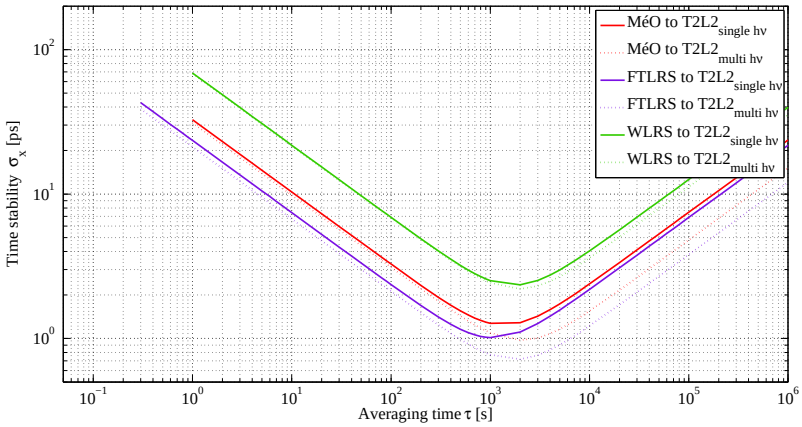

Figure 5.14.: Time stability of the one-way time transfer from a ground station A to T2L2

of a ground to space time transfer for the three considered laser ranging stations MéO, FTLRS and WLRS; the solid lines show the respective result when the T2L2J2 instrument is operating in single-photon mode, and the dotted lines when operated in multi-photon mode.

Before calculating the overall time stability for a ground to ground transfer, some considerations about the experiment operation should be addressed.

5.3.1.2. Operational aspects of the common view time transfer

There are several aspects to be considered before proceeding to the calculation of the overall time transfer stability.

Chapter 5.2 mentioned already the return rate $R_{\mathrm{return}} = f_{\mathrm{rep}} \cdot P_{\mathrm{det}}$, which is reduced by P_{det} as compared to the emitted laser rate, due to the operation in single- or few-photon mode of the ground stations. In a τ-σ_x chart, this shifts the stability curve to the right. As

for any measurement, it has to be assured that the measurement rate stays on a reasonable level.

The second aspect is the actual length of a dataset that may be acquired in common view mode. The image in Fig. 5.15 shows the satellite passes over our considered three ground stations. The minimum considered elevation was generally set to 10° in this simulation,

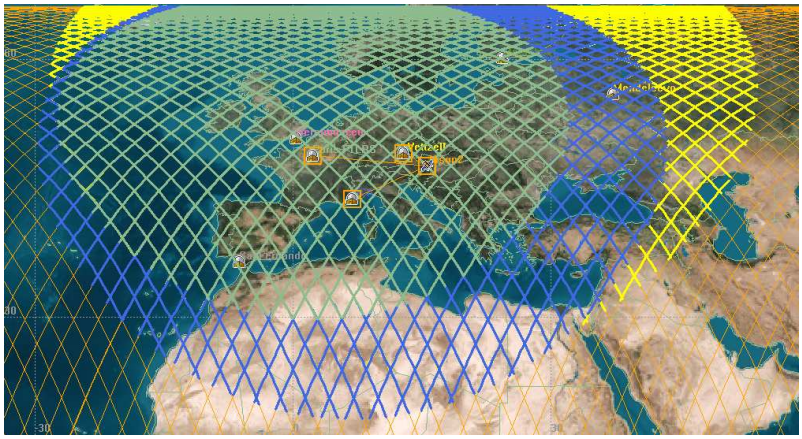

Figure 5.15.: Jason 2 passes over the SLR stations MéO in Grasse (blue), FTLRS in Paris (green) and WLRS in Germany (yellow)

except for the FTLRS that is supposed to be located on the roof of the Observatoire de Paris in the Paris city center; therefore, the minimum elevation was set to 20°.
Common acquisitions for a ground A to ground B time transfer rely on the establishment of a pair of the mentioned data triplets $\{t_s,\ t_b,\ t_r\}_A$ and $\{t_s,\ t_b,\ t_r\}_B$.
These exist only for common pass portions: In the case of a time transfer between MéO and the FTLRS in Paris, the common portion is dictated by the Paris elevation constraint and on the order of 560 seconds.
In the case of a MéO to WLRS time transfer the common portion lasts about 700 seconds.
One sees that the acquisitions stay in the white noise regions of the time stability (Fig 5.14); the overall behavior of the instrumentation above the maximum pass length ($<$ 1,000 s) is therefore of purely theoretical value.

The third point concerns the averaging performed in the time transfer scheme: The paragraph above described that for common view configuration, an averaging over the whole length of the common pass may be performed.
Additionally, a further averaging may performed using consecutive passes: For western Europe stations, the passes repeat six to seven times per day (one half ascending, i.e. coming from SW, heading to NE, the other half descending from NW to SE). The passes shift from day to day and the whole scheme repeats with a period of 10 days.
We may now assume that the overall noise in the instrumentation (stations and T2L2J2) is independent from one pass to another (i.e. white) and continue to average over the six to seven passes of a day. In a second step, we may further average over a couple of days. This procedure, regularly employed in TWSTFT, is addressed in the following section.

5.3.1.3. Time transfer in common view

The time stability of a time transfer from ground station A to ground station B is simply calculated by a squared sum of the individual contributors:

$$\sigma_{x,AB_{\mathrm{CV}}}(\tau) = \left(\sigma^2_{x,AS}(\tau) + \sigma^2_{x,BS}(\tau)\right)^{1/2} \tag{5.42}$$

Fig. 5.16 depicts two such time transfers, between MéO and FTLRS (placed at OP in Paris) and between MéO and WLRS. Parts (a) and (c) give the time stability over one common pass (until integration times of 500 and 700 s, respectively).
Parts (b) and (d) give the averaging performed over the six to seven passes per day and then further averaged over up to ten days. One has to keep in mind, that the used averaging times τ' (abscissae) reflect the actual elapsed time and not the acquisition time.
Please note that the curves (b) and (d) may only indicate a lower level of the time stability

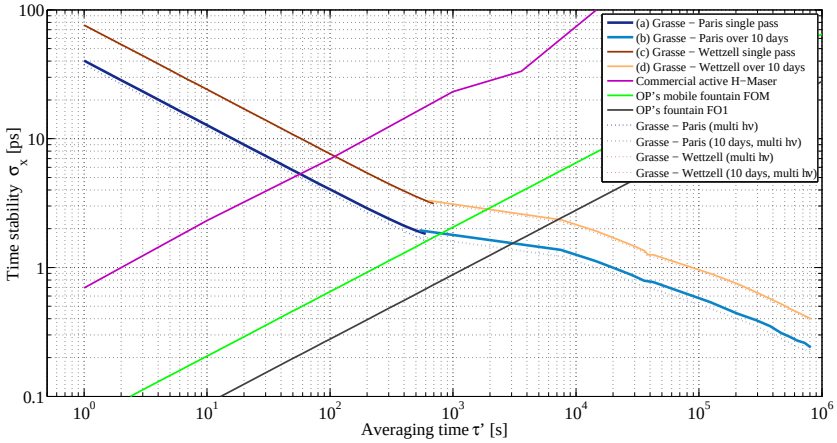

Figure 5.16.: Time stability of two ground to ground time transfers, including averaging over multiple passes

since pure white noise behavior was assumed; there may appear other long-term not random processes that inhibit this assumption.

The figure further shows the time stability of some frequency standards like some Cesium fountains of the Observatoire de Paris (OP/SYRTE) and a commercial hydrogen maser.

The graphic indicates that T2L2 will permit to compare high performance frequency standards for integration times of some hundreds to thousands (over some passes) of seconds.

5.3.2. Time stability budget for non-common view time transfer

Before proceeding to the calculation of the time stability of a time transfer in non-common view configuration, some aspects concerning the procedure have to be addressed.

5.3.2.1. Operational aspects of the non-common view time transfer

The concept of time transfer with T2L2 in non-common view is inherently different from the one in common view; Fig. 5.17 clarifies this facet with the T2L2J2 on-board time frame: In common view operation, i.e. when two (or more) SLR stations A and B fire on the satellite, the received events $t_{b,A}$ and $t_{b,B}$ have a well-defined temporal relation: The separating time

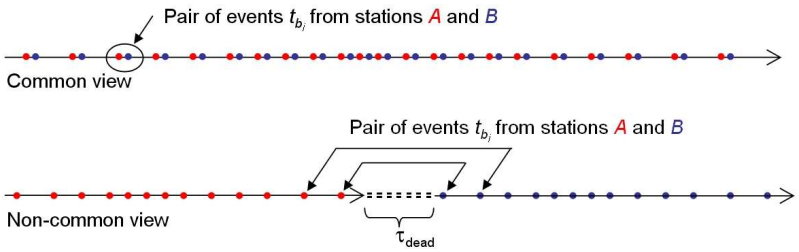

Figure 5.17.: Time scales aboard Jason 2: Common view and non-common view events

interval relies on the DORIS oscillator, whose actual frequency (and drift and so forth) is perfectly determined from the whole dataset of one pass (compare to Section 5.1.3).

Yet, for non-common view time transfer, the whole datasets with the $t_{b,A}$ and $t_{b,B}$ are separated by a gap[14] of τ_{dead}. Due to the instability of the DORIS oscillator, there is a particular uncertainty about the τ'_{dead} that is actually seen by the oscillator. Both the interval τ'_{dead} and the error on its estimation are common to the whole set of dates t_b. The error on the estimated value is described by Equation (5.19) and introduces some hundreds to thousands of ps in the time stability and uncertainty budget.

This is the reason why the non-common view time transfer relies on the repetitive acquisition of consecutive passes over longer periods (some days) in order to provide some viable data. For all passes, the error may equally be assessed by Equation (5.19), even when the oscillator behaves different each time; therefore the whole dataset is afflicted with a dispersion of the same type (see Section 5.1.3).

In the following, two examples for non-common view time transfer are discussed, one between USA and France and one between France and China.

Transatlantic time transfer This section considers a time transfer between the SLR station in Greenbelt, Maryland (East coast of United States) and the MéO station in Grasse without going into detail concerning the respective equipment in Greenbelt as performed in the previous sections for MéO, FTLRS and WLRS. The system is a mobile NASA/Honeywell MOBLAS station operating a 200 ps green Nd:YAG laser and providing a typical Normal Point r.m.s. of about 50 ps on Jason 1 (see Fig. A.3 in the Appendix).

The only possible way for a time transfer with Grasse are the ascending passes over Greenbelt (Fig. 8.4 in the Appendix), with Jason 2 passing over the MéO station some minutes later. There are three passes of that type per day, with a mean duration of 760 s over Greenbelt and 780 s over MéO. The dead time is on the order of 350 s, thus introducing about 600 ps in the stability and the uncertainty budget due to oscillator noise.

A way to mitigate the long dead times and thus the accumulation of oscillator noise in the non-common view configuration is to follow the oscillator behavior with an intermediate laser ranging station, located in the uncovered zone. It is not necessary that this station intervenes directly in the time transfer (with a sophisticated clock, for instance), as long it may provide absolute time tags t_s and t_r (with the corresponding t_b aboard).
In order to efficiently cover the "dead-time"-zone, an assisting laser station should be located

[14] This is some value between the last $t_{b,A}$ and the first $t_{b,B}$ in a virtual common time frame including clocks A and B. This time frame that does not exist and represents what we just want to establish with the time transfer.

most closely to the great-circle that connects the two primary stations and well in the middle between them (ideally). For the case of Greenbelt and Grasse, this point falls unfortunately in the middle of the North Atlantic. The next SLR stations close to this point in Europe

Figure 5.18.: A transatlantic time transfer may be assisted by the English Herstmonceux or the Finnish Metsahovi station

(most NW) are the English Herstmonceux station and the Finnish Metsahovi station. A simulation shows that the dead time could largely be reduced to about 210 and 270 s, respectively. By this means, the oscillator noise could be reduced by around the half.

Eurasian time transfer Another interesting time transfer over a long baseline stretches from France to China, namely to the Shanghai and/or Chanchun stations in the very East. Such an experiment is further appealing since the Shanghai Observatory itself developed and operates an optical time transfer system (LTT, Laser Time Transfer [33]), together with the Changchun station[15]. In addition, such an experiment would permit to calibrate the young TWSTFT network in China. The possible configuration includes about two usable passes per day for Shanghai and about three for Changchun. For a conventional time transfer,

Figure 5.19.: Eurasian time transfer between Grasse and Shanghai or Changchun

the mean dead time between the stations Grasse and Changchun is of about 580 s, and for

[15]The LTT scheme implies the laser stations to fire on the satellite instrument in predefined temporal windows, what necessitates a modification of the employed laser systems.

Shanghai of 780 s. Just as for the transatlantic time transfer, one lacks laser stations that fulfill the above-mentioned requirements for an intermediate station. The Maidanak station in Uzbekistan is quite far off the great circle connecting Grasse and Shanghai or Changchun: Consequently, it may only track half of the passes and reduce the dead time to 360 and 280 s, respectively.

Once again, the Finnish station in Metsahovi may in some sense extend OCA's passes over the Eurasian continent and thus reduce dead time for all passes to values about 380 s for Shanghai and 160 s for Changchun. The Russian station in Moscow (Mendeleevo) may prolongate even farther: Dead times are reduced to 305 and 100 s, respectively.

In the following section, the different expectable performances of the assisted and not-assisted non-common view time transfer between USA, France and China are discussed.

5.3.2.2. Time transfer in non-common view

For non-common view time transfer, the earliest common point τ_0' (of sets A and B) occurs after the first integration phase over station A (designated with $\bar{\tau}_A$) and after the "blackout" between the stations (τ_{dead}), giving the corresponding τ_0':

$$\tau_0' = \bar{\tau}_A + \tau_{\text{dead}} \tag{5.43}$$

The stability of one single set (of acquisition over A and B) reads:

$$\sigma_{x,AB_{\text{NCV}}}(\tau') = \left(\sigma_{x,AS}^2(\bar{\tau}_A) + \sigma_{x,BS}^2(\tau' - \tau_0') + \delta t_{\text{pred}}^2\right)^{1/2} \tag{5.44}$$

since the two measurement series are necessarily independent.
In order to improve that time transfer, these series may be repeated over and over again: Assuming further random noise relation between the series, the stability of Equation (5.44) at the end of the pass over B, $\sigma_{x,AB_{NCV}}(\bar{\tau}_B')$, may be ameliorated by the number of passes through $\sqrt{N_{\text{passes}}}$, at the respective τ' corresponding to the repeat rate of the passes.

For the USA-France time transfer with Greenbelt, there are three possible passes per day, with an interval of 100 min between them; after 18 to 20 hours, the whole cycle repeats. Fig. 5.20 shows the respective time stability when averaging over up to ten days. It is clearly visible that the noise of the DORIS oscillator inhibits a competitive time transfer when dead times become important. The graphic shows a time transfer between Greenbelt, Maryland and Grasse without any intermediate station (blue curve) and with the English Herstmonceux station (violet) as assistance. It further shows a time transfer with Changchun, China, assisted by the Russian Mendeleevo station (red); all time stabilities are governed be the oscillator noise of some hundreds of ps (for dead times of some hundred seconds). The only way to reduce the noise is to acquire all passes over several days; however, it is not sure that there won't come up some systematic related flicker or other noise over longer periods.

The only highly precise curve is presented in green: For the Grasse - Changchun time transfer, one pass per day may be tracked and completely covered by the Mendeleevo and Maidanak station; in this way, the oscillator may be monitored at a high level. Hence, the phase relation between acquisitions A and B are known and the oscillator noise δt_{pred} is zero. Consequently, this configuration permits to establish a first intercontinental time transfer on the 20 ps level.

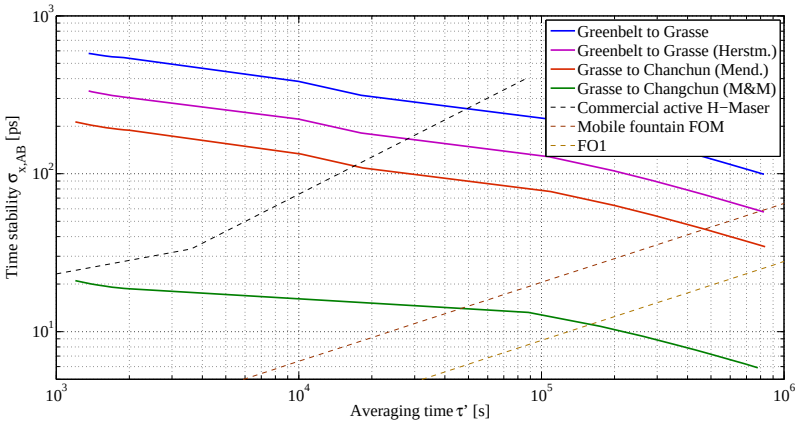

Figure 5.20.: Averaging of subsequent passes for non-common view time transfer between France, USA and China

Nevertheless it has to be remarked that the overlap between the respective passes over the four different laser stations is on the order of two minutes, for a minimum elevation of only 10°. This puts high demands on the laser ranging instrumentation and means that the weather conditions should be rather good over the whole continent; in other words, this is some serious sport, but worthwhile to try.

5.4. Summary II: Clock to clock time transfer uncertainty

The present chapter highlighted measurement precision and uncertainties due to systematic measurement errors that one encounters in a time transfer with the T2L2 scheme from a clock A to a clock B.

We may finally proceed to the calculation of the whole resulting uncertainty budget: The combined uncertainty u_C is calculated with the quadratic sum of the type A and the type B contributors [45]. The type A contributors are the standard deviations from the mean, that is the r.m.s. of the single measurement (precision), divided by the square root of the number of measurements [67, p. 728].
Table 5.8 summarizes all contributors[16] for a time transfer from ground clock A to space clock S (T2L2). The uncertainty of a ground to space time transfer with the SLR-based

Table 5.8.: Uncertainty budget for ground to space time transfer

System	Contributor	Type	$u_{C,AS}$ [ps]	Reference
T2L2	Timer	A	≈ 0	Eq. (5.2) on p. 116
		B	≈ 0	"
	Photodetection	A	1	Table 5.3 on p. 125
		B	2.7	"
Mission	DORIS (CV)	A/B	≈ 0	Eq. (5.14) on p. 126
	Geometry	A	≈ 0	Eq. (5.20) on p. 129
		B	3	Eq. (5.21) on p. 129
Other	General Relativity	A/B	≈ 0	Eq. 5.24 on p. 133
	Atmosphere	A	0.6	Eq. (5.23) on p. 132
		B	≈ 0	"
Laser station	Start detection	A	0.1	Eq. 5.26 on p. 134
	Return (MéO)	A	0.9	Eq. (5.30) on p. 137
	Return (FTLRS)		1.7	Eq. (5.38) on p. 139
	Return (WLRS)		3.7	Eq. (5.33) on p. 138
	Ground timer (2×)	A	0.2	Eq. (5.40) on p. 139
	Calibration (MéO)	B	15	Table 5.6 on p. 140
	Calibration (FTLRS)		20	"
	Calibration (WLRS)		15	"
	T/F vs. SLR cal.	B	25	Table 5.7 on p. 141
	Sum		≈ 31	

T2L2 scheme is thus found to be on the order of 30 ps for all types of laser stations and common view configuration.

For the determination of a ground (station clock A) to ground (station clock B) time transfer we calculate the quadratic sum of the combined uncertainties $u_{C,AS}$, $u_{C,BS}$ and the time prediction error δt_{pred} when performing non-common view time transfer.
Table 5.9 finally gives this uncertainty for common-view and non-common-view configurations. One finds that the uncertainty in the T2L2 common view time transfer is expected

[16] Please note that for the T2L2 instrument, the values for single photon operation (according to Table 5.3) were chosen.

Table 5.9.: Uncertainty budget for ground to ground time transfer

Time transfer	δt_{pred} [ps]	$u_{C,AB}$ [ps]
Common view	–	44
Greenbelt - Grasse	600	602
Greenbelt - Grasse (with Herstmonceux)	350	353
Grasse - Changchun	1100	1101
Grasse - Changchun (with Mendeleevo)	210	215
Grasse - Changchun (with Mendelevo & Maidanak)	-	46

to be about 44 ps for all types of laser stations.

For long-baseline time transfers, i.e. in non-common view configurations, the uncertainty approaches the nanosecond level when working solely with the two principal stations. In order to fully exploit the potential of the T2L2 scheme, intermediate stations as cited above should be employed in order to follow the evolution of the DORIS oscillator. Further, the establishment of a synthetic oscillator by the monitoring through the worldwide network of SLR stations (and DORIS in addition) should allow to significantly reduce the error on the time prediction during the dead times.

5.5. Conclusion

The whole time transfer chain with T2L2 from ground clock A to ground clock B was studied. The study included experimental data derived from the T2L2 flight instrument, the DORIS space clock and laser ranging stations.

It could be shown that the time transfer scheme with T2L2 will be able to compare today's most stable clocks including atomic fountains. The time transfer exhibits a time stability of some ps for 1,000 seconds of integration time, depending on the employed laser station and the photon level on the T2L2J2 detector. This is the specified value.
Since the passes over the laser stations usually last less than 1,000 seconds, the measurements are governed by white noise; this may be averaged in order to achieve a precision of the whole time transfer χ_{AB} of some picoseconds.
Subsequent time transfer sets during consecutive satellite passes may possibly be further averaged in order to achieve sub-picosecond performance.
The time transfer scheme is still open to some amelioration by improving the performance of the laser station's detection system (i.e. working in multi-photon mode with time walk correction).

The performance of non-common view time transfer is deteriorated by the drift of the DORIS oscillator. This may be mitigated by employing intermediate laser stations monitoring the oscillator; examples were given where the effective dead time may be reduced from some hundred to hundred seconds or even zero. In the last case, the time transfer between Grasse and Changchun in China, it is possible to continuously follow (for one pass per day) the whole satellite track by employing the Russian laser ranging stations in Moscow (Mendeleevo) and Uzbekistan (Maidanak). This transposes the common-view performance to this intrinsic non-common view configuration and will represent a new milestone in optical time transfer.

Further, a complete uncertainty budget of all employed instrumentation was developed. The overall uncertainty was found to be governed by the two calibrations that have to be performed in the laser ranging station: The internal, "standard" SLR equipment calibration and the calibration between the time/frequency and the SLR system's temporal and spatial reference points. The overall uncertainty is thus assessed to be well below 50 ps.
This performance will allow to perform calibrations of existing microwave time transfer systems such as TWSTFT and GPS [68]. The calibrations of Two-Way systems employ a transportable Two-Way station that travels between a set of time institutes throughout Europe. The best performance measured so far is in the 1 nanosecond range [25]. T2L2 on Jason 2 will permit to reduce this number further, by more than one order of magnitude and further allows to track down hidden systematics that are common to all TWSTFT systems and not resolvable by conventional methods.

This chapter showed the concatenation of all calibration and performance data obtained from the T2L2J2 flight instrument test campaigns described in Chapter 3, together with typical performance of the T2L2 ground segment, the laser stations. This permitted to assess the overall performance of a time transfer with T2L2 on Jason 2. The error budget was presented as a poster during the 2008 EFTF (European Frequency and Time Forum) at Toulouse.

After its launch in June 2008, the instrument will undergo an in-orbit evaluation before being able to be scientifically exploited. A first part of this evaluation is represented by a

collocation campaign of the FTLRS and MéO, in a common clock experiment. This will notably allow to cancel out all geometric effects, along with the clock noise. The second step will be a common campaign with the Observatoire de Paris, scheduled for April/May 2009: This campaign implies the installation of the FTLRS on the roof of the observatory and of OP's mobile fountain (FOM) at Calern. By this means, a comparison of the ultra-stable frequency standards of OP (like FO1 or FO2 atomic fountains) with the FOM via T2L2 will be performed (or an assessment of T2L2 by these clocks, depending on what direction one is looking).

The results of the present chapter, representing a theoretical baseline of the T2L2J2 time transfer performance, may be compared to the performance found in the various envisaged real-world experiments that will be performed over the two to three year mission time.

6. T2L2: Conclusion and future

6.1. Conclusion of the described activities for T2L2 on Jason 2

The described activities around the metrological test bed for the T2L2J2 flight model allowed to fully characterize it in terms of calibration data and performance assessment.

The primary objective of the hitherto presented study was to meticulously study the technical characteristics of the T2L2 instrument embarked on the Jason 2 satellite. The scientific parts of the T2L2J2 instrument had been build by the industrial partners EREMS and SESO upon detailed technical specifications developed by the OCA team. As well during, for the validation of the engineering model, as after the integration of the final flight model, two very important aspects had to be studied:

First, different technical parameters of the instrument had to be calibrated. This concerned on the one hand the effect of instrumental settings (like polarization voltages of the detectors or detection thresholds) on the outcome of the different performed measurements (date, laser pulse amplitude etc.). On the other hand it concerned the impact of external parameters like the actual geometry of the experiment (instrument orientation with respect to laser station) or the level of Earth-diffused sunlight on the measurement. These investigations are of vital interest in order to (a) operate the instrument in a secure, stable and efficient way, and (b) in order to correct the raw data that is retrieved from the satellite for the scientific exploitation.

Second, the accordance to the metrological specifications of the instrument, in other words its performance, had to be demonstrated. The T2L2 instrument on Jason 2 being the first of its kind in terms of complexity and metrology capability, the monitoring of its performance had to be undertaken during its whole development process, from definition to acceptance test.

A prefabricated laboratory device fulfilling the demands of the characterization of the T2L2J2 flight model evidently does not exist. A major part of the present thesis is thus represented by the conception, integration and operation of such a test device. This versatile and complex test bed, fruit of a successful teamwork of the RDM group of OCA, comprehended all operational aspects of the T2L2 scheme as it is established in orbit. The T2L2 test bed (Chapter 3.1) permitted to fully characterize the T2L2J2 instrument in terms of calibration and performance assessment.

A first, very comprehensive test campaign performed in the CNES clean room facilities at Toulouse allowed to collect large amounts of data for all kinds of measurement configurations. A second campaign allowed to verify the performances of the T2L2J2 instrument in the environment of the Jason 2 satellite; this measurement campaign was performed in the satellite assembly hall of THALES Alenia Space in Cannes, during the integration of Jason 2.

After completion of these two test campaigns the acquired data has been analyzed in detail in order to build a basis for the raw data correction that is implemented in the Centre de Mission Scientifique (CMS) of T2L2. The performance analysis of the different T2L2 subsystems demonstrated the event timer having an intrinsic precision of less than 2 ps, permitting a minimum time stability of 60 fs for an integration time of 1,500 s. The optical

timing scheme permits a 30 ps precision in single-photon mode with a time stability on the picosecond level (or even below) after an integration time of a typical satellite pass over a ground station. Both calibration and performance analysis, carried out by Etienne Samain and the author, are documented in two substantial reports [40, 41]; in order to keep the current document on a digestible level, they have been described in some reduced and more reader-accessible form in Chapters 3.3 and 3.2.

The obtained metrology performance data further allowed me to establish an updated error budget (Chapter 5). This improved overall error, or if one prefers performance budget, covers the whole T2L2 time transfer scheme and is mainly based on the experimental data on the T2L2J2 flight model and representative laser stations as well as on some theoretical data that had to be modeled in the absence of empiric studies (as for the LRA retroreflector). The time stability of a clock to clock time transfer in common view mode allows to compare today's most stable clocks including atomic fountains. The time transfer exhibits a time stability of some picoseconds for 1,000 seconds of integration time. The absolute uncertainty of a time transfer with T2L2 was found to be below 50 ps; it is mainly governed by the calibration between the time/frequency and the SLR system's temporal and spatial reference points. This calibration procedure is currently subject of development.
This comprehensive error budget thus represents a benchmark to which the measurements in life-size may be compared.

To summarize, the present study permitted to accompany the T2L2 instrument for Jason 2 from its detailed conception to its first exploitation in orbit, which started in July 2008. It laid a basis for the successful exploitation of the time transfer experiment and a caliper for its assessment in terms of time/frequency metrology.

6.2. Actual status

The Jason 2 satellite was successfully launched on June 20, 2008 from Vandenberg Air Force Base in California. After first health tests on satellite level, the T2L2 instrument

Figure 6.1.: Launch of the Jason 2 satellite aboard a Delta II launcher at Vandenberg Air Force Base in the early morning of June 20, 2008 (9:46 h UTC). Photograph © NASA, USA.

was switched on for the first time on June 25. The first recovered telemetry data showed satisfying data, corresponding to expectations. The first measured "scientific" data, the cw background level (sun noise) was also identified to be as expected.

The timing mode was first activated on June 30. The first identified laser pulse time tags corresponded to the ones emitted from the FTLRS (performed on July 1). The measured energy showed a very satisfying link budget. A deeper analysis is underway.
First data triplets $\{t_s, t_b, t_r\}$ have been identified on a pass of July 2, 2008 with six laser stations.

The data analysis encounters some challenges since, in fact, only very few laser stations deliver their data in the so-called Full Rate format[1], contrary to the resolution at the occasion of the ILRS meeting held at the EGS General Assembly 2002 in Nice.

At the time of the compilation of this document, the implementation of the Scientific Mission Center, responsible for the delivery of scientifically usable data (i.e. pre-treated for time transfer) is in full progress at OCA.

[1]The Full Rate format ensures, besides many others, the delivery of both the start as well as the return epoch in picoseconds.

6.3. Outlook: Future of T2L2

The T2L2 experiment aboard Jason 2 permits among others the validation of the time transfer by laser link scheme. In this sense, T2L2J2 may be regarded as a precursor mission to further evolved time transfer systems. There are three major groups in which the instrumentation may develop to address most different scientific topics.

The first one evidently is the pure time transfer, performed between ground and space clocks or between different ground clocks. Applications could be future positioning systems such as Galileo (what had already been proposed, but could get on the table anew), or fundamental physics missions based on highly precise optical atomic clocks like EGE (Einstein Gravity Explorer [11]) or SAGAS ([10]).

A second group is constituted by the concept one-way laser ranging as proposed in TIPO [24] and ODYSSEY [69]. One-way laser ranging will easily be simulated by the T2L2 operation what is a step forward towards the realization of such a system on an interplanetary mission.

The third evolution of the T2L2 instrument is represented by laser transponders that replace the passive reflection device by an active laser terminal [70].

The T2L2 scheme itself would profit from numerous possible improvements on instrument level that could not be realized in the Jason 2 version. The first to mention are the different subsystems that came along with the Jason 2 mission: The time transfer would profit from a more stable clock if performing non-common view time transfer. The second topic is the retroreflector: A single corner cube would not disperse the impinging laser pulses into a longer "pulp" what would allow higher precision on the return pulse. It would further allow the collocation of detection and reflection reference points (as studied in the T2L2 implementation on a CNES Myriade micro-satellite) thereby reducing geometry errors. A further evolution would also include an advanced noise rejection system, featuring more narrow spectral filters and in particular some sort of spatial filtering by employing a selective field-of-view (e.g. by employing a liquid crystal mask becoming transparent for a specific region on the FOV). By this means the signal-to-noise ratio could be raised what finally allows for a better precision on the measurement. Finally, a next version of T2L2 could profit from higher bandwidth detectors and electronics allowing more precise detection and timing. In this aspect, future versions of T2L2 could profit from the developments of ILIADE, that will be discussed in the second part of the thesis, as it currently profits from the developments of T2L2.

An amelioration of the T2L2 scheme does not uniquely rely on an amelioration of the space instrument, though, but also of the ground segment. A higher laser repetition rate, while roughly maintaining the laser pulse energy (in order to guarantee similar detection precision), would allow to gain a higher number of measurements whereof the averaging over an orbit pass would profit. A two-color approach, even though connected to high implementation difficulties, would further reduce the white noise connected to the residual uncertainty in atmospheric correction. Further, shorter pulse lengths would allow a more precise detection for all three timings, in particular those with low energies (return pulse). Below a pulse length of about 20 ps atmospheric dispersion will start to temporally stretch the laser pulses; for shorter pulse lengths, this would have to be counteracted by a pre-compensation, i.e. by impressing a negative chirp on the laser pulse before it leaves the telescope in order to arrive chirp-free (transform-limited) at the space detector.

This refers to considerations that have to be undertaken for next-generation satellite laser

ranging. Future schemes could rely on frequency combs (that will be discussed shortly after, Section 7.2.3.1), featuring high repetition rate, rather short pulse widths (not necessarily femtosecond scale) and an active atmospheric dispersion compensation; the latter would allow at the same time to probe all atmospheric parameters. On the detection side of such a frequency comb (compare to Fig. 7.7), one could profit by employing interference filters (such as Fabry-Perot) that completely match to the comb structure (adapting the free-spectral range to the repetition rate). By this means one would more efficiently filter background noise from a rather broad spectrum as compared with a single line filter.

In summary, there are many ways in that the T2L2 scheme or its derivatives may evolve in the future in order to provide ever more precise time transfer or distance measurement. In this sense, many of the future instrumental activities based on laser ranging go in the same direction. This is in particular true regarding the activity that is undertaken at OCA in order to unify interferometry and laser ranging by time-of-flight measurement; this topic is addressed in the next part of this document.

Part II.

ILIADE – Towards distance measurement on wavelength scale

7. Measuring distances in space

7.1. Scientific applications dealing with distance measurement in space

Measuring distances in space is of vital interest for the exploration of our solar system and the universe. The first and foremost application that comes into mind is the navigation of spacecraft itself: In order to allow a spacecraft to perform its maneuvers at the right time and the right place, its position or distance from a point on Earth has to be known in an accurate manner. But there are various other applications that rely on the knowledge of the separation of a spacecraft from Earth or another object.

Today, most of these applications are covered by radio frequency methods but the same trend as in time/frequency metrology is manifesting equally here: The need for ever higher accuracy and precision pushes the system designers to augment the used frequency range. Also here, lasers and optical methods become the tools of choice.

The following sections will shortly highlight some of the envisaged space applications that require a very high level of distance measurement and thus need a priori optical methods. The shown selection is not intended to represent a comprehensive list but rather to illustrate the different fields of applications. These may be classified into two categories, (1) where the distance measurement is needed for the metrology of the overall system, and (2) where the distance itself is the quantity being investigated.

7.1.1. Distance measurement for metrology

Two-satellite space telescopes After the remarkable success of space telescopes such as Hubble or XMM/Newton, new generations are envisaged with increased size and thus resolution and collected signal strength. These systems are becoming too bulky or to heavy to fit in a single launcher, or have to build large structures in space. Therefore, this new generation of space telescopes will be constituted by several spacecraft that represent different subsystems of a bigger instrument.

An example is the XEUS mission of the ESA Cosmic Vision Programme, an X-ray telescope, composed of a collector spacecraft carrying the collection optics and a second spacecraft carrying the detector [71]; the latter has to be maintained at a distance of 50 m from the first; this distance is defined by the focal length of the telescope. The requirements on the distance measurement are 60 µm in the longitudinal direction and 300 µm in the transversal axes.

Other examples for a separation into two spacecraft are the Gamma-Ray Imager (GRI, [72]), proposed as a successor of ESA's INTEGRAL mission, the joint ASI (Italian Space Agency) and CNES developed hard X-ray telescope Simbol-X [73] and an ESA sun coronagraph mission.

Table 7.1.: Requirements of satellite to satellite distance measurement of some proposed missions

Mission	Relative accuracy [µm]	S/C separation [m]
XEUS	Longitudinal axis: 60	100 – 150
	Transversal axes: 290	
Simbol-X	Longitudinal axis: 1,000	30
	Transversal axes: 150	
DARWIN	All axes: 32	7 – 170
LDI	0.0023 between 1 and 100 mHz	10,000
LISA	40 pm/$\sqrt{\text{Hz}}$	$5 \cdot 10^9$

Synthetic aperture space telescopes A very similar domain is represented by planned space telescopes in which the light collecting mirror is segmented and distributed on several satellites, sending the collected light towards another satellite where the optical beams are combined and form an interference pattern. The set of small telescopes distributed across a given area allows for achieving the same resolution of a virtual monolithic telescope with an aperture containing the apertures of the sub-telescopes. In order to be able to form the interference pattern, the light coming from the sub-apertures has to travel exactly the same path length. The maximum difference between the optical paths of all the light beams shall be smaller than the coherence length of the light, which is typically very short (incoherent stellar light).

The optical path length has to be measured by a high-performance metrology system and controlled within the specified margin by electric propulsion thrusters. The final path difference is then directly derived and controlled within a small fraction of the observation wavelength from the interference fringes thus relaxing the demands on the distance metrology system.

An example of these missions is the ESA mission DARWIN [74], a large multi-aperture optical interferometer. Working with the so-called "Nulling"-interferometry, it shall detect in particular telluric planets around their nearby stars. The requirements of DARWIN, imposed by the coherence length of the planetary and stellar light, is an absolute distance measurement with an accuracy of some tens of microns in all axes.

A mission similar to DARWIN but on a smaller scale, the project PEGASE has been co-proposed to CNES [75]. Another such nulling interferometry is prepared by NASA, called TPF (Terrestrial planet finder) [76].

Earth gravity field mapping Another domain is the mapping of the Earth's gravity field by monitoring the distance between two similar spacecraft flying closely behind another. The Earth gravity field harmonics exercise slightly different forces on the satellites' centers of mass and thus change the inter-satellite distance. A currently operational example of this type of mission is GRACE of NASA and DLR [77], in which the inter-satellite distance is measured by a radio frequency (K-band) ranging system.

Future versions of this experiment envisage optical techniques, like in the Japanese SSI (Satellite to Satellite Interferometry, [78]) or the ESA-studied LDI (Laser Doppler Interferometry, [79]) projects. Typical requirements are some nanometers precision in a frequency range of some mHz.

Earth and planetary navigation and geodesy Today, the task of spacecraft navigation is mainly performed by radio frequency methods like GPS for satellites on a low Earth orbit (LEO) or using the ground tracking stations. However, the most precise orbit determination for use in geodesy may only be provided by satellite laser ranging (SLR).

For far objects, such as satellites probing the solar system, NASA and ESA use the Deep Space Network (DSN); it consists of a global network of huge radio antennas that emit pseudo-random signals modulated on the HF carrier. The distance information may then be retrieved by time-of-flight (TOF) measurement of the signal. Another method is the use of the Doppler method, by simply emitting a HF sine wave towards the satellite. The receiver locks onto this frequency and re-emits the signal, mostly on a slightly different frequency: On ground, the frequency difference is used to determine the distance by integration from a known to the actual position. This method lately revealed remarkable findings with the discovery of an "anomalous" (i.e. against expectations) acceleration of the two Pioneer spacecraft 10 and 11 that just left the solar system beyond Saturn's orbit [80, 81].

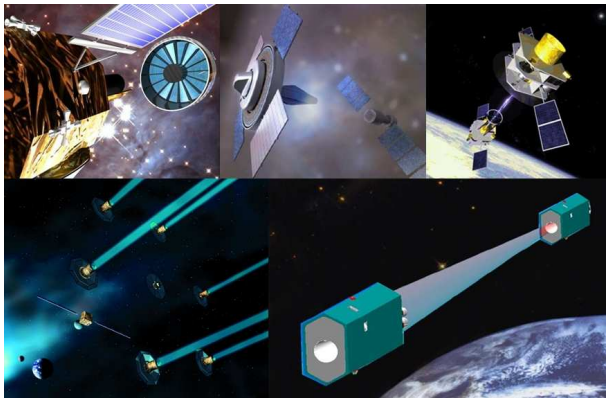

Figure 7.1.: Artist's impression of XEUS, GRI, Simbol-X, DARWIN and LDI.
Images © ESA and CNES, respectively

Further, both interplanetary navigation and geophysics would largely profit from optical distance metrology: Today, the internal mass distribution and the gravity field of planets [82, 83] may only be obtained from the distance of the orbiting spacecraft from Earth (such as Mars Global Surveyor or Mars Express). A finer monitoring of the satellite distance (ideally coupled with some altimeter) would greatly enhance our understanding of the internal structures of our neighboring planets and thus the formation of the solar system.

One recognizes that the described scientific domains as near-Earth and interplanetary navigation, next generation astronomy as well as geophysics would largely profit from the level of accuracy that is only offered by optical distance metrology since the spacecraft separation directly intervenes in the operation of the considered instrument.

7.1.2. Distance as central observable

The second class of space missions that require highly precise length measurements are fundamental physics missions that directly exploit distances as the central observable.

Gravitational wave detection Today's most famous example in this group of fundamental physics missions is probably LISA [84, 85] that aims for the detection of very slight deformations of spacetime due to the passage of a gravitational wave. This type of space deformation is extremely weak and in order to detect the corresponding distance variation with a sufficient sensitivity, the baseline has to be very long. For LISA, three identical satellites are separated by 5 million kilometers, and the demanded accuracy is still on the challenging level of 40 pm/$\sqrt{\text{Hz}}$.

Further tests of General Relativity The search for gravitational waves is just one example of the numerous ways to test General Relativity. The scientific community develops further space mission proposals such as the Chinese-led ASTROD [86] and its smaller precursor mission ASTROD 1 [87] that aim for various tests of General Relativity like gravitational wave detection and the determination of the PPN (Parametrized Post-Newtonian) parameters γ and β to a level of accuracy of 10^{-7}, amongst other goals. Another experiment addressing the determination of PPN parameters as well as the solar angular momentum and Lense-Thirring effect is LATOR (Laser Astrometric Test of Relativity), proposed by JPL [88]. Envisaged as multiple spacecraft missions, these experiments rely on very precise distance measurement over very long baselines.

In the context of General Relativity tests, OCA proposed the one-way laser ranging scheme (TIPO [24]) as mentioned in Sections 2.2.1 and 6. It relies on the technology of T2L2 by timing laser pulses from Earth laser stations on a very far space probe with a precise and stable clock; by this means, differential distance measurements with unprecedented precision become possible that may be used for various GR tests.

A further advantage of optical methods is that they allow in particular experiments with a line of sight very close to the sun (between Earth and the spacecraft for TIPO, e.g.) as compared to radio frequency based schemes (that suffer the enormous sun ionosphere). This permits experiments investigating the Shapiro-delay of light due to the attraction of large bodies (in this case the sun). The best test of this delay has been performed via the frequency shift on radio links between Earth and the Cassini spacecraft [89], to a level of 10^{-5}. The mentioned optical schemes would permit an enhancement of this measurement by at least two orders of magnitude.

Gravitational anomalies During the last two decades there have been detected some anomalies in the movement of very far spacecraft. The Pioneer Anomaly has been pointed out above. A second disagreement between prediction by actual gravitational theory (based on General Relativity) is the so-called Fly-by Anomaly [90] that revealed slightly different Δv values as expected.

Also a sort of test of General Relativity, various missions investigating these anomalies have been proposed in the framework of ESA's Cosmic Vision Programme as the already mentioned ODYSSEY [69] mission that would profit from one-way laser ranging.

The previous sections showed the inherent need of various space-based scientific instruments for highly precise distance measurement techniques. The requested levels of accuracy may often only be accounted for by employing optical techniques.

The next chapter presents an overview of optical schemes that allow for high levels of performance.

7.2. Technologies addressing the problem

In this chapter some central techniques of optical distance measurement are highlighted.

Generally one may distinguish between techniques that use the pure optical carrier wave, and other techniques using a signal modulated on this carrier.

7.2.1. Interferometry on the optical carrier

7.2.1.1. Classical single-wavelength interferometry

The most common way for distance determination is simple interferometry of an optical wave generated by a continuous monochromatic and coherent laser source. The setup may be of Michelson or Mach-Zehnder type as imaged in Fig. 7.2. The laser emits an optical

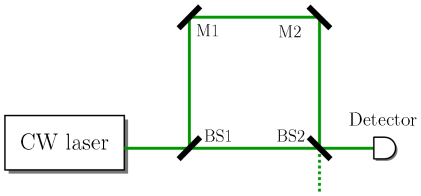

Figure 7.2.: Mach-Zehnder interferometer: The light is divided by the beam splitter BS1, retarded by Δt in the long branch, and recombined on the second beam splitter BS2.

wave that may be described by its electrical field:

$$E(t) = E_0 \exp(2\pi i \nu_0 t) \tag{7.1}$$

with E_0 the amplitude of the electrical field and ν_0 the frequency. The light passes through the beam splitter BS1 (semi transparent mirror, e.g.) and is recombined by the second semi-transparent mirror BS2. The two beams feature an electrical field on the detector of:

$$\begin{aligned} E_1(t) &= kE_0 \exp(2\pi i \nu_0 t) \\ E_2(t) &= kE_0 \exp(2\pi i \nu_0 (t - \Delta t)) \end{aligned} \tag{7.2}$$

with k being a transmittance constant. The power on the detector P is obtained by:

$$P = |E_1 + E_2|^2 = 2k^2 P_0 \cos(\phi_0) \tag{7.3}$$

with $P_0 = |E(t)|^2 = |E_0 \exp(2\pi i \nu_0 t)|^2$, but we may arrange the experiment such that: $P_0 = |E_0|^2$

One sees that the power on the detector depends on the phase angle ϕ_0, or the length L:

$$\phi_0 = 2\pi \cdot \nu_0 \cdot \Delta t = 2\pi \frac{L}{\lambda} \tag{7.4}$$

The length L is an ambiguous value with a range of half of the used wavelength. In order to resolve the phase angle unambiguously over the wavelength, the measurement is often performed in quadrature, i.e. by dephasing one of the paths by $\pi/2$; the phase may then be calculated out of the two power measurements.

Another very common technique is to slightly change the optical frequency in one of the arms of the interferometer by a known amount Δf. This frequency change may be obtained

with an acousto-optic modulator, for instance. The optical power on the detector is then modulated by the frequency Δf and the phase ϕ_0 is contained in the changing part of the signal:

$$P(t) = 2k^2|E_0|^2 \cos(2\pi\Delta f t + \phi_0) \tag{7.5}$$

This "heterodyne" detection has the advantage of being able to transform the amplitude or photometric power measurement in an electronic phase measurement which often allows better resolution and thus precision.

The major inconvenience with mono-frequency interferometry is the ambiguity of the phase measurement which is modulo 2π. In order to retrieve an absolute notion of a measured length, other techniques have to be employed additionally.
The next sections show different schemes that partially resolve the inherent ambiguity problem.

7.2.1.2. Multiple-wavelength interferometry

A common technique is to employ several different wavelengths. In its simplest form, two optical frequencies are used simultaneously, but without that they are interfering themselves (DWI, double-wavelength interferometry). The two different wavelengths λ_1 and λ_2 give two phase measurements:

$$\phi_1 = \frac{2\pi L}{\lambda_1} = \frac{2\pi\nu_1 L}{c} \text{ and } \phi_2 = \frac{2\pi L}{\lambda_2} = \frac{2\pi\nu_2 L}{c} \tag{7.6}$$

These two phases are sensitive to path variations ΔL on the order of the optical wavelengths, what puts high demands on the stability of the whole setup.

Dändliker [91] describes an effective means of directly measuring the phase difference $\Delta\phi = \phi_1 - \phi_2$ in a heterodyne setup (see Fig. 7.3) by mixing the two outputs with the two phases. The phase difference yields:

$$\Delta\phi = 2\pi\frac{L}{\Lambda} \tag{7.7}$$

with Λ being the synthetic wavelength:

$$\Lambda = \frac{\lambda_1\lambda_2}{|\lambda_1 - \lambda_2|} \tag{7.8}$$

This method has the advantage, apart from a reduced sensitivity to path length changes, that the ambiguity range is extended to the synthetic wavelength Λ.

There are various other methods how a two-wavelength interferometer may be implemented in detail. Further, the scheme may be extended to several wavelengths and thus multiple synthetic wavelengths (MWI) in order to cover important ambiguity ranges (see [92, 93, 94] for example). If one manages to resolve single wavelengths (at the smallest synthetic wavelength), one may additionally perform single-wavelength interferometry in order to perform absolute distance measurement with nanometer accuracy.

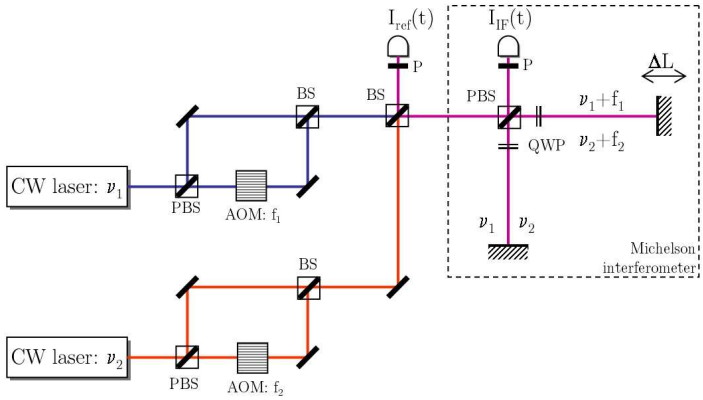

Figure 7.3.: Optical setup of Dändliker's [91] two-wavelength superheterodyne interferometer: From each laser, two slightly different frequencies ν_1, $\nu_1 + f_1$ and ν_2, $\nu_2 + f_2$ are generated in two orthogonal polarizations. The combination of the beams produce the reference signal $I_{ref}(t)$ and the measurement signal $I_{IF}(t)$ in the Michelson-type interferometer (PBS, polarizing beam splitter; BS, beam splitter; AOM, acousto-optic modulator; P, polarizer; QWP quarter-wave plate).

MSTAR The MSTAR sensor (Modulation Sideband Technology for Absolute Ranging) developed at the JPL [95] mainly in the framework of the Terrestrial Planet Finder (TPF, see above) is a combination of double-wavelength interferometry and carrier modulation techniques since it employs a carrier phase modulation. The two wavelengths that form the synthetic wavelength Λ are obtained from the spectral sidebands produced by the phase modulation of a single carrier (in the radio frequency range).
The smallest generated synthetic wavelength yields phase measurements with an accuracy of 0.13 µm, thus being able to resolve the wavelength and to perform single-wavelength interferometry. The experiment further aims to perform distance measurements on the 100 m scale.

Stabilization by a frequency comb Generally, the measurement accuracy suffers from instability and uncertainty of the used optical and thus synthetic wavelengths. A way to stabilize the optical frequencies is proposed and tested by Schuhler et al. [96] by employing a frequency comb (see Section 7.2.3.1) to stabilize two laser sources. By this means, a very small synthetic wavelength of $\Lambda \approx 90$ µm ($\Delta\nu \approx 3.3$ THz) could be produced, yielding a distance measurement accuracy of about 160 µm. In principle, the scheme allows absolute distance measurement by detuning one of the used laser sources, and a thus generated chain of highly accurate synthetic wavelengths. The authors could further demonstrate an accuracy of 8 nm over 800 mm [97], corresponding to a relative accuracy of 10^{-8}.

7.2.1.3. Frequency-sweeping interferometry

The use of various optical frequencies in DWI or MWI makes the interferometry system rather complex since the number of sources and optical elements increases. Another way is frequency sweeping interferometry (FSI). This technique consists in using a single tunable laser, whose frequency is swept over a known range [98, 99, 100]. Fractional fringes are measured at the beginning and the end of the sweep (giving the number F) and the integer

number N of fringes is counted during the sweep. The path length may then be determined by:

$$L = \frac{\Delta\phi}{2\pi}\Lambda = (F + N)\ \Lambda \tag{7.9}$$

Once again, the phase value $\Delta\phi$ may be determined over an ambiguity range of the synthetic wavelength Λ from Equation (7.8), with $\lambda_{1,2}$ being the frequency border of the sweep. With this method, distances may be discerned with accuracies of some microns: Cabral [101] and his team could demonstrate an accuracy of 10 µm over a distance of 1 m.

A major drawback is that this method is sensitive to movements of the ranged target, whose generated fringes may difficultly be distinguished from the sweeping-induced fringes. Yet, workaround methods exist as well, as demonstrated by Swinkels [102].

7.2.1.4. Dispersive or white-light interferometry

White-light interferometry (WLI) is a method using the interference of spectrally broadband (i.e. white) light which has a short coherence length (on the order of the wavelength). Interference is only possible when the path length difference of both interferometer arms is smaller than the coherence length of the source.

A WLI is thus usually used for the contact-free measurement of the topography of test pieces with high depth resolution. Contrary to other interferometers that use light of longer coherence length (lasers), surfaces with steps or rough surfaces may be measured with some nanometers of accuracy [103].

Joo and Kim [104] propose a means of absolute distance measurement with an evolution of WLI using a femto-second laser as an approximated white-light source. The method is based on the measurement of the optical path delay between consecutive femtosecond laser pulses. The authors demonstrated a non-ambiguity range (NAR) of 1.5 mm with a resolution of 7 nm over a maximum distance reaching 0.9 mm.

In the literature, there may still be found loads of different interferometer implementations, exotic ones, most based on MWI, and for the most different applications. I want to spare the reader a more in-depth study of the field and pass to the other important field of optical distance measurement, that is to say, by the modulation of the optical carrier.

7.2.2. Modulation of the optical carrier

7.2.2.1. Time-of-flight measurement

The most straightforward method for distance ranging is the time-of-flight measurement of optical pulses. As we well know, the precision of SLR and LLR today is in the range of some millimeters. For these applications, the performance is mainly limited by the low photon return level and atmospheric perturbation.

But better time-of-flight performance is absolutely imaginable: The performance of the T2L2 test bed (refer to Fig. 3.31) yields already a precision of less than 700 µm with a tenfold amelioration when integrating over some hundred seconds. It is on this aspect that focuses this part of the present work (Chapter 8.3).

7.2.2.2. Sinusoidal carrier amplitude modulation

Many distance measuring devices relying on a modulated optical carrier are based on a simple sine intensity modulated signal. The modulated light is emitted towards the target, reflected and collected by a fast photodetector. After bandpass filtering the signal, its phase is compared (giving Δt) to the reference signal (the modulation frequency f_{mod}). One determines the phase ϕ:

$$\phi = 2\pi f_{\text{mod}} \Delta t = 2\pi \frac{L}{\Lambda} \tag{7.10}$$

with again a synthetic wavelength determined by the modulation frequency:

$$\Lambda = \frac{c}{f_{\text{mod}}} \tag{7.11}$$

The are extremely diverse implementations, depending on the demands of the application, ranging from the hardware shop's laser rangefinder at 150 €, to the high fidelity micrometer-yielding frequency-comb based metrology device:

Commercial laser rangefinder for the construction sector The technological advances of the recent years in terms of semiconductor laser sources has made it possible to obtain laser rangefinders affordable for various applications (available in hardware shops). The scheme is based on the intensity modulation of a laser diode or an LED. Absolute distances are derived by sweeping through some synthetic wavelengths (from some MHz to GHz). Accuracies of

Figure 7.4.: Low budget commercial laser rangefinders.
Photographs © Bosch and Leica, Germany, respectively

some millimeters may be obtained by these devices.

High frequency intensity modulation In most of the modulation-based distance meters, the modulation frequency is chosen relatively high in order to allow for a more precise phase measurement. The modulation may be performed by directly modulating the source such as in the project of NRAO (National Radio Astronomy Observatory, Virginia) [105] where the bias current of a laser diode is varied at 1.5 GHz. The authors achieve a precision of less than 20 µm over distances of about 120 m.

Another possibility is to use a constant laser beam whose intensity is varied by a fast modulator as performed by Fujima et al. [106]. The 28 GHz modulated beam is reflected by the target and then down-modulated by a second optical waveguide intensity modulator in order to reduce the phase information to a conveniently measurable frequency range. The achieved measurement accuracy is between 1 and 3 µm for distances between 5 and 100 m.

A third possibility is to obtain a sinusoidal modulation by beating the laser wave with a slightly frequency-shifted part of itself.

Frequency comb based modulation In another approach, a femtosecond laser is used as the means of modulating the optical carrier. In an experiment of the Japanese NRLM, a frequency comb (Section 7.2.3.1) generates 80 fs pulses separated by a 20 ns repetition rate [107, 108]. In the frequency domain, the optical pulse train appears as a series of frequency teeth (thus comb). The frequency response of an optical detector to the laser pulses features again a frequency comb due to the possible combinations of intermode beats. These frequencies are perfectly referenced by the optical pulse train that in turn is locked to a stable reference clock. After passing on a retroreflector, the pulse train is detected by a fast photo detector. Then, phase measurements on very high harmonics of the repetition frequency are performed (at 10 GHz, the 209th harmonic, for instance) with a standard phase meter. The team around Minoshima thus attains a resolution of 1 µm and an accuracy of 5 µm over a distance of 240 m.

7.2.3. Combining carrier and modulation measurements

The ensemble of the previously cited schemes represents remarkable implementations of optical distance meters. Many of the presented systems yield performances on the micrometer level and some even below.

Yet, only few of them feature a a sufficient non-ambiguity range for space missions, most do well on the millimeter level but not any further. Even fewer schemes really bridge the gap between single-wavelength interferometry (thus sub-wavelength measurements) and larger scales: Only the JPL-developed MSTAR yields this possibility with convenient maximum ranges (what still has to be demonstrated experimentally).

It is clear that the connection between sub-wavelength scale and larger distances has to be achieved with a combination of the different methods. In the context of precise distance metrology, many of the previously presented systems already employ femtosecond lasers, or frequency combs. In the next sections I shall present how this unique tool of metrology is predestined to do the job of bridging the described gap.

In a first part, the basic properties of a frequency comb shall be described. Then follows the description of one possible implementation, proposed few years ago. The next chapter then deals with the project ILIADE at the Observatoire de la Côte d'Azur that aims at using such a frequency comb for ultra-high resolution absolute distance metrology on arbitrary scales.

7.2.3.1. Excursus: The frequency comb

The nowadays popular femtosecond laser or frequency comb is a special form of a mode locked laser, emitting very short pulses at a constant repetition rate. There may be found various implementations, from solid state to fiber lasers.

In order to illustrate the main features of a frequency comb, this section will concentrate on the one type that still represents *the* workhorse of modern optical frequency metrology (in particular spectroscopy), namely the Titan-Sapphire femtosecond laser. This laser was in fact the first of its species.

Mode locking was already brought up in Chapter 4: In order to generate short optical pulses, one needs to establish a fixed phase relationship among all of the lasing longitudinal modes inside a laser cavity. This mode locking consists in forcing a higher net gain for modes leading to the formation of a pulse train as compared to cw operation [109, p. 57]. This can be achieved with different techniques, using an acousto-optic modulator (active),

or passively by saturable absorption, for instance. Shortest pulse widths are achieved with passive methods. The Ti:Sapphire femtosecond laser uses a special, very effective means of passive mode locking, the Kerr effect. In the typical setup of this laser (depicted in Fig. 7.5), the Ti:S crystal serves both as laser gain material and passive mode locking by the formation of a Kerr lens. The Ti:S crystal is often pumped by a frequency doubled continuous Nd:YAG

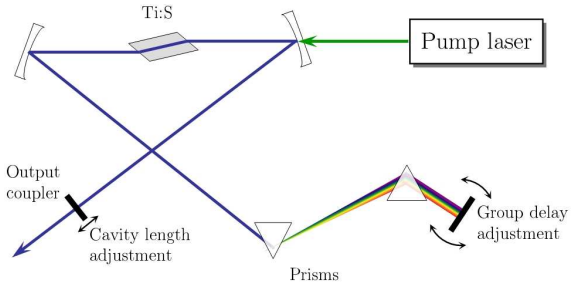

Figure 7.5.: Schematic of a typical Ti:Sapphire femtosecond laser (according to [110])

laser (such as the ubiquitous Verdi of Coherent). The Ti:S crystal has a very broad spectral bandwidth spanning from 670 to 1,070 nm with a maximum at 800 nm, thus allowing for short pulses. The Ti:S crystal further features a non-linear index of refraction which manifests as an increase of index of refraction as the optical intensity increases [110]. With a Gaussian beam profile in the cavity, equally a Gaussian index profile is generated in the crystal. This leads to a self-focusing of the beam, what further increases intensity and thus the focusing. Since short pulses have high peak power, they are favored in contrast to cw operation.

Fig. 7.5 further shows a pair of prisms: These are used to minimize group velocity dispersion in the Ti:S crystal that would temporally spread the pulses. Often, so-called "chirped" mirrors are used for the same job.

This principally simple setup represents the KLM (Kerr-lens mode locked) Ti:S femtosecond laser featuring ultra-short pulses. Due to dispersion in the cavity, the group velocity (of the pulse envelope) and the phase velocity are not equal. This leads to a shift of the carrier with respect to the pulse envelope from one pulse to another, as shown in Fig. 7.6. The

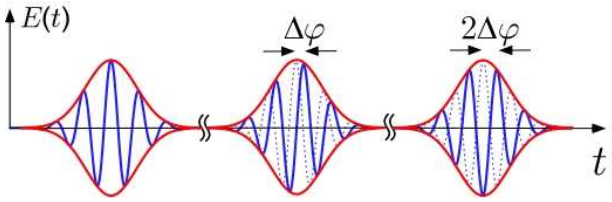

Figure 7.6.: Carrier-envelope delay of a free-running femtosecond laser

carrier-envelope delay $\Delta\varphi$ is given by [110]:

$$\Delta\varphi = \left(\frac{1}{v_g} - \frac{1}{v_p}\right) l_c \, \omega_c \, \mathrm{mod} 2\pi \tag{7.12}$$

with v_g and v_p being the group and phase velocity, respectively, l_c the cavity length and ω_c the carrier frequency.

In the spectral domain the laser features a comb of frequency lines separated by the repetition rate f_{rep}. These equally spaced comb lines are shifted from zero by a certain offset frequency, often denoted as f_{ceo} as it corresponds to the carrier-envelope offset of the pulses. Indeed, the frequency of an individual comb line reads:

$$f_n = n \cdot f_{\mathrm{rep}} + f_{\mathrm{ceo}} \text{ with } f_{\mathrm{ceo}} = \frac{\Delta\varphi \ f_{rep}}{2\pi} \tag{7.13}$$

where n is a large integer value. The frequency response is imaged in Fig. 7.7. In order to be

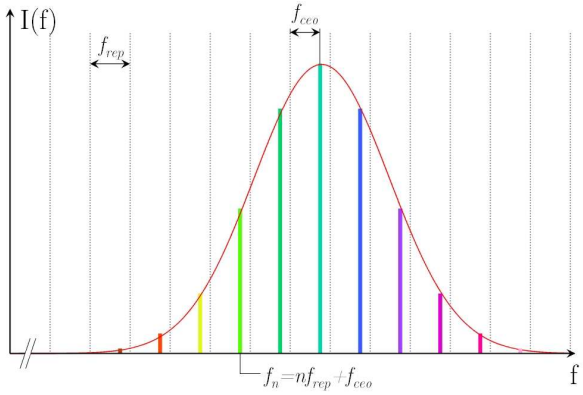

Figure 7.7.: Spectral properties of a frequency comb

able to use this type of laser for precision optical metrology it is necessary to precisely control both degrees of freedom (f_{rep} and f_{ceo}) of the comb. The repetition rate of the laser may easily be controlled by changing the length of the cavity[1], e.g. putting one of the mirrors on a piezoelectric transducer.

The determination of the offset frequency f_{ceo} is often performed by heterodyning different laser harmonics [111, p. 117]. This method consists in beating the n^{th} harmonic of a comb line with the m^{th} harmonic of another comb line. In its most obvious version, this is done with $n = 1$ and $m = 2$. This "$f - 2f$" technique relies on the external frequency doubling of a lower frequency f_1 which is defined by:

$$f_1 = n \cdot f_{\mathrm{rep}} + f_{\mathrm{ceo}} \tag{7.14}$$

The frequency doubled optical wave $2f_1 = 2n \cdot f_{\mathrm{rep}} + 2f_{\mathrm{ceo}}$ is then multiplied with a higher frequency of the spectrum f_2:

$$f_2 = 2n \cdot f_{\mathrm{rep}} + f_{\mathrm{ceo}} \tag{7.15}$$

The beat note of $2 \cdot f_1 \times f_2$ is now directly f_{ceo}. Usually it is set to zero by changing the swivel angle of the cavity end mirror behind the prisms [110]. However, in order to be able to perform this $f - 2f$-control the comb has to span at least one octave. This is typically achieved by further broadening of the comb spectrum. Spectral broadening is mostly achieved by employing highly non-linear microstructured optical fibers (PCF, photonic crystal fiber) that generate new frequencies by self-phase modulation (SPM). By this means it is able to obtain an octave-spanning spectral distribution, often called a "supercontinuum" (Fig. 7.8).

[1] In fact, changing the cavity length has also an effect on the group-phase delay, but this will not be discussed here in detail.

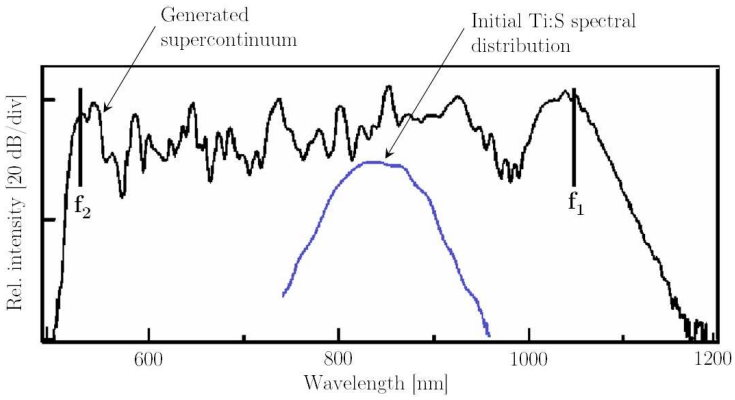

Figure 7.8.: Supercontinuum generated by an air-silica microstructured fiber

After spectrum broadening and control of the offset frequency f_{ceo} and the repetition rate f_{rep}, we have now the versatile tool known as a frequency comb. It notably permits to relate the optical frequencies unambiguously and with high precision to a microwave standard such as a Cesium clock. The other way round is also possible: As pointed out in the beginning of this work (Section 1.1), an optical clock uses a frequency comb to downconvert an optical atomic transition frequency into the radio frequency world. In this version, the comb spacing is controlled with a lock of one comb tooth on an optical clock frequency.

The frequency comb thus permits to transport the exactitude of a clock reference from the radio domain into the optical domain and vice versa. It is for this reason that the frequency comb is also becoming a tool of choice for optical distance measurement.

An excellent introduction into the field of frequency combs is given in [110, 112, 113].

7.2.3.2. The scheme proposed by Ye

A scheme on everybody's mind today when talking about absolute distance measurement with frequency combs is the proposal of Jun Ye of the JILA institute of University of Colorado, Boulder and NIST from 2004 [114]. It consists in unifying time-of-flight measurement of the femtosecond laser pulses and pulse interferometry in a single approach. The scheme is depicted in Fig. 7.9. Either the repetition frequency f_{rep} of the femtosecond laser is locked onto a stable frequency reference (like a clock) or one of the comb teeth is locked on some optical transition (optical clock mode). Further, the slippage of the carrier-envelope phase is inhibited by some control method like the $f-2f$ method. This enables stable interferometric operation on the carrier contained in the laser pulses.

The laser emits its pulse train into a Michelson-type interferometer, as shown in Fig. 7.9. For some arbitrary distance in the measurement arm, there appear pulse pairs (from the two arms) in the recombining path, with an arbitrary distance of Δt_1. A fast photodetection device is able to resolve this time span. In order to resolve the absolute distance L in the measurement arm, the repetition frequency is changed in order to approach the two pulses

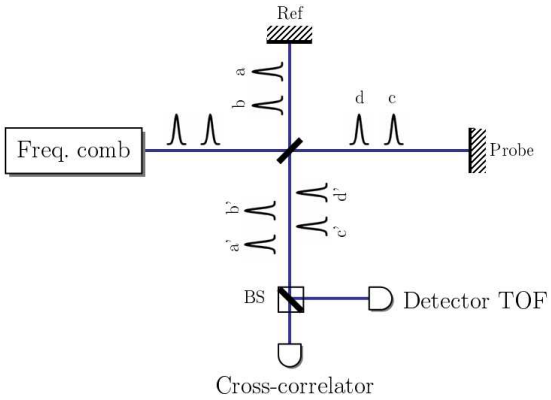

Figure 7.9.: The scheme proposed by J. Ye for measuring absolute distances with a frequency comb

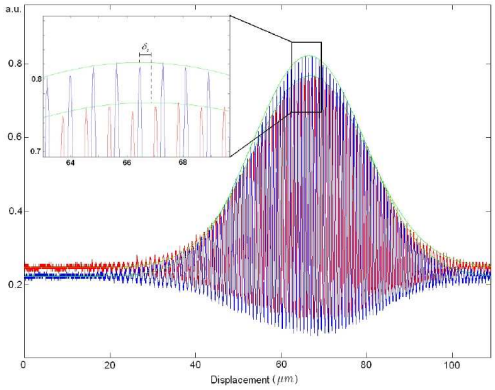

Figure 7.10.: Comparison of two cross-correlation patterns obtained by Cui et al. (from [115])

in a pair until they finally overlap. L may then be derived by solving following equations:

$$\begin{aligned} \frac{2L}{c} &= \frac{n}{f_{\text{rep1}}} - \Delta t_1 \\ &= \frac{n}{f_{\text{rep2}}} - \Delta t_2 \end{aligned} \tag{7.16}$$

with n being an integer, $f_{\text{rep1,2}}$ the respective repetition rates before and after the change, and $\Delta t_{1,2}$ the respective distance between the pulses before and after the change.

In a second step, the repetition rate is further adjusted in order to fully overlap the two pulses on a fringe-resolving cross-correlator what leads to a final resolution below wavelength scale. This correlator usually exists of some non-linear material, for instance BBO (Barium Borate), where a second harmonic is generated. The initial wavelength is then blocked and the harmonic fed onto a photodetector. The typical cross-correlation traces (see Fig. 7.10 for an example) are generated by scanning the pulses over short distances (what is achieved here by scanning f_{rep}).

Very recently, this experiment has been performed for a first time by a Dutch group of the Technical University of Delft [115]. The group actually had no means to change the laser's

repetition rate, but varied the length of the reference arm. Over a range of about 15 cm they could prove an accuracy better than an optical fringe by comparison with a reference interferometer.

The implementation of not more than a single experiment based on Ye's proposal up to now reveals its inherent difficulties: Though variable repetition rate frequency combs today are commercially available, a stable operation during a frequency sweep is somewhat more difficult to achieve (due to repetition frequency instability or phase-envelope noise). Further, this method suffers from a certain complexity because of employing non-linear optics. Another drawback is the limited resolution of pulse interferometry, albeit reaching sub-wavelength scale.

An alternative to the proposal of Ye is the approach of the ILIADE team of OCA that is presented in the next chapter.

8. The project ILIADE at OCA

The common project "ILIADE" between two research groups at OCA was initiated out of the realization that a combination of their respective competences in terms of length measurement would create new synergies. The group of the ARTEMIS UMR possesses tens of years of experience in the design of extremely high-performance interferometers for use in gravitational wave detectors, notably VIRGO and LISA. On the other hand, the Géosciences Azur group[1] has been performing satellite and lunar laser ranging on the highest level for more than 30 years.

It seemed evident to unify these complementary skills for the development of new distance measurement technologies for the use in future space missions as pointed out in Section 7.1.

The emergence of the frequency comb as a central tool in optical frequency metrology rapidly convinced the ILIADE team to use it as a keystone for the connection of carrier and carrier envelope (i.e. modulation) techniques.

The following chapters show the baseline of the envisaged experiment and some of the first feasibility experiments carried out for the modulation part of the experiment.

8.1. Combining interferometry and chronometry

The ILIADE project aims at demonstrating the feasibility of a distance measurement method based on a frequency comb. This method should have the aptitude to measure arbitrary, absolute distances over long scales with a resolution largely better than the micron.

For this reason, single-wavelength interferometry should be implemented for nanometer accuracy together with time-of-flight (TOF) measurement for long distances. An implementation as proposed by J. Ye [114] was rejected for the complexity, the limited resolution of pulse interferometry and in particular for the implementation difficulties related to the needed continuous variation of the repetition frequency of the laser.

After some iterations and many discussions between Nice and Calern, to which the author could contribute, a baseline concept of the experiment was worked out; this baseline concept is presented in the following section.

8.1.1. The ILIADE baseline experiment

The general architecture of the ILIADE experiment consists of a Michelson interferometer in which a frequency comb emits its pulses (Fig. 8.1). The frequency comb is carrier-envelope phase controlled by some harmonics method (like the $f-2f$ scheme) and its repetition rate is phase-locked to an external frequency reference such as a Cesium clock.

The general idea in the ILIADE concept is to use both the pulsed aspect (for TOF) and the continuous aspect (distinct frequency lines representing continuous laser waves) of the comb laser:

[1] Former GEMINI UMR of OCA.

The pulses returning from the reference arm and from the measurement arm are both spectrally filtered in order to recover only a single comb line. By this means, the pulses are transformed into a continuous wave on which single-wavelength interferometry may be performed. This is preferably performed on two adjacent comb lines in order to perform a heterodyne detection, with the repetition rate issued from the Cesium clock as a reference. The spectral

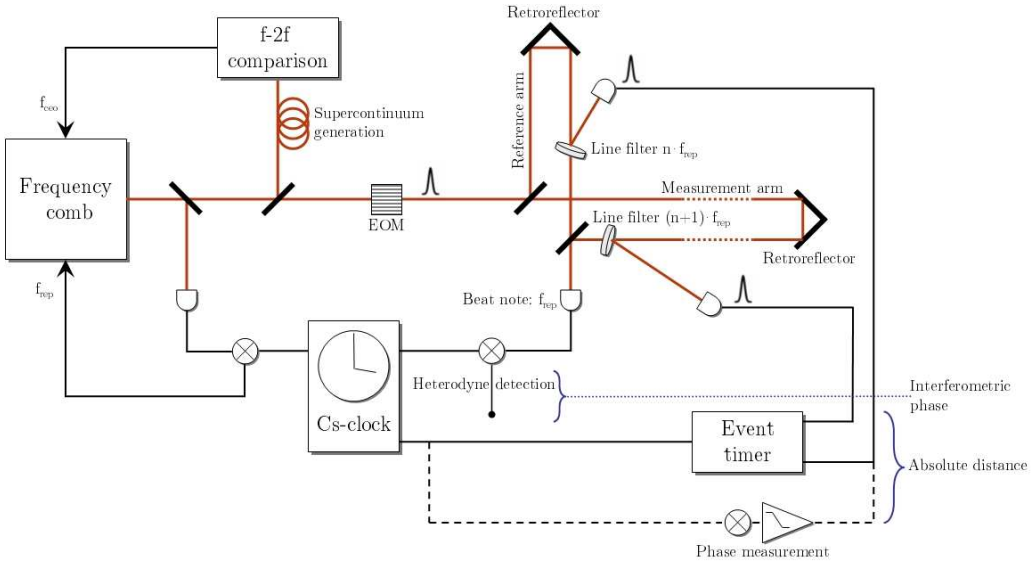

Figure 8.1.: Experimental setup of the ILIADE scheme

filter (a Fabry-Perot for instance) thus rejects all but one line of the comb spectrum; one may assume that the pulse form may not be altered drastically by this manipulation.

The absolute distance may then be determined by time-of-flight measurement between the pulses from the reference and the measurement arm. In order to resolve the ambiguity between the pulses, these may be modulated (on-off, EOM in Fig. 8.1) by applying, for instance, a pseudo-random code of a suitable length. Once the absolute distance has been determined, the modulator may be left in transmission mode in order to perform interferometry. The goal for the TOF measurement is to resolve distances below the wavelength scale in order to directly pass to interferometry on the carrier.

Additionally, a phase measurement is envisioned as a backup to the TOF measurement. In the case that the timing scheme is not able to resolve sub-wavelengths, a direct phase measurement on the synthetic wavelength generated by the pulse train (at f_{rep}) shall be performed to bridge this gap, since it is more obvious to reach this resolution by phase measurement than with the somewhat more complex chronometry employing an event timer. In any case both methods are studied with the first experiments presented in the chapters hereafter (8.2 and 8.3).

It has to be noted that this scheme is a baseline experiment concept that may undergo modifications in the course of its development; it serves for exploring the technological possibilities to combine interferometry and time-of-flight measurement in a single approach and not for as an end in itself.

8.1.2. Design issues

In the present envisaged experiment concept there are three major parts that drive the detailed design of the setup: These are the laser and its control, the narrow linewidth filters and the measurement devices.

Laser type The type of the laser is both driven by the application and the experiment implementation. As the ILIADE scheme aims for space applications, a more lightweight fiber based system is preferred, even though it is not yet necessary for the feasibility demonstration of the experiment. One of the most important parameters is the repetition rate and the spectrum of the laser. The selection of one single comb line for the single-wavelength interferometry entails a very high repetition rate: In order to guarantee a sufficient power level for interferometry, the spectral distance of the comb lines has to be stretched at a maximum; for clarification, the Ti:S laser described in Section 7.2.3.1 would feature more than 150,000 comb lines at a repetition frequency of 1 GHz, leading to some µW of power per line for 1 W continuous power.

Equally, the natural comb spectrum envelope (compare to Fig. 7.7) should be chosen sufficiently narrow to reduce the total number N of contained comb teeth. This entailing broader pulses, it has to be found a trade-off between comb line power and pulse length for precise chronometry; however, the requirements of chronometry should not go below the picosecond scale. It rests rather the concern that a narrow comb may be sufficiently stretched to span an octave for the $f - 2f$ control.

As a frequency comb with the required specifications is not yet available on the market, a "workhorse" laser is under design at the Institut Carnot de Bourgogne (ICB of the University of Bourgogne) with which the ILIADE team cooperates in an ANR-financed study. This special laser is described in Chapter 8.1.3.

Line filters In order that the interferometric measurement works properly, it is necessary to filter single lines out of the spectrum. This guarantees a clear heterodyne signal (if filtering two adjacent modes). A high repetition rate further relaxes the requirement on the finesse $\mathcal{F}$ of a Fabry-Pérot interference filter, since its linewidth δf may approach bigger values, up to f_{rep}. It is further required that the whole rest of the spectrum is rejected by the filter, such that the free spectral range (FSR) covers half of the laser's spectrum. The finesse is given by:

$$\mathcal{F} = \frac{FSR}{\delta f} \tag{8.1}$$

Setting in Equation (8.1) δf to f_{rep} and $FSR = \frac{1}{2}\Delta f$, and with $\Delta f = N \cdot f_{\mathrm{rep}}$ one concludes that the finesse should be on the order of the number of modes:

$$\mathcal{F} > \frac{N}{2} \tag{8.2}$$

It is obvious that these specifications may difficultly be fulfilled by using a typical, commercially available some-hundred MHz laser with 100 fs pulses. Envisaging a system with $f_{\mathrm{rep}} = 10$ GHz, though, and pulse length FWHM=1 ps, the finesse has not to be higher than $\mathcal{F} = 22$.

Measurement devices The three measurement devices for the interferometric phase, the synthetic wavelength phase and the timing are the central core of the ILIADE study. These devices are under study to demonstrate their feasibility. In particular, the aspect of bridging the gap from the macroscopic world (synthetic wavelength ranges) to the microscopic world (optical carrier) is in the focus of the actual work.

Once the devices have demonstrated the required performances, the implementation of the whole scheme may be commenced. I will touch on the different ILIADE development phases in the Section 8.1.4.

8.1.3. The ICB source

The pulsed laser provided by the ICB team is in fact a pulse compressor based on the beat frequency of two cw lasers, whose lines are separated by a small frequency amount f_{rep}. The planned setup for ILIADE is depicted in Fig. 8.2. The upper left part shows the generation of

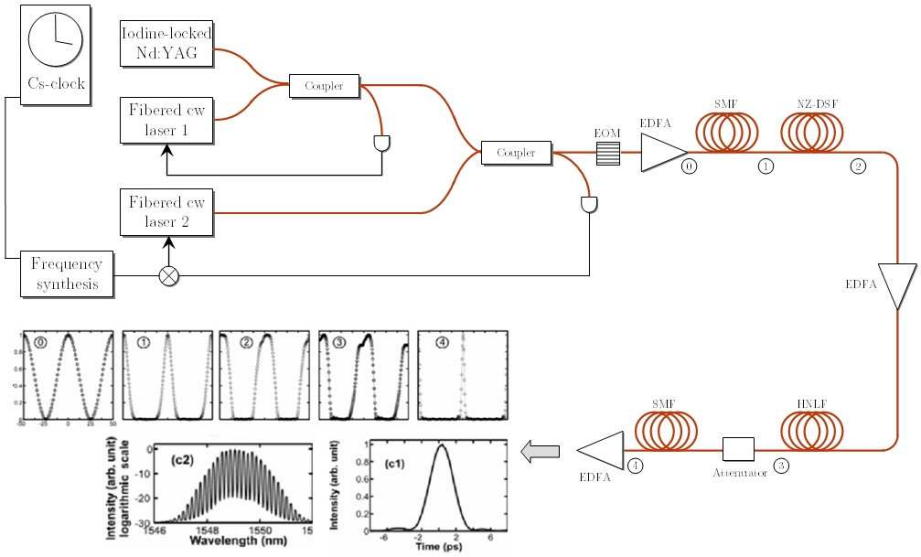

Figure 8.2.: The high frequency comb source provided by ICB. The graphic also indicates the pulse length and form after each compressor stage

two stabilized laser lines, whereas the right part depicts the actual compressor as described in [116].

The basic idea is to compress a sine wave (modulated on the optical carrier) into short pulses. For the generation of the sine, two fibered laser sources are used: One is locked to a stable Nd:YAG laser which is itself referenced to an iodine molecular transition. The other fiber laser is adjusted to be shifted by 20 GHz from the first laser's frequency. This frequency shift is controlled via a phase lock by comparing the beat note of the two lasers with the output of a highly stable RF frequency synthesis.

The pulse compressor works in the following way: The laser beam (featuring a sinusoidal modulation with 50 ps rep rate) first passes a fibered phase modulator (EOM, at 130 MHz) in order to inhibit Brillouin scattering in the following fibers and is then amplified in an Erbium-doped fiber amplifier (EDFA). The laser radiation is then compressed a first time by four-wave mixing in an $\approx$ 8,000 m long single-mode fiber (SMF) featuring anormal dispersion.

A second fiber of ≈ 7,700 m length with normal dispersion transforms the generated Gaussian pulses into parabolic shaped pulses. After passing through a second amplifier, a highly non-linear fiber (HNLF) of 500 m impresses, by phase automodulation, a linear chirp on the pulses. A last anormal dispersive single-mode fiber compresses the pulses down to values of about 8 ps.

The generated train of picosecond pulses features a spectral response of about 20 comb lines (at -10 dB) which facilitates the implementation of the Fabry-Pérot filters in the ILIADE setup.

On the other hand, the ICB source has of course some inconveniences such as the very high modulation frequency what complicates the electronics development. Further, internal implementation issues such as the Brillouin scattering are not completely resolved, but under investigation. However, the ICB sources represents a very interesting tool for the feasibility demonstration of the ILIADE experiment.

8.1.4. ILIADE development

The development of the ILIADE scheme is carried out in five partially parallel and iterative phases:

1. Design and demonstration of the chronometry and phase measurement.
   The final goal is to achieve an accuracy of less than 1 µm over not more than some tens of seconds of integration time. The instrumentation is issued from SLR and T2L2 developments, whereof some characteristics have been pointed out in this document. The evaluation of these devices is presented in the Chapters 8.2 and 8.3. They may be considered as the first generation. Currently, a second generation is under detailed development and will soon (summer 2008) be investigated as well. Out of these tests we may infer if a third generation if necessary.

2. Implementation and test of the ICB source:
   This activity concerns the implementation of the ICB pulse compressor source in the laboratory of the Observatoire de Nice. The tests concern detailed pulse characterization, that will be performed with FROG measurements[2]. Further, these measurements include the verification of the coherence length, the stability of the frequency offset, the length stability of the fibers and other issues.

3. Laser stabilization and two-frequency interferometry:
   This phase will allow the OCA team to learn to control the frequency noise of a fiber laser by locking the seed laser of the ICB source onto an iodine reference. Further, this step will investigate the frequency control operability in a simplified interferometric setup (the T2M telemeter).

4. Design and test of the line filters:
   The study will investigate how the Fabry-Pérot spectral filters may correctly be tuned to the chosen comb lines. Further, the precise control (by temperature, e.g.) of the filters will be addressed.

[2]Frequency-resolved optical gating (FROG) is a derivative of autocorrelation based on second-harmonic generation, and permits to measure ultrafast optical pulse shapes.

5. Detailed design and implementation of the setup:
   The last phase covers the detailed design and finally the assembly of the different elements of the ILIADE scheme in a common setup. The implementation of the measurement setup will start with tests of the chronometry and phase modulation signals in air. After that, the measurements will be performed in vacuum, first with measurements at short or zero arm length difference. By this means, the three measurements interferometric phase, synthetic wavelength phase and chronometry may be assessed in terms of noise contribution without being disturbed by residual fluctuations in the source repetition rate or carrier frequency. Finally the system will be characterized by measuring the three signals with a target retroreflector being placed on a high precision translation stage and calibrated with a reference interferometer.

After these work packages a sixth phase could include a replacement of the ICB source by a smaller fiber based frequency comb.

My activity is situated exclusively in part (1) of the described project phases and concerns in particular the experimental evaluation of some already existing metrology devices (phase and time-of-flight measurer). This work is described in the following two chapters.

8.2. Phase measurement

The phase measurement is of primordial significance in the ILIADE scheme, used both in the heterodyne interferometric detection and (though as a backup system) in the synthetic wavelength measurement on the modulated carrier. Some purely electronic assessment tests on existing phase measurement hardware have been performed in the beginnings of the ILIADE activity. It has to be noted that this activity had to be suspended due to the vast operations that had to be undertaken for T2L2.

The electronic measurement of two signals' respective phase may generally be measured using an analogue multiplier such as a diode. However, this solution has sundry drawbacks such as the need for equal and constant amplitudes, high noise figures and high sensitivity to temperature variation. For this reason, today this function is mostly carried out using digital signal processing techniques.

These devices are typically based on comparators that convert the incoming sine into logic signals. In one version, the two signals are then summed by an exclusive-or operation in an XOR-gate. The duty cycle of the resulting signal is now a measure of the relative phase between the two input signals (Fig. 8.3, middle). The duty cycle may then be interpreted either by a fast counter or analogously, by low-pass filtering this signal and measuring the resulting DC voltage on an ADC (analog-to-digital converter). The resolution of the phase measurement then depends on the resolution of the ADC.

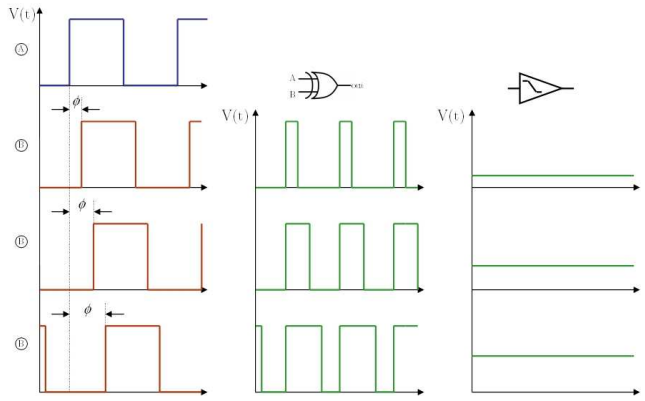

Figure 8.3.: Digital phase measurement by logical conversion, XOR-operation and duty cycle measurement with a low-pass filter

OCA disposes of such a device that has been developed for the phase-lock-loop of the local oscillator of an anterior T2L2 prototype event timer. It is based on the analogue voltage read-out technique. Yet, for the performed test in the ILIADE framework the implemented ADC could not be used since it would have necessitated the programming of an FPGA for its read-out. The DC voltage has thus been fed out to an external high-fidelity voltmeter.

For the evaluation of this phase measuring device, a low noise frequency synthesizer, referenced to a clock has been employed. The signal was split, one of the two signals delayed by putting in cables of different lengths and fed onto the measurement device. As the phase noise present on the signal (though very low due to the high quality synthesis) is common on both channels of the device, we may assume that the measurement noise is mainly coming from the measurement device and the voltmeter.

After some troubleshooting, a precision on the voltage measurement of about 3 µV could

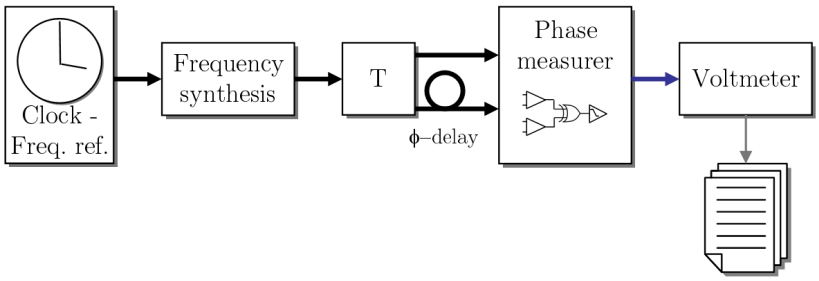

Figure 8.4.: Scheme of the electronic phase measurement evaluation

been shown, the half-wavelength (π) range being 1.6 V. This means a relative precision of about $2 \cdot 10^{-6}$. An analysis with some different, discrete phase delays further showed a good linearity of the device. In principle, the phase measurer promises to reach the wavelength scale for very short integration times (precision was determined for an acquisition of 10 seconds with 10 Hz measurement rate). The tests have been performed on an RF frequency of 200 MHz (corresponding to the synthetic wavelength); in that configuration, a precision of 1.4 µm could be demonstrated. For use at higher frequencies, such as some GHz, the circuitry has to be adopted; assuming a similar performance, a precision well below the wavelength seems achievable.

However, it was observed that the measurement device was subject to some serious drifts and fluctuations, inhibiting absolute phase measurements. This behavior has in particular been investigated in some long term tests (see Fig. 8.5), performed in a temperature-controlled environment (thermally stable chamber). The phase measurer circuitry is equally equipped with an on-board temperature sensor. The long-term quasi-linear phase drift

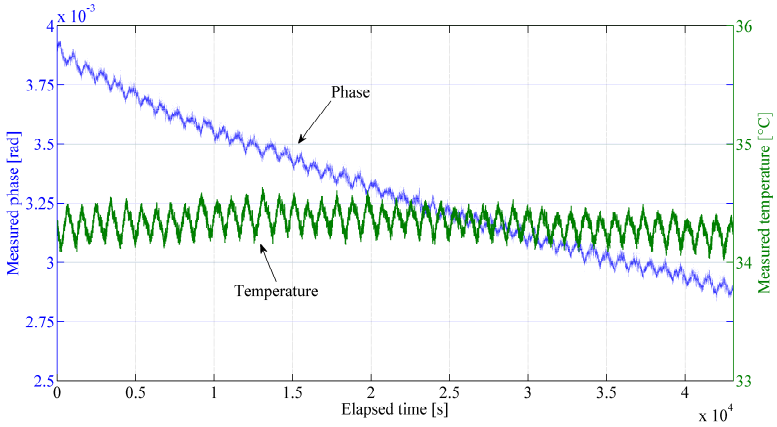

Figure 8.5.: Raw phase and temperature measurement data over 12 hours

amounts to $9.2 \cdot 10^{-5}$ rad/h (22 µm/h at 200 MHz) and is probably due to aging of the electronics and not to some real phase evolution (variation in cable lengths).

A Fourier analysis of the phase and temperature data revealed the sine-like fluctuation to have a time constant of about 1 mHz ($\approx$ 15.7 min); the effective range of the fluctuation is about $2.6 \cdot 10^{-5}$ rad (some microns). It could not be determined conclusively whether the phase measurement follows the temperature or if there is some common origin for both

fluctuating measurements. The first variant is, however, more probable. A residual temperature fluctuation range of about 0.4 °C present on the phase measurer PCB may, under circumstances, account for some microns differential propagation delay on the board.
Further, the high and low levels of ECL XOR-gates generally are quite temperature dependent; this fact is already taken account of in the electronic layout by providing a differential output, but a residual effect may still be present.

In order to assess the shorter term fluctuations, both the drift and the quasi-sinusoidal fluctuation have been removed from the data. Then the time stability (root of TVAR) has been calculated which is given in Fig. 8.6. The corrected plot evidently shows relatively pure

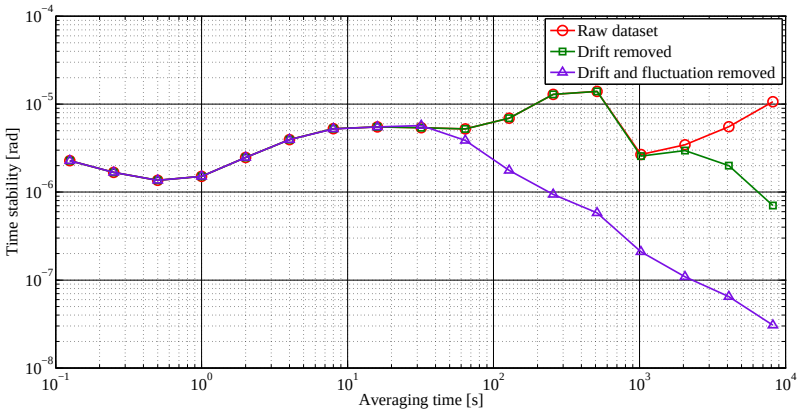

Figure 8.6.: Time stability of long term phase measurement, corrected for drift and fluctuation

white noise behavior after some tens of seconds integration time due to the data manipulation.
The three plots reveal noise processes with time constants from fractions to tens of seconds whose origins are unclear. The stabilization of this phase measurement circuitry has to be subject of further investigation in order to achieve stable and robust measurements and be able to integrate sufficiently long time to attain sub-wavelength scale. Up to now, the device allows for high resolution measurements (near-micron scale) deteriorated by a poor repeatability. Generally, the technology promises to achieve results in accordance with the ILIADE requirements.

As stated above, this experimental activity had to be suspended for the preparation of T2L2-related activities before providing more conclusive results.

8.3. Timing experiments

The timing of the laser pulses is a significant contribution to the absolute distance measurement in the ILIADE scheme. In the current project philosophy, the aim is to achieve sub-wavelength scale directly with time-of-flight measurement. Since electronics evidently are not capable to resolve signals on femtosecond scale, this goal may only be achieved by averaging over a large number of measurements. For white noise, the precision of the mean is related to the precision of a single measurement (single-shot r.m.s.) by:

$$\sigma_M = \frac{\text{r.m.s.}}{\sqrt{N_{\text{meas}}}} \tag{8.3}$$

with N_{meas} being the number of performed measurements.

The goal is thus to obtain the largest possible number of acquisitions that are subject to only white noise. Integration over a long time span is not an attractive option since flicker phase noise originating in the measurement apparatus may set in. The preferred solution is thus to use a high measurement rate.
Further, the measurement scheme should allow for stable operation over a certain time span, depending on the application (some hours, e.g.).
In a time stability plot, these two requirements manifest as a $\tau^{-1/2}$-slope falling down to a femtosecond level and staying on that level for some 10^4 seconds, for instance.

The investigation of fast (in the two senses of rate and high bandwidth) photodetection and timing electronics has been started at OCA using existing equipment that has been developed or acquired for the T2L2 activity. In this sense, T2L2 initially permitted to perform studies for the ILIADE project. However, only few activities could be performed up to now, due to the T2L2 activity concerning the technical as well as the human resources (in particular the author's time).

In the following two experiments will be shown that demonstrate the limits of the currently existing detection and timing equipment. At the time being, new devices are in preparation by Etienne Samain, notably based on high bandwidth (some tens of GHz) detectors and electronics (last ECL logic family) that will be evaluated before long.

8.3.1. Optical timing in laser cavity clock mode

The goal of the following experiments is to demonstrate high rate event timing of laser pulses. Different to the final ILIADE scheme, no real distance measurement (like in a Michelson interferometer) is performed. The devices that emulate the ILIADE systems described in Fig. 8.1 are the HighQ laser, a fast InGaAs avalanche photodiode (3 GHz) and the Dassault standard event timer, that have all been described in Chapter 3.1. The timing performance of that particular photodiode had already been determined in the preparation of the T2L2J2 test bed (Section 3.1.3).

One limitation of this setup lied in the sensitivity of the photodetector towards the laser pulse amplitude since the detector (or better the following electronics) features a simple fixed-threshold detection; amplitude variations cause temporal variations of the detected pulse edge. In order to minimize this effect, the threshold is usually set at a very low level. A further way to mitigate this problem is to operate the detector in saturated mode, that is to say, at very high incident pulse energies in order to reproduce always the same output. This procedure was realized for the T2L2 test bed as well as in the following experiment.

Another limitation is the HighQ laser synchronization to the external reference. Residual phase drifts and fluctuations of the laser pulses with respect to the reference clock signal (due to the non-perfect lock of the HighQ synchronization electronics) are directly visible in the outcome of the timings. For this reason, the residual phase noise was made common for laser and timer by reversing the referencing: The laser cavity was left free-running, and an RF reference signal was fabricated by dividing the cavity-generated (internal photodetector) signal to 10 MHz, which was fed to the Dassault event timer (Fig. 8.7). By this means, the mechanical cavity of the laser represents the clock reference of this setup. Since the Dassault

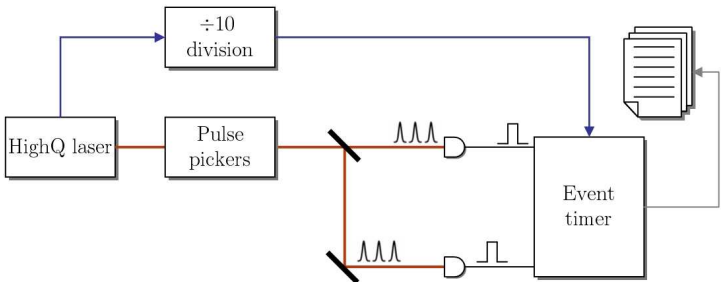

Figure 8.7.: Experiment setup in laser cavity clock mode: The HighQ laser/pulsepicker assembly emits a 2 kHz pulse train onto the fast photodetectors. The event timer's frequency synthesis is referenced to the mechanical laser cavity.

event timer is not able to operate at a high rate (with a dead time of some hundred µs), the setup was also complemented by the pulse pickers and associated electronics that had undergone some enhancing modification by the manufacturer ConOptics. The pulse pickers permitted an optical down-selection of the laser rate to a usable rate of 2 kHz.

At first, this setup permitted to ameliorate the synchronous measurement with one detector of the T2L2J2 test bed as shown in Fig. 3.31. In this mode, the dates, retrieved from a single detector, are calculated modulo 0.5 ms (for 2 kHz rep rate).
This amelioration is shown, as a time stability plot, in Fig. 8.8; the synchronous measurement reaches below a time stability of 100 fs at 1 second integration time. However, this

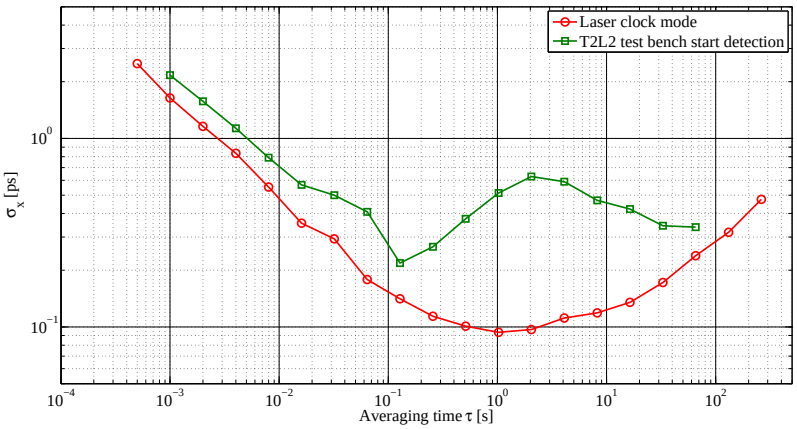

Figure 8.8.: Time stability of synchronous timing in laser cavity clock mode

scheme does not allow to integrate the measurements over a sufficient time span to attain

better precision; this is probably due to some secondary effects of the free-running cavity frequency noise on the event timer.

Using both detectors, as depicted in Fig. 8.7, allows to perform quasi-distance measurements more similar to the ILIADE scheme. For this purpose a second photodetector, similar to the first, is employed and connected to the second Dassault timer stage. The time stability is then calculated over the difference of the two timings that corresponds to a distance information (here, the difference in the path length from beam splitter to the detectors).

Just as in the time stability chart of the synchronous measurement (Fig. 8.8), the stability of this differential experiment (Fig. 8.9) reaches its flicker floor already after some seconds. Since the initial precision is about two times more elevated, the flicker floor is also higher

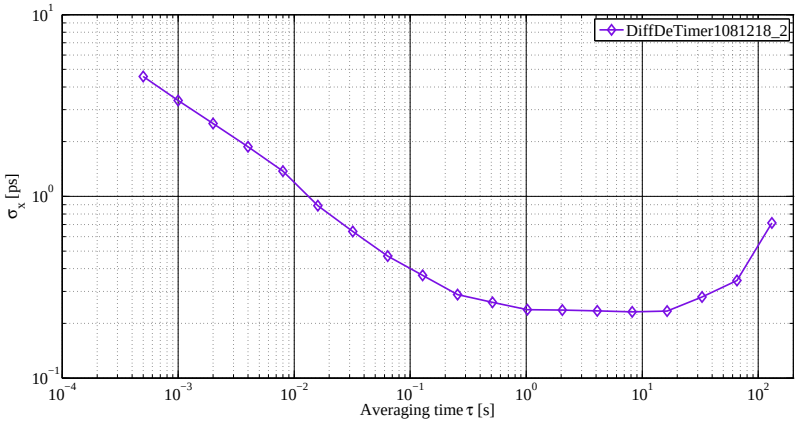

Figure 8.9.: Time stability of differential acquisition in cavity clock mode

than in the synchronous experiment. As the differential measurement in principle cancels phase fluctuations coming from the laser source (since they are common on both detectors and for a small distance), the cavity clock mode does not bring further advantages.

The following section shows a slightly different implementation of the differential measurement reaching a better precision.

8.3.2. Optical timing with electronic pulse picking

The setup that is described in the following is based on an electronic selection of the pulses rather than an optical one as performed with the electro-optic modulators (pulse pickers). The setup[3] is sketched in Fig. 8.10. The HighQ laser cavity emits its 100 MHz infrared pulse train onto the two similar detectors (InGaAs APD). The generated electronic pulse train (logic signals issued from the comparators) is divided by 50,000 employing a fast RS-flipflop that is reset by a 2 kHz signal. These logical pulses are then timed by the Dassault event timer. Both the laser cavity and the timer are phase locked to a common reference clock signal (Cesium standard).

The fact of dividing the pulse train in the electronic rather than in the optical domain has the advantage of not introducing noise due to pulse amplitude fluctuations that could be generated by the pulse pickers. These fluctuations are in reality not fully common on

[3]This experiment has been performed by Etienne and Alexandre Samain in the framework of a TIPE (Travail d'Initiative Personnelle Encadré) project of Alexandre's under-graduate school (classe préparatoire).

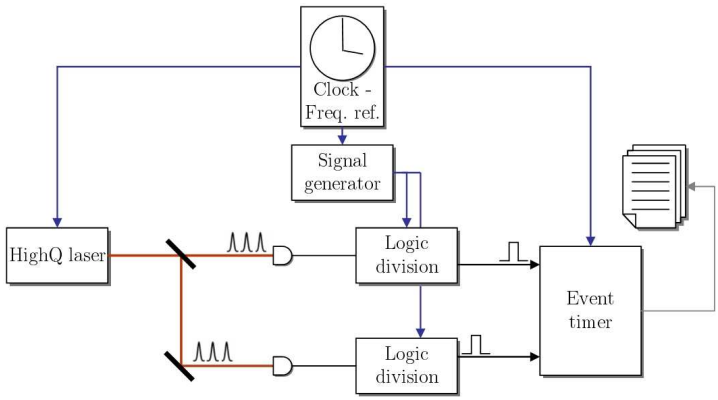

Figure 8.10.: Measurement setup for optical timing with electronic division

the two detectors, since, though both being of the same type, the electronic circuits are not identical.
The drawback of sending the whole 100 MHz pulse train onto the detectors is that they cannot be operated in saturated mode since this would represent a too high optical power level. Hence, this scheme still is sensitive to amplitude changes that may be caused by the laser itself (what probably takes place on a longer term, rather than from pulse to pulse).

The time stability plot of the differential measurement between the two detectors and the two timer stages is shown in Fig. 8.11. The initial precision (at $\tau = 0.0005$ s) of about 5 ps

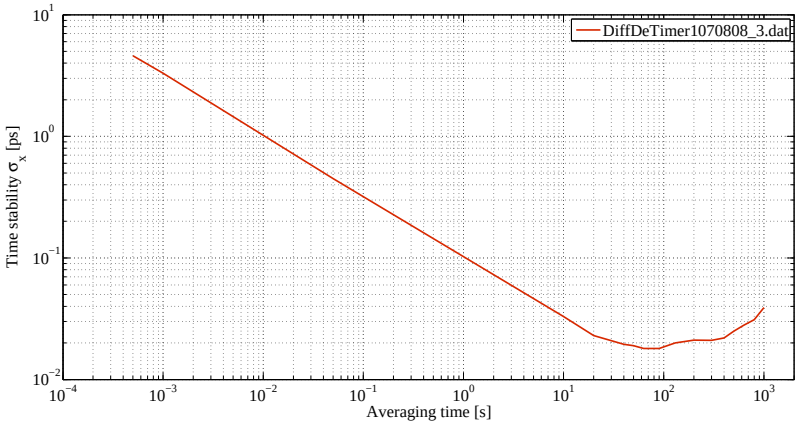

Figure 8.11.: Time stability plot of the differential measurement

is dictated by the second Dassault timer stage that features this level of performance; the other timer stage as well as the detectors feature a precision of less than 2 ps. One observes that it is possible to acquire 100,000 measurements without leaving the white phase noise domain allowing to approach a time stability of nearly 10 fs. After some tens of seconds instrumental noise is setting in.

By using a ten times higher timing rate instead of 2 kHz and a better initial precision of, say, 1 ps, one would possibly obtain a time stability of 1 fs after 50 seconds of integration. These are the two fronts that the OCA team is currently working on with the development of fast and high bandwidth detectors (with comparators) and timers. In particular, the sen-

sitivity of the detectors towards amplitude variations will be counteracted by implementing either a constant fraction or derivative detection.

8.4. Discussion

The measurements that were so far performed on the timing and phase measurement devices (that may be named the "first generation") showed promising results.

The performed electronic phase measurements nearly reach the wavelength scale in terms of resolution and precision. However, still some efforts have to be undertaken in terms of stabilizing the electronics in order to perform longer acquisitions and to assure a robust repeatability of the measurement (what enables the notion of "absolute" measurement). Further, the measurements have to be expanded onto the optical domain, employing adequate detection.

The timing measurements that have been performed on the equipment offered by the T2L2J2 campaign give the indication that the event timing precision may soon reach the wavelength scale, i.e. femtosecond precision. The experiments already demonstrated a time stability of below 20 fs after some tens of seconds integration time.

In order to attain the needed more than tenfold improvement, the future development has to focus on two aspects:
First, the inherent precision of the detection chain has to be brought on a minimum. This concerns in first order the photodetectors that represent the most fragile part in the chain. Today's high bandwidth detectors (some tens of GHz bandwidth) offer rise times of less than 10 ps what should enable detection precision of some hundred femtoseconds. Further, the timer has to offer a better precision; supposing the same principle as the T2L2J2 event timer (compare Section 2.3.5.2), a higher vernier frequency and a higher bandwidth read-out circuitry should do the job.

The second aspect is the number of measurements that allows to ameliorate the precision of a batch of data. For this reason, the measurement rate has to be brought to a maximum, in order to perform the measurement in a convenient time span and also to stay away from instrumental noise that usually comes in after some seconds to some tens of seconds (surely depending on the level).

Another aspect concerns the stabilization of the measurement devices over a longer time span in order to not deteriorate the measurement by performing it over a longer time span; in terms of time stability of a phase or epoch this means the prevailing of the TVAR on its flicker floor over a longer time span (e.g. hours or days) depending on the application without rising to higher values as it is the case for the measurements shown here (compare Fig. 8.8, 8.9 and 8.11).

All these topics are currently reconciled in the design of a new event timer and photodetection version based on the last family of fast ECL logic available on the market. For the time being, the first prototypes have been manufactured and the functional troubleshooting has been finished. In a first time, these devices will be evaluated by still employing the HighQ laser. A part of this development will also find its use in the calibration of laser stations participating in absolute time transfer with T2L2 on Jason 2.

In a second time, the build and probably still enhanced detection and timing devices will be used in conjunction with the ICB-designed 20 GHz laser that will be set up in the Nice laboratories. This will gradually allow the transition from the described ILIADE projects phases (1) to (2) (Section 8.1.4).

Conclusion and outlook

This thesis presents the results of experimental studies on some very advanced techniques for time and length metrology. The study on the T2L2J2 instrument allowed to provide important calibration data for its scientific exploitation. Further, the performance of the sole instrument and an estimation of the performance of the whole scheme has been given. Preliminary experiments on a first generation of measurement devices for ILIADE showed promising results giving reason to continue in this direction.

Both instrumental activities cross-fertilize themselves through their synergies in terms of technology. The two projects employ a large amount of resources and it is for this reason that I would like to put them into some bigger context.

The T2L2 experiment on Jason 2

The T2L2 instrument, in orbit since June 20 of this year already permits to compare today's most stable atomic clocks over large distances. Apart from the time/frequency metrology itself, this space experiment has various scientific applications such as an investigation of a possible drift on the fine structure constant α and a measure of the anisotropy of speed of light. It further contributes to the Jason 2 mission itself by providing a calibration of the on-board oscillator and allowing an enhanced laser ranging performance.

The calibration and performance assessment of the T2L2 flight instrument and its different preceding models (prototypes, engineering model) lay a basis for the successful exploitation of the instrument in space. My contribution to this important activity in the preparation of the T2L2 experiment on Jason 2 is documented in the present thesis.

The context of the activity at OCA is somewhat more vast: It further includes the detailed preparation and design of the mission what has been performed in the years 2004 and 2005; a third, very important aspect, also from the resource (human and financial) viewpoint is the modernization of the Calern fixed laser ranging station MéO (formerly Laser-Lune), in order to be able to serve as the T2L2 reference station (and other objectives). This operation, equally started in summer 2005, lasted nearly simultaneously until the launch of Jason 2 and tied up a high amount of human and financial resources. The MéO operation included, amongst others, the replacement of the azimuth and elevation axes motorization, the complete renovation of the steel dome, the design of its motorization and bearing, a new design of the optical path and the laser, the coating of the telescope mirrors, their re-alignment, and finally the establishment of a new software for the operation.
The team around the FTLRS mobile station is also directly concerned by T2L2, preparing different campaigns, for example at the Observatoire de Paris for the comparison of atomic fountains.

A last big activity is of course the preparation of the raw data, the retrieval of the date triplets, their correction and finally their first exploitation in terms of time transfer, which is all performed by the T2L2 Science Team (CMS) of OCA.

In order to illustrate the extent of the T2L2 project, Table A.5 (given in the Appendix) names the people that have been, currently are, or will be working for the project. The T2L2 operation at OCA accounts for about 30 man-years of work (assuming MéO as a part of T2L2), without even counting the time of the Calern workshop and technical service or the contribution by the Technical Division of CNRS.

The instrumental activity around the T2L2 instrument is now terminated, a new phase begins with the exploitation of the space instrument and its scientific interpretation. The successful operation and scientific exploitation will allow, on a longer term, new concepts for future time transfer systems or related instruments, such as one-way laser ranging or laser transponders. A particular fruitful impact will come from the technology developed for ILIADE, which will pursue its experimental research phase.

The ILIADE activity

The ILIADE project is on a completely different development stage as compared to T2L2. ILIADE started from the initial idea to conciliate the different competences at OCA, in the fields of interferometry and time-of-flight measurement. During the first months of my thesis I could contribute to the numerous brainstorming discussions between the ARTEMIS and GEMINI (now Géosciences Azur) teams in order to arrive at a conceptual design including the famous frequency comb. First experimental results at the "time-of-flight" group revealed so far that the aimed wavelength scale precision is within reach: The required performance may be achieved by employing some more advanced technology which is under preparation right now. The T2L2 project clearly mitigated the activity for ILIADE since nearly all human resources in our group were absorbed by it. But this circumstance may also be regarded positively, as T2L2 allowed to acquire some valuable equipment that have been and will further be used for ILIADE developments. It has to be noted that the fund acquisition for ILIADE went on slower than hoped, with one ESA tender on absolute distance measurement with frequency combs going to Menlo Systems (the company of the Hänsch people) and a first proposal refused by ANR.

The acceptance of the last proposal to ANR, in cooperation with the ICB of the University of Bourgogne (supplying a new type of laser source) and the continued support by CNES, along with the liberated resources in our group, represents some boost for the experimental activity of ILIADE. In the coming months and years its novel concept for absolute distance measurement shall be proved. This will be accompanied by new developments in terms of detectors, electronics and timers, what may in term be fruitful for future time transfer activities. It is further possible that the ILIADE scheme may be used for time transfer as well and that all activities will, in some way, merge to generate new ideas, for time transfer, distance measurement, or different fields of applications as atmospheric sounding (LIDAR) or optical altimetry.

Appendix

Table A.1.: Laser systems considered for the T2L2J2 test bed

Company	**Product**	**Technology**	**FWHM** [ps]	$\mathbf{f_{rep}}$ [MHz]	$\mathbf{P_{av}}$ [W]	**Synchro**	**Options**	**Price** [kE]
Alphalas	Picolas-532-50	Nd:YVO_4 (mode locked)	10	100	50	no	see variant CD	18.6
	Picolas-532-50-CD	Cavity Dumping	10	DC to 1	?	yes	-	42.4
AOT	ACE	Nd:YVO_4	500	25/50/100	0.5	no	MOPA available	37 + doubling
Fianium	FemtoPower	fibered	5	80	0.2	no	higher power	40
High Q Laser	Picotrain	Nd:YVO_4, SESAM	6	100	1.5	yes	Pulse elongation	102 (all)
JDS Uniphase	Microchip	Nd:YAG based chip	500	?	0.5	no	-	?
Lumera	FCS-532	?	8	160	10	no	-	85
	Rapid	Nd:YVO_4	12	DC to 0.5	2	?	Pulse elongation	138
Spectra Physics	Vanguard 2000-HM 532	Diode pumped	12	80	?	no	-	60
Toptica/PicoQuant	Pico-TA 110	Seed + MOPA	100	5 to 80	?	?	Fiber coupling	40 + doubling
	Lynx	? + SESAM	7	100	0.8	no	-	?

Table A.2.: Excerpt from BIPM's Circular T monthly publication, April 10, 2008

CIRCULAR T 243 ISSN 1143-1393
2008 APRIL 10, 14h UTC

BUREAU INTERNATIONAL DES POIDS ET MESURES
ORGANISATION INTERGOUVERNEMENTALE DE LA CONVENTION DU METRE
PAVILLON DE BRETEUIL F-92312 SEVRES CEDEX TEL. +33 1 45 07 70 70 FAX. +33 1 45 34 20 21 tai@bipm.org

1 - Coordinated Universal Time UTC and its local realizations UTC(k). Computed values of [UTC-UTC(k)]
and uncertainties valid for the period of this Circular. From 2006 January 1, 0h UTC, TAI-UTC = 33 s.

Date 2008 0h UTC	FEB 28	MAR 4	MAR 9	MAR 14	MAR 19	MAR 24	MAR 29	Uncertainty/ns		
MJD	54524	54529	54534	54539	54544	54549	54554	uA	uB	u
Laboratory k	[UTC-UTC(k)]/ns									
AOS (Borowiec)	2.9	4.2	4.5	5.5	6.1	5.8	5.0	1.5	5.1	5.3
APL (Laurel)	-14.1	-18.7	-14.6	-11.6	-6.6	-9.6	-5.6	1.5	5.1	5.3
AUS (Sydney)	127.3	109.1	108.0	120.1	129.3	114.4	116.4	1.5	5.1	5.3
BEV (Wien)	3.3	4.6	6.1	8.0	6.0	2.4	3.4	1.5	5.1	5.3
BIM (Sofiya)	-6135.7	-6152.7	-6163.7	-6164.1	-6173.3	-6197.1	-6226.8	2.0	7.1	7.4
BIRM (Beijing)	-4741.1	-4772.1	-4803.3	-4837.0	-4875.8	-4910.0	-4937.8	2.0	20.0	20.1
BY (Minsk)	226.9	236.3	245.3	255.9	263.4	262.7	279.5	7.0	20.0	21.2
CAO (Cagliari)	-1674.2	-1671.9	-1706.2	-1730.2	-1747.2	-1773.7	-1791.8	1.5	7.1	7.2
CH (Bern)	-11.5	-11.6	-10.2	-12.8	-11.6	-31.7	-114.1	0.6	1.5	1.6
CNM (Queretaro)	-47.4	-30.2	-21.4	-5.9	-6.8	-14.5	-14.7	5.0	5.1	7.1
CNMP (Panama)	119.5	135.4	141.4	154.0	169.6	189.3	200.3	3.0	5.1	5.9
DLR (Oberpfaffenhofen)	-10.2	-11.1	-6.3	-2.2	4.3	8.0	11.8	0.7	5.1	5.2
DTAG (Frankfurt/M)	170.8	171.3	172.9	183.0	188.3	172.8	166.8	4.0	10.0	10.8
EIM (Thessaloniki)	-0.6	-1.4	3.0	-0.9	2.4	2.0	1.9	3.0	20.0	20.3
HKO (Hong Kong)	53.1	50.4	42.9	36.7	43.3	44.2	34.5	2.5	5.1	5.7
IFAG (Wettzell)	-377.1	-366.2	-355.0	-350.4	-339.5	-334.6	-328.1	0.7	5.1	5.1
IGMA (Buenos Aires)	-	-	-	-	-	-	-	-	-	-
INPL (Jerusalem)	-	-	-	-	-	-	-	-	-	-
IT (Torino)	-3.1	-3.2	-3.6	-5.4	-2.4	1.1	4.7	0.5	1.5	1.6
JATC (Lintong)	6.2	12.1	10.8	4.5	-1.7	-5.5	-7.5	1.4	4.9	5.1

Table A.3.: Calibration file `ChrE070420_8.cfg` of T2L2J2 event timer

```
Fichier de configuration de l'instrument T2L2J2
\\T2l2j2\Documents\Data\T2L2J2\BT2C\Mesures\ChrE070420_8.cfg

10000 Periode
20000 Periode
10 Intervalle
20 Nombre d'harmonique Ve
  65649990.3238779                 0  65222401.8016205                 0  Harmonique Ve
  16324448.8405002 -21544401.2396418 -20568536.9281614 -17392458.609458  Harmonique Ve
  12325.9152533507 -4823.54852884585 -9744.34507949416 -13380.6343816397 Harmonique Ve
 -9734.36459614931 -49406.6375294405  36633.317863604  -22339.395856208  Harmonique Ve
  666.547940156034 -53.0532822071584  1688.68503069326  475.689434123997 Harmonique Ve
 -23412.4489920026  12647.1692151451 -16906.5050943535 -13647.8030207564 Harmonique Ve
  1482.362666117    2364.69274951085 -1807.72978863642  2980.08314733986 Harmonique Ve
 -11749.0162703123 -8948.33207390168 -14710.7979093393  14832.7162838889 Harmonique Ve
  804.661067930586  1224.28534561955 -2027.1735041314   68.4489531804825 Harmonique Ve
 -126.307843028858  132.543910733126  2364.5517676308   1870.42423096997 Harmonique Ve
  576.33657924208   490.929290549559 -2047.24822173139 -74.665582964925  Harmonique Ve
  623.59956549293   155.750986724916 -20.0772724874852 -2632.45660871811 Harmonique Ve
  4.37951722307588  1148.57633616831  1500.45915019976 -70.8235017918615 Harmonique Ve
  1159.32836782186 -1411.6914923063   49.8809542447364  492.847770277092 Harmonique Ve
  412.55504769849   653.256347574137  981.007433716852 -642.938234806408 Harmonique Ve
  1058.70649885765  338.927343561736  100.612365502588  33.9772738567845 Harmonique Ve
  154.791801680403  10.0481973589258  162.833677379332  122.101569566133 Harmonique Ve
  26.3393295516545  79.7737042729692  36.160201875861   21.770445828132  Harmonique Ve
  99.7321372106377 -25.5703562868096 -12.7570594757496 -6.1283477901501  Harmonique Ve
  92.1846040927329 -68.8163796412113 -73.9308203926325  32.5453087371676 Harmonique Ve
16687 Temps pair/impair Co
6763 Temps impair/pair Co
0.2 Erreur Max Resolution Ve
7709.80350877193 Ref Amplitude 0 Min Cal
57963.849122807  Ref Amplitude 0 Max Cal
6954.77972027972 Ref Amplitude 1 Min Cal
58251.2          Ref Amplitude 1 Max Cal
13829.6666915544 Ref Temps Cal
18775.3281278507 Ref Temps Cal
3829.33751633002 Ref Temps Cal
8774.77170148018 Ref Temps Cal
```

Figure A.1.: R.m.s. precision of the Normal Points of WLRS.
© ILRS, USA

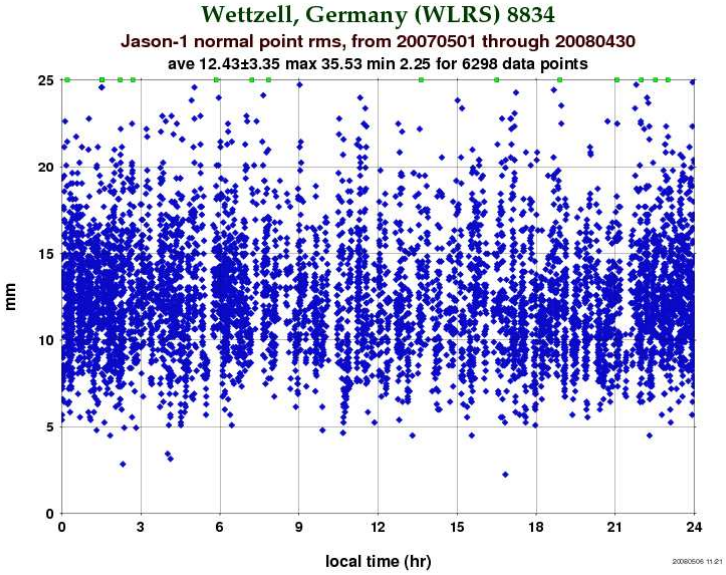

Figure A.2.: R.m.s. precision of the Normal Points of FTLRS in Burnie.
© ILRS, USA

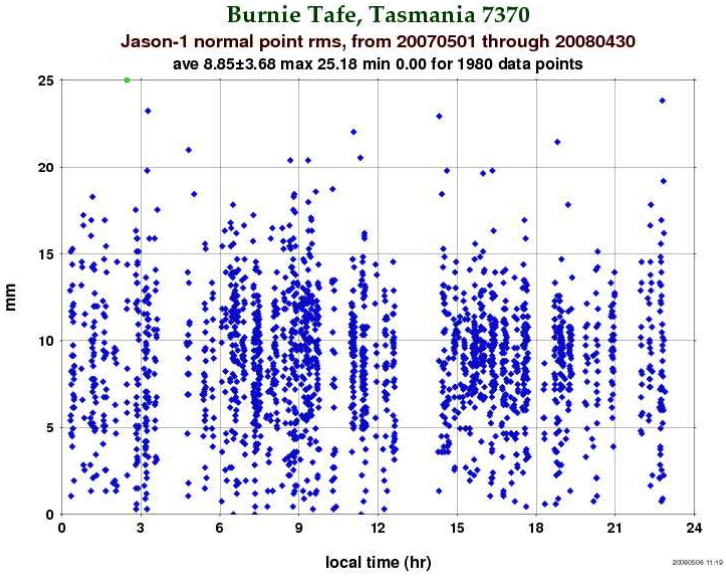

Figure A.3.: R.m.s. precision of the Normal Points of MOBLAS/Greenbelt.
© ILRS, USA

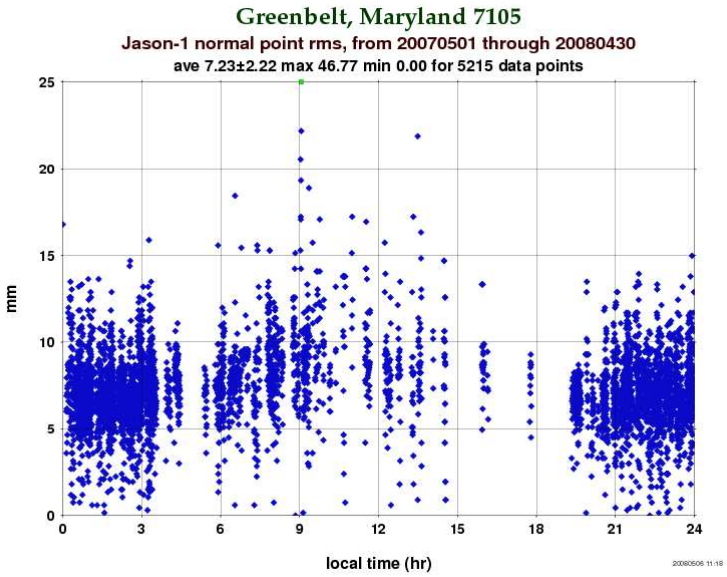

Figure A.4.: Non-common view time transfer between Greenbelt, MD and Grasse

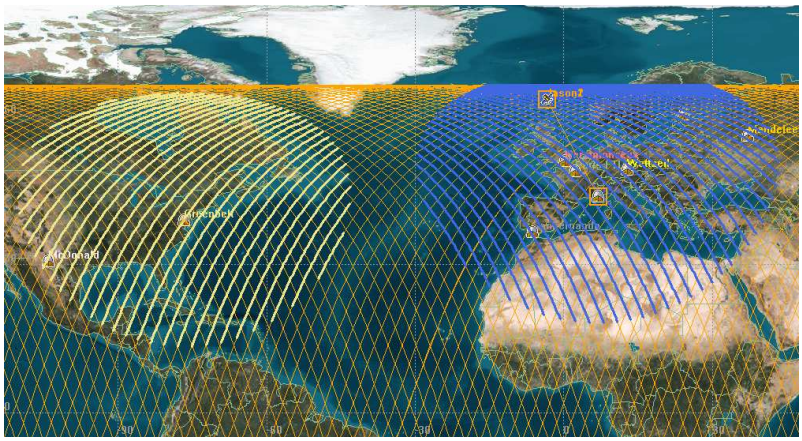

Table A.4.: Human resources working for the T2L2 project at OCA

Name	Activity	EET [yrs]
Etienne Samain	PI, all	100
Dominique Albanese	MéO, TestBed	3
Françoise Baumont	Time	0.05
Philippe Berio	Data, Science	0.05
Etienne Cuot	MéO	1.5
Robert Dalla	MéO, Test Bed	1
Aurélien Dréan	MéO, Test Bed	2.5
Julien Dufour	MéO	0.5
Olivier Dupont	MéO, Test Bed	2
Pierre Exertier	Data, Science	0.4
Maurice Furia	FTLRS	0.05
Olivier Laurain	Data	0.05
Jean-François Mangin	MéO	2
Grégoire Martinot-Lagarde	MéO	0.3
Olivier Minazzoli	Science	0.9
Jean-Louis Oneto	Time	0.05
Franck Para	MéO, Test Bed	2.5
Jocelyn Paris	MéO	3
Francis Pierron	FTLRS	0.05
Monique Pierron	FTLRS	0.05
Jean-Marie Torre	MéO	3
Hervé Viot	MéO	0.1
Patrick Vrancken	Design, Test Bed	3
Jonathan Weick	Design	2.5
Cheng Zhao	Test Bed	0.5

EET: Estimated equivalent time in years;
Data: Analysis and correction of the raw data; Design: Theoretical mission analysis and design; FTLRS: Preparation of the mobile station for T2L2; MéO: All sorts of activities for the MéO laser ranging station; Science: Exploitation in terms of time transfer; Test Bed: Concept, design, integration and operation of the metrological test bed; Time: Adaptation of Time/frequency infrastructure.

Bibliography

[1] S. Hawking, *A Brief History of Time: From the Big Bang to Black Holes.* Bantam, 1990.

[2] C. Audoin and B. Guinot, *Les fondements de la mesure du temps.* Masson, 1998.

[3] S. A. Diddams, J. C. Bergquist, S. R. Jefferts, and C. W. Oates, "Standards of time and frequency at the outset of the 21st century," *Science*, vol. 306, pp. 1318–1324, Nov. 2004.

[4] T. Parker and D. Matsakis, "Time and frequency dissemination: Advances in GPS transfer techniques," *GPS World*, vol. 15, no. 11, pp. 32–38, 2004.

[5] P. Defraigne and C. Bruninx, "GPS time and frequency transfer: State of the art," 2005.

[6] C. Salomon, N. Dimarq, A. Clairon, G. Santarelli, P. Laurent, P. Lemonde, P. Uhrich, L. G. Bernier, G. Busca, P. Thomann, E. Samain, P. Wolf, F. Gonzalez, P. Guillemot, S. Leon, F. Nouel, C. Sirmain, and S. Feltham, "Ultra stable clocks on board the International Space Station: The ACES project," in *Journées 2001 - Systèmes de référence spatio-temporels. Influence of geophysics, time and space reference frames on Earth rotation studies*, N. Capitaine, Ed., vol. 13, 2003, p. 185.

[7] A. Seidel, M. Hess, J. Kehrer, W. Schäfer, M. Kufner, M. Siccardi, L. Cacciapuoti, I. Sanches, and S. Feltham, "The ACES MicroWave Link: Instrument design and test results," in *Proc. of the IEEE International Frequency Control Symposium joint with the 21st European Frequency and Time Forum*, Geneva, Switzerland, 2007, pp. 1295–1298.

[8] W. Lewandowski and J. Nawrocki, "Satellite time-transfer: Recent developments and projects," 2005.

[9] B. Fonville, D. Matsakis, A. Pawlitzki, and W. Schäfer, "Development of carrier-phase-based Two-Way Satellite Time and Frequency Transfer (TWSTFT)," in *Proc. of the 36th Precise Time and Time Interval (PTTI) Systems and Applications Meeting*, Washington DC, USA, 2004, pp. 149–164.

[10] P. Wolf, C. Bordé, A. Clairon, L. Duchayne, A. Landragin, P. Lemonde, G. Santarelli, W. Ertmer, E. Rasel, F. Cataliotti *et al.*, "Quantum physics exploring gravity in the outer solar system: The SAGAS Project," *ArXiv e-print*, 2007.

[11] S. Schiller, G. Tino, P. Gill, and C. e. a. Salomon, "EGE (Einstein Gravity Explorer) - A class-M mission proposal for Cosmic Vision 2015-2025," *Proposal to the ESA Cosmic Vision Programme*, 2007.

[12] P. Fridelance, "L'expérience LASSO," Ph.D. dissertation, Université Paris 6, 1995.

[13] P. Fridelance, E. Samain, and C. Veillet, "T2L2 - Time transfer by Laser link: A new optical time transfer generation," *Experimental Astronomy*, vol. 7, pp. 191–207, 1997.

[14] P. Guillemot, K. Gasc, I. Petitbon, E. Samain, P. Vrancken, J. Weick, D. Albanese, F. Para, and J.-M. Torre, "Time Transfer by Laser Link: The T2L2 experiment on Jason 2," in *Proc. of the International Frequency Control Symposium*, Miami, USA, 2006, pp. 771–778.

[15] P. Guillemot, I. Petitbon, K. Gasc, E. Samain, D. Albanese, R. Dalla, M. Furia, J. Paris, J.-F. Mangin, J. Torre, P. Vrancken, and J. Weick, "Time Transfer by Laser Link: The T2L2 experiment onboard the Jason-2 space vehicle," in *Proc. of the 20th European Frequency and Time Forum - EFTF*, Braunschweig, Germany, 2006.

[16] B. Serene, "The LASSO experiment," in *Proc. of the 11th Annual Precise Time and Time Interval (PTTI) Appl. and Planning Meeting*, Nov. 1979, pp. 145–170.

[17] B. Serene and P. Albertinoli, "The LASSO experiment on the Sirio-2 spacecraft," *ESA Journal*, vol. 4, no. 1, pp. 59–72, 1980.

[18] C. Veillet, P. Fridelance, D. Feraudy, Y. Boudon, P. J. Shelus, R. L. Ricklefs, and J. R. Wiant, "LASSO observations at McDonald and OCA/CERGA: A preliminary analysis," in *Proc. of the 24th Annual Precise Time and Time Interval (PTTI) Applications and Planning Meeting*, Jun. 1993, pp. 113–122.

[19] C. J. L. Veillet, D. Feraudy, J. M. Torre, J. F. Mangin, P. Grudler, F. S. Baumont, J. C. Gaignebet, J. L. Hatat, W. Hanson, and A. Clements, "LASSO, two-way, and GPS time comparisons: A (very) preliminary status report," in *Proc. of the 22nd Annual Precuse Time and Time Interval (PTTI) Applications and Planning Meeting*, May 1990, pp. 575–582.

[20] E. Samain and P. Fridelance, "Time Transfer by Laser Link (T2L2) experiment on MIR," *Metrologia*, vol. 35, no. 3, pp. 151–159, 1998.

[21] E. Samain, D. Albanese, F. Baumont, E. Cuot, R. Dalla, P. Fridelance, K. Gasc, P. Guillemot, S. Léon, J. Mangin, J. Oneto, J. Paris, I. Petitbon, M. Ravet, J. Torre, P. Vrancken, and J. Weick, "The T2L2 Ground Experiment: Time transfer in the picosecond range over a few kilometres," in *Proc. of the 20th European Frequency and Time Forum - EFTF*, Braunschweig, Germany, 2006.

[22] E. Samain, P. Vrancken, D. Albanese, J. Paris, and J. Weick, "Etalonnage et mesure des performances de l'instrument spatial," Observatoire de la Côte d'Azur, Tech. Rep., 2005.

[23] P. Vrancken, E. Samain, D. Albanese, and F. Para, "T2L2 metrological test bed," Observatoire de la Côte d'Azur, Tech. Rep., 2006.

[24] E. Samain, "One Way Laser Ranging In The Solar System : TIPO," *EGS XXVII General Assembly*, vol. 27, p. 5808, 2002.

[25] D. Piester, B. Blanzano, K. Jaldehag, G. de Jong, P. Whibberley, J. Achkar, L. Lorini, J. Becker, I. Sesia, H. Ressler, and O. Koudelka, "Calibration of six European TWSTFT Earth stations using a portable station," in *Proc. of the 20th European Frequency and Time Forum - EFTF*, Braunschweig, Germany, 2006, pp. 460–467.

[26] Y. Menard, L. Fu, F. Parisot, S. Kaki, A. Ratier, and R. Cheney, "The Jason 2 mission: Monitoring ocean surface topography from space," Presentation to the EUMETSAT Scientific and Technical Group, 2002.

[27] "Laser Retroreflector Array (LRRA) description," JAXA, Tech. Rep. [Online]. Available: http://god.tksc.jaxa.jp/ad2/lrra/main.html

[28] H. Fagard, "DORIS Network 2006 review: Evolution, maintenance and collocations," 2006.

[29] P. Guillemot, E. Samain, and I. Petitbon, "T2L2 / Jason-2 spécification de l'instrument," 2006, TP3-JT2L2-SP-320-CNES.

[30] J. Weick and E. Samain, "Bilan de liaison Jason 2," Observatoire de la Côte d'Azur, Tech. Rep., 2005.

[31] E. Samain, "Timing of optical pulses by a photodiode in the Geiger mode," *Applied Optics*, vol. 37, pp. 502–506, Jan. 1998.

[32] G. Kirchner, private communication.

[33] Y. Fumin, H. Peicheng, I. Prochazka, Z. Zhongping, C. Wanzhen, W. Yuanming, Z. Haifeng, Z. You, F. Cunbo, and H. Xingwei, "Situation of the LTT experiment," in *Proc. of the International Laser Ranging Service - ILRS Fall Meeting*, Grasse, France, 2007.

[34] P. Vrancken, E. Samain, J. Weick, and P. Guillemot, "The T2L2 metrological test bed," in *Proc. of the IEEE Frequency Control Symposium joint with the 21st European Frequency and Time Forum*, Geneva, Switzerland, 2007, pp. 307–311.

[35] P. Vrancken, E. Samain, D. Albanese, P. Guillemot, and F. Para, "The T2L2 flight model calibration and performance determination campaign," in *Proc. of the International Laser Ranging Service - ILRS Fall Meeting*, Grasse, France, 2007.

[36] Andor Technology PLC, "DW436/436N/436O characteristics."

[37] C. Wehrli, "Extraterrestrial solar spectrum," *Physikalisch-Meteorologisches Observatorium and World Radiation Center - WRC*, no. 615, p. 10, 1985.

[38] P. Guillemot, J. Dutrey, J. Vega, M. Chaubet, D. Chebance, C. Sirmain, G. Santarelli, D. Chambon, P. Laurent, and M. Rousselet, "The PHARAO time and frequency performance verification system," in *Proc. of the IEEE International Frequency Control Symposium and Exposition*, Montreal, Canada, 2004, pp. 785–789.

[39] P. Guillemot, private communication.

[40] E. Samain, P. Vrancken, D. Albanese, P. Guillemot, and F. Para, "Essais métrologiques MV BT2C T2L2J2," Observatoire de la Côte d'Azur, Tech. Rep., 2008.

[41] ——, "Essais métrologiques MV BT2F T2L2J2," Observatoire de la Côte d'Azur, Tech. Rep., 2007.

[42] P. Vrancken, E. Samain, and P. Guillemot, "Design and test of the T2L2 (Time Transfer by Laser Link) optical subsystem," *Proceedings of the SPIE*, vol. 7003, 2008.

[43] E. Samain, P. Vrancken, J. Weick, and P. Guillemot, "T2L2 flight model metrological performances," in *Proc. of the IEEE Frequency Control Symposium joint with the 21st European Frequency and Time Forum*, Geneva, Switzerland, 2007, pp. 1291–1294.

[44] E. Samain, P. Guillemot, D. Albanese, B. Chauvineau, P. Exertier, S. Leon, O. Minazzoli, F. Para, J. Paris, I. Petitbon, J.-M. Torre, P. Vrancken, and J. Weick, "T2L2 (time transfer by laser link) current status," in *Proc. of the International Laser Ranging Service - ILRS Fall Meeting*, Grasse, France, 2007.

[45] B. Taylor and C. Kuyatt, "Guidelines for evaluating and expressing the uncertainty of NIST measurement results," 1993. [Online]. Available: http://physics.nist.gov/Document/tn1297.pdf

[46] J. Eichler and H. J. Eichler, *Laser: Bauformen, Strahlführung, Anwendungen.* Springer, 2003.

[47] E. Samain and R. Dalla, "Time walk compensation of an avalanche photo-diode with a linear photo-detection," in *Proc. of the 13th International Laser Ranging Workshop*, Washington DC, USA, 2002.

[48] J. Nicolas, F. Pierron, M. Kasser, P. Exertier, P. Bonnefond, F. Barlier, and J. Haase, "French Transportable Laser Ranging Station: Scientific objectives, technical features, and performance," *Applied Optics*, vol. 39, no. 3, pp. 402–410, 2000.

[49] J. Nicolas, "La station ultra mobile - De l'obtention d'une exactitude centimétrique des mesures à des applications en océanographie et géodésie spatiale," Ph.D. dissertation, Université de Nice - Sophia Antipolis, Dec 2000.

[50] W. Schlüter, R. Dassing, R. Kilger, and U. Schreiber, "The Fundamental Station Wettzell - current status and future plans," in *Proceedings of the International Workshop on Geodetic Measurements by the collocation of Space Techniques on Earth (GEMSTONE)*, Koganei, Japan, January 1999.

[51] Hamamatsu Corporation, "Photodiode technical information."

[52] J. Weick, "Bilan d'erreurs T2L2J2," Observatoire de la Côte d'Azur, Tech. Rep., 2007.

[53] *NIST/SEMATECH e-Handbook of statistical methods*, 2008. [Online]. Available: http://www.itl.nist.gov/div898/handbook

[54] D. Allan, "Clock Characterization Tutorial," in *Proc. of the 15th Annual Precise Time and Time Interval (PTTI) Meeting*, 1983, pp. 459–475.

[55] N. Zelensky, J. Berthias, and F. Lemoine, "DORIS time bias estimated using Jason-1, TOPEX/Poseidon and ENVISAT orbits," *Journal of Geodesy*, vol. 80, no. 8, pp. 497–506, 2006.

[56] J. Jespersen, "Introduction to the time domain characterization of frequency standards," in *Proc. of the 23th Annu. Precise Time and Time Interval (PTTI) Meeting*, 1991, pp. 83–102.

[57] E. Samain, J. F. Mangin, C. Veillet, J. M. Torre, P. Fridelance, J. E. Chabaudie, D. Feraudy, M. Glentzlin, J. van Pham, M. Furia, A. Journet, and G. Vigouroux, "Millimetric Lunar Laser Ranging at OCA (Observatoire de la Côte d'Azur)," *Astronomy and Astrophysics Supplement*, vol. 130, pp. 235–244, Jun. 1998.

[58] E. Aaron, "Jason 2 range correction - GLAS," ITE Inc., Tech. Rep., 2006.

[59] V. Mendes, G. Prates, E. Pavlis, D. Pavlis, and R. Langley, "Improved mapping functions for atmospheric refraction correction in SLR," *Geophysical Research Letters*, vol. 29, no. 10, pp. 53–1, 2002.

[60] V. Mendes and E. Pavlis, "High-accuracy zenith delay prediction at optical wavelengths," *Geophysical Research Letters*, vol. 31, no. 14, 2004.

[61] P. L. Bender, "Atmospheric refraction and satellite ranging," in *Proc. of the Symposium on Refraction of Transatmospheric Signals in Geodesy*, 1992, pp. 117–125.

[62] L. Kral, I. Prochazka, and K. Hamal, "Optical signal path delay fluctuations caused by atmospheric turbulence," *Optics Letters*, vol. 30, no. 14, pp. 1767–1769, 2005.

[63] O. Minazzoli and B. Chauvineau, "Relativistic analysis of an Earth-satellite time transfer," in *Proc. of the International Laser Ranging Service - ILRS Fall Meeting*, Grasse, France, Sep. 2007.

[64] P. Fridelance, "Influence of atmospheric turbulence on the uplink propagation in an optical time transfer," *Applied Optics*, vol. 36, no. 24, pp. 5969–5975, 1997.

[65] G. Kirchner, F. Koidl, J. Blazej, K. Hamal, and I. Prochazka, "Time-walk-compensated SPAD: multiple-photon versus single-photon operation," *Proceedings of the SPIE*, vol. 3218, p. 106, 1997.

[66] D. Hardy, "Space flight heritage of optical fiber cables," 2005.

[67] I. Bronstein, K. Semendjajew, G. Musiol, and H. Mülig, *Taschenbuch der Mathematik*, 3rd ed. Verlag Harri Deutsch, 1997.

[68] E. Samain, P. Guillemot, P. Exertier, D. Albanese, P. Vrancken, F. Para, J. Paris, J. M. Torre, I. Petitbon, and S. Léon, "Time Transfer by Laser Link - T2L2 : An opportunity to calibrate RF links," in *Proc. of the 22nd European Frequency and Time Forum - EFTF*, Toulouse, France, 2008.

[69] B. Christophe, P. H. Andersen, J. D. Anderson, S. Asmar, Ph, O. Bertolami, R. Bingham, F. Bondu, Ph, S. Bremer, J. M. Courty, H. Dittus, B. Foulon, P. Gil, U. Johann, J. F. Jordan, B. Kent, C. Lämmerzahl, A. Lévy, G. Métris, O. Olsen, J. Pàramos, J. D. Prestage, S. V. Progrebenko, E. Rasel, A. Rathke, S. Reynaud, B. Rievers, E. Samain, T. J. Sumner, S. Theil, P. Touboul, S. Turyshev, P. Vrancken, P. Wolf, and N. Yu, "Odyssey: a solar system mission," *Experimental Astronomy*, vol. 23, no. 2, March 2009.

[70] J. Degnan, "Asynchronous laser transponders for precise interplanetary ranging and time transfer," *Journal of Geodynamics*, vol. 34, no. 3-4, pp. 551–594, 2002.

[71] A. Parmar, T. Peacock, M. Bavdaz, G. Hasinger, M. Arnaud, X. Barcons, D. Barret, A. Blanchard, H. Bohringer, M. Cappi *et al.*, "XEUS - The X-ray evolving universe spectroscopy mission," *Arxiv e-print*, 1999.

[72] J. Knödlseder, "Prospects in space-based gamma-ray astronomy," *Experimental Astronomy*, vol. 20, no. 1, pp. 3–13, 2005.

[73] P. Ferrando, A. Goldwurm, P. Laurent, O. Limousin, J. Martignac, F. Pinsard, Y. Rio, J. Roques, O. Citterio, G. Pareschi *et al.*, "SIMBOL-X, a formation flying-mission for hard X-ray astrophysics," *ArXiv e-print*, 2005.

[74] C. Fridlund, "Darwin- The infrared space interferometry mission," *ESA Bulletin*, vol. 103, pp. 20–63, 2000.

[75] M. Ollivier, J. Le Duigou, D. Mourard, O. Absil, F. Cassaing, E. Herwats, L. Escarrat, B. Chazelas, F. Allard, R. Clédassou *et al.*, "PEGASE: a DARWIN/TPF pathfinder," *Proceedings of the International Astronomical Union*, vol. 1, no. C200, pp. 241–246, 2006.

[76] D. Coulter, "NASA's terrestrial planet finder missions," in *SPIE Conference Series*, J. C. Mather, Ed., vol. 5487, Oct. 2004, pp. 1207–1215.

[77] B. D. Tapley and C. Reigber, "The GRACE mission: status and future plans," *EOS Transactions*, vol. 81, no. 48, 2000.

[78] Y. Fukuda, T. Otsubo, T. Yoshino, and S. Okubo, "A new project of gravity mission studies in Japan."

[79] S. Cesare, "Laser Doppler interferometry mission for the determination of the Earth's gravity field," Alcatel Alenia Space, Tech. Rep., 2005, Executive Summary, ESTEC Contract No: 18456/04/NL/CP.

[80] J. Anderson, P. Laing, E. Lau, A. Liu, M. Nieto, and S. Turyshev, "Indication, from Pioneer 10/11, Galileo, and Ulysses Data, of an apparent anomalous, weak, long-range acceleration," *Physical Review Letters*, vol. 81, no. 14, pp. 2858–2861, 1998.

[81] ——, "Study of the anomalous acceleration of Pioneer 10 and 11," *Physical Review D*, vol. 65, no. 8, p. 82004, 2002.

[82] J. Duron, J. Marty, G. Balmino, P. Rosenblatt, S. Le Maistre, and V. Dehant, "Martian gravity field mean model and its time variations from Mars Global Surveyor and Odyssey data," *American Geophysical Union Fall Meeting*, 2007.

[83] M. Beuthe, J. Barriot, M. Pätzold, and P. Rosenblatt, "Local gravity fields from Mars Express residual Doppler data," *American Geophysical Union Fall Meeting*, 2004.

[84] K. Danzmann and A. Rüdiger, "LISA technology-concept, status, prospects," *Classical Quantum Gravity*, vol. 20, no. S1-S9, pp. 1–9, 2003.

[85] S. L. Larson, "LISA: A modern astrophysical observatory," in *Proc. of the 33rd SLAC Summer Institute on Particle Physics (SSI 2005): Gravity in the Quantum World and the Cosmos*. Menlo Park, USA: Stanford University eConf, 2005.

[86] T. Appourchaux, R. Burston, Y. Chen, M. Cruise, H. Dittus, B. Foulon, P. Gill, L. Gizon, H. Klein, S. Klioner, S. Kopeikin, H. Krueger, C. Lämmerzahl, A. Lobo, X. Luo, H. Margolis, W.-T. Ni, A. Pulido Paton, Q. Peng, A. Peters, E. Rasel, A. Rüdiger, E. Samain, H. Selig, D. Shaul, T. Sumner, S. Theil, P. Touboul, S. Turyshev, H. Wang, L. Wang, L. Wen, A. Wicht, J. Wu, X. Zhang, and C. Zhao, "Astrodynamical Space Test of Relativity using Optical Devices I (ASTROD I) - A class-M fundamental physics mission proposal for Cosmic Vision 2015-2025," *ArXiv e-prints*, vol. 802, Feb. 2008.

[87] W.-T. Ni, Y. Bao, H. Dittus, T. Huang, C. Lämmerzahl, G. Li, J. Luo, Z.-G. Ma, J. F. Mangin, Y.-X. Nie, A. Peters, A. Rüdiger, E. Samain, S. Schiller, S. Shiomi, T. Sumner, C.-J. Tang, J. Tao, P. Touboul, H. Wang, A. Wicht, X.-J. Wu, Y. Xiong, C. Xu, J. Yan, D.-Z. Yao, H.-C. Yeh, S.-L. Zhang, Y.-Z. Zhang, and Z.-B. Zhou, "ASTROD I: Mission concept and Venus flybys," *Acta Astronautica*, vol. 59, pp. 598–607, Oct. 2006.

[88] S. G. Turyshev, H. Dittus, M. Shao, K. L. Nordtvedt, Jr., C. Lämmerzahl, S. Theil, W. Ertmer, E. Rasel, R. Foerstner, U. Johann, S. Klioner, M. Soffel, B. Dachwald, W. Seboldt, V. Perlick, M. C. W. Sandford, R. Bingham, B. Kent, T. J. Sumner, O. Bertolami, J. Paramos, B. Christophe, B. Foulon, P. Touboul, P. Bouyer, T. Damour, S. Reynaud, C. Salomon, A. Brillet, F. Bondu, J. . Mangin, E. Samain, C. Erd, J. C. Grenouilleau, D. Izzo, A. Rathke, S. W. Asmar, M. Colavita, and Y. Gursel, "Fundamental physics with the Laser Astrometric Test Of Relativity," *ArXiv General Relativity and Quantum Cosmology e-prints*, Jun. 2005.

[89] B. Bertotti, L. Iess, and P. Tortora, "A test of General Relativity using radio links with the Cassini spacecraft," *Nature*, vol. 425, no. 6956, pp. 374–6, 2003.

[90] P. Antreasian and J. Guinn, "Investigations into the unexpected delta-v increases during the Earth gravity assists of Galileo and NEAR," *AIAA/AAS Astrodynamics Specialist Conference and Exhibit*, 1998.

[91] R. Dändliker, R. Thalmann, and D. Prongue, "Two-wavelength laser interferometry using superheterodyne detection," *Optics Letters*, vol. 13, no. 5, pp. 339–341, 1988.

[92] K. Bechstein and W. Fuchs, "Absolute interferometric distance measurements applying a variable synthetic wavelength," *Journal of Optics*, vol. 29, no. 3, pp. 179–182, 1998.

[93] E. Gelmini, U. Minoni, and F. Docchio, "Tunable, double-wavelength heterodyne detection interferometer for absolute-distance measurements," *Optics Letters*, vol. 19, no. 3, pp. 213–215, 1994.

[94] R. Dändliker, Y. Salvadé, and E. Zimmermann, "Distance measurement by multiple-wavelength interferometry," *Journal of Optics*, vol. 29, no. 3, pp. 105–114, 1998.

[95] O. Lay, S. Dubovitsky, R. Peters, J. Burger, S. Ahn, W. Steier, H. Fetterman, and Y. Chang, "MSTAR: A submicrometer absolute metrology system," *Optics Letters*, vol. 28, no. 11, pp. 890–892, 2003.

[96] N. Schuhler, Y. Salvadé, S. Lévêque, R. Dändliker, and R. Holzwarth, "Frequency-comb-referenced two-wavelength source for absolute distance measurement," *Optics Letters*, vol. 31, no. 21, pp. 3101–3103, 2006.

[97] Y. Salvadé, N. Schuhler, S. Lévêque, and S. Le Floch, "High-accuracy absolute distance measurement using frequency comb referenced multiwavelength source," *Applied Optics*, vol. 47, no. 14, pp. 2715–2720, 2008.

[98] D. Xiaoli and S. Katuo, "High-accuracy absolute distance measurement by means of wavelength scanning heterodyne interferometry," *Measurement Science and Technology*, vol. 9, pp. 1031–1035, Jul. 1998.

[99] B. Swinkels, T. Wendrich, N. Bhattacharya, A. Wielders, and J. Braat, "Absolute distance metrology for space interferometers," *Proc. of the SPIE*, vol. 5879, pp. 216–222, 2005.

[100] L. Perret, P. Pfeiffer, and A. Chakari, "Multi-target range finder with optical continuous frequency modulation," *Proceedings of the SPIE*, vol. 6189, 2006.

[101] A. Cabral, J. Rebordão *et al.*, "Accuracy of frequency-sweeping interferometry for absolute distance metrology," *Optical Engineering*, vol. 46, p. 073602, 2007.

[102] B. Swinkels, "High-accuracy absolute distance metrology," Ph.D. dissertation, Technische Universiteit Delft, 2006.

[103] J. Schwider and L. Zhou, "Dispersive interferometric profilometer," *Optics Letters*, vol. 19, no. 13, pp. 995–997, 1994.

[104] K. Joo and S. Kim, "Absolute distance measurement by dispersive interferometry using a femtosecond pulse laser," *Optics Express*, vol. 14, no. 13, pp. 5954–5960, 2006.

[105] J. Payne, D. Parker, and R. Bradley, "Rangefinder with fast multiple range capability," *Review of Scientific Instruments*, vol. 63, no. 6, pp. 3311–3316, 1992.

[106] I. Fujima, S. Iwasaki, and K. Seta, "High-resolution distance meter using optical intensity modulation at 28 GHz," *Measurement Science and Technology*, vol. 9, no. 7, pp. 1049–52, 1998.

[107] K. Minoshima and H. Matsumoto, "High-accuracy measurement of 240-m distance in an optical tunnel by use of a compact femtosecond laser," *Applied Optics*, vol. 39, pp. 5512–5517, 2000.

[108] ——, "High-precision distance measurement using the frequency comb of an ultrashort pulse laser," in *Conference on Lasers and Electro-Optics Europe - CLEO/Europe*, Munich, Germany, 2005.

[109] C. Rullière, *Femtosecond Laser Pulses: Principles and Experiments*. Springer, 2005.

[110] S. Cundiff, J. Ye, and J. Hall, "Optical frequency synthesis based on mode-locked lasers," *Review of Scientific Instruments*, vol. 72, p. 3749, 2001.

[111] J. Ye and S. Cundiff, *Femtosecond Optical Frequency Comb Technology*. Springer, 2005.

[112] S. Cundiff and J. Ye, "Colloquium: Femtosecond optical frequency combs," *Reviews of Modern Physics*, vol. 75, no. 1, pp. 325–342, 2003.

[113] T. Udem, R. Holzwarth, and T. Hänsch, "Optical frequency metrology," *Nature*, vol. 416, no. 6877, pp. 233–237, 2002.

[114] J. Ye, "Absolute measurement of a long, arbitrary distance to less than an optical fringe," *Optics Letters*, vol. 29, no. 10, pp. 1153–1155, 2004.

[115] M. Cui, R. Schouten, N. Bhattacharya, and S. Berg, "Experimental demonstration of distance measurement with a femtosecond frequency comb laser," *Journal of the European Optical Society*, vol. 3, 2008.

[116] C. Finot, J. Fatome, S. Pitois, and G. Millot, "All-fibered high-quality low duty-cycle 20 GHz and 40 GHz picosecond pulse sources," *IEEE Photonics Technology Letters*, vol. 19, no. 21, pp. 1711–1713, 2007.

List of acronyms

ACES	Atomic Clock Ensemble in Space
ADC	Analog-to-Digital Converter
AIV	Assembly, Integration and Verification
AMR	Advanced Microwave Radiometer
ANR	Agence Nationale de la Recherche
APD	Avalanche PhotoDiode
ARIMA	AutoRegressive-Moving Average (technique)
ARTEMIS	Astrophysique Relativiste, Théories, Expériences, Métrologie, Instrumentation, Signaux
ASI	Agenzia Spaziale Italiana
BDL	Bureau Des Longitudes
BIPM	Bureau International des Poids et Mesures
BOLI	Boîtier Linéaire
BONL	Boîtier Non-Linéaire
CCD	Charge-Coupled Device
CDMA	Code Division Multiple Access
CDR	Critical Design Review
CIE	Commission Internationale de l'Eclairage
CMS	Centre de Mision Scientifique
CNES	Centre National des Etudes Spatiales
CNRS	Centre National de la Recherche Scientifique
CSPAD	Compensated Single Photon Avalanche Diode
CV	Common view
cw	continuous wave
DAC	Digital-to-Analogue Converter
DC	Direct current
DCF77	*German longwave time signal* (IFRB call sign)
DIODE	Détermination Immédiate d'Orbite par Doris Embarqué
DOLL	Deep-space Optical Laser Link
DORIS	Détermination d'Orbite et Radiopositionnement Intégrés par Satellite
DWI	Double-Wavelength Interferometry
E.R.	Extinction Ratio
ECL	Emitter-Coupled Logic
EFTF	European Frequency and Time Forum
EGE	Einstein Gravity Explorer
EGS	European Geophysical Society
EGSE	Electronic Ground Support Equipment
EHF	Extremely High Frequency
EMC	ElectroMagnetic Compatibility
EREMS	Etudes, Réalisations Electroniques, Micro-systèmes (company)

ESA	European Space Agency
EUMETSAT	EUropean organisation for the exploitation of METeorological SATellites
FIFO	First-In, First-Out
FM	Frequency Modulation
FOM	Fontaine Mobile
FOV	Field Of View
FPGA	Field-Programmable Gate Array
FSI	Frequency Sweeping Interferometry
FSR	Free Spectral Range
FTLRS	French Transportable Laser Ranging Station
FWHM	Full Width at Half Maximum
GCT	Geocentric Coordinate Time
GEO	GEostationary Orbit
GIOVE	Galileo In-Orbit Validation Element
GLONASS	GLObalnaya NAvigatsionnaya Sputnikovaya Sistema (Global Navigation Satellite System)
GNSS	Global Navigation Satellite System
GPS	Global Positioning System
GUM	Guide to the expression of Uncertainty in Measurement
HF	High Frequency
ICB	Institut Carnot de Bourgogne
IDS	International DORIS Service
IERS	International Earth rotation and Reference systems Service
IFAG	Institut für Angewandte Geodäsie (today: Bundesamt für Kartographie und Geodäsie)
IFRB	International Frequency Registration Board
IGN	Institut Géographique National
ILRS	International Laser Ranging Service
InGaAs	Indium Gallium Arsenide
IR	Infra-Red
ISS	International Space Station
JAXA	Japan Aerospace eXploration Agency (Uchū-Kōkū-Kenkyū-Kaihatsu-Kikō)
JPL	Jet Propulsion Laboratory
KDP	KaliumDihydrogenPhosphat (Potassium-Dihydrogen-Phosphate)
LASER	Light Amplification by Stimulated Emission of Radiation
LASSO	LAser Synchronization from Stationary Orbit
LC	Inductance-capacitance (oscillating circuit)
LED	Light Emitting Diode
LIDAR	LIght Detection And Ranging
LLR	Lunar Laser Ranging
LNE	Laboratoire national de métrologie et d'essais
LORAN	LOng RAnge Navigation
LRA	Laser Retro Reflector
LTA	Lithium TAntalate
LTT	Laser Time Transfer
MASER	Microwave Amplification by Stimulated Emission of Radiation
MCP	Micro-Channel Plate

MEO	Medium Earth Orbit
MI	Modèle d'Ingeniérie
MIL Std	Military Standard
MOBLAS	MOBile LASer (ranging station)
MPQ	Max-Planck Institut für Quantenoptik
MV	Modèle de Vol
MVR	Mesure de Vitesse Radiale
MWI	Multiple Wavelength Interferometry
MWL	Microwave Link
MéO	Métrologie Optique
NA	Numerical Aperture
NAR	Non-Ambiguity Range
NASA	National Aeronautics and Space Administration
NCV	Non-common view
Nd:YAG	Neodymium-doped Yttrium Aluminum Garnet
NEP	Noise Equivalent Power
NI-Daq	National Instrumentation Data Acquisition (card)
NIST	National Institute of Standards and Technology
NOAA	National Oceanic and Atmospheric Administration
NTP	Network Time protocol
OCA	Observatoire de la Côte d'Azur
OP	Observatoire de Paris
OSTM	Ocean Surface Topography Mission (= Jason 2)
PC	Personal Computer
PCB	Printed Circuit Board
PCF	Photonic Crystal Fiber
PDR	Preliminary Design Review
PHARAO	Projet d'Horloge Atomique par Refroidissement d'Atomes en Orbite
PI	Principal Investigator
PIN	Positive Intrinsic Negative (diode)
PLL	Phase-Lock-Loop
PMT	Photo-Multiplier Tubes
PN	Pseudo Noise
PPN	Parametrized Post-Newtonian
PPS	Pulse per second
PRARE	Precise Range And Range-Rate Equipment
PROTEUS	Plate-forme Reconfigurable pour l'Observation, les Télécommunications et les Usages scientifiques (Reconfigurable Platform for Observation, Telecommunications and Scientific Applications)
PTB	Physikalisch-Technische Bundesanstalt
QR	Qualification Review
R&D	Research and Development
RDM	Recherche et Développement en Métrologie
RF	Radio Frequency
RSAM	Resonant Saturable Absorber Mirror
SAA	South-Atlantic Anomaly
SAGAS	Search for Anomalous Gravity in Space

SESAM	SEmiconductor Saturable Absorber Mirror
SESO	Société Européenne de Systèmes Optiques (company)
SHG	Second Harmonic Generation
SHM	Space Hydrogen Maser
SI	Système International d unités
SIRIO	Satellite Italiano di Ricerca Industriale Orientata
SLR	Satellite Laser Ranging
SPAD	Single-Photon Avalanche Diode
SSALTO	Segment Sol multimissions d'ALTimétrie, d'Orbitographie et de localisation précise
SSE	Sous-Système Electronique
SSO	Sous-Système Optique
SYRTE	Systèmes de Références Temps-Espace
T2L2	Time Transfer by Laser Link
T2L2J2	T2L2 on the Jason 2 satellite
TA	Temps Atomique
TAF	Temps Atomique Français
TAI	Temps Atomique International
TCXO	Temperature Controlled Crystal Oscillator
TDT	Terrestrial Dynamical Time
TEM	Transverse Electromagnetic Mode
Ti:S	Titan-Sapphire (crystal)
TM	TeleMetry
TOF	Time-Of-Flight
TOPEX	TOPography EXperiment for Ocean Circulation
TTL	Transistor-Transistor Logic
TWSTFT	Two-Way System for Time and Frequency Transfer
UDP	User Datagram Protocol
USNO	United States Naval Observatory
USO	Ultra-Stable Oscillator
UT1	Universal Time N°1
UTC	Universal Time, Coordinated
VLBI	Very Long Baseline Interferometry
WLI	White-Light Interferometry
WLRS	Wettzell Laser Ranging Station
WSOA	Wide-Swath Ocean Altimeter
XEUS	X-ray Evolving Universe Spectroscopy

List of figures

Paintings on pages 1 (00:20) and 161 (Cheval rouge) © by Meissner.

List of tables